University of Liège
Faculty of Applied Sciences
Urban & Environmental Engineering

University of Newcastle
Faculty of Engineering and Built Environment
Priority Research Centre for Geotechnical Science & Engineering

Hydro-mechanical modelling of multiphase flow in naturally fractured coalbeds applied to CBM recovery or CO_2 storage

Thesis submitted for the degree of
Philosophiae Doctor in Applied Sciences

Presented by

François BERTRAND

Submitted on September 27, 2019
Defended on February 28, 2020

Generated on March 2, 2020

This research was funded by the "FRIA-F.R.S.-FNRS"

Fonds pour la formation à la Recherche
dans l'Industrie et dans l'Agriculture

Rue d'Egmont, 5
1000 Bruxelles

And the "Wallonie-Bruxelles International" Agency

Wallonie-Bruxelles International

Place Sainctelette, 2
1080 Bruxelles

Jury:

Prof. Frédéric COLLIN	(Supervisor)	University of Liège (Belgium)
Prof. Olivier BUZZI	(Co-supervisor)	University of Newcastle (Australia)
Prof. Robert CHARLIER		University of Liège (Belgium)
Prof. Cedric GOMMES		University of Liège (Belgium)
Prof. Anne-Catherine DIEUDONNÉ		Delft University of Technology (The Netherlands)
Prof. Pierre BÉSUELLE		University of Grenoble (France)
Prof. Thierry MASSART		Free University of Brussels (Belgium)
Prof. Jean-Michel PEREIRA		Ecole des Ponts - ParisTech (France)

STATEMENT OF ORIGINALITY

I hereby certify that the work embodied in the thesis is my own work, conducted under normal supervision. I confirm that the thesis contains no material which has been accepted, or is being examined, for the award of any other degree or diploma in any university or other tertiary institution, with the exception of the approved partner university associated with this Dual Award Doctoral Degree. To the best of my knowledge and belief, the thesis contains no material previously published or written by another person, except where due reference has been made. I give consent to the final version of my thesis being made available worldwide when deposited in the University of Newcastle Digital Repository and its equivalent at the partner university, subject to the provisions of the Copyright Act 1968 and any approved embargo.

F. Bertrand

ACKNOWLEDGMENT OF AUTHORSHIP

I hereby certify that the work embodied in this thesis contains published papers of which I am a joint author. I have included as part of the thesis a written declaration endorsed in writing by my supervisor, attesting to my contribution to the joint publications.

By signing below I confirm that François Bertrand contributed to write the papers entitled *A fully coupled hydro-mechanical model for the modeling of coalbed methane recovery* (published), *Cleat-scale modelling of the coal permeability evolution due to sorption-induced strain* (under review for publication on March 2, 2020) and *Application of the FE2 method to the hydro-mechanical modelling of multiphase flow in fractured coalbed* (in preparation on March 2, 2020), for which he developed and implemented some constitutive models.

F. Collin

Remerciements

Cette thèse est le fruit d'un travail personnel mais c'est aussi, et surtout, des rencontres. Je tiens à remercier toutes les personnes qui ont enrichi ma réfélexion, par de longues discussions ou parfois au détour d'un couloir.

Mes premiers remerciements vont bien sûrs à mes deux promoteurs, Frédéric et Olivier.

A Frédéric, merci de m'avoir donné l'opportunité de travailler sur un sujet aux multiples facettes. J'en retiens des intérêts économiques, des enjeux de société et bien sûr des défis scientifiques. Merci de m'avoir confié un sujet de thèse pionnier pour notre équipe. J'y ai vu l'opportunité d'explorer librement différents aspects : de la mécanique, de l'hydraulique, des couplages multi-physiques, des mathématiques, du multi-échelle, de la modélisation, de l'expérimental,... Bref, je ne me suis pas ennuyé. Par-dessus tout, merci pour son soutien de tous les instants tout au long de ces années.

A Olivier, merci de m'avoir fait découvrir les joies et les peines du laboratoire. Cela a permis d'apporter une nouvelle dimension à cette thèse. Merci qui plus est de m'avoir fait découvrir un pays si extraordinaire Down Under. Que de paysages magnifiques visités au cours de mon séjour à Newcastle. Merci pour l'acceuil.

Il y a eu Liège, Newcastle... et Grenoble. Merci à Jacques et Pierre de m'avoir acceuilli à Grenoble quelques samaines dès le début de ma thèse pour aborder les questions multi-échelles. Il m'aura finalement fallu du temps pour revenir sur cet aspect qui clotûre ma thèse.

Sur cette route, il y a eu quelques étapes importantes, notamment les réunions du comité de thèse. Merci à Robert, Cédric et Frédéric de m'avoir accompagné un bout de chemin et de m'avoir orienté dans mes recherches lors de nos réunions.

Le travail de chercheur implique aussi de partager ses connaissances. Il y a bien sûr eu les conférences mais je retiens aussi les activités d'enseignement. Elles ont parfois été source de désillusions mais aussi, de temps en temps, d'émerveillement et de satisfaction d'avoir pu transmettre. Merci à Robert et Simon pour nos échanges pédagogiques au cours de ces années.

Le doctorat, c'est un peu combiner études et travail, avoir un bureau et des collègues avec qui j'ai pu lier des liens d'amitié. Merci à Julien avec qui j'ai partagé mes journées, formuler un problème avec lui était déjà le début d'une solution. Merci à Anne-Catherine pour sa légendaire bonne humeur, j'entends encore parfois son rire dans le couloir. Je me demande si j'y serais sans elle. Merci à Benjamin pour son soutien dans mes premières épreuves de débuggage et son aide en général. Merci à tous ceux que j'ai croisés par ici, Simon, Benoît, Georgia, Elnaz, Sanae, Gilles, Albert, Kien et Liliana, ou par là-bas, Marina, Giusy, Andrea, Federico, Louis-Marin, Davide, Rita, Mattia et Yang. Cette thèse était une aventure humaine formidable grâce à vous. J'en garde des vidéos plein la tête.

Un merci particulier à mes soutiens financiers. Merci au FNRS de m'avoir procuré une liberté de chercher, ce n'est réellement pas qu'un slogan. Merci au WBI de m'avoir inspiré au bout du monde.

Enfin, tout simplement merci à ma famille, à ma sœur et à mes parents, pour leur soutien indéfectible. Nous traversons les épreuves ensemble.

Abstract

This thesis is dedicated to the modelling of multiphase flows in naturally fractured rocks and, in particular, to the recovery of methane, or reversely to the storage of carbon dioxide, in coalbeds. In this context, some hydro-mechanical couplings can likely affect the permeability of the reservoir. On the one hand, the increase in effective stress after the reservoir depletion tends to decrease the permeability. On the other hand, the matrix shrinkage following gas desorption tends to increase the permeability. These phenomena are highlighted with some experimental tests carried out in laboratory. Some numerical models are developed in this thesis to properly take into account the permeability evolution during the gas production/storage. As coal is rarely dry *in situ*, constitutive models are developed for unsaturated conditions. These models are implemented in the finite element code Lagamine.

The first model is developed at the macroscale, as generally followed in the literature for reservoir modelling. Then, fractures and matrix blocks are directly modelled with a microscale model. Particular attention is paid to the applicability of unsaturated formalism to a single fracture (modelled with an interface finite element). The numerical permeability model at the fracture scale is also compared to the analytical solution of a simple geometry. Finally, in order to model a reservoir, the modelling of the representative elementary volume is integrated in a multiscale approach with the finite element square method.

The first part of the thesis presents the context of the research. After a literature review of some remarkable experimental results, an experimental study on a Australian coal is then presented in the second part. The macroscale (reservoir scale), the microscale (laboratory scale) and the multiscale (from the laboratory to the reservoir) models are then presented in distinct parts. Finally, the last part contains the general conclusions of the thesis.

Résumé

Cette thèse est consacrée à la modélisation des écoulements multiphasiques au sein de réservoirs naturellement fracturés, plus particulièrement à la production du méthane des couches de charbon ou au stockage de dioxide de carbone dans ces veines de charbon. Dans ce contexte, des couplages hydro-mécaniques peuvent affecter la perméabilité du réservoir. D'une part, l'augmentation des contraintes effectives après une baisse de pression du réservoir tend à diminuer la perméabilité. D'autre part, le retrait de la matrice de charbon suite à la désorption du gaz tend à augmenter la perméabilité. Ces phénomènes sont mis en évidence par des essais hydro-mécaniques réalisés en laboratoire. Des modèles numériques sont dévéloppés afin de tenir compte de l'évolution de la perméabilité au cours de la production ou du stockage de gaz. A noter que le charbon est rarement sec *in situ*, les modèles constitutifs sont donc écrits en non-saturé. Ces modèles sont ensuite implémentés dans le code élément fini Lagamine.

Le premier modèle est développé à l'échelle macroscopique, comme ce qui se fait régulièrement dans la littérature pour les modélisations de réservoirs. Ensuite, un modèle microéchelle est développé pour décrire directement le comportement des fractures et des blocs matrice. Une attention particulière est portée à l'applicabilité du formalisme non-saturé à l'échelle d'une fracture unique (modélisée par un élément fini interface). Le modèle numérique de perméabilité à l'échelle de la fracture est aussi comparé à la solution analytique d'une géométrie simple. Finalement, ce modèle à l'échelle élémentaire est intégré dans une approche multi-échelle grâce à la méthode des éléments finis au carré en vue d'une modélisation à l'échelle d'un réservoir.

La première partie de la thèse présente le contexte des recherches. Ensuite, après une revue bibliographique de quelques résultats expérimentaux remarquables, la deuxième partie présente une étude expérimentale menée sur un charbon australien. Les modèles macro-échelle (échelle du réservoir), micro-échelle (échelle du laboratoire) et multi-échelle (du laboratoire au réservoir) sont ensuite présentés dans des parties distinctes. Enfin, la dernière partie contient les conclusions générales de la thèse.

Preface

The work presented in this thesis has been published or is under consideration for publication in different scientific journals. You will find below a list of these publications or expected ones. In order to improve the readability, these papers have been extended, merged and linked to constitute the thesis. Some introduction and conclusions parts are also added.

Macroscale [Bertrand et al., 2017]:

Bertrand, F., Cerfontaine, B., and Collin, F. A fully coupled hydro-mechanical model for the modeling of coalbed methane recovery. *Journal of Natural Gas Science and Engineering*. (2017).

Microscale [Bertrand et al., 2019]

Bertrand, F., Buzzi, O., and Collin, F. Cleat-scale modelling of the coal permeability evolution due to sorption-induced strain. *Journal of Coal Geology*. (2019).

Multiscale [Bertrand et al., 2020] :

Bertrand, F., Buzzi, O., Bésuelle, P., and Collin, F. Hydro-mechanical modelling of multiphase flow in naturally fractured coalbed using a multi-scale approach. *Journal of Natural Gas Science and Engineering*. (2020).

Moreover, the results of the research were also presented in the form of posters or presentations at different national and international conferences or seminars. In chronological order:

Macroscale simple-porosity model:
Efficiency of shaft sealing for CO_2 sequestration in coal mines. Workshop EAGE "Geomechanics and Energy". Celle (Germany). 12 to 15 October 2015.

Macroscale dual-porosity model, hydraulic part:
Geomechanical aspects of coalbed methane (CBM) production : Flow model formulation. RUGC 2016. Liège (Belgium). 24 to 27 May 2016.

Macroscale dual-porosity model:
Hydro-mechanical modelling of coalbed methane flows: A hypothetical reservoir example. Contact FNRS Day on "Geomechanics and Couplings". Gembloux (Belgium). 9 February 2017.

Macroscale dual-porosity model:

Simulation of coalbed methane flows, hydro-mechanical modelling in a particular fractured reservoir. 79th EAGE conference. Paris (France). 12 to 15 June 2017.

Macroscale dual-porosity model:

Hydro-mechanical modelling of a coalbed methane production well via a dual-porosity approach. GeoProc 2017. Paris (France). 5 to 7 July 2017.

Microscale direct model:

Modelling of the permeability alteration of coal due to sorption. Lagashop 2018. Delft (The Netherlands). 31 January to 2 February 2018.

Macroscale and microscale models comparison:

Modelling of the permeability evolution of coal due to sorption: Review of different scales analysis. PhD UoN Seminar. Newcastle (Australia). 23 July 2018.

Experimental results and microscale model:

Laboratory-scale study on the swelling behaviour of coal due to CO2 injection. 5th CO2 Geological Storage Workshop. Utrecht (The Netherlands). 21 to 23 November 2018.

Multiscale model:

Hydro-mechanical modelling of multiphase flow in coalbed by computational homogenization. 16th International Conference of IACMAG. Turin (Italy). 1 to 4 July 2020.

Contents

List of Symbols

Acronyms

AMM	Abandoned mine methane
ASTM	American Society for Testing and Materials
CBM	Coalbed methane
CCS	Carbon dioxide Capture and Storage
CMM	Coal mine methane
CSG	Coal seam gas
UCG	Underground coal gasification

Greek Symbols

1 $_w$	Water compressibility	$M\ ^1LT^2$
	Species	
	Linear sorption-induced strain coefficient	
	Volumetric sorption-induced strain coefficient	$ML\ ^3$
	Bishop's stress parameter	
	Discrete variation of a quantity	
	Infinitesimal variation of a quantity	
$_{ij}$	Kronecker symbol	
t	Time step	T
t	Sub time step	T
	Second coordinate for the parent finite element	
	External surface of the domain	$ML\ ^1T\ ^2$
	Swelling pore strain parameter	
$_0$	External reference surface of the REV	L^2
$_c$	Contact boundary between matrix blocks	L^2
$_{\overline{q}}$	Boundaries with imposed flux $\overline{q}$	L^2
$_{\tilde{q}}$	Boundaries with imposed flux $\tilde{q}$	L^2
	Geometric transmissivity function along the channel	L^3

$_{n}$	Knudsen number	
$_{ob}$	Penalty coefficient for the outer boundary flow	$L\ ^{1}T\ ^{1}$
	Tortuosity	
	Cleat size distribution index	
$_{m}$	First Lamé parameter of the matrix	$ML\ ^{1}T\ ^{2}$
μ	Dynamic viscosity	$ML\ ^{1}T\ ^{1}$
μ_{f}	Friction coefficient	
μ_{g}	Gas viscosity	$ML\ ^{1}T\ ^{1}$
μ_{r}	Viscosity ratio	$ML\ ^{1}T\ ^{1}$
μ_{w}	Water viscosity	$ML\ ^{1}T\ ^{1}$
	Poisson's ratio	
$_{m}$	Poisson's ratio of the matrix	
$_{ij}$	Poisson's ratios of the equivalent medium	
	Volume of the control space	L^{3}
$_{0}$	Reference volume of the REV	L^{3}
$_{e}$	Volume of a finite element e	L^{3}
$_{f}$	Volume of the fractures	L^{3}
$_{g}$	Gas volume	L^{3}
$_{g}$	Void volume	L^{3}
$_{g}$	Gas mass flux in the channel	$MT\ ^{1}$
$_{v}$	Void volume	L^{3}
$_{w}$	Water mass flux	$MT\ ^{1}$
	Porosity	
$_{l}$	Geometric transmissivity of the channel	L^{2}
$_{0}$	Initial porosity (t 0)	
$_{f}$	Porosity from fractures	
	Phase	
	Shape factor	$L\ ^{2}$
	Density	$ML\ ^{3}$
$_{c}$	Coal density	$ML\ ^{3}$
$_{g}$	Gas density	$ML\ ^{3}$
$_{s}$	Solid density	$ML\ ^{3}$
$_{v}$	Water vapour density	$ML\ ^{3}$
$^{0}_{v}$	Density of saturated water vapour	$ML\ ^{3}$
$_{w}$	Water density	$ML\ ^{3}$
$_{g\,f}$	Gas density in the cleats	$ML\ ^{3}$

$\rho_{g,f}$	Gas density in the fracture	$[ML^{-3}]$
$\rho^{d}_{g,f}$	Density of dissolved gas in water	$[ML^{-3}]$
$\rho_{g,std}$	Gas density at standard conditions	$[ML^{-3}]$
ρ_{g_0}	Reference gas density	$[ML^{-3}]$
ρ^{Ad}_{g}	Density of gas adsorbed on the matrix	$[ML^{-3}]$
ρ_{w_0}	Reference water density	$[ML^{-3}]$
σ_{ij_0}	Initial stresses	$[ML^{-1}T^{-2}]$
σ_{ij}	Cauchy stress tensor	$[ML^{-1}T^{-2}]$
σ'_{ij}	Effective stress tensor	$[ML^{-1}T^{-2}]$
τ	Shear stress	$[ML^{-1}T^{-2}]$
$\tau_{c,w}$	Channel tortuosity of the water phase	$[-]$
τ_{cgw}	Channel tortuosity of the gas phase	$[-]$
Θ	Number of sites covered by adsorbed molecules	
θ	Angle	$[-]$
$\tilde{\sigma_{ij}}$	Jaumann stress rate	$[ML^{-1}T^{-3}]$
ε	Small perturbation	
ε_b	Bulk strain	$[-]$
ε_p	Pore strain	$[-]$
ε_{b_s}	Bulk sorption-induced strain	$[-]$
ε_{ij}	Strain tensor	$[-]$
ε_{p_s}	Pore sorption-induced strain	$[-]$
Ξ	Volume fraction	$[-]$
ξ	First coordinate for the parent finite element	
Ξ_g	Gas volume fraction	$[-]$
Ξ_l	Liquid volume fraction	$[-]$
Ξ_s	Solid volume fraction	$[-]$
ζ	Tortuosity parameter	$[-]$
ε_{vs}	Volumetric sorption-induced strain	$[-]$
$\varepsilon_{(ii)_s}$	Linear sorption-induced strain in the direction i	$[-]$

Roman Symbols

$[A]$	Matrix of partial derivatives of coordinates for a parent continuum element
$[A^I]$	Matrix of partial derivatives of coordinates for an interface element
$[B]$	Matrix of partial derivatives of shape functions for a parent continuum element

$[B^I]$	Matrix of partial derivatives of shape functions for an interface element	
$[C_{mm}]$	Mechanical constitutive matrix	$[ML^{-1}T^{-2}]$
$[K_{mm}]$	Mechanical stiffness matrix	$[ML^{-1}T^{-2}]$
$\Delta\mathcal{H}$	Differential enthalpy of adsorption	$[ML^2T^{-2}N^{-1}]$
$\Delta\mathcal{S}^0$	Standard molar integral entropy at saturation	$[ML^2T^{-2}N^{-1}\theta^{-1}]$
$\mathcal{A}$	Adsorbed gas content parameter	$[-]$
$\mathcal{C}_g$	Integration constant	$[T^{-1}]$
$\mathcal{C}_w$	Integration constant	$[T^{-1}]$
$\mathcal{K}$	Some internal variables	
$\mathcal{M}_g$	Gas molecules	
$\mathcal{N}$	Interpolation function	
$\mathcal{O}-$	Vacant surface sites	
$\mathcal{P}$	Point with coordinates x_i	
$\mathcal{T}$	Sorption time	$[T]$
$\mathcal{Z}$	Integration constant	$[LT^{-1}]$
$\mathcal{Z}_g$	Integration constant	$[LT^{-1}]$
$\mathfrak{N}$	Power-law function describing a fractal distribution	
$\bar{l}$	Gas mean free path	$[L]$
$\overline{q}$	Boundary flow	$[LT^{-1}]$
$\overline{q}_g$	Gas boundary flow	$[LT^{-1}]$
$\overline{q}_w$	Water boundary flow	$[LT^{-1}]$
$\bar{t}_i$	External traction force	$[ML^{-1}T^{-2}]$
$\{f\}$	Global nodal force components	
$\{u\}$	Global nodal displacement components	
$\{U^{Node}\}$	Column vectors of nodal displacements	$[L]$
$\{V^{Node}\}$	Column vectors of nodal velocities	$[LT^{-1}]$
$\{X^{Node}\}$	Column vectors of nodal positions	$[L]$
A	Area or Boundary surface area	$[L^2]$
a	Constant of proportionality	$[-]$
a'	Constant of proportionality	$[-]$
a''	Constant of proportionality	$[-]$
b	Biot's coefficient	$[-]$
b_g	Klinkenberg number	$[-]$
b_{ij}	Biot's coefficient tensor	$[-]$
C	Concentration	$[NL^{-3}]$

c	Kundt and Warburg's constant	$[-]$
C_g	Gas concentration	$[NL^{-3}]$
C_{ijkl}	Constitutive mechanical (stiffness) tensor	$[ML^{-1}T^{-2}]$
D_f	Fractal dimension	$[-]$
d_g	Collision diameter of a gas molecule	$[L]$
d_p	Pore diameter	$[L]$
D_{β}^{α}	Diffusion coefficient of the species α through β	$[L^2T^{-1}]$
$D_{\beta}^{\alpha^{\divideontimes}}$	Effective diffusion coefficient of the species α through β	$[L^2T^{-1}]$
D_{ijkl}	Compliance tensor	$[M^{-1}LT^2]$
E	Mass exchange between matrix blocks and fractures	$[MT^{-1}]$
E_i	Young's moduli of the equivalent medium	$[ML^{-1}T^{-2}]$
E_m	Young's modulus of the matrix	$[ML^{-1}T^{-2}]$
F_i	Force vector	$[ML^{-2}T^{-2}]$
f_i	Flux	$[ML^{-2}T^{-1}]$
F_E	Energetically equivalent external nodal forces	
f_{g_i}	Internal total flux of gas	$[ML^{-2}T^{-1}]$
f_{g_L}	Longitudinal gas mass flux	$[ML^{-2}T^{-1}]$
$f_{g_T}^{k}$	Transverse gas mass flux	$[ML^{-2}T^{-1}]$
F_{ij}	Deformation gradient tensor	$[-]$
F_I	Energetically equivalent internal nodal forces	
F_{OB}	Out of balance forces	
f_{w_i}	Internal total flux of water	$[ML^{-2}T^{-1}]$
f_{w_L}	Longitudinal water mass flux	$[ML^{-2}T^{-1}]$
G_m	Shear modulus of the matrix blocks	$[ML^{-1}T^{-2}]$
G_{ij}	Shear moduli of the equivalent medium	$[ML^{-1}T^{-2}]$
H	Height	$[L]$
h	Fracture aperture	$[L]$
h^{min}	Minimum fracture aperture	$[L]$
h_b	Hydraulic fracture aperture	$[L]$
H_g	Henry's coefficient	$[-]$
h_g	Height of the gas stratum in the fracture	$[L]$
h_w	Height of the water stratum in the fracture	$[L]$
$J_{g_i}^{g}$	Diffusive mass flux of gas in the gas phase	$[ML^{-2}T^{-1}]$
$J_{g_i}^{w}$	Diffusive mass flux of water vapour	$[ML^{-2}T^{-1}]$
J_{ij}	Jacobian matrix	$[-]$

$J^g_{l_i}$	Diffusive mass flux of dissolved gas in the liquid phase	$ML^{2}T^{1}$
$J^g_{m_i}$	Diffusive mass flux of gas in the matrix	$ML^{2}T^{1}$
K	Global stiffness matrix	
k	Permeability	L^2
k_0	Initial permeability (t 0)	L^2
k_B	Boltzmann constant	$ML^2T^{2}{}^{1}$
K_c	Equilibrium constant of a reaction	
k_e	Effective intrinsic permeability	L^2
K_m	Bulk modulus of the matrix blocks	$ML^{1}T^{2}$
K_n	Normal stiffness of the fracture	$ML^{2}T^{2}$
K_n^0	Normal stiffness of the fracture for zero-displacement	$ML^{2}T^{2}$
K_p	Cleat stiffness	$ML^{1}T^{2}$
K_s	Shear stiffness of the fracture	$ML^{2}T^{2}$
k_{cleat}	Cleat permeability	L^2
k_{rg}	Relative permeability to gas	
k_{rw}	Relative permeability to water	
L	Fracture length	L
l	Width of the contact zone	L
L_c	Macroscopic characteristic length	L
l_c	Microscopic characteristic length	L
l_u	Length of a capillary tube	L
L_{ij}	Velocity gradient field	T^{1}
l_{REV}	Size of the REV	L
M	Mass	M
m	Material	L
M_g	Gas mass content	M
M_m	P-wave modulus of the matrix	$ML^{1}T^{2}$
M_w	Water mass content	M
$M^d_{g\,f}$	Gas mass dissolved in the water in the fracture	M
$M^g_{g\,f}$	Gas mass in the gas phase in the fracture	M
$M^{Ad}_{g\,m}$	Gas mass adsorbed in the matrix	M
M_{m_g}	Gas molecular mass	MN^{1}
M_{m_w}	Water molecular mass	MN^{1}
N	Number of sets of fractures	
N_i	Unit vector normal to the surface of the REV	

n_i	Unit vector normal to the boundary	
n_{rg}	Exponent parameter for the stauration degree formulation	
n_{rw}	Exponent parameter for the stauration degree formulation	
p	Pressure	$ML^{-1}T^{-2}$
p_0	Initial pressure ($t = 0$)	$ML^{-1}T^{-2}$
p_a	Atmospheric pressure	$ML^{-1}T^{-2}$
p_c	Capillary pressure	$ML^{-1}T^{-2}$
p_e	Entry capillary pressure	$ML^{-1}T^{-2}$
p_f	Fracture pressure	$ML^{-1}T^{-2}$
p_g	Gas pressure	$ML^{-1}T^{-2}$
p_g	Virtual gas pressure	$ML^{-1}T^{-2}$
p_g^f	Fluctuation of gas pressure	$ML^{-1}T^{-2}$
P_L	Langmuir pressure	$ML^{-1}T^{-2}$
p_m	Matrix pressure	$ML^{-1}T^{-2}$
p_w	Water pressure	$ML^{-1}T^{-2}$
p_w	Virtual water pressure	$ML^{-1}T^{-2}$
p_w^f	Fluctuation of water pressure	$ML^{-1}T^{-2}$
$p_{g\,f}$	Gas pressure in the fractures	$ML^{-1}T^{-2}$
$p_{g\,m}$	Gas pressure in the matrix	$ML^{-1}T^{-2}$
$p_{g\,m}^0$	Initial gas pressure in the matrix	$ML^{-1}T^{-2}$
$p_{g\,m}^{lim}$	Limit gas pressure	$ML^{-1}T^{-2}$
$p_{g\,m}^{max}$	Maximum gas pressure in the matrix	$ML^{-1}T^{-2}$
$p_g^{Ad^{lim}}$	Limit adsorbed gas pressure	$ML^{-1}T^{-2}$
p_g^{Ad}	Adsorbed gas pressure in the matrix	$ML^{-1}T^{-2}$
$p_g^{Ad^b}$	Adsorbed gas pressure in equilibrium with the fracture pressure	$ML^{-1}T^{-2}$
P_{ij}	First Piola-Kirchhoff stress tensor	$ML^{-1}T^{-2}$
p_{rb}	Rebound pressure	$ML^{-1}T^{-2}$
p_{res}	Reservoir pressure	$ML^{-1}T^{-2}$
p_{res}^{crit}	Critical reservoir pressure	$ML^{-1}T^{-2}$
p_{w_0}	Reference water pressure	$ML^{-1}T^{-2}$
Q	Source term	$ML^{-3}T^{-1}$
q	Flow	LT^{-1}
q_f	Flow between two parallel plates	LT^{-1}
Q_g	Gas source term	$ML^{-3}T^{-1}$

q_g	Input gas flux	$[ML^{-2}T^{-1}]$
q_i	Flow vector	$[LT^{-1}]$
q_L	Longitudinal flow	$[LT^{-1}]$
q_N	Total flow through N fractures	$[LT^{-1}]$
q_T	Transverse flow	$[LT^{-1}]$
Q_w	Water source term	$[ML^{-3}T^{-1}]$
q_w	Input water flux	$[ML^{-2}T^{-1}]$
q_{g_i}	Advective flow vector of the gas phase	$[LT^{-1}]$
q_{g_L}	Longitudinal flow of the gas phase	$[LT^{1}]$
q_{g_T}	Gas transverse flow	$[LT^{-1}]$
$q_{g_{well}}$	Mass gas production rate	$[ML^{-2}T^{-1}]$
q_{l_i}	Advective flow vector of the liquid phase	$[LT^{-1}]$
q_{l_L}	Longitudinal flow of the liquid phase	$[LT^{1}]$
$q_{w_{ob}}$	Income water mass flow on the outer boundary	$[ML^{-2}T^{-1}]$
$q_{w_{well}}$	Mass water production rate	$[ML^{-2}T^{-1}]$
R	Universal gas constant	$[ML^2N^{-1}\theta^{-1}T^{-2}]$
r	Radius	$[L]$
R_{ij}	Rotation matrix	$[-]$
s	Coordinate along the channel	$[L]$
S_g	Gas mass storage term	$[ML^{-2}]$
S_r	Saturation degree	$[-]$
S_r^*	Normalized saturation	$[-]$
S_w	Water mass storage term	$[ML^{-2}]$
$S_{r,res}$	Residual saturation	$[-]$
$S_{r_g,res}$	Gas residual saturation degree	$[-]$
S_{r_g}	Gas saturation degree	$[-]$
T	Temperature	$[\theta]$
t	Time	$[T]$
T_i	Projection of the local stress tensor in global coordinates	$[ML^{-1}T^{-2}]$
t_i	Traction vector	$[ML^{-1}T^{-2}]$
T_t	Transverse transmissivity of the fracture	$[M^{-1}L^2T^1]$
T_{well}	Transmissibility factor of the well	$[L^3]$
u_i	Displacement vector	$[L]$
u_i^f	Fluctuation displacement field	$[L]$
u_i^λ	Equivalent displacement in the contact zone	$[L]$

u_n	Normal displacement	$[L]$
u_n^{max}	Maximal normal displacement allowed	$[L]$
u_{l_k}	Coordinate of the degree of freedom l at node k	
V	Volume	$[L^3]$
v_i	Velocity vector	$[LT^{-1}]$
v_i^*	Admissible virtual velocity field	$[LT^{-1}]$
V_L	Langmuir volume	$[L^3M^{-1}]$
v_g	Gas molecular velocity	$[LT^{-1}]$
V_g^{Ad}	Adsorbed volume per unit of mass	$[L^3M^{-1}]$
w	Matrix width	$[L]$
W_E^*	External virtual work	$[ML^2T^{-2}]$
W_G	Gauss weight at the integration point IP	
W_I^*	Internal virtual work	$[ML^2T^{-2}]$
w_{ij}	Spin rate tensor	T^{-1}
X_i	Coordinates in the reference configuration	$[L]$
x_i	Coordinates in the current configuration	$[L]$

Superscripts

$[.]^e$	Quantity related to a finite element e
$[.]^F$	Quantity on the follow boundary
$[.]^L$	Quantity on the lead boundary
$[.]^M$	Macroscale quantity
$[.]^m$	Microscale quantity
$[.]^T$	Transposed object
$\dot{[.]}$	Time derivative
${}^{\diamond}[.]$	Quantity given in the orthotropic axes

List of Figures

List of Tables

Dubito, ergo sum. Cogito, ergo sum.

René Descartes

Part I

Introduction

1. Context of the research

1.1 Introduction

Coal is now mined for many centuries, it was already an essential raw material during the Industrial Revolution from the 18th century. Two different primary uses of coal can be distinguished: the *coking coal* for steel production and the *steam coal* for power generation [Lange, 2010]. Steam engines to power locomotives and boats in the 19th century are a famous example of coal use. From the 1880s, steam turbines fueled by coal are also used to generate electricity [McNerney et al., 2011]. Coal production peaked in the first half of the 20th century, then it was followed by competition from nuclear power and cheaper oil and gas to generate electricity. With the decline of industrial processes using coal and its bad reputation, coal is often seen as a thing of the past. In Belgium, mining ceased rationally because of high operating costs; the last colliery in Wallonia closed in 1984. However, coal still represents about 40% of the current worldwide electricity production. Australia is one of the biggest net exporters of coal [International Energy Agency - IEA, 2016].

Many mining accidents over the years have contributed to the bad reputation of coal. Indeed, the methane released from coal seams during mining operations explodes when it is ignited, the *firedamp* was referred as the "miner's curse" [Thakur et al., 2014]. Gas is therefore vented into the atmosphere to increase safety. However, it raises environmental issues because methane is a greenhouse gas that contributes to climate change. More than an environmental challenge, it is a real economic loss since *coalbed methane* (CBM) is recognized as a valuable energy resource after the "energy crisis" of the 1970s [Flores, 1998]. Regarding terminology, *coalbed methane* (CBM) is the methane that resides within coal seams. In the United States, CBM production refers to the extraction of methane from unmineable coal seam. The equivalent term in Australia is the *coal seam gas* (CSG). It should not be confused with *underground coal gasification* (UCG) which is a method of converting undisturbed coal into a combustible gas. Finally, methane released or produced from coal during mining activities is termed *coal mine methane* (CMM) while methane recovered from closed mines is called the *abandoned mine methane* (AMM) [Moore, 2012, Flores, 2013]. Whatever its name, coalbed methane again draws attention to coal as a energy resource. Moreover, un-mined coal seams are also interesting reservoirs in the context of *Carbon dioxide Capture and Storage* (CCS) [White et al., 2005].

However, despite coal is mined for many centuries, its behaviour is not yet fully understood in the context of CBM recovery or CCS. Considering coal as a porous medium into which flows occur is a subject recently explored in the history of coal. It is now of great interest to improve the accuracy of methane production or carbon storage modelling [Peng et al., 2017]. This thesis aims to contribute to research in this perspective. First, few concepts related to coal and coalbed methane are introduced in this part of the thesis to understand the issues involved in this work.

1.2 Coal and coalbed methane formation

1.2.1 Coal formation

Coal is an organic sedimentary rock formed from the accumulation of plant debris. Coal formation occurred mainly during the Carboniferous period [1] when vegetation was covering the land with huge swampy forests in humid climatic zones. Plant debris were allowed to persist in some swamp environments due to the lack of oxygen and also because some microorganisms able to oxidize the lignin did not exist yet. Over geological time, different layers of organic material and sediments such as mud or sand were deposited one on top of the other. Then, buried layers were subjected to heat and pressure, which progressively altered the organic material physically and chemically; water, oxygen, nitrogen, carbon dioxide and hydrocarbons gases were forced out of the organic matter, increasing its carbon content. Over millions of years, through a diagenetic alteration called *coalification*, material that had been plants became coal (Figure I–1) [Ayoub et al., 1991, Arnold, 2013]. Due to the high compaction rate of plant debris, an initial accumulation of 15m of organic debris produces only a 50cm thick coal seam.

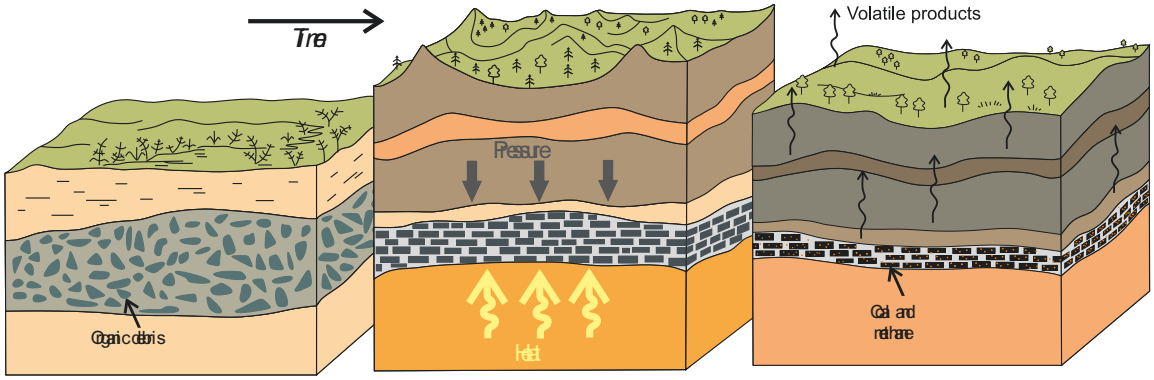

Figure I–1 – Coalification process. *Modified from* [Ayoub et al., 1991].

The fact that coal is widely distributed indicates that termination of plant decay by flooding and subsequent burial was relatively common. Because of the variety of the vegetation and the diverse conditions of accumulation, coal is merely a generic term [Berkowitz, 1979]. For practical purpose, coal is defined by Schopf as containing at least 50% by weight and 70% by volume of carbonaceous material produced by the induration of plant residues [Schopf, 1956]. These residues of coalified plants are called *macerals*, they are the main constituents of the organic matter of coal. Three major maceral groups are recognized: vitrinite, inertinite and liptinite. Vitrinites are the most abundant, they derived from woody tissues.

1.2.2 Coal classifications

Several ways have been established to classify coals. Indeed, coal can not be considered as a unique material because of the differences in the kinds of original plant precursors (*coal type*), in the degree of coalification (*coal rank*) and in the range of impurities (*coal grade*) [Schopf, 1956]. The interest of these classifications is to distinguish coals according to their properties.

Classification by coal type is based on the depositional origin of the coal and the maceral–mineral mixture resulting from that origin. There are typically two categories: *humic* (banded) coals, formed primarily from wood and reed, and *sapropelic* (unbanded) coals, developed from organic mud [O'Keefe et al., 2013]. Maceral composition influences directly the macroscopic appearance of coal such as its

1. Carboniferous occurred from 359 million to 299 million years ago. Its name derives from the Latin words "carbo" (coal) and "fero" (I bear).

brightness: it ranges from *bright* (vitrinite-rich) to *dull* (liptinite- and inertinite-rich) materials. More precisely, four major lithotypes are recognized: *vitrain* (bright), *clarain* (between vitrain and durain), *durain* (dull) and *fusain* (dull and fibrous) [Stopes, 1919].

Coal rank refers to the degree of metamorphosis of the organic material, it is independent from the coal type. In order of increasing maturity, the coal ranks defined by the ASTM [2] are *peat*, *lignite*, *subbituminous*, *high-volatile bituminous*, *medium-volatile bituminous*, *low-volatile bituminous*, *semi-anthracite*, *anthracite*, and *meta-anthracite* [ASTM, 2012]. Obviously, it forms a continuous series.

In general, because rank is a function of temperature and time, it increases with depth. This phenomenon is known as the Hilt's law [Hilt, 1873], it holds true provided that the thermal gradient is entirely vertical [Thomas, 2002]. The coal rank can be determined by several parameters which are good indicators of the thermal history of coal: fixed carbon (FC) content, volatile matter (VM) content, moisture (w) content, calorific value or *vitrinite reflectance* [3].

In addition to moisture, volatile matter and fixed carbon contents, the *Proximate analysis* [ASTM, 2002] includes also ash (a). Ash is the noncombustible portion of coal, it is due to the presence of minerals after mineralization from a groundwater flowing or since the depositional environment. Contrary to oil and gas, as coal is solid, it will incorporate any inorganic material from the original swamp environment. In most cases, ash is an undesirable residue because it does not contribute to the heating value of coal. Therefore, ash content is associated with the purity of coal and different grades may be defined.

Although relationships are never universal from basin to basin or even seam to seam, coal type, rank and grade are important features as they influence many attributes of a coal reservoir including gas type, gas quality, maximum gas holding capacity, calorific value, pore distribution and permeability [Moore, 2012].

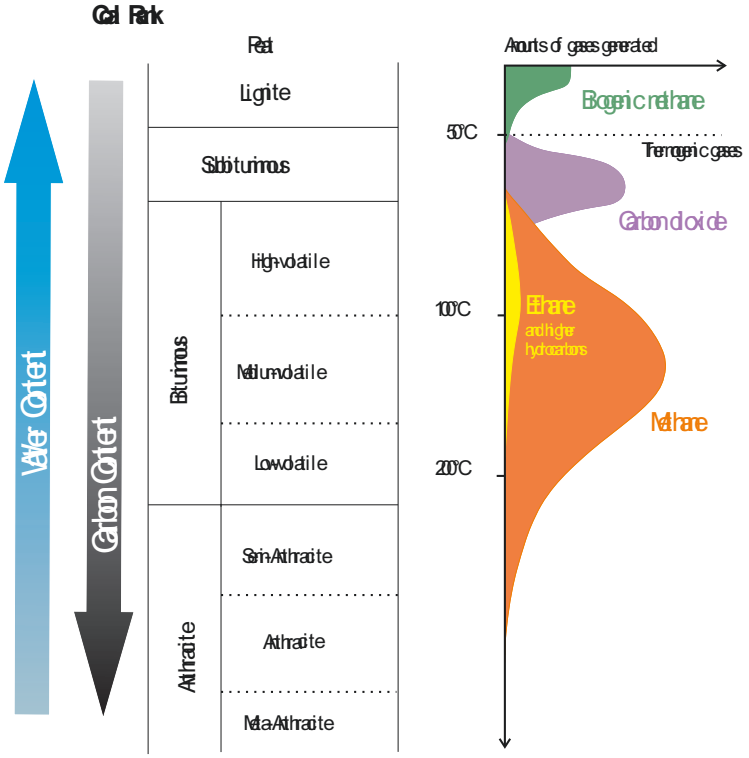

Figure I–2 – Coal rank and gas generated. *Modified from* [Gao et al., 2014].

2. American Society for Testing and Materials.

3. The reflexivity of the vitrinite increases gradually with coal maturity; this phenomenon is used to determine coal rank by measuring the percentage of the light reflected from a polished sample.

1.2.3 Gases formation

CBM can be found almost anywhere there is coal because gas formation is part of the genesis of coal. Most gas retained in coal seam has been produced *in situ* by microbial or thermal processes. Depending on its origin, gas is termed biogenic or thermogenic but both are composed predominantly of methane (95%), with minors amounts of heavier hydrocarbons, carbon dioxide and nitrogen [Seidle, 2011].

Figure I–2 shows the relative amounts of gases generated throughout maturation of coal. It can be observed that generation of methane peaks in the bituminous rank.

1.3 Coal structure

Coals are naturally fractured reservoirs. Consequently, as shown in Figure I–3, coalbed is constituted of small blocks separated by fractures termed *cleats*. Most numerical models developed to simulate coalbed methane reservoirs are based on this type of physical structure of coal [Harpalani and Schraufnagel, 1990]. The cleat system is important for the CBM production, it is the principal permeability pathway for water and gas during production.

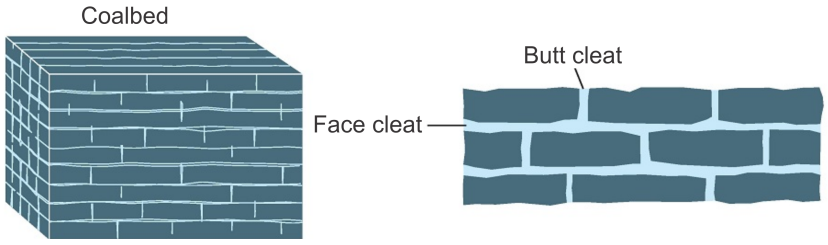

Figure I–3 – Schematic coalbed structure. *From* [Al-Jubori et al., 2009].

Coal is therefore a system of matrix blocks and fractures. The fracture system has a low storage capacity and high fluid transmissibility while the matrix system has a low fluid transmissibility but a high storage capacity. Indeed, micropores serve as the storehouse for large quantities of methane held by an adsorption mechanism [Harpalani and Schraufnagel, 1990]. Hence, CBM production consists to desorb gas molecules from the internal surface of coal.

1.4 Coalbed methane production

1.4.1 Unconventional reservoir

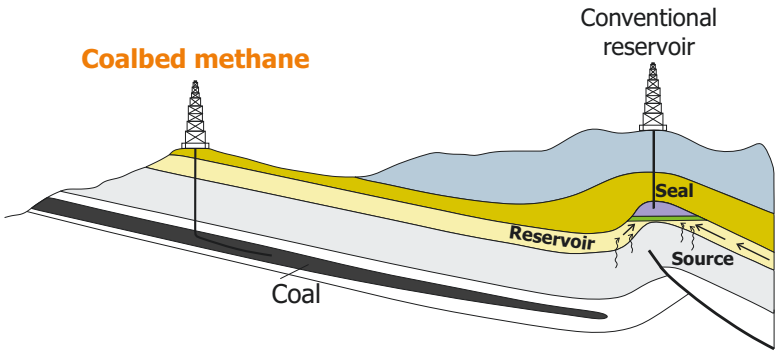

Figure I–4 – Conventional reservoir *versus* Coalbed methane reservoir.

In conventional hydrocarbons reservoirs, oil and gas are stored in a porous and permeable host rock where gas is compressed into the pore space. Indeed, hydrocarbons have been trapped by an overlaying impervious rock after they migrated from a source rock to the reservoir. Coalbed methane is distinct from a conventional reservoir as coal sourced the gas it holds (Figure I–4). Of course, some of the methane escaped from coal over geologic time, but it remains in the coal as free gas [4] in the coal fractures or sorbed gas in the coal matrix [Moore, 2012].

Most of the methane is stored in the coal matrix by *adsorption*. *Adsorption*, or simply *sorption*, is the attachment of the gas molecules to the surface of coal particles by Van der Waals forces. Gas molecules form a monolayer close to the liquid state on the internal surface area of the coal matrix. Thanks to the large specific surface of coal particles, coal can store more gas by sorption on the matrix (90%) than by compression in the cleats. Sorption is so efficient that coal can contain per unit volume six to seven times more gas than sandstone from a conventional reservoir [Seidle, 2011]. For coals, pore surface area is therefore more crucial than the pore volume in terms of gas holding capacity.

In fact, the amount of sorbed gas depends on pressure, temperature and moisture content; the amount of sorbed gas increases with pressure and it varies inversely with temperature and moisture content. Sorption isotherms are used to describe the relation between the pressure and the gas content for any temperature, the most famous equation is probably the Langmuir's isotherm [Langmuir, 1918].

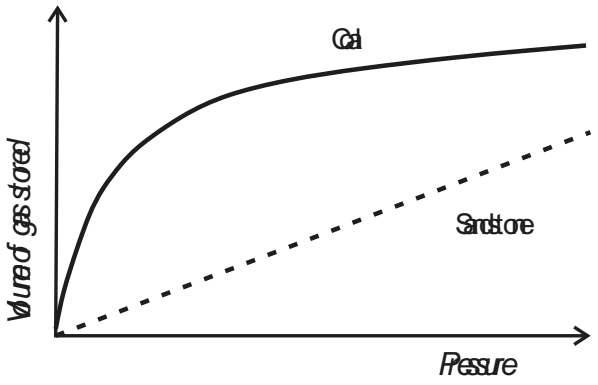

Figure I–5 – Comparison of the quantity of gas stored in coal reservoir and conventional reservoir. *Modified from* [Jones et al., 1987].

1.4.2 Reservoir depletion

CBM production consists to reduce the pressure of the reservoir to initiate desorption. This corresponds to the intersection of the reservoir pressure and the isotherm. Desorption then follows the isotherm until abandonment of the production (Figure I–6) [Al-Jubori et al., 2009].

Coal deposits are usually aquifers, coal cleats are initially water saturated for most of the reservoirs. It is therefore the hydrostatic pressure that maintains the gas adsorbed in the coal matrix; it is a kind of seal for this unconventional reservoir. CBM production normally first requires the mobilization of water in the cleats to reduce the reservoir pressure. This reduction of pressure in the coal seam is followed by the desorption of methane from the matrix. Gas molecules then diffuse through the matrix, migrate through the cleat system, and finally reach the wellbore or the mine shaft (Figure I–7) [Al-Jubori et al., 2009].

4. Methane molecules, CH_4, have a high degree of symmetry and therefore present a lack of permanent electric dipoles. As bonding between dipoles is the dominant mechanism for liquefaction, methane can only liquify at very low temperature. Methane-rich liquid does not coexist with liquid water [Carroll, 2014].

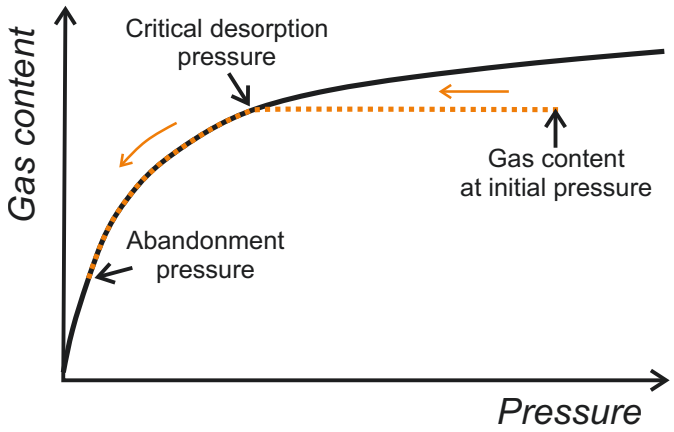

Figure I–6 – *Gas content-Pressure* path followed during coal seam methane production. *Modified from* [Ayoub et al., 1991].

Due to the coal structure, transport of gas through coalbed comprises two steps: diffusion through the narrow pores of the matrix and viscous (Darcy) flow in the cleats [Gilman and Beckie, 2000, Lu and Connell, 2007]. These two parts are consecutive and the global rate is therefore controlled by the greater resistance. Both extremes -high permeability seams dominated by diffusion transport, or short diffusion path seams controlled by advective flows- are known to exist, e.g. in the U.S. Pocahontas coal dominated by permeability and Pittsburgh seam controlled by diffusion [Kissell, 1972].

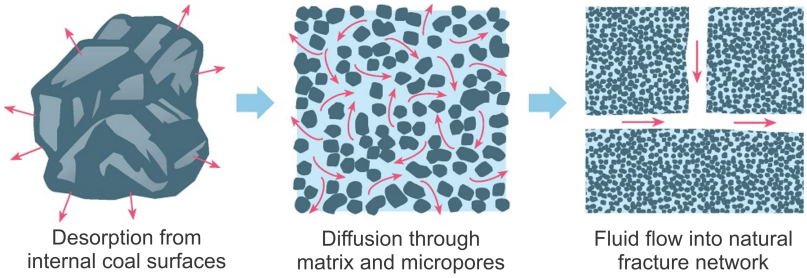

Figure I–7 – Gas migration in coal seam, [Al-Jubori et al., 2009].

Figure I–8 compares the production of gas in conventional and coalbed reservoirs. In a conventional reservoir, where gas is compressed in the pore space, gas production declines with time as water production increases. In coalbelds, where methane is adsorbed on the internal surface of the coal matrix and cleats are mainly filled with water, the production starts by dewatering the fractures and the maximum methane production is reached only later [Ayoub et al., 1991].

In consequence, a single-phase flow of water is encountered at the beginning of the CBM production. By continuing the pumping, methane is desorbing and gas bubbles form. The medium is now partially saturated with gas, the water relative permeability of coal decreases. Continuing the production, gas saturation increases and a two-phase flow regime is reached. Spatially, it leads to the sequence shown in Figure I–9: two phases are encountered close to the well while the medium is saturated with water further away. Over time, during the production, this sequence moves outward from the wellbore [Koenig et al., 1989, Harpalani and Schraufnagel, 1990].

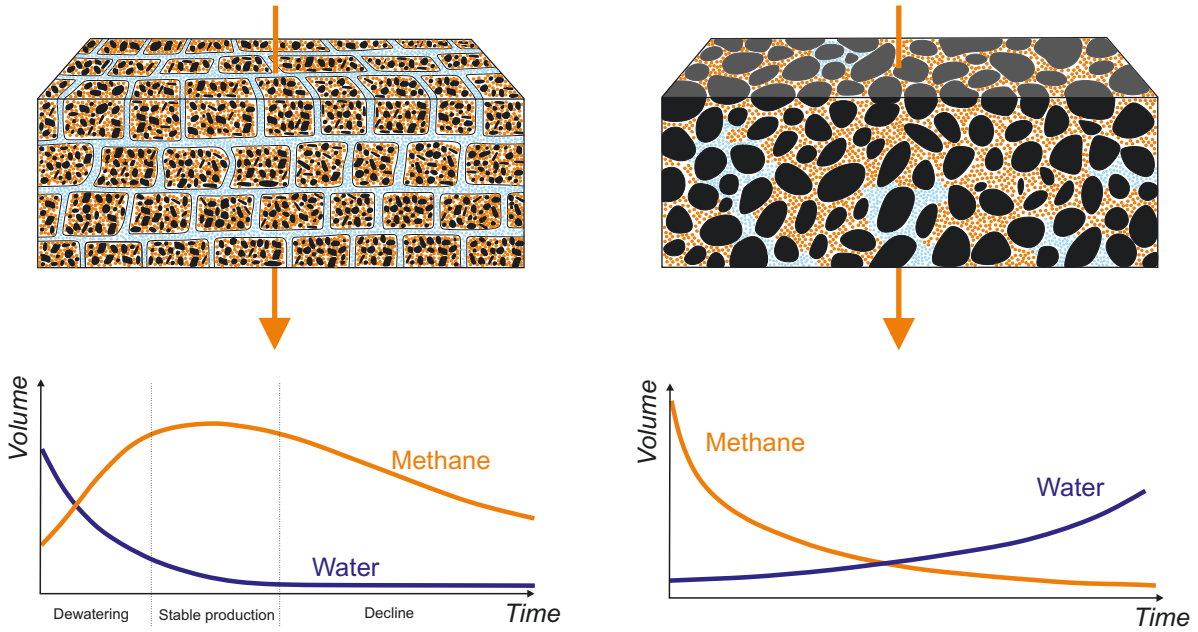

Figure I–8 – Comparison of storage and production of gas in coalbed (left) and conventional (right) reservoirs. *Modified from* [Ayoub et al., 1991].

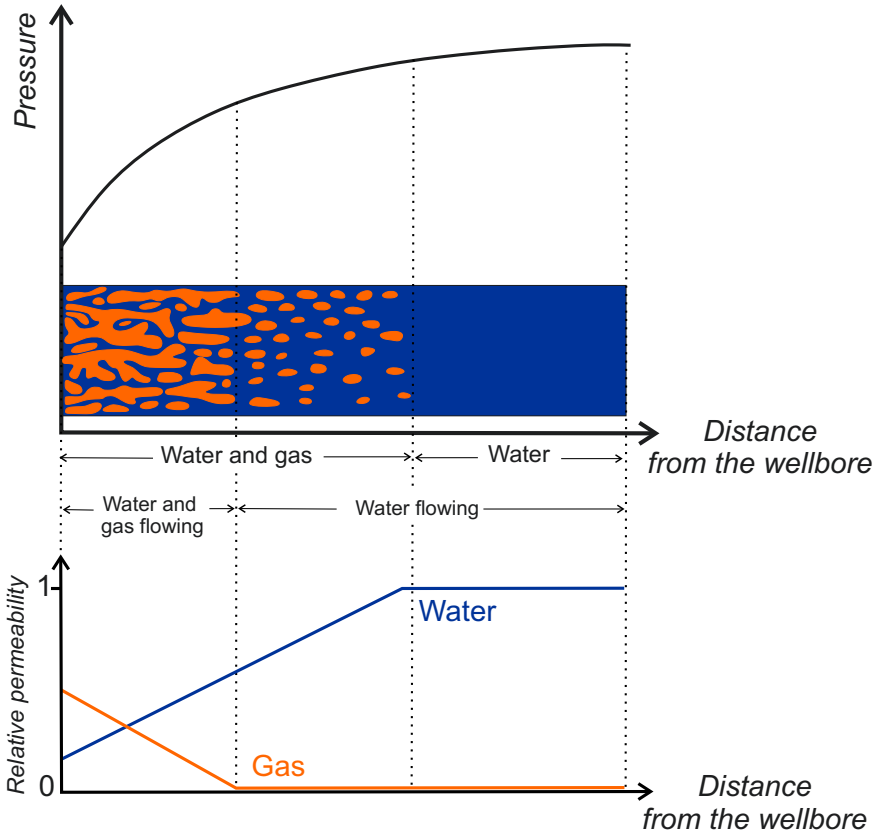

Figure I–9 – Three stages of coalbed methane production. *Modified from* [Koenig et al., 1989].

Cleats contain minor amounts of free gas but they are characterized by a high ability to transmit gas, *i.e.* permeability; they are several orders of magnitude more permeable than the coal matrix. Cleats are therefore responsible for the fluid flow from the reservoir to the well and any change of the cleat network will likely translate into modifications of the reservoir permeability. In particular, two distinct

phenomena are known to result from reservoir pressure depletion, which have opposing effects on coal permeability [Gray et al., 1987, Mazumder et al., 2012]:

> The first phenomenon is the reservoir compaction due to the increase in the effective stress after the reservoir depletion. It tends to decrease the permeability.
>
> The second is the matrix shrinkage following the gas desorption from the coal. It increases the cleat permeability.

When injecting gas instead of producing it, the reverse competing phenomena are observed. There is a decrease of effective stress tending to increase the permeability and a swelling of the matrix tending to decrease the permeability.

1.4.3 Enhanced recovery

The recovery of coalbed methane can be improved by stimulation treatment, producing the so-called *enhanced coalbed methane* (ECBM). The most used is certainly the *hydraulic fracking* but CO_2 injection and thermal stimulation also have interesting effects on coal properties.

1.4.3.1 Hydraulic fracking

Hydraulic fracking consists to subject coal to sufficient pressure to form and extend fractures by continued injection of fluid. A solid proppant such as sand is carried with the fluid to hold the fractures open. They can extend 60-150 m from the wellbore and they create highly conductive flow paths for water and gas to migrate to the wellbore [Jeffrey et al., 1989, U.S. Environmental Protection Agency, 2009]. However, since fracking is a controversial method, some countries in Europe (France, Bulgaria, Germany and Ireland) introduced some anti-fracking laws banning this extraction method, mainly by considering shale gas. In some cases, there is little benefit in stimulating fracture if the gas flow is restricted by desorption, as permeability is already high.

1.4.3.2 Thermal stimulation

One way to enhance diffusivity is to increase the coalbed temperature. The increase in temperature also facilitates desorption by reducing the sorption capacity. Thermal stimulations could be therefore interesting to enhance the production [Shahtalebi et al., 2016]. However, the coal thermal conductivity value is low [5] to distribute heat over a large scale [Salmachi and Haghighi, 2012]. For sure, this technique should only be considered if the cost associated with the heating is offset by the benefits obtained by accelerating the methane production. Note that thermal dilatation may have a negative impact on the permeability.

1.4.3.3 CO_2 injection

Concerning the CO_2-ECBM, carbon dioxide has a higher affinity for coal and thus displaces methane locked within the matrix [Puri et al., 1990, Mazzotti et al., 2009]. Coal deposits are therefore considered as interesting reservoirs for the Carbon dioxide Capture and Storage; injecting carbon dioxide enhances the recovery of gas resource while CO_2 is sequestrated and does not contribute to climate change [White et al., 2005]. However, there may be a net swelling with the resorption of CO_2, what could have a detrimental impact on the permeability [Shi et al., 2006]. CO_2-ECBM is further explored in section 1.5 dedicated to carbon storage.

5. About 0 35W m K [Herrin and Deming, 1996].

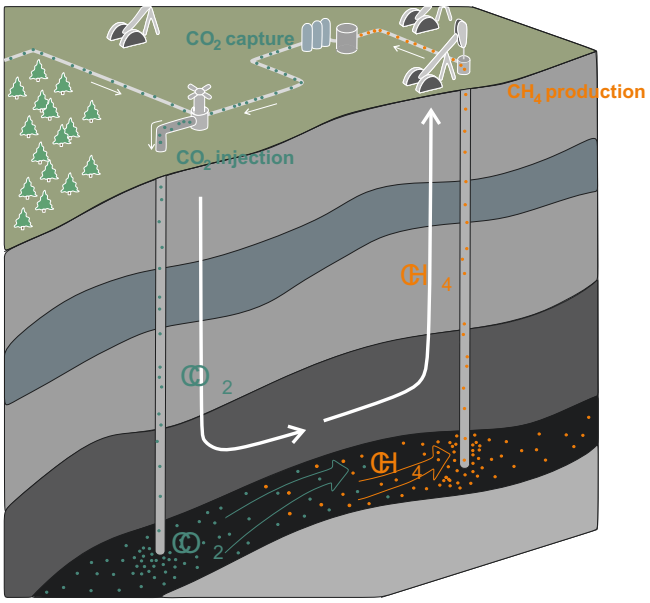

Figure I–10 – Illustration of the combination of carbon dioxide storage with methane recovery enhancement.

1.4.4 Production statistics

Coal deposits are widely distributed over the earth, about 70 countries have coal-bearing regions. Wherever there are coal basins, there is methane. Worldwide CBM resources [6] are estimated to 256 trillion cubic meters (9,037 trillion cubic feet); most of which are located in Russia, Canada, China, Australia, and the USA. This estimate of the global coal gas resources has historically been assessed from a mining perspective. But there is a large amount of coal that cannot be mined and it may be therefore conservative because coals present at depths that make them uneconomical to recover often hold large volumes of gas which would be commercially viable to exploit [Seidle, 2011]. It has been estimated recently that 79 trillion cubic meters of CBM are potentially recoverable globally [7] [Godec et al., 2014].

Many countries, including the USA, Australia, China, India and Canada, already exploit CBM. The first recorded well was drilled in 1931 in the USA in West Virginia [Ayoub et al., 1991].

1.4.4.1 USA

It is in the 1980s that the American CBM production really began with the commercial exploitation of three major basins: the Black Warrior Basin (Alabama), the San Juan Basin (New Mexico, Utah, Colorado) and the Powder River Basin (Wyoming and Montana) (Figure I–11). Although these basins are now in decline, they are expected to produce significant methane for one or two decades [Moore, 2012].

Thanks to these three majors basins, the USA is currently the largest CBM producer in the world. There are about 90,000 CBM wells in the USA. In the last years, they produced between 1 and 2 trillion cubic feet annually (Figure I–12), what represents almost 10% of their natural gas production in the best years.

6. Resources refer to estimated volumes while reserves refer to known volumes that can be recovered under technical and economic conditions. As a result, reserves represent only a portion of the estimated resources.

7. In comparison, worldwide proved natural gas reserves are 186 trillion cubic meters (6,566 trillion cubic feet) [BP, 2015].

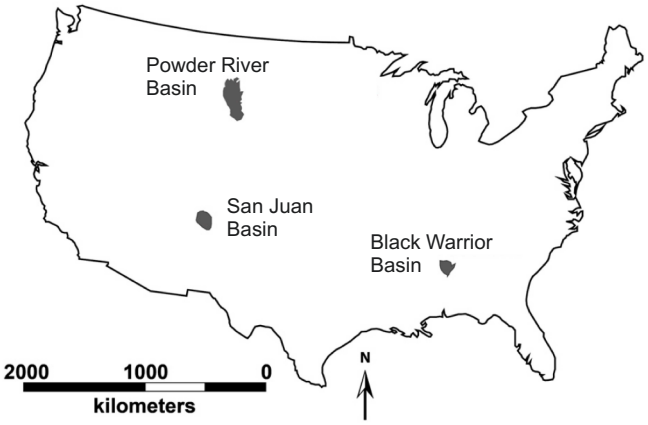

Figure I–11 – Major coal basins producing CBM in the USA. *Modified after* [Moore, 2012]

CBM developments were initially in coals of higher rank, in the Black Warrior and San Juan basins, because these coals can generate and contain more gas, returning a higher profit margin. However, CBM industry is also well established in the Powder River basin, last data mentioned more than 17,000 producing wells (and 8000 shut-in wells), making 1133 millions of cubic feet per day [Palmer, 2010]. The CBM exploitation in the Powder River basin is characterized by large amounts of production of water, over 678 million barrels of water were produced in 2006 alone [Moore, 2012].

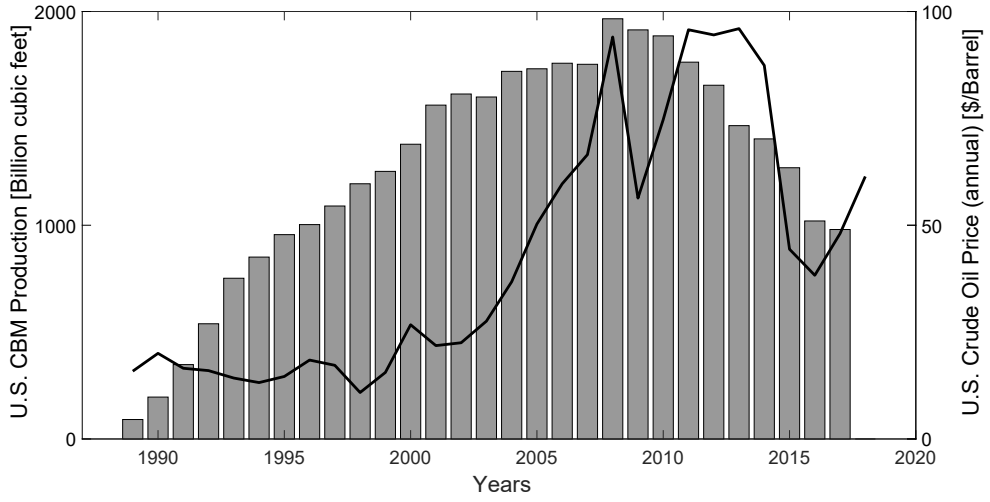

Figure I–12 – Estimated production in the USA. *Data from the U.S. Energy Information Administration*.

1.4.4.2 Australia

Figure I–13 presents the Coal Seam Gas production in Australia, the commercial production started in 1996. The production is really significant since the beginning of the century after the Queensland Government decided that 13% of all state electricity had to be generated by gas by 2005. That requirement has been increased to 18% by 2020 [Queensland Government, 2007].

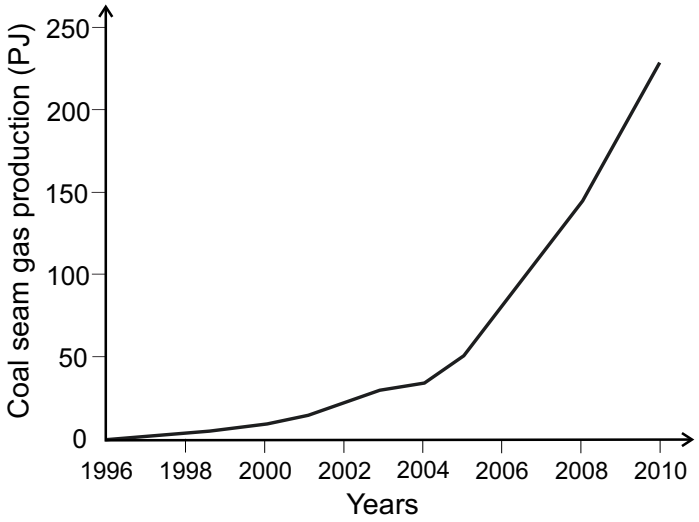

Figure I–13 – Coal Seam Gas production in Australia from 1996 to 2010. 1 Petajoule (PJ) 1 Billion cubic feet. *Data from Geoscience Australia*.

CSG is extracted mostly in subbituminous coals in the Bowen and Surat basins (Figure I–14) [Moore, 2012]. In contrast, in New South Wales, the Sydney Basin has a smaller number of wells since the NSW government has been more cautious to grant exploration licences. In Victoria, there is a moratorium on onshore unconventional gas exploration and development since 2012 [Evershed, 2018]. In the Northern Territory and Western Australia, the unconventional gas reserves are primarily gas shale, which requires hydraulic fracking.

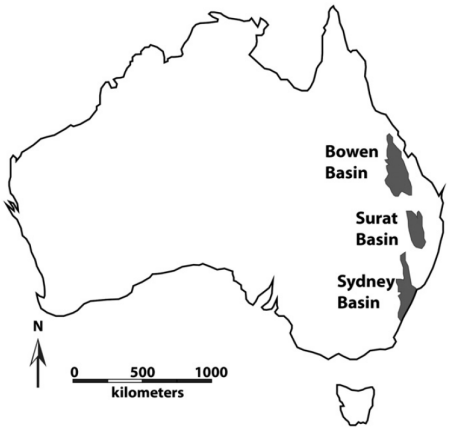

Figure I–14 – Coal basins producing CBM in Australia. *Modified after* [Moore, 2012]

1.4.4.3 Belgium

In Belgium, resources are smaller and the country has not been able yet to get a CBM industry started. Nevertheless, there is potential for coalbed methane in Belgium. Indeed, 6 to 9 billions tons of coal would be still present in the walloon basement (Figure I–15), what could represent 100 to 300 billions m^3 of methane. If we can recover 10 to 20 billions m^3 of methane, it would represent 3 to 10 years of the belgian gas consumption.

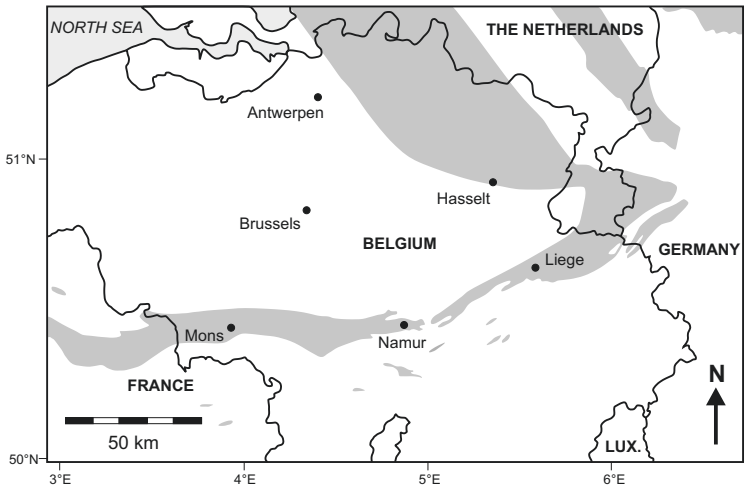

Figure I–15 – Map of the outcropping or shallow subsurface coal basins (shaded area) in and around Belgium. *Modified from [Piessens and Dusar, 2004].*

The production of coalbed methane is not planned in a short term in Belgium. However, the recovery of methane from an abandoned coal mine just started in April 2019 in Anderlues to produce electricity (Figure I–16). This site was previously used for seasonal storage of natural gas [Dieudonné et al., 2015]. Now, two engines are generating 3MW from gas constituted of 94%vol. methane. This gas is present at 0 7 bar in the old galleries of the mine and it is uncompressed to 0 2 bar to be used by the generators with a flow of $300 m^3 \ h$. It is expected that no compressor is required for the next 15 years. Note the produced carbon dioxide is not injected back in the mine. The production should start in others abandoned mines of Wallonia in a near future.

Figure I–16 – One of the engines generating 1 5MW at the foot of the headframe from an abandoned coal mine in Anderlues (Belgium). Photo taken on 06/06/2019.

1.5 Carbon dioxide storage

Geological sequestration of carbon dioxide has great potential to compensate anthropogenic emissions and meet the Paris Agreement's ambition on tackling climate change [Intergovernmental Panel on Climate Change - IPCC, 2015]. Global ambition aimed at avoiding the most serious impacts of climate change by keeping the global atmospheric temperature increase to well-below 2°C and pursuing efforts to keep warming below 1.5°C above pre-industrial levels. To achieve these targets, Carbon dioxide Capture and Storage (CCS) will require an unprecedented rate of deployment, to eventually capture and store between 1.8 and 6 billion tonnes of CO_2 per year. The current rate is only 37 million tonnes captured and stored [Havercroft and Consoli, 2018].

Beside depleted oil and gas reservoirs and deep saline aquifers [Rathnaweera et al., 2016], un-mined coal seams are interesting reservoirs in the context of CCS [White et al., 2005]. Because of the high specific surface area of coal (ranging from 20 to $300m^2$ g [Berkowitz, 1985]), large volumes of CO_2 may be trapped by sorption [Faiz et al., 2007]. As mentioned above, injection of carbon storage may also enhance the production of natural gas. Carbon dioxide could therefore be sequestrated with a net profit or moderate costs while compensating the emissions from the use of the extracted methane [Gunter et al., 1997].

At reservoir pressure and temperature conditions, it is not unusual for carbon dioxide to enter supercritical conditions (critical point at 7 $38MPa$ and 31 $1°C$). This supercritical fluid state is generally encountered in sequestration sites deeper than $800m$ due to the pressure and temperature found at this depth [Aminu et al., 2017]. The physical and transport properties of supercritical fluids lie between those of a gas and those of a liquid [Nikolai et al., 2019]. In particular, the density of the fluid is that of a liquid. As a result, more gas can be stored in the macropores of the deeper rocks. However, in coal, CO_2 is stored by sorption in the matrix; sites as shallow as $300m$ may be considered since the maximum storage capacity of CO_2 in the coal matrix may already be reached for bulk pressures of $3MPa$ [White et al., 2005].

Today, ECBM is not a mature technology as no industrial injection site (at least one million tons per year) is operational. However, many pilot projects are testing CO_2 injection in research and development sites [Brochard, 2011, Godec et al., 2014]. The initial project, known as Allison Unit CO_2-ECBM pilot [Reeves et al., 2003], took place in 1995 in the San Juan Basin in the USA. Despite permeability measurements at the site revealed the permeability decreased from 100 to $1mD$ [8], methane production did improve. During its six years of operation (1995-2001), the project recovered 45 million cubic meters of incremental CBM and stored 270,000 metric tons of CO_2, recovery of methane was improved from 77% under traditional practices to 95% of original gas in the pilot zone area using injection. The test was therefore considered successful and it was concluded that there was significant geological storage capacity globally in unmineable coal seams. Following this initial project, several pilots were developed few years later in Canada, Poland and Japan, in thin bituminous coal seams. But these projects were generally not considered successful for various reasons, including swelling reducing the permeability. In addition, the performance of these projects was impacted by some design and implementation issues. Subsequent research and pilot testing has built upon these lessons and show notable success [Godec et al., 2014].

In American coal basins, there is a potential of sequestration for about 90 billion tons of CO_2 [Reeves, 2003]. To put in perspective, total estimated annual emissions were between 5 and 5.5 billion tons of CO_2 in the USA in the last years. More recently, from the CBM potentially recoverable globally, it has been estimated that the worldwide potential storage of CO_2 is nearly 488 billion tons [Godec et al., 2014]. The potential in regions where coal has been widely mined is significantly reduced because of the risk of leakage [Christensen and Larsen, 2004].

8. 1 Darcy $10^{-12}m^2$.

2. Outline of the thesis

2.1 Issues

Changes of coal properties during methane production or carbon storage are a critical issue. Indeed, ignoring geomechanical processes certainly leads to errors in the evaluation of coalbed methane production as the permeability of the reservoir is affected [Gu et al., 2005].

For any model, it is important to establish how well it represents the reality of the reservoir behaviour; *i.e.* that the assumptions and approximations still allow the process of interest to be satisfactorily represented [Moore, 2012]. In existing CBM models, sorption- and stress-induced coal permeability alteration is a remarkable aspect which is improperly simplified [Wei et al., 2007]. Therefore, "it is clear that further work is required in order to improve our understanding of the reservoir behaviour of coal permeability [Moore, 2012]".

Ideally, a numerical model would detail the material microstructure with separate descriptions of each constituent. However, direct modelling of the entire microstructure is usually not possible due to the high computational expense it would require at the scale of a reservoir.

In consequence, large-scale models are generally phenomenological in nature: the behaviour of all the constituents is represented collectively by closed-form macroscopic constitutive equations. The phenomenological approach has limits because improving the macroscale models by taking into account more and more micromechanical effects makes it more and more difficult to formulate. In order to simplify their formulation, these models are generally based on a number of assumptions. It is sometimes highly restrictive. Moreover, the complexity of the behaviour is shifted to a troublesome identification of parameters [Massart, 2003].

Over the past few decades, many permeability models have been developed for coal reservoirs [Somerton et al., 1975, Schwerer et al., 1984, Seidle et al., 1992, Palmer et al., 1996, Gilman and Beckie, 2000, Pan and Connell, 2007, Lu and Connell, 2007, Connell et al., 2010, Gu and Chalaturnyk, 2010, Pan and Connell, 2012, Chen et al., 2013, Shi et al., 2014, Lu et al., 2016, Chen et al., 2017] to name a few, but these models are either analytical formulations or macroscopic models.

An alternative description is the use of a multi-level approach. The idea is to model the micromechanical effects explicitly on their specific length scale through a direct modelling and couple their homogenized effects to the macroscale. When solving the boundary value problems at both scales using a finite element method, the approach is termed the *finite element squared* (FE^2) method [Kouznetsova et al., 2001]. To our knowledge, this method has never been applied to coal before.

2.2 Objectives

In order to optimize coalbed methane recovery or carbon dioxide storage, this thesis aims to improve the description of the coal permeability evolution. To this purpose, different modelling scales are considered. The final model is implemented in the framework of the finite element square method. This multiscale approach allows not to model all the microstructural details for the full domain by using a fine scale *representative elementary volume* (REV) to describe the microstructure. The response to loading of the REV is linked to the macroscale to dictate the macromechanical behaviour of the porous medium (Fig-

ure I–17). For now, this method has only been employed for saturated conditions [Frey, 2010, Marinelli, 2013, Van den Eijnden, 2015]. The objective is therefore to extend the method to partially saturated conditions and take into account the coupled phenomena observed during the gas recovery/storage in coalbeds.

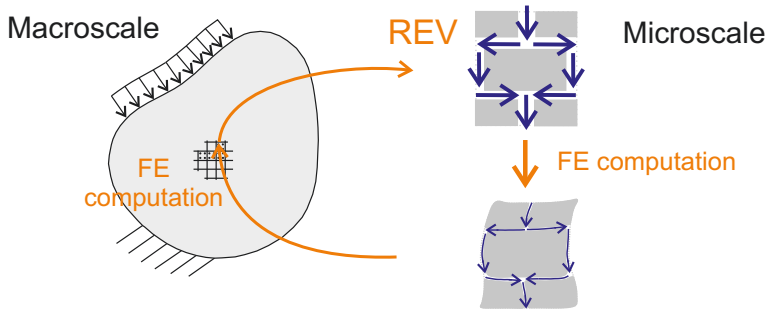

Figure I–17 – FE^2 approach.

Before the development of this multiscale model, a macroscale and a microscale models are first considered. Indeed, the literature on coal modelling is devoted to macroscale models and it makes sense to start there. Secondly, it is because the microscale model serves for the modelling at the REV scale in the multiscale approach. The main objective of this microscale part is to present a multiphase flow model in a single fracture since the applicability of traditional unsaturated models is not trivial at this scale.

The models are originally developed for methane recovery modelling, but can be used reversely for the modelling of carbon dioxide storage in shallow coal seams. These models are not developed for the modelling of ECBM, it is out of the scope of the thesis. All the models are implemented in the finite element code Lagamine. For an extensive description of the Lagamine code, the reader should refer to [Charlier, 1987, Habraken, 1989].

2.3 Outline

The thesis consists of four main parts briefly described hereafter.

Experimental observations This part of the thesis provides a better understanding of the behaviour of the material before developing the models. A literature review of the behaviour and properties of coal is first presented. In addition, an experimental study on the complex hydro-mechanical interactions between coal and carbon dioxide was also carried out as part of this thesis.

Macroscale This part is dedicated to the presentation of a macroscopic [1] model enriched with microscale considerations. It is the kind of approach which can be found in the literature. However, this part is more than a literature review, it presents a consistent model taking advantages of different models from the literature. As it will be presented, the model is based on a dual-porosity approach to reproduce as well as possible the hydro-mechanical couplings. The model is implemented in the finite element code Lagamine and is used for the modelling of one production well.

Microscale In this part, the model is written at the scale [2] of the coal constituents: matrix blocks and cleats. From a mechanical point of view, the coal matrix is assumed linearly elastic and the

1. The term macroscopic is used to refer to the scale of the reservoir.
2. The generic term microscopic is used to denote the scale of the matrix blocks, usually ranging between few milimeters and few centimeters.

complex behaviour of the material is obtained from the assembly with the cleats. These cleats are modelled thanks to interface elements. In this part, a model for each constituent is presented. The implementation of the model is verified by comparison with the analytical solution on a simple geometry. This model is the one used to solve the boundary problem at the REV scale.

Multiscale By employing homogenization and localization equations, macroscopic variables such as water and gas flows are computed knowing the pore pressure state at the microscopic scale. The FE^2 method used to develop this multi-scale model is first summarized and then implemented for multiphase flow conditions in the particular case of coal, a naturally fractured rock with sorption properties. Finally, the multiscale hydro-mechanical model is used for the modelling of methane production at the scale of one production well.

Part II

Experimental observations

Introduction Part II

Before proceeding to modelling, this part of the thesis aims to understand the material to be modelled. It has been briefly contextualized in the introduction part. This part on experimental observations allows now to better quantify coal properties.

Few experimental results from the literature are first presented. It is not exhaustive, we focus on properties and experiments highlighting behaviours that affect the gas flow through coal. In this purpose, different elements are reviewed: material structure, mechanical properties, sorption properties, swelling behaviour and permeability evolution.

Then, an experimental study was carried out in laboratory to support our understanding of coal behaviour by investigating the interactions of the features listed above. All the characterization tests are performed on samples obtained from the same coal block. It allows to know the properties of the material for which the permeability evolution with pressure is measured.

3. Literature review

The literature review first investigates the coal structure where the cleat network is identified by tomography imaging. This structure is known to affect the mechanical and hydraulic properties of the material. The mechanical behaviour is studied with compressive tests. Several kinds of properties are reviewed for the hydraulic and hydro-mechanical behaviours: sorption properties, swelling behaviour and permeability evolution.

3.1 Material structure

The structure of coal reflects its history. The coalification process is associated with the elimination of water due to both consolidation and chemical changes. Low rank coals have hydrophilic properties since it contains a number of oxygen functional groups [Yu et al., 2013]. At this stage, the water content is 30-65%wt [Allardice, 1991]. These coals behave like a gel, they swell and shrink significantly (about 30%vol.) with the loss and gain of water [Evans, 1973]. Water is retained in several forms, in a free phase and a bound phase, and some of the water can only be removed by raising the temperature to provoke decomposition of the functional groups [Allardice and Evans, 1971].

Throughout the coalification, the functional groups hydroxyl (OH), carboxyl ($COOH$), methoxyl (OCH_3), and carbonyl (CO) are decomposed and the carbon content increases [Murata et al., 2000]. As the carboxyl and hydroxyl groups are removed, coal is progressively losing its colloidal nature and hydrophilicity [Evans, 1973, Deevi and Suuberg, 1987]. Hydrophobicity of coal increases until bituminous coal with increasing coal rank and carbon content, and with decreasing oxygen and hydroxyl content [Gutierrez-Rodriguez et al., 1984].

Most coals presents some bands which are parallel to the planes of deposition of the material. Bright bands are derived mainly from wood while dull bands are formed from miscellaneous debris [Evans and Pomeroy, 1966]. Based on its appearance, four major lithotypes of coal are distinguished [1] [Stopes, 1919]:

Vitrain *occurs in bands or lenticles of a few millimeters. Brilliant, glossy and vitreous in texture. It is macroscopically structureless and homogeneous and breaks with a well-marked rectangular fracture perpendicular to the bedding, and a conchoidal fracture in other direction.*

Clarain *is bright, streaky or striated coal with a silky lustre. It is not so uniformly brillant and homogeneous as vitrain and lacks its conchoidal fracture.*

Durain *is hard, compact, dull coal. Macroscopically, it is pratically structureless and is greyish to dull black in colour. It occurs in both thick and thin bands. Fractures surfaces are finely granular and irregular.*

Fusain *is fibrous, friable dull charcoal-like material. It breaks down readily to fine dust which soils the hands, and is usually greyish black in colour.*

1. Definitions given by [Evans and Pomeroy, 1966].

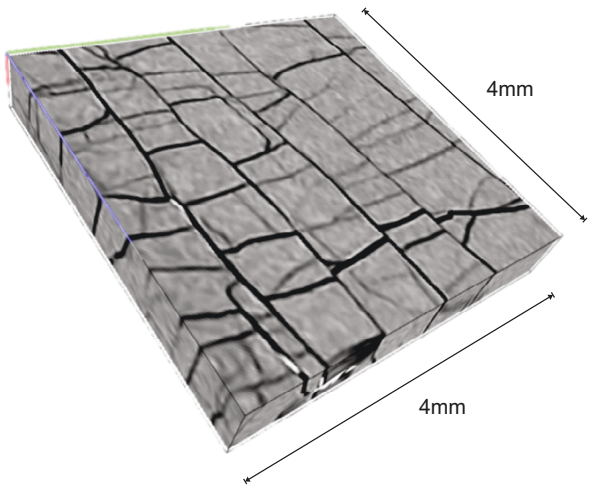

Figure II–1 – 3D visualisation of coal cleat structure obtained by tomography imaging (after filters). *From* [Jing et al., 2016].

Coal is generally naturally fractured, the divisions are known as cleats. They may originate from the decrease of the matrix volume due to dehydratation and devolatilization during coalification [Laubach et al., 1998]. But cleat formation is still a matter of debate, tectonic stress and strain may also play a role as the seam is being buried [Moore, 2012].

Figure II–1 shows a tomography (voxel size 4 1μm) of a coal specimen [2] of few millimetres [Jing et al., 2016]. There are two sets of orthogonal opening-mode fractures: the more continuous *face cleats* and the less continuous *butt cleats* (or cross cleats) intersecting the face cleats at an angle of generally 80-90°. Cleats typically have nearly indiscernible aperture, it ranges from 3 to 40μm [Laubach et al., 1998]. From the analysis of the tomography image, an average cleat aperture of 12 6μm (deviation 0 26μm) is measured for this specimen [Jing et al., 2016]. Figure II–2 gives a schematic representation of this structure.

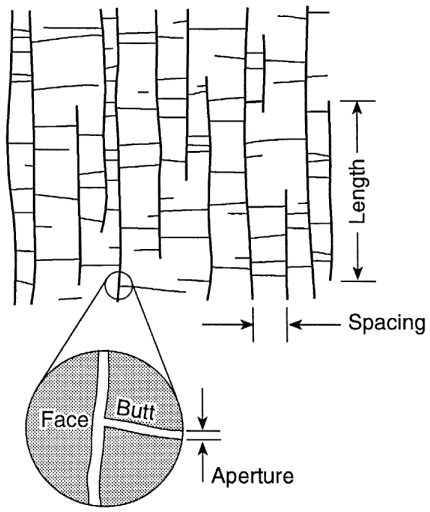

Figure II–2 – Schematic cleat system. *From* [Laubach et al., 1998].

Different tendencies are observed in the geometry parameters depending on coal type and rank. Fracturing is generally most abundant in bright bands of coal [Paterson et al., 1992]. Fracture spacing can range from fractions of a millimeter in vitrain layers to few centimeters or even non-apparent in durain [Dawson and Esterle, 2010]. Coal rank plays also a role in the cleat development, cleat frequency in-

2. Bright coal sample from Moura mine of Bowen Basin in Australia, medium volatile bituminous coal.

creases from lignite to low-volatile bituminous coal and then decreases above that rank [Moore, 2012].

This cleat network is important for the permeability. Coal is more permeable in the direction of the face cleats but the permeability is also affected by the geometry of the cleat system: spacing and height, aperture width and connectivity [Clarkson and Bustin, 1997]. Bright coals are more permeable than dull coals and it was interpreted due to the greater abundance of cleating in the bright coals [Smyth and Buckley, 1993]. Cleat frequency has often been noted to decrease as a function of bed thickness [Harpalani and Chen, 1997]. Moreover, it is also generally observed that the less frequent the cleats, the greater the length of any individual cleat [Dawson and Esterle, 2010].

In addition to the porosity formed by the network of fractures, there are micropores in the coal matrix. Micropores diameters in coal range from 0.5 to 1 *nm* [Paterson, 1986]. Because micropores are so plentiful, coal is characterized by a high internal surface area (ranging from 30 to 300 $m^2\ g$) [Berkowitz, 1985]. There does not appear to be a transitory pore system between the microporosity and the macroporosity; coal is a dual-porosity system [Harpalani and Chen, 1997].

Moreover, weak bonds between successive layers of deposition are also a natural direction of fractures at the scale of the seam. For example, successive hard bands may be separated by a very thin layer of fusain which provides little cohesive properties [Evans and Pomeroy, 1966]. All these discontinuities play a critical role in both the mechanical and the hydraulic behaviour of the rock.

3.2 Mechanical properties

Coal is generally an elasto-brittle [3] geomaterial and its behaviour is essentially linear-elastic prior to yielding/failure [Berkowitz, 1979]. Coals of all ages and ranks are fragile rocks, with little mechanical strength compared to conventional reservoir rocks [Seidle, 2011]. Coal may deform plastically [Newman, 1955], or perhaps visco-elastically [Levine, 1996], but the non-elastic behaviour of coal is less documented. For the elastic behaviour, orthotropy has been mentioned in the literature [Szwilski, 1984], it could be explained by the conditions of sedimentation (transverse isotropy) and the presence of different sets of fractures.

To illustrate the mechanical behaviour, some experimental results obtained by [Medhurst and Brown, 1998] from a series of triaxial compression tests are presented hereafter. This remarkable study was carried out on 61*mm* (40 tests), 101*mm* (4 tests), 146*mm* (9 tests) and 300*mm* (4 tests) diameter samples from coal obtained by core drilling in three different coal seams (D Upper, D and B Lower) undertaken in Moura mine in Queensland (Australia). Different confinements were tested, the samples were first loaded isotropically until the desired confining pressure was reached and then loaded axially at rates of between 1% and 2% axial strain per hour. The samples are categorized based on their brightness following Table II–1.

Category	Description	Scale
C1	Bright	>90% bright
C2	Bright banded	60-90% bright
C3	Interbanded bright and dull	40-60% bright
C4	Dull with minor bright	10-40% bright
C5	Dull banded	1-10% bright
C6	Dull	<1% bright

Table II–1 – Coal categories based on brightness. *From* [Medhurst and Brown, 1998].

3. Coal may evolve from a glassy brittle structure to rubbery, plastic structure following injection of carbon dioxide acting as a plasticizer [Larsen et al., 1997, Brochard, 2011].

Figure II–3 shows the deviatoric stress evolution with axial strain for some 300*mm* diameter coal samples at confining stress in the range 0 2 0 8*MPa*. The brightness category of each sample is given in Table II–2 with a summary of the results obtained. Sample L1-4 consists of almost totally bright coal and is much weaker than the other samples, the duller sample L2-1 is stronger than the C3/C4 samples. Beyond the peak strength, coal samples are softening.

Sample Number	Brightness category	Confinement [MPa]	Strength peak [MPa]	*E* [GPa]	
L1-1	C4/C3	0.2	12.60	2.11	0.25
L1-4	C2	0.2	8.81	1.73	0.29
L1-2	C3/C4	0.4	13.33	2.40	0.26
L2-1	C5/C4	0.8	20.52	2.48	0.24

Table II–2 – Summary of test results for 300*mm* diameter coal samples. *From* c.

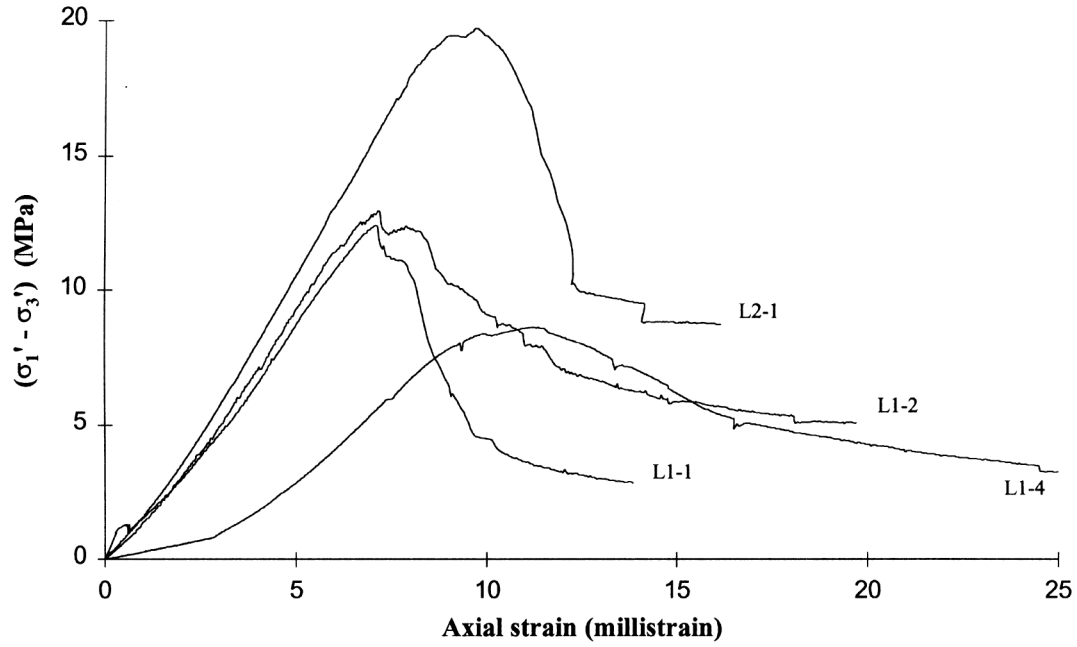

Figure II–3 – Axial stress - strain behaviour of 300*mm* diameter coal samples, Moura D Upper seam (Queensland, Australia). *From* [Medhurst and Brown, 1998].

3.2.1 Peak strength

In Figure II–4, the peak strengths obtained with the 40 tests carried out on 61*mm* diameter samples are plotted in function of the confinement for each coal seam (left) and for each brightness category (right). The first plot illustrates the difficulty in determining a trend even plotting the results by coal seam. While the strength values for Pits 17DU and 16DU display a fairly consistent trend of increasing strength with increasing confinement, the results from Pit 18BL show a much wider variation. This apparent variability may be explained by the brightness profile. Plotting the results (right) as high brightness (C2), mid to high brightness (C2/C3/C4), mid brightness (C3/C4) and dull (C5) samples, clear groups can be observed. This demonstrates the sensitivity of the strength to the relative proportions of cleating in each sample.

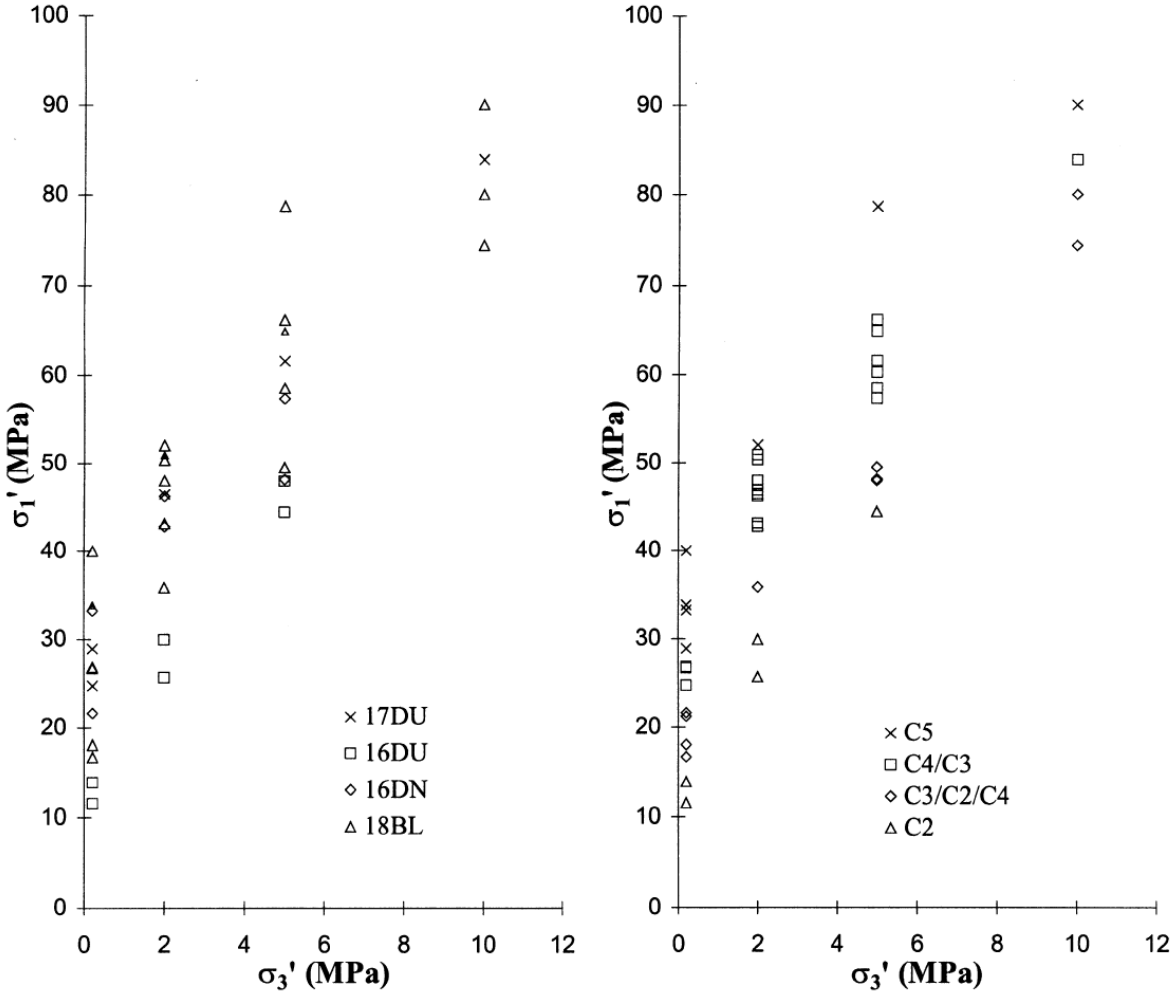

Figure II–4 – Peak strengths of 61*mm* diameter samples plotted for each coal seam and each brightness category. *From* [Medhurst and Brown, 1998].

A distinct mechanism of failure is observed depending on the confining pressure. At confinement less than 1MPa, an axial splitting failure mode (parallel to the major principal stress and emanating from the dominant cleat planes) is recognized while a shearing failure mechanism appears at higher confining pressures (Figure II–5).

I - Axial splitting

low confinement → high sample dilation

II - Shearing

high confinement → low sample dilation

Figure II–5 – Mechanisms of coal failure. *From* [Medhurst and Brown, 1998].

3.2.2 Elastic deformation behaviour

Figure II–6 presents a plot of the Young modulus *versus* the confinement pressure for the 61*mm* samples distinguished by their brigthness category. A similar plot is displayed in Figure II–7 for the Poisson's ratio. There is no clear dependence of these elastic moduli on the confining pressure. It usually indicates a low porosity of the material [Brown et al., 1989]. Scattering of the measured elastic moduli in relation to brightness category appears to be random. Indeed, it is likely the stiffness is sensitive not only on the overall brightness scale but also to the location and thickness of cleated bands within the sample.

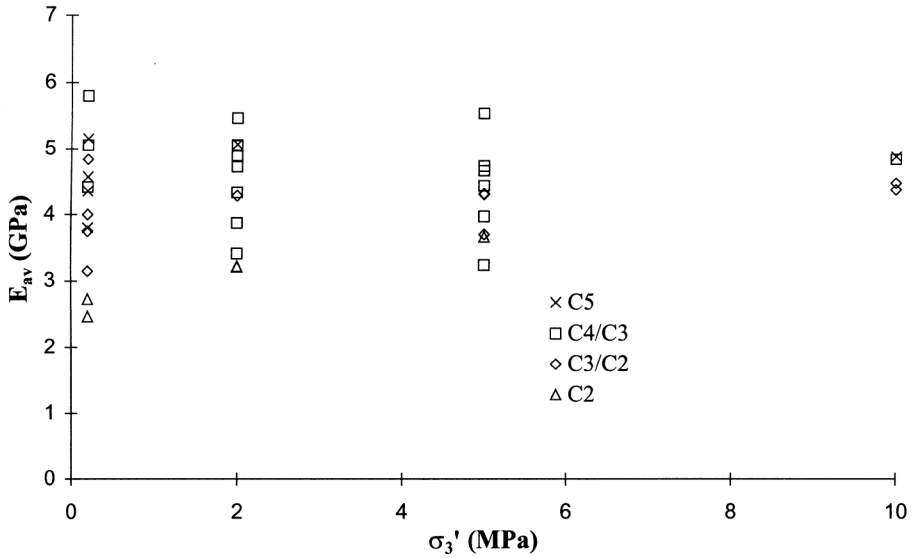

Figure II–6 – Elastic modulus against confining stress for 61*mm* diameter coal samples. *From* [Medhurst and Brown, 1998].

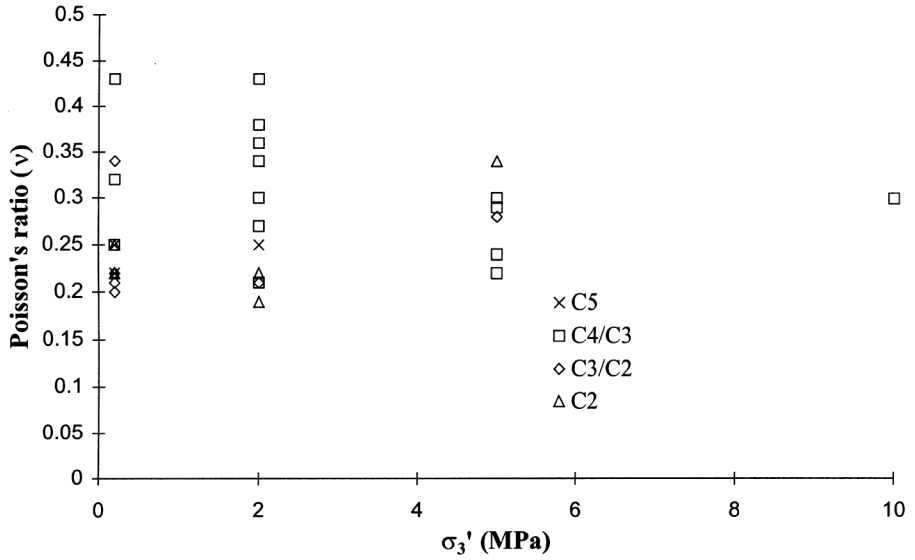

Figure II–7 – Poisson's ratio against confining stress for 61*mm* diameter coal samples. *From* [Medhurst and Brown, 1998].

Figures II–8 and II–9 illustrate the variation in elastic moduli with sample size. In Figure II–8, the Young modulus shows a non-linear decrease with increasing sample size. There is an asymptotic trend towards a value between approximately 1 5 and 2 0GPa. It is mentioned by [Medhurst and Brown,

1998] that this value is consistent with other estimates of elastic moduli for *in situ* coal. Concerning the Poisson's ratio, there is no apparent trend with sample size.

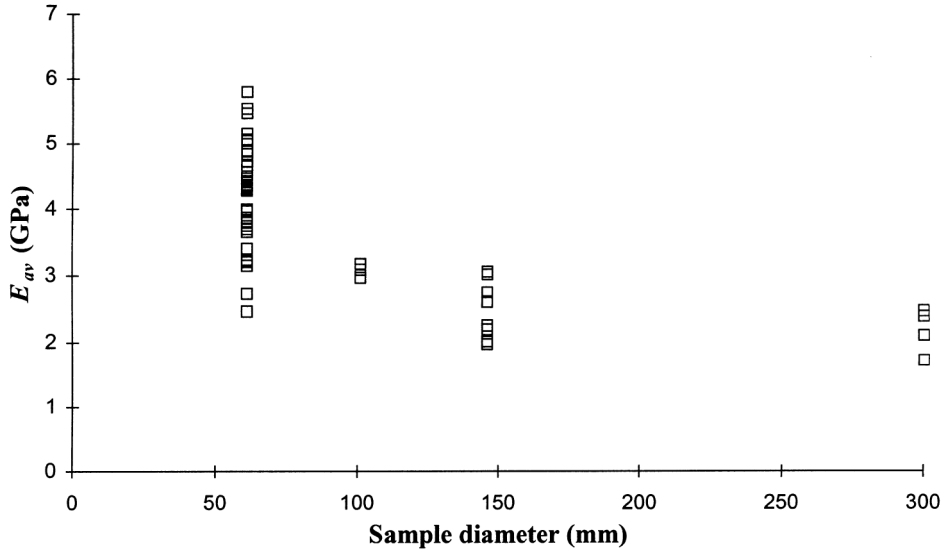

Figure II–8 – Effect of sample size measurements of elastic modulus. *From* [Medhurst and Brown, 1998].

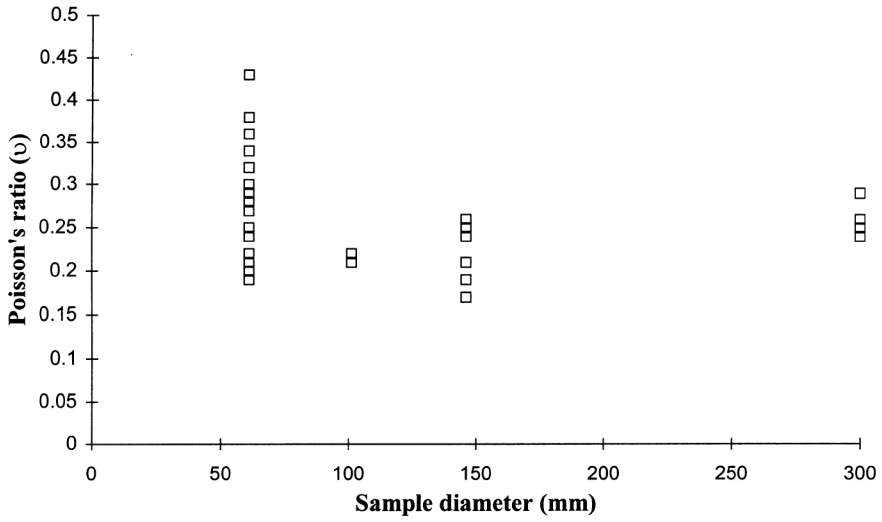

Figure II–9 – Effect of sample size measurements of Poisson's ratio. *From* [Medhurst and Brown, 1998].

3.3 Sorption properties

Figure II–10 shows for different coal basins from Belgium some experimental methane sorption data as a function of the bulk methane pressure [Coppens, 1967]. These data are fitted with a hyperbolic isotherm model explained hereafter.

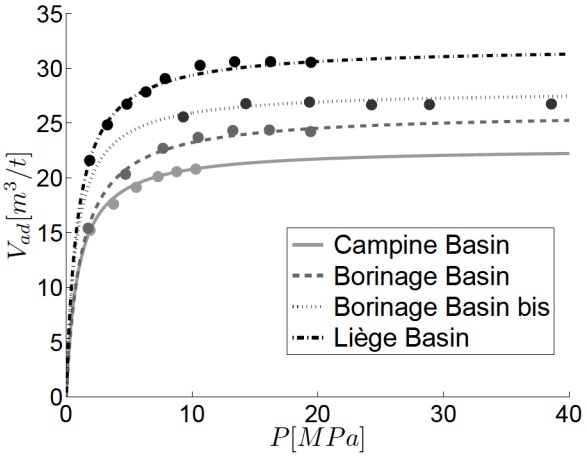

Figure II–10 – Langmuir's isotherm fitting for methane sorption data published by [Coppens, 1967].

Adsorption isotherm is the most widely used technique to describe gas adsorption (characterized by Van der Waals force), it is a relation giving the maximal quantity of adsorbed gas as a function of gas pressure at a given temperature. The Langmuir model [Langmuir, 1918] is extensively used for describing methane adsorption/desorption on coal because of its ability to close fit experimental data. The Langmuir model is a special form of the multilayer Brunnauer-Emmet-Teller (BET) model for which each adsorbate molecule in the first layer serves as an adsorption site for an adsorbate molecule into the second layer, the second layer for the third layer, and so on (Figure II–11) [Brunauer et al., 1938].

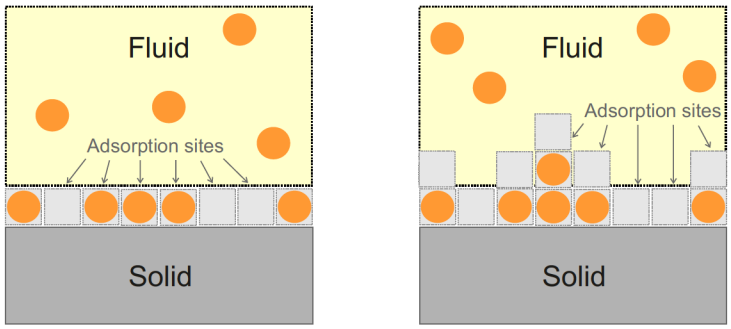

(a) Langmuir (b) BET

Figure II–11 – Sketches of the Langmuir and BET models.

The Langmuir's isotherm may be derived considering the following equilibrium equation:

$$\mathcal{M}_g + O- \rightleftharpoons O-\mathcal{M}_g \tag{II–1}$$

where $\mathcal{M}_g$ represents the gas phase molecules, $O-$ the vacant surface sites and $O-\mathcal{M}_g$ the species adsorbed on the surface. At equilibrium, the rate of forward reaction is equal to rate of backward reaction and the corresponding equilibrium constant K_c is given by:

$$K_c = \frac{[O-\mathcal{M}_g]}{[\mathcal{M}_g]\cdot[O-]} \tag{II–2}$$

$[O-\mathcal{M}_g]$ and $[O-]$ are respectively proportional to the surface coverage of adsorbed molecules Θ and the vacant surface $1-\Theta$. As $[\mathcal{M}_g]$ is proportional to the pressure of gas p, then a new equilibrium constant writes

$$K_c' = \frac{\Theta}{(1-\Theta)\cdot p} \tag{II–3}$$

Hence, the surface coverage is:

$$\Theta = \frac{K' \cdot p}{1 + K' \cdot p} \tag{II–4}$$

in which K'_c depends on temperature and enthalpy change for the process. The total adsorbed volume V_g^{Ad} equals $\Theta \cdot V_L$, where V_L is the monolayer adsorption capacity, it represents the volume adsorbed for an infinite pressure. The total adsorbed volume is finally written as follows:

$$V_g^{Ad} = \frac{V_L \cdot p}{P_L + p} \tag{II–5}$$

where P_L is the Langmuir pressure corresponding to $\frac{1}{2}V_L$. These two parameters, P_L and V_L, are used to control the shape of the curve to best fit some experimental data. The maximum sorption capacity V_L is independent of the temperature and pressure while the Langmuir pressure P_L is temperature-dependent parameter. Theoretically, P_L may be related to the enthalpy and the entropy for adsorption [Myers, 2002, Li et al., 2018]:

$$P_L = p_a \exp\left(-\frac{\Delta\mathcal{S}^0}{R}\right) \exp\left(\frac{\Delta\mathcal{H}}{RT}\right) \tag{II–6}$$

where p_a is the atmospheric pressure, R is the universal gas constant, T is the temperature, $\Delta\mathcal{S}^0$ is the standard molar integral entropy at saturation, and $\Delta\mathcal{H}$ is the differential enthalpy of adsorption. This $\Delta\mathcal{H}$ is the difference between the activation energy for desorption and adsorption [Xia et al., 2006]. A higher value of $\Delta\mathcal{H}$ corresponds to a stronger adsorbate-adsorbent binding energy since a larger energy barrier needs to be overcome for desorption. The entropy $\Delta\mathcal{S}^0$ is the difference between the entropy of the adsorbed phase when the surface is fully covered by adsorbate molecules and the entropy of the bulk phase at atmospheric pressure [Xia et al., 2008].

Figure II–10 shows the fitting obtained with the Langmuir's parameters given in the table below.

Basin	V_L $[m^3/t]$	P_L $[MPa]$
Campine	22.75	0.95
Borinage	26	1.2
Borinage bis	28	0.8
Liège	32	0.9

Table II–3 – Langmuir's parameters fitting methane sorption data published by [Coppens, 1967].

Note that when considering multiple gases in competition on sorption sites, the Langmuir's isotherm has to be extended to multicomponent adsorption isotherms [Ruthven, 1984, Clarkson and Bustin, 2000, Yu et al., 2008].

Adsorption occurs mostly in the organic regions of the coal matrix [Brochard, 2011]. Coal type may affect both adsorption capacity and desorption rate. Bright (vitrinite-rich) coals have a greater adsorption capacity and a slower desorption rates than their dull (often inertinite-rich) equivalents because of their highly microporous structure [Crosdale et al., 1998]. Vitrinite can adsorb up to five times more gas than inertinite or liptinite [Brochard, 2011].

Sorption properties may also vary with coal rank. Figure II–12 conceptually shows the CO_2 and CH_4 sorption capacity as a function of coal rank. Changes of CO_2 sorption capacity with coal rank are minor, whereas those with CH_4 can be significant [Bustin, 2002, Reeves, 2003].

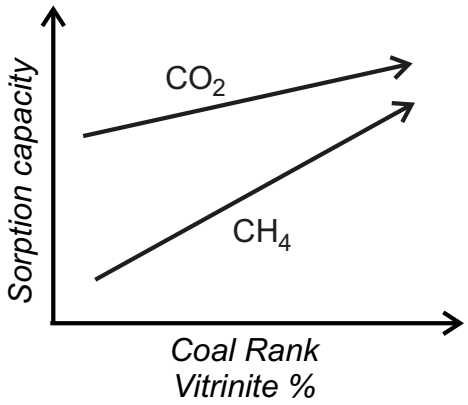

Figure II–12 – CO_2/CH_4 Sorption capacities versus Coal Rank. *Modified from* [Bustin, 2002].

3.4 Swelling behaviour

The first relationship between the swelling/shrinkage strain and the pore pressure that was proposed in order to derive a permeability model was a simple linear relationship [Gray et al., 1987]. However, it was later shown that this linear model overestimates the effect of swelling/shrinkage at high adsorption pressures [Levine, 1996]. Figure II–13 shows some data of swelling strain with CO_2 sorption measured in laboratory by various researchers [Levine, 1996, George and Barakat, 2001, Ottiger et al., 2008, Day et al., 2008]. The swelling due to sorption varies widely from one coal sample to the other given the variability of the organic content.

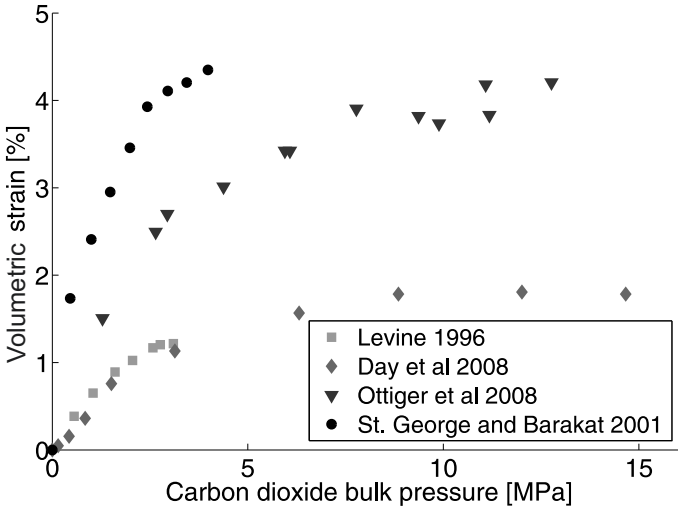

Figure II–13 – Compilation of stabilized swelling CO_2 strain data from the literature ([Levine, 1996], [George and Barakat, 2001], [Ottiger et al., 2008] and [Day et al., 2008]).

More accurately, it can be observed that swelling strain can be modelled using the same hyperbolic form as Langmuir's equation:

$$\varepsilon_{vs} \quad \frac{\varepsilon_L \; p}{P_L \quad p} \tag{II–7}$$

where ε_L is the Langmuir's strain and P_L the Langmuir's pressure.

However, many researchers consider that the volumetric sorption-induced strain ε_{vs} is approximately proportional to the volume of adsorbed gas [Sawyer et al., 1990, Harpalani and Chen, 1995, Seidle et al.,

1995, Cui and Bustin, 2005]:

$$_{vs} \qquad V_g^{Ad} \tag{II–8}$$

where is the volumetric strain coefficient. This linear law with the adsorbed content is often chosen [Cui and Bustin, 2005] given its easier applicability knowing the discrepancy with the experimental results.

Figure II–14 shows the evolution of the volumetric strain with the methane content. These data are fitted with a linear model giving the volumetric strain evolution with the bulk pressure shown in Figure II–15. Overall, 3 parameters are used but only one is new since the parameters required for the sorption isotherm are reused.

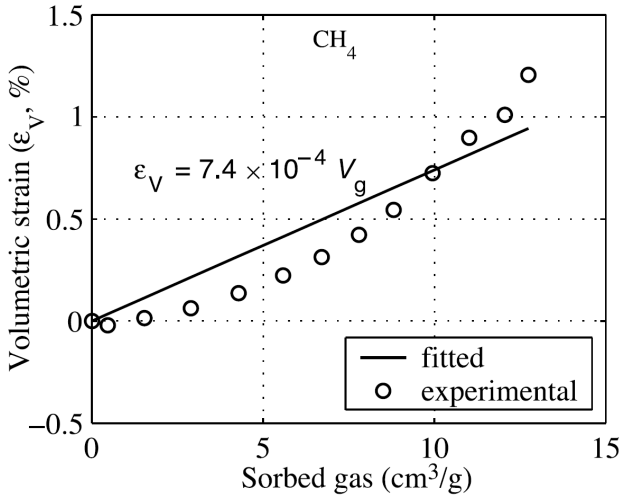

Figure II–14 – Volumetric strain with CH_4 content. *From* [Cui and Bustin, 2005].

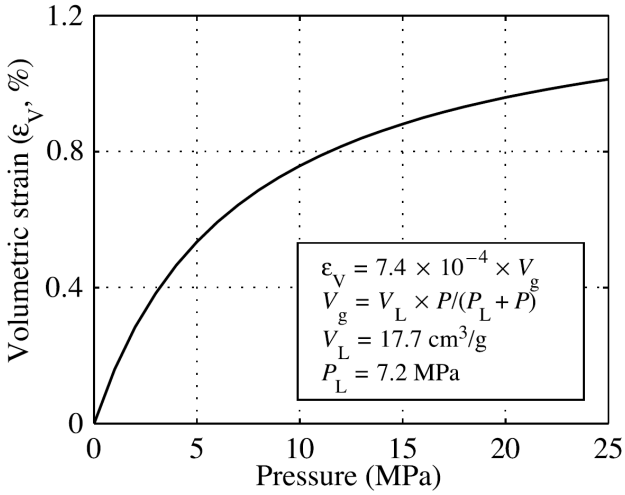

Figure II–15 – Volumetric strain with CH_4 pressure. *From* [Cui and Bustin, 2005].

Coal swells more with the injection of carbon dioxide than methane. It is the reason why CO_2-ECBM shows a decrease of the permeability of the reservoir. Indeed, a CO_2 molecule placed between the polymer chains of coal disrupts partly the original structure if the available volume between the chains is smaller than the actual volume of the CO_2 molecule [Mazumder et al., 2011].

3.5 Permeability

In the context of CBM recovery, the permeability is certainly, with the gas content, the most important property of the reservoir, it defines the level of transportability of the fluid. A low permeability can result in uneconomic production rates even if gas volume is high. Coal permeability is greatly affected by its structure, the cleat network, which may vary with coal type and rank (see section 3.1). Matrix "permeability" is typically orders of magnitudes lower than fracture permeability in the same coal [Moore, 2012]. Cleat aperture and frequency are therefore the most important physical attributes of the reservoir.

Using permeability data for wells producing methane from coal seams in the San Juan and the Black Warrior basins, and for which cleat spacing (frequency) was studied, Figure II–16 shows the relationship between cleat aperture (deduced from parallel-plate model), number of cleats per inch (frequency) and permeability [Laubach et al., 1998]. It illustrates how the effective permeability increases with increasing cleat frequency and/or with increasing aperture.

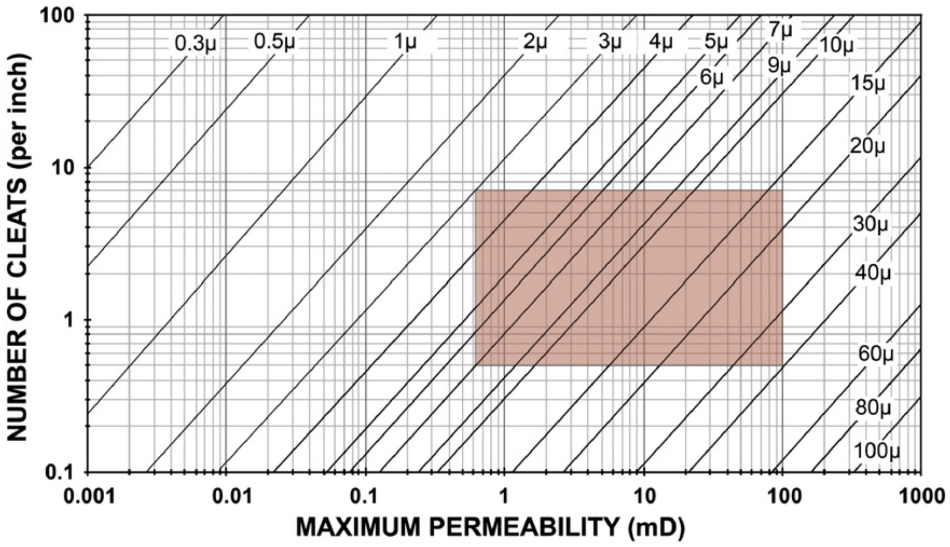

Figure II–16 – Relationship between cleat aperture, number of cleats (per inch) and permeability. Developed for the San Juan and Black Warrior basins. *From* [Moore, 2012] *modified from* [Laubach et al., 1998].

The permeability of coal reservoirs varies widely from seam to seam, it is in the wide range of $1\mu D$ to $1D$. Permeability decreases with increasing depth almost without exception. It is the most predictable relationship, although the permeability corresponding to a depth is different from basin to basin. Figures II–17 and II–18 show two examples of this relationship in one basin in Poland [McCants et al., 2001] and another one in Australia [Moore, 2012]. Variation in permeability at any particular depth is in part related to coal type as well as the difficulty in obtaining reliable permeability measurements [Moore, 2012].

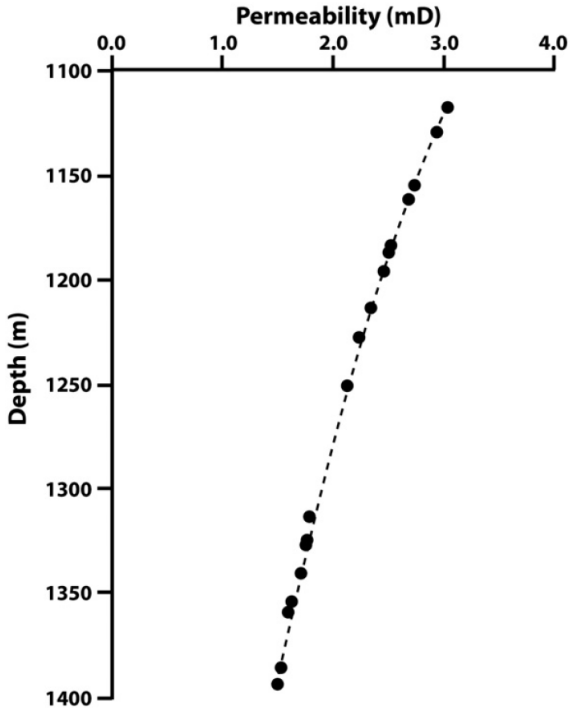

Figure II–17 – Relationship between permeability and depth for some coals in the Upper Silesian Coal Basin, Poland. *From* [Moore, 2012] *modified from* [McCants et al., 2001].

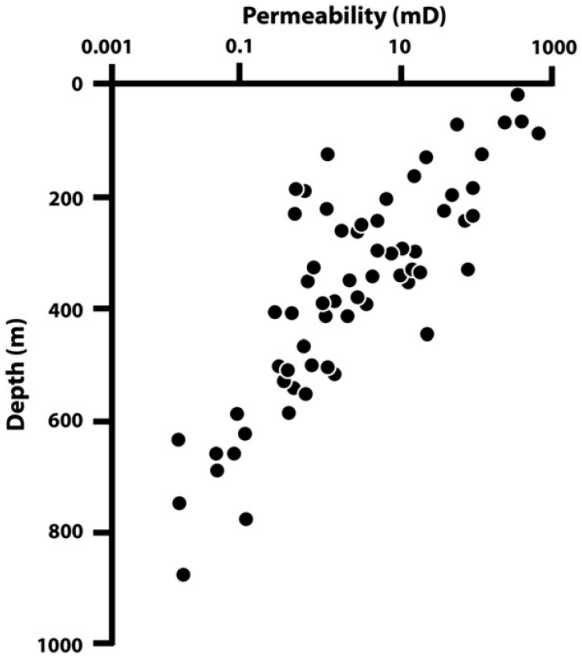

Figure II–18 – In situ coal bed permeability versus depth in a Permian coal basin in Australia. *From* [Moore, 2012].

In laboratory, some experiments early showed the permeability measured using carbon dioxide or methane was less than the permeability measured with air or nitrogen [Patching, 1965, Somerton et al., 1975]. Some researchers [Siriwardane et al., 2009, Wang et al., 2011] used a transient method to measure the gas permeability but others also employed a steady-state method [Robertson et al., 2007, Espinoza

et al., 2014, Wang et al., 2017]. Due to the length scale of the laboratory specimens, it is possible that permeability measurements are biased compared to *in situ* measurements since major fractures are less likely to be sampled. For instance, Espinoza *et al* measured permeabilities only in the range 0 00001 to 0 01mD [Espinoza et al., 2014]. Tomography imaging (resolution 25μm) on these specimens showed that the major cleats were mineralized (calcite).

Permeability results obtained by Robertson and Christiansen on coal samples collected in Wyoming (Anderson core) and Utah (Gilson core) are presented below [Robertson et al., 2007]. Different gases, overburden pressures and pore pressures were tested giving a good overview of the coupling phenomena.

Figures II–19 and II–20 show the permeability changes resulting from varying the overburden pressure. Nitrogen pore pressure is held constant during these first tests in order to highlight the effect of the overburden pressure. The two cores present a wide difference in permeability but both show an important increase of the permeability with the decrease of the stress. Indeed, cleats have a larger compressibility than the matrix and the cleat aperture is highly impacted by the mechanical stress state.

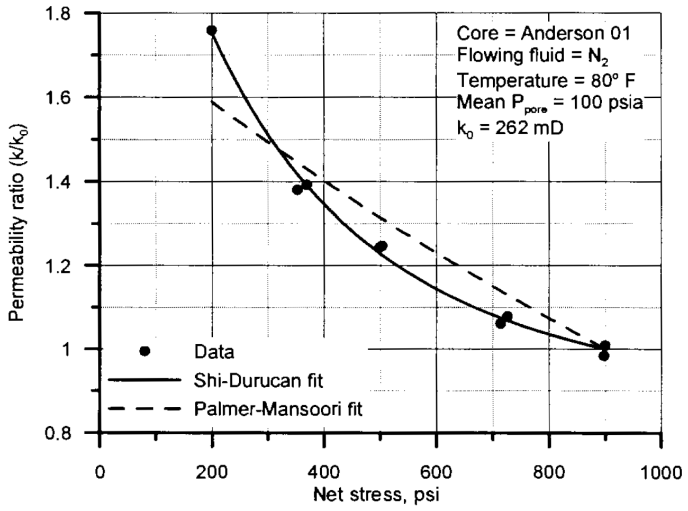

Figure II–19 – Plot showing the permeability changes of the Anderson 01 core as a function on net stress. *From* [Robertson et al., 2007].

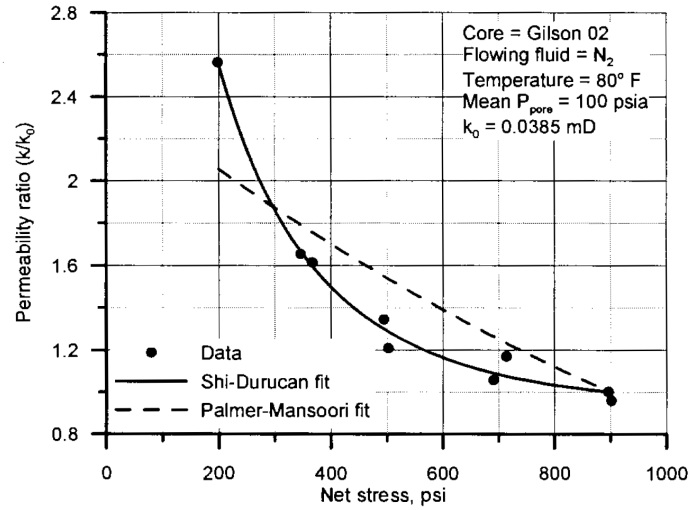

Figure II–20 – Plot showing the permeability changes of the Gilson 02 core as a function on net stress. *From* [Robertson et al., 2007].

These permeability data are fitted with some analytical models we do not discuss in this section. Actually, many models exist in the literature for the coal permeability evolution with the stress state and bulk pressure. A review of some analytical models may be found in [Pan and Connell, 2012] where about twenty models are presented. In fact, many of them are based on a relationship between permeability and porosity that we will try to avoid in this thesis. The interesting parts of some models will be presented as we progress in the development of our own models.

Varying pore pressure while holding the confining pressure to 1000psia [4] highlights the effect of the swelling on the permeability. Figures II–21 and II–22 display the permeability evolution as a function of pore pressure for the two cores. Initial permeabilities were measured at pore pressures of about 100psia and are displayed in the figures. Initial permeability to CO_2 is the lowest while the permeability to N_2 is the highest. It results from the distinct swelling behaviour of coal between the different gases.

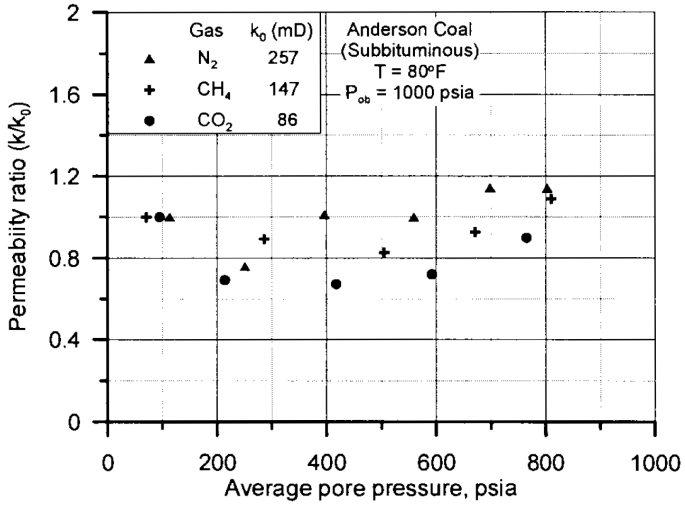

Figure II–21 – Permeability as a function of pore pressure for three gases using the Anderson 01 coal core. *From* [Robertson et al., 2007].

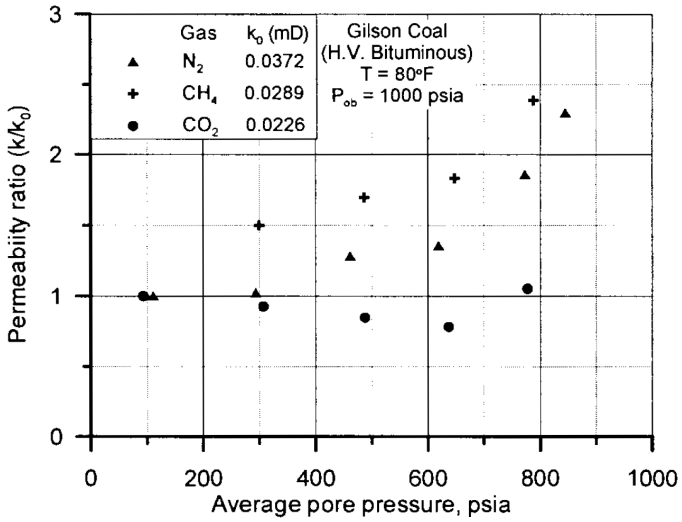

Figure II–22 – Permeability as a function of pore pressure for three gases using the Gilson 02 coal core. *From* [Robertson et al., 2007].

4. Pounds per square inch (absolute), 1psia 6895*Pa*.

For both cores, it is observed that the nitrogen permeability ratio increases as pore pressure increases. It means that the sorption-induced strain has very little effect with nitrogen while increasing the pore pressure (decreasing the "net" stress) opened the fractures and thus increased the permeability. The results are different for carbon dioxide. As pore pressure increases, the permeability initially decreases because of a larger swelling induced for these gases compared to nitrogen. Then, as pore pressure continue to increase, the swelling is overcome by the decreasing net stress and the permeability increases. For methane, the behaviour is different for the two cores. Methane permeability ratio shows the same behaviour as carbon dioxide with the Anderson core and the same as nitrogen with the Gilson core. The effect of sorption-induced strain was measured much less with the Gilson core compared to the Anderson core and carbon dioxide is therefore the only gas causing enough swelling to decrease the permeability.

4. Experimental study

This section presents an experimental study of the coupled hydro-mechanical behaviour of coal, with an emphasis on the evolution of coal permeability with CO_2 injection pressure. As coal permeability is particularly reliant upon the cleat network, this experimental study includes a tomography imaging and some thin sections to study the geometry of the coal specimens used for the permeability tests. CO_2 injection implies gas sorption in the coal matrix, it is measured by a sorption test determining the sorption isotherm of the material. Then, the structural rearrangement of the coal matrix induced by CO_2 sorption is measured by a swelling test with free boundary conditions. In the reservoir conditions, the material is constrained like in the permeability tests, the swelling of the matrix impacts therefore the initial cleat aperture. As carbon dioxide storage (CCS) or coalbed methane production (CBM) are highly coupled problems, mechanical properties of the matrix and the cleats impact the permeability evolution. For this reason, uniaxial and triaxial tests are also carried out to study the mechanical behaviour of the material.

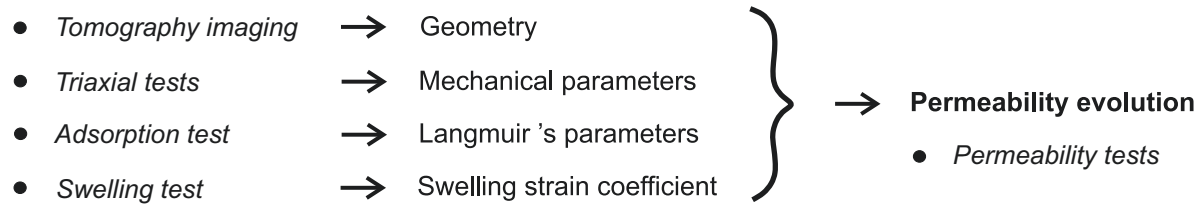

Figure II–23 – Overview of the experimental tests carried out

The original objective of this study is to acquire a comprehensive description of a unique coal by following the different items presented in the literature review: material structure (tomography imaging and thin section), mechanical properties (uniaxial and triaxial tests), sorption isotherm, swelling behaviour and permeability. Knowing the geometry of the cleat network, the mechanical properties and the swelling behaviour of the material, any consistent model should be able to predict the permeability evolution experimentally observed. In practice, various difficulties related to the identification of the geometry of the material have finally limited the ambitions of use of this experimental study.

The experimental methods are first presented and then the experimental results.

4.1 Experimental methods

The experimental method part consists of sample collection, sample preparation and characterization, and experimental procedures.

4.1.1 Sample collection

Several coal blocks were collected from an open pit mine (Glendell) from the Upper Hunter Valley, New South Wales, Australia. The coal belongs to the Late Permian [1] Wittingham coal measures which

1. Permian period lates from 299 million to 252 million years ago.

were deposited over the marine sediments of the Maitland Group as a regressive, coal-bearing fluvio-deltaic sequence [Uren, 1985, Golab et al., 2006]. Mineable coal seams at Glendell range in thickness from 0 3m to 3 5m.

4.1.2 Sample preparation and characterization

In order to characterize the material, a Proximate Analysis is followed. Different specimen are cored and cut in one of the coal block collected and a tomography imaging and some thin sections are carried out for two of the specimens.

4.1.2.1 Proximate Analysis

The Proximate Analysis [ASTM, 2007a], originally developed in the coal mining industry, determines the percentage of different categories of components. It considers coal is constituted of four components: the fixed carbon (FC), the volatile matter (VM), the ash (a) and the moisture (w).

A coal specimen was ground to powder and the fraction passing the $250\mu m$ sieve was used for the proximate analysis. The ash and the volatile matter are determined by establishing the losses in weight following respectively the ASTM procedure D3174 [ASTM, 2011] and D3175 [ASTM, 2007b]. The sample was first dried as detailed in ASTM D3175. The fixed carbon was determined subtracting the ash and volatile matter from 100% [ASTM, 2007a]. The proximate analysis was carried out by the Laboratory of Building Materials of the University of Liège (Belgium). Table II–4 gives the percentage of volatile matter, ash and fixed carbon in dry basis (d). Fixed carbon and volatile matter are expressed in dry ash free basis (daf) in Table II–5.

Parameter		Measurement 1 %	Measurement 2 %
Fixed carbon	(FC)	53 90	53 86
Volatile matter	(VM)	32 80	33 01
Ash	(a)	13 30	13 13

Table II–4 – Proximate analysis in dry basis (d).

Parameter		Measurement 1 %	Measurement 2 %
Fixed carbon	(FC)	62 17	62 00
Volatile matter	(VM)	37 83	38 00

Table II–5 – Proximate analysis in dry ash free basis (daf).

In order of increasing maturity, the ASTM defines different coal ranks [ASTM, 2012]. Fixed carbon and volatile matter contents are good indicators of the thermal history of the rock. Given the results of the Proximate Analysis, the studied material classifies as a high-volatile bituminous coal [Moore, 2012].

4.1.2.2 Specimen preparation

Three cylindrical specimens and one cubic specimen were cored and cut from the coal block (see dimensions in Table II–6). The coal specimens were dried for 24 hours in a 105°C oven before testing (sorption, swelling and permeability tests). Note that coal structure may be irreversibly altered upon drying, but it is particularly observed for low-rank coals [Deevi and Suuberg, 1987, Meyers, 2012]. It was chosen to dry the material since moisture content influences sorption properties [Joubert et al., 1973, Krooss et al., 2002]. Indeed, as the tests were carried out at different times and different locations,

the objective is to test the specimens in the same conditions, on dried material.

The cubic specimen was used for a swelling test. The three cylindrical specimens were first used for mechanical tests (loading in the elastic range) and two of these specimens were then scanned by tomography and used for the coupled permeability tests.

Sample	Geometry	Tests
B5s0	Cube (50*mm*)	Swelling test, and Proximate Analysis and adsorption test on powder
B5s1	Cylinder (*h* 79 87*mm*; 52 97*mm*)	UCS test (failure)
B5s2	Cylinder (*h* 76 79*mm*; 52 81*mm*)	Tomography imaging, triaxial tests and permeability test.
B5s3	Cylinder (*h* 84 84*mm*; 52 81*mm*)	Tomography imaging, thin section, triaxial tests and permeability test.

Table II–6 – Specimens cored in the same coal block for the experimental campaign (*h* is the height of the specimen and its diameter).

4.1.2.3 Tomography imaging

Most numerical models developed to simulate coalbed methane reservoirs are based on a coal structure consisting of small blocks of intact coal matrix separated by cleats [Harpalani and Schraufnagel, 1990]. In order to determine the size of coal blocks, a tomography imaging was carried out on two cylindrical specimens that were later used for the coupled hydro-mechanical tests (section 3.5). The imaging was conducted at Monash University, Melbourne, Australia, using a Zeiss Xradia 520 Versa. The specimens were scanned with a 27 37μm voxel size.

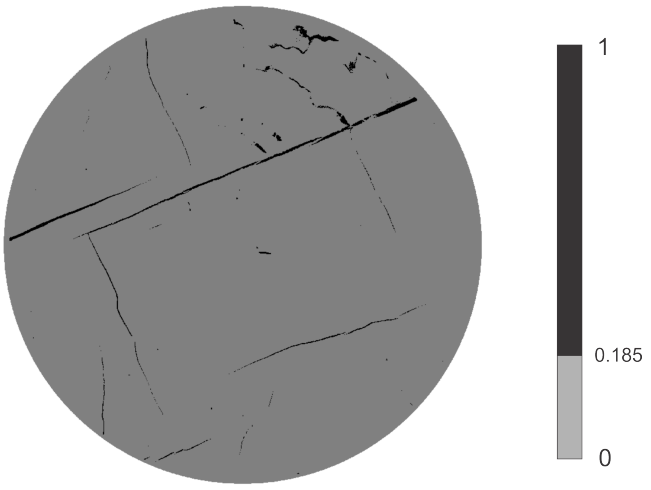

Figure II–24 – Tomography B5s2 (diameter 53*mm*).

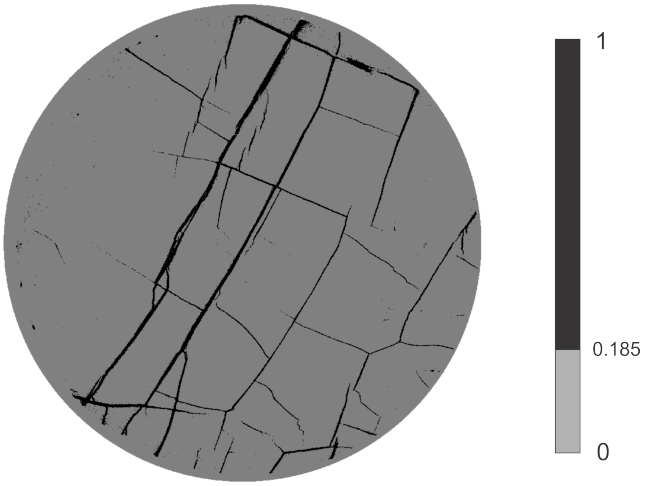

Figure II–25 – Tomography B5s3 (diameter 53*mm*).

The tomography reveals a network of orthogonal cleats with a spacing of less than 10*mm* in specimen B5s3 and about 20*mm* in B5s2 (see cross sections in Figures II–24 and II–25). This network is in black, it means its density is actually higher than the matrix. Any threshold in the binarization procedure is found to reveal empty fractures with the chosen voxel size. It is not uncommon to observe that some of the cleats are mineralized. The nature of minerals was not investigated in this study, they generally belong to two groups: clay minerals and carbonates [Faraj et al., 1996]. Mineralization has a negative impact on the permeability because it impedes the movement of fluids in the cleats [Tremain et al., 1991].

4.1.2.4 Thin sections

Thin sections were carried out by the Sedimentary Petrology Laboratory of the University of Liège (Belgium) to complement the tomography images which did not allow to observe open cleats with the voxel size used. The specimens were indurated with araldite resin before cutting and grinding them. Thin sections in Figure II–26 were obtained with transmitted light microscopy in order to highlight the voids created by the fractures. This Figure presents two different areas (4mm wide each) of a vertical section obtained from the sample B5s3. A network of open fractures with a spacing of about 1*mm* or less can be observed. It is a lower scale than the mineralized fractures observed with the tomography imaging. Note the horizontal fracture in the second picture is partly mineralized. Bioturbation was also identified with reflected light microscopy.

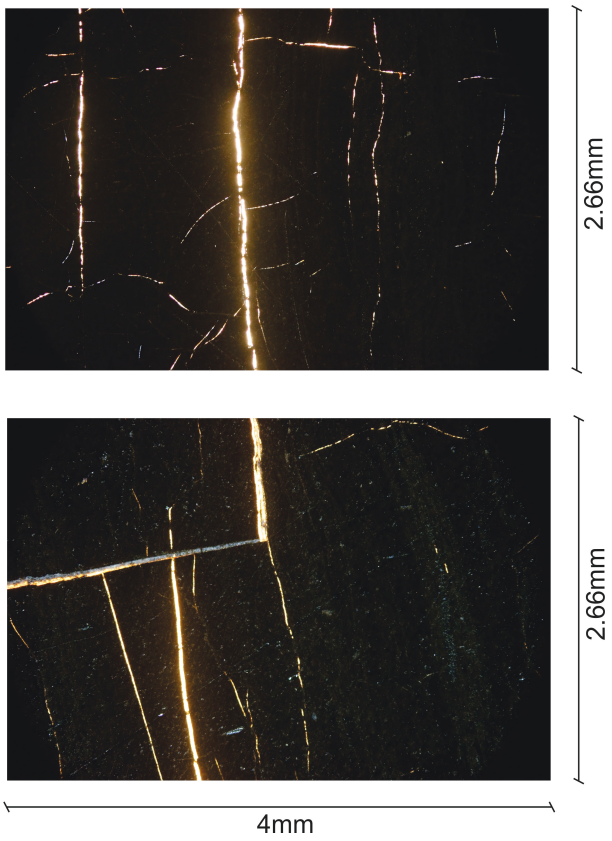

Figure II–26 – Vertical thin section of the specimen B5s3 (4*mm* wide).

4.1.3 Experimental procedures

4.1.3.1 Compression tests

Uniaxial compression tests with a loading rate of 0 001*mm s* were used to estimate the elastic properties of the coal specimens. Several loading-unloading cycles were applied in the elastic range before the specimen was taken to failure. The tangent Young's modulus (E_{50}) was estimated on an unloading path at 50% of compressive strength $_c$. Strain gages were glued on the specimen to measure the radial and the axial strains, in order to estimate Poisson's ratio.

Triaxial tests are controlled in force (rate[2] 0 0182*kN s*) instead of displacement to be able to stop the tests far before the failure to use the same specimens for the permeability tests. The maximum axial stress applied is 33% of $_c$ measured with a UCS test carried out on a specimen from the same coal block. The sample is first loaded under isotropic conditions until the confinement value is reached, then a deviatoric stress is applied on the sample.

4.1.3.2 Sorption

The carbon dioxide sorption isotherm was measured using an apparatus developed at the University of Mons (Belgium) around a high-pressure magnetic suspension balance provided by Rubotherm GmbH [De Weireld et al., 1999, Gensterblum et al., 2010, Billemont et al., 2013]. The apparatus allows sorption measurements for temperatures between 0 and 120°C with pressure ranging from 0 to 16MPa (see full technical details in [De Weireld et al., 1999]). The sorption test consists of measuring the variation of mass of the coal specimen (reduced to powder) following an increase of CO_2 pressure. The adsorbed amount is determined from the apparent mass change of the sample during the procedure:

$$M \quad M_{measured} \; p \quad M^0_{sample} \tag{II–9}$$

2. This rate was chosen to apply an axial force corresponding to the confinement of 500*kPa* in one minute.

where M^0_{sample} is the original sample mass measured after sample outgassing at 105°C under vacuum during 12h and $m_{measured}\ p$ is the mass measured at pressure p at the given constant temperature. Any buoyancy effect is taken into account by measuring a baseline isotherm using the Helium method [Billemont et al., 2013]. Stabilized adsorbed quantities for different injection pressures define the sorption isotherm. For the sorption test, the coal was crushed and sieved to keep particles between 180 and 325μm. Adsorbed quantities were measured on a dry sample for different pressures until 4 5MPa at a temperature close to 18°C.

Sorption data are fitted by a Langmuir's isotherm. Equation (III–89) is a hyperbolic equation which relates the maximal quantity of adsorbed gas to gas pressure at a given temperature with two parameters, V_L and P_L.

4.1.3.3 Swelling test

For this test, displacement sensors (RDP Group D5W series) were mounted on three sides of the cubical specimen using supports directly glued to the coal. The specimen was then placed in a high pressure triaxial cell filled with CO_2 and the gas pressure was increased incrementally. The swelling or shrinkage induced by the gas sorption or desorption was measured by the displacement sensors and a volumetric strain was computed for each pressure step. Four pressure steps of 0 5MPa, 1 5MPa, 2 5MPa and 3 5MPa, were applied, along a loading and an unloading path, to check reversibility of deformation (Figure II–27). An equilibration time of one week was used and it was checked deformation was less than 10 ^{4} between day 6 and day 7 of each step.

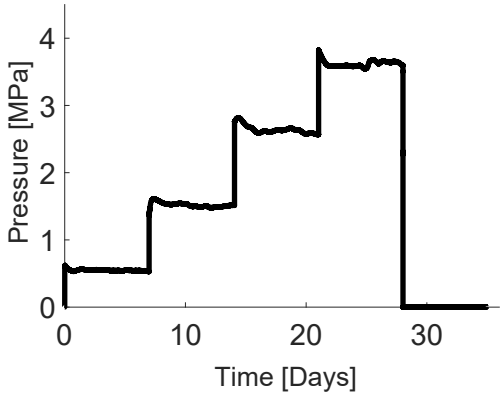

Figure II–27 – Pressure steps applied during the swelling test.

4.1.3.4 Hydro-mechanical tests

Some coupled tests were performed on two cylindrical coal specimens to highlight the effect of net confining stress and CO_2 pressure on the permeability of the coal.

A Hoek cell is used to apply a confinement pressure on the specimens which were constrained vertically by a stiff frame (Figure II–28). The specimens were placed between two porous disks, a bottom cap for the gas supply and a top cap for the gas release. The stack of caps and specimen were placed inside a neoprene membrane and an certain level of lateral confinement was applied to reduce the likelihood of gas leakage. The bottom cap was connected to a rigid tank (total volume of 0 00732m^3) and a gas cylinder (either air or CO_2) used to inject gas (for the adsorption phase) and conduct the gas permeability measurements. During the tests, the boundary conditions were as follows:

Axial deformation is prevented

Radial confinement is applied

The gas pressure at bottom of the specimen is equal to the injection pressure

- The pressure at the top of the specimen is either equal to the injection pressure (when the top valve is closed) or atmospheric (when the top valve is open).

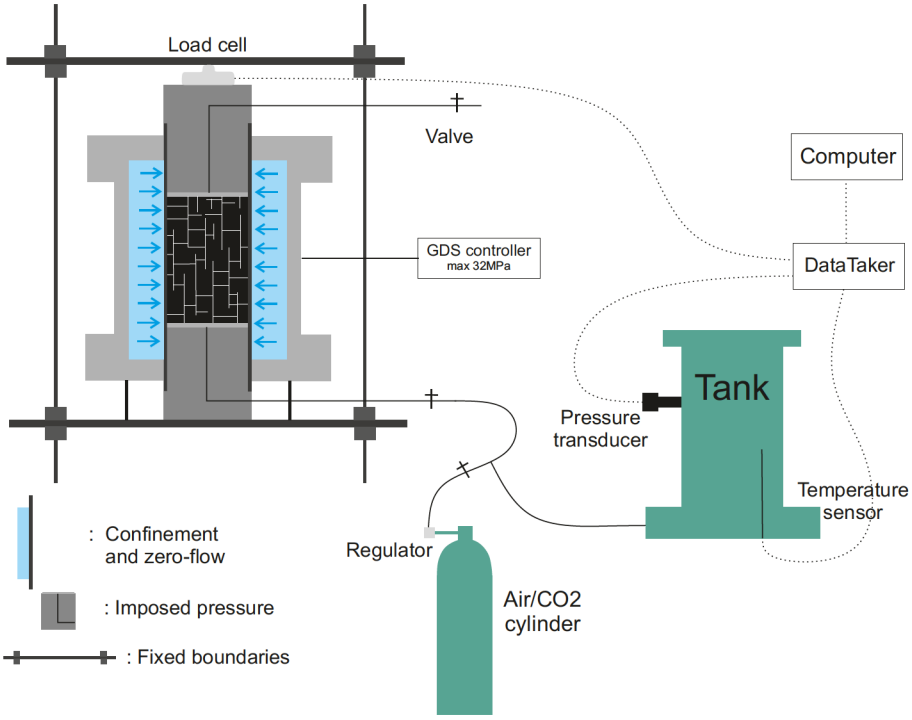

Figure II–28 – Set up of the permeability test (not to scale).

The permeability is determined from the pressure decay measured in the tank [Yoshimi and Osterberg, 1963]. The procedure detailed below is followed:

1. Install the chosen pressure in the tank with the release valve after the specimen closed. The sealing is ensured by a confinement pressure higher than the injection pressure.
2. Wait for equilibrium controlling the temperature sensor, the load cell and the GDS controller.
3. Close the valve from the gas cylinder.
4. Open the release valve after the specimen and measure with the pressure transducer the pressure decay in the tank.
5. After a decrease of pressure of few percent, the release valve is closed and it is checked the leakage is negligible compared to the gas flow during the test.

The test is completed out with different injection pressures, different confinement pressures and two dry specimens. Figure II–29 shows the pressure decays (normalised by the initial pressure) measured in the tank for air and CO_2 for a given pressure. The gas permeability is estimated from the pressure decay measurements using the following equation:

$$\bar{k} = \frac{V\ H\ \mu}{A\ p_a} \left[\frac{-\ln\left(\frac{p_{\Delta t}(p_0+2p_a)}{p_0(p_{\Delta t}+2p_0)}\right)}{\Delta t} \right] \tag{II–10}$$

where V is the volume of the tank, H and A are respectively the height and the area of the specimen, μ is the viscosity of the gas, p_a the atmospheric pressure, p_0 the initial pressure and $p_{\Delta t}$ the pressure in the tank after a time Δt.

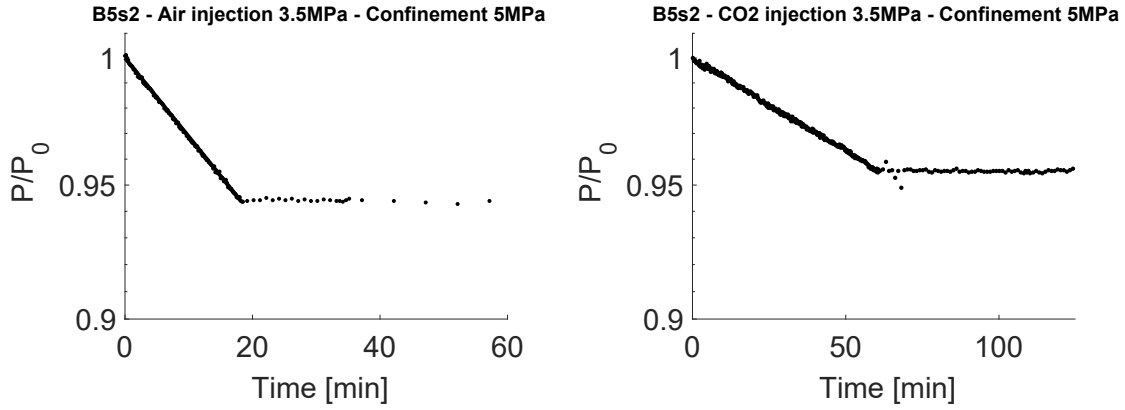

Figure II–29 – Pressure decays measured in the tank for gas (air and CO_2) injection 3 5MPa and confinement 5MPa.

Since the assumption of the relative pressure in the tank being much smaller than atmospheric pressure does not hold herein, Equation (II–10) is slightly different from the equation given in [Yoshimi and Osterberg, 1963] and that was later used by [Romero et al., 2005, Villar et al., 2005, Tang et al., 2011] to estimate the gas permeability of different types of soil. Developments to obtain the new formula are given hereafter.

The time rate of change of the mass of gas in the tank is by definition

$$V\frac{d\ _{0t}}{dt} \qquad _{0t}\ v_{0t}\ A \tag{II–11}$$

where V is the volume of the tank, $_{0t}$ and v_{0t} denote respectively the mass density of gas and the volume flux of gas per unit area at the bottom of the sample (z 0) at any time t, and A is the bottom area of the sample.

Then, the gas mass continuity at the height z in the specimen writes as follow in steady state conditions

$$\frac{d}{dz} \quad _{zt}v_{zt} \qquad 0 \tag{II–12}$$

where $_{zt}$ is the mass density of gas at z and t and v_{zt} is the volume flux of gas per unit area at the same place at the same time. Note that since the quantity of gas in the tank is much bigger than the gas stored in the sample, gas desorption from the matrix is negligible compared to the gas release from the tank. Steady state conditions are therefore considered for both air and CO_2.

As the permeability of the material is small enough to consider an isothermal expansion [3] of the gas in the tank during the test, the gas density at height z is simply proportional to the pressure at this height. From the continuity equation, we have therefore

$$p_a \quad u_{zt}\ v_{zt} \qquad p_a \quad p_t\ v_{0t} \tag{II–13}$$

where p_a is the atmospheric pressure, u_{zt} is the relative pressure in the sample at z at any time and p_t is the corresponding relative pressure in the tank.

From the experiments performed by Darcy on a column of sand [Darcy, 1856], it follows that the flow v_{zt} m s through a porous medium is proportional to the total pressure drop. This law is valid for a slow and viscous flow, *i.e.* at small Reynolds numbers (Stokes' flow). It writes:

$$v_{zt} \qquad \frac{\bar{k}}{\mu}\frac{du_{zt}}{dz} \tag{II–14}$$

3. Assumption of isothermal expansion of air in the tank has been shown to be valid for permeability values not exceeding 3 10 $^{10}m^2$ [Davies and Booth, 1961, Yoshimi and Osterberg, 1963].

where $\bar{k}$ is the intrinsic permeability of the sample and μ is the dynamic viscosity of the gas.

Introducing equation (II–14) in equation (II–13), the following equation is obtained

$$-\frac{\bar{k}}{\mu}(p_a+u_{zt})\,du_{zt} = (p_a+p_t)\;v_{0t}\;dz \tag{II–15}$$

Integration of this equation from $z=0$ ($u_{zt}=p_t$) and $z=h$ ($u_{zt}=0$) yields

$$\frac{\bar{k}}{\mu}p_t\left(p_a+\frac{p_t}{2}\right) = (p_a+p_t)\;v_{0t}\;h \tag{II–16}$$

Then, replacing v_{0t} in equation (II–11) by

$$v_{0t} = \frac{\bar{k}}{\mu}\frac{p_t}{h}\frac{(p_a+\frac{p_t}{2})}{(p_a+p_t)} \tag{II–17}$$

leads to

$$V\frac{\mathrm{d}\rho_{0t}}{\mathrm{d}t} = -\rho_{0t}\frac{\bar{k}}{\mu}\frac{A}{h}\frac{p_t(p_a+\frac{p_t}{2})}{(p_a+p_t)} \tag{II–18}$$

Moreover, the isothermal expansion of gas in the tank allows to write

$$\frac{d\rho_{0t}}{\rho_{0t}} = \frac{dp_t}{p_a+p_t} \tag{II–19}$$

Combining this equation and equation (II–18), we find

$$\frac{dp_t}{p_t(p_a+\frac{p_t}{2})} = -\frac{A\,\bar{k}}{V\,h\,\mu}dt \tag{II–20}$$

Finally, integrating this equation between $t=0$ ($p_t=p_0$) and $t=\Delta t$ ($p_t=p_{\Delta t}$), the formula (II–10) is obtained.

4.2 Experimental results

4.2.1 Mechanical properties

Figure II–30 shows the results of an unconfined compression test conducted on specimen B5s1. The compressive strength was measured at 9.8MPa and the Young modulus was measured at $E_{50}=1.40$GPa on a loading path and at $E=1.94\pm0.32$GPa when using the four unloading phases. Measurement of radial strain returned a Poisson's ratio of $\nu=0.15\pm0.014$. A second test carried out on a specimen cored in a second coal block (from the same seam) showed a compressive strength of 12.93MPa and a modulus $E_{50}=2.40$GPa. It indicates a variability of the mechanical properties inside the same seam. It is the reason why it was relevant to carry out some mechanical tests on the samples used for the permeability measurements.

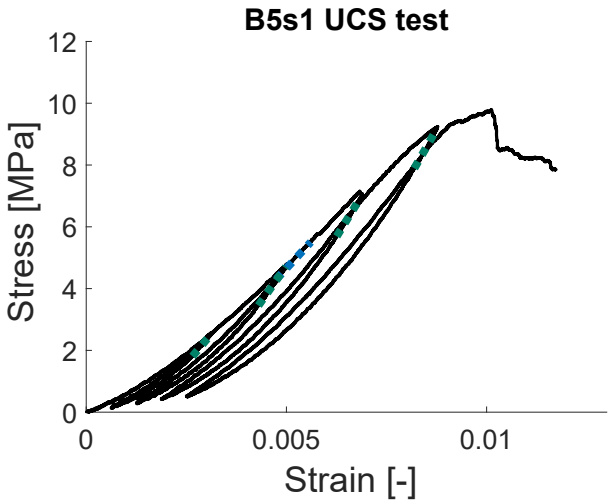

Figure II–30 – UCS test on specimen B5s1: stress-strain curve

Figure II–31 presents the stress-strain response under radial confinement. A non-linear response is clearly visible at zero or low confinement. Also, the initial stiffness of the coal is seen to increase with the degree of confinement, which is explained by the fact that increasing the confinement leads to a closure of the fractures present in the coal. Closing these fractures, the stiffness becomes independent of the degree of confinement, i.e. all the curves are close to being parallel and represent the stiffness of the coal matrix.

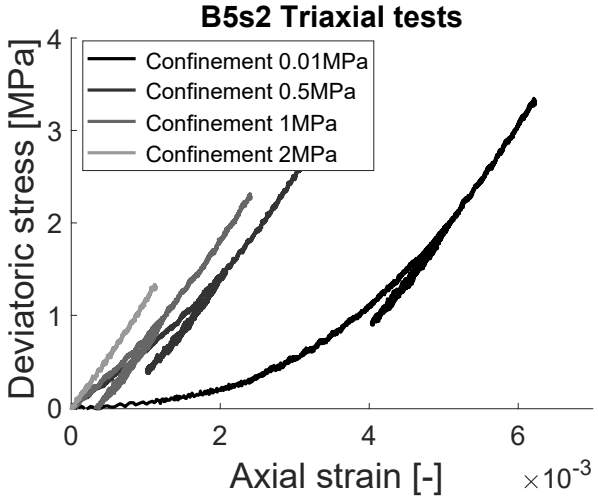

Figure II–31 – Triaxial tests on specimen B5s2: stress-strain curve.

The Young modulus determined during the unloading phases appears to be constant, for the values of confinement applied (Figure II–32). The elastic modulus of the coal matrix is therefore considered constant and equal to 1 21 0 021GPa. For the Poisson ratio, a value of 0 128 0 033 was deem representative of the material.

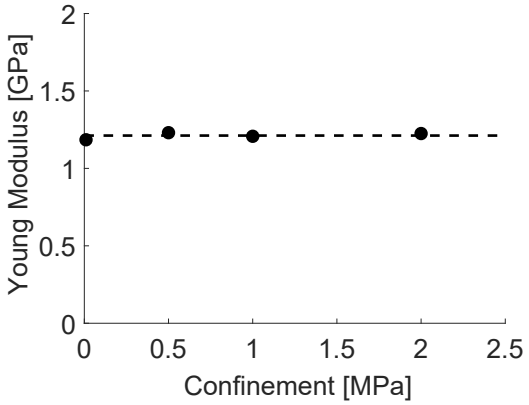

Figure II–32 – Triaxial tests on specimen B5s2: Young modulus.

The same observation was made following the triaxial test on the specimen B5s3 (Figures II–33 and II–34). The Young modulus and the Poisson's ratio of the coal matrix were estimated to be 1 21 0 019GPa and 0 158 0 051 respectively. Note that specimens B5s2 and B5s3 were not loaded to failure, as these specimens were needed for the coupled tests.

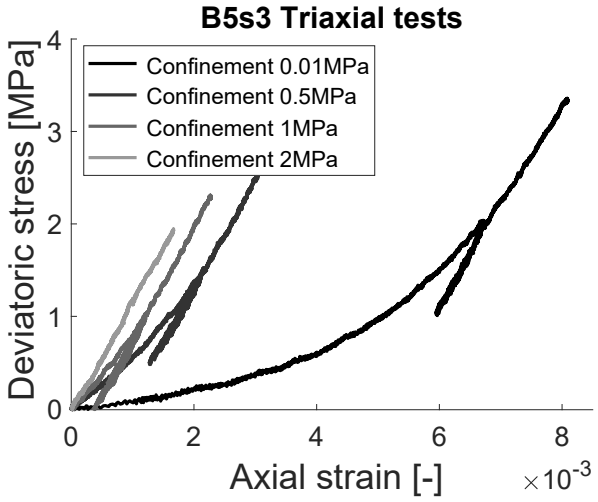

Figure II–33 – Triaxial tests on specimen B5s3: stress-strain curve.

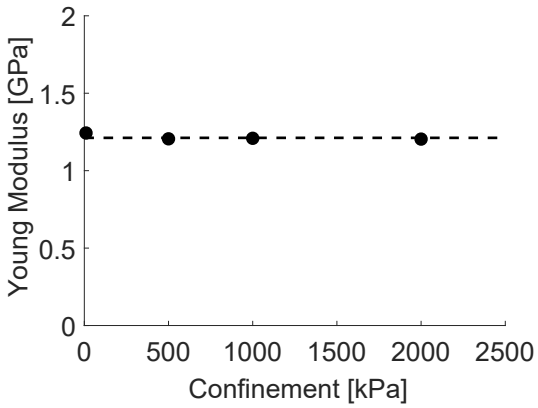

Figure II–34 – Triaxial tests on specimen B5s3: Young modulus.

The non-linearity of the stress strain response at the beginning of loading suggests that the normal

stiffness of cleats is not constant but progressively increases with cleat closure until the point where the measured stiffness is that of the matrix. All mechanical parameters can ultimately be determined by back-analysis of these results.

4.2.2 Sorption isotherm

Sorption measurements were conducted twice with results reported in Tables II–7 and II–8.

Temperature T^oC	Pressure MPa	Adsorbed quantity $mol\ kg$
17.9	0.093	0.460
17.8	0.514	0.927
17.9	1.385	1.285
17.8	1.995	1.439
17.7	2.153	1.478
17.7	2.507	1.547
17.8	2.668	1.579
17.7	3.010	1.629
17.6	3.541	1.700
17.6	4.522	1.832

Table II–7 – Sorption test results - Measurements 1.

Temperature T^oC	Pressure MPa	Adsorbed quantity $mol\ kg$
18.4	0.087	0.448
18.5	0.521	0.926
18.4	1.031	1.166
18.4	1.491	1.312
18.4	1.989	1.433
18.5	2.497	1.535
18.3	2.984	1.621
18.5	3.483	1.684
18.4	4.480	1.814

Table II–8 – Sorption test results - Measurements 2.

These adsorbed quantities may be converted into gas volume for room temperature conditions (20°C). These data are plotted in Figure II–35 and fitted with a Langmuir model [Langmuir, 1918]. The parameters defining the isotherm are given in Table II–9.

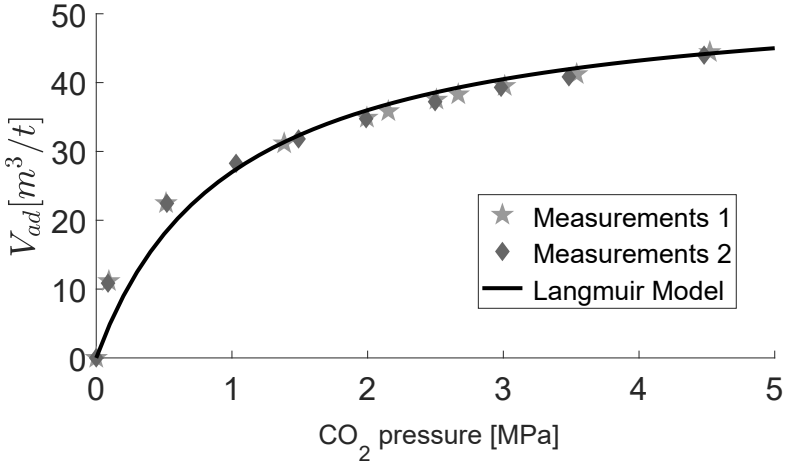

Figure II–35 – Experimental sorption data fitted by the Langmuir's isotherm (Parameters from Table II–9).

Parameter		Value	
Langmuir's volume	V_L	54	m^3 t
Langmuir's pressure	P_L	1	MPa

Table II–9 – Langmuir's parameters obtained from curve fitting of the experimental sorption data.

4.2.3 Swelling strain

The volumetric strain evolution is given in Figure II–36, which shows that most deformations occur within the first few hours of the test. Each swelling increment lasted one week and the value of the stabilized volumetric strain is displayed as a function of the pressure in Figure II–37. The stabilized strain is in the same range as other data collected in the literature from different CO_2 injection experiments.

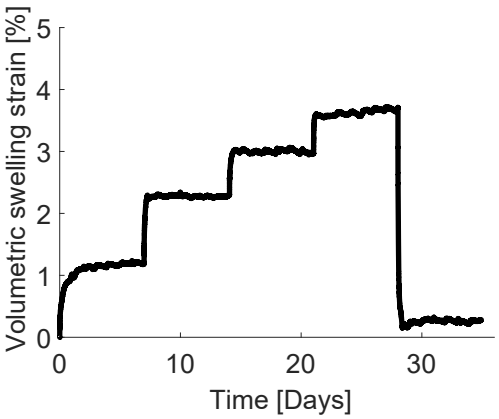

Figure II–36 – CO_2 volumetric swelling strain.

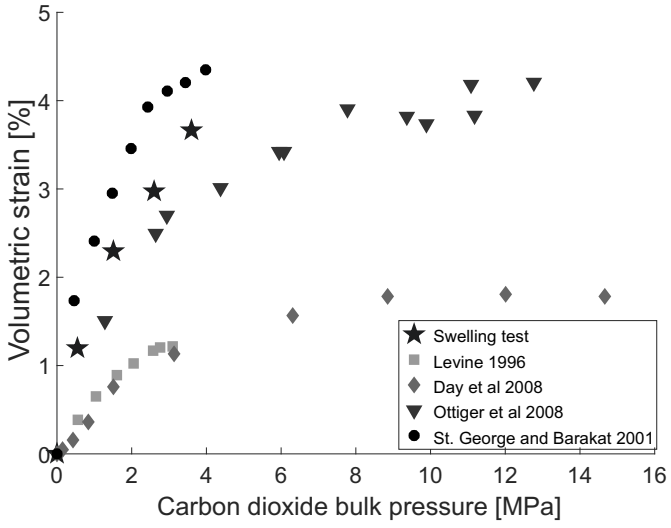

Figure II–37 – Stabilized swelling CO_2 Strain compared to literature ([Levine, 1996], [George and Barakat, 2001], [Ottiger et al., 2008] and [Day et al., 2008]).

As discussed in the literature review, many researchers consider that the volumetric sorption-induced strain $_{vs}$ is approximately proportional to the volume of adsorbed gas [Sawyer et al., 1990, Harpalani and Chen, 1995, Seidle et al., 1995, Cui and Bustin, 2005]. The adsorbed gas volume is calculated using

the Langmuir's isotherm Equation (II–5) with parameters calibrated (Table II–9) from the sorption test carried out on coal particles. The sorption strain coefficient used in Equation (II–8) to define the "Linear model" was found to be 0 8$kg\ m^3$ (Figure II–38). A hyperbolic model is also tested using two parameters with Equation (II–7). Parameters used in Figure II–38 are $_L$ 0 054 and P_L 2MPa. As expected, this second model allows to improve a bit the fitting of the experimental results.

These swelling strain parameters were determined for the bulk material. However, considering a matchstick geometry under free boundary conditions, cleats do not play a role in the stabilized swelling strain. Therefore, these swelling parameters may also be considered representative of the coal matrix.

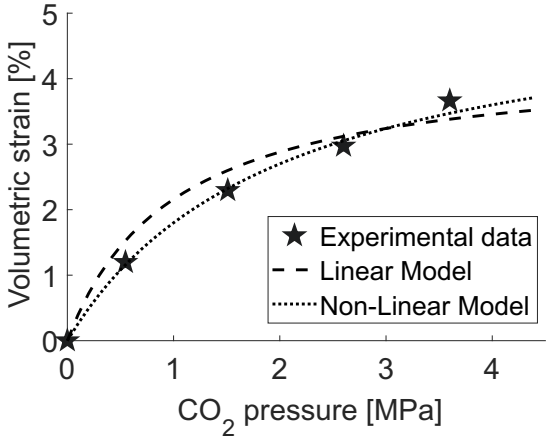

Figure II–38 – Evolution of the stabilized swelling strain with the injection pressure.

4.2.4 Permeability results

Equation (II–10) is used to estimate the permeability from the pressure decay measured during the coupled tests carried out on specimens B5s2 and B5s3. For instance, the permeability is 3 5 10 $^{17}m^2$ for the set of data reported in Table II–10. All the permeability values obtained from the tests carried out with a 5MPa confinement on the specimens B5s2 and B5s3 are displayed [4] in Figures II–39 and II–40, respectively. Increasing the pressure of air injected at the base of the specimens was found to result in an increase of permeability. In contrast, with carbon dioxide, the opposite trend was observed, i.e. the permeability decreases when the CO_2 pressure augments.

Tank volume	V	0 00732 m^3
Specimen area	A	8761 6 mm^2
Specimen height	h	76 79 mm
Initial pressure	p_0	3 460 MPa
Final pressure	p_t	3 266 MPa
Time	t	1091 s
Dynamic viscosity (p_0, 18^oC)	μ	18 636 10 $^6Pa\ s$

Table II–10 – Example of data set used to estimate permeability through equation II–10: Specimen B5s2 with confinement 5MPa and air injection pressure 3 46MPa.

4. Permeability values are displayed in function of injection pressure (initial tank pressure). This pressure actually differs from the equivalent pressure to which the permeability is measured given the variation of pressure between the two extremities of the sample.

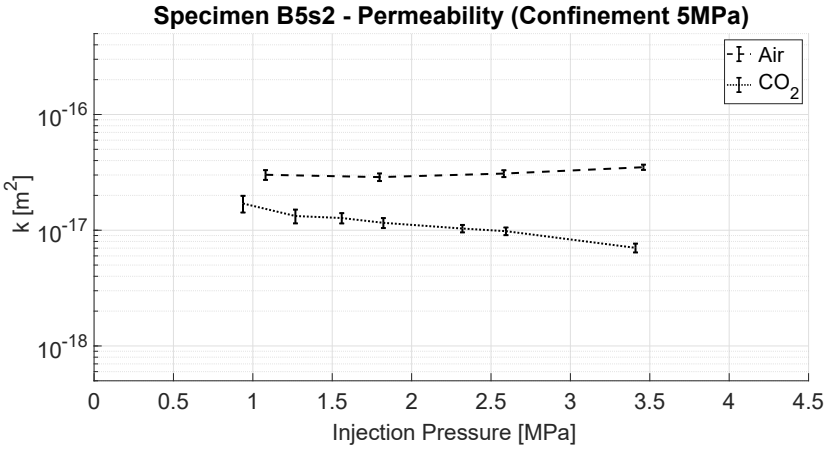

Figure II–39 – Permeability evolution with air and CO_2 pressures for specimen B5s2 (confinement 5MPa).

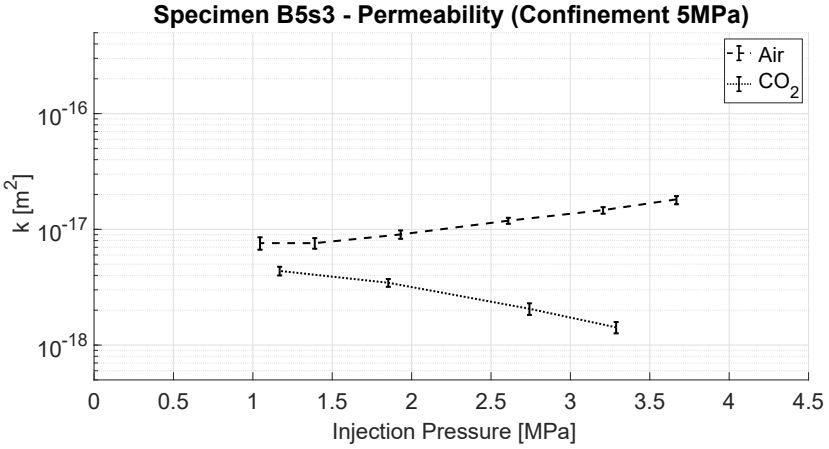

Figure II–40 – Permeability evolution with air and CO_2 pressures for specimen B5s3 (confinement 5MPa).

Different degrees of confinement were also applied to specimen B5s3 in order to highlight a possible effect of boundary conditions like it is observed *in situ* with the depth of the reservoir. Results are presented in Figures II–41 and II–42 for air and carbon dioxide, respectively. The following trends were observed:

The higher the confinement, the lower the permeability, all other things being equal.

The permeability drops as the injection pressure of carbon dioxide augments, except at low confinements, which is due to local opening of the cleats by the pressurised CO_2.

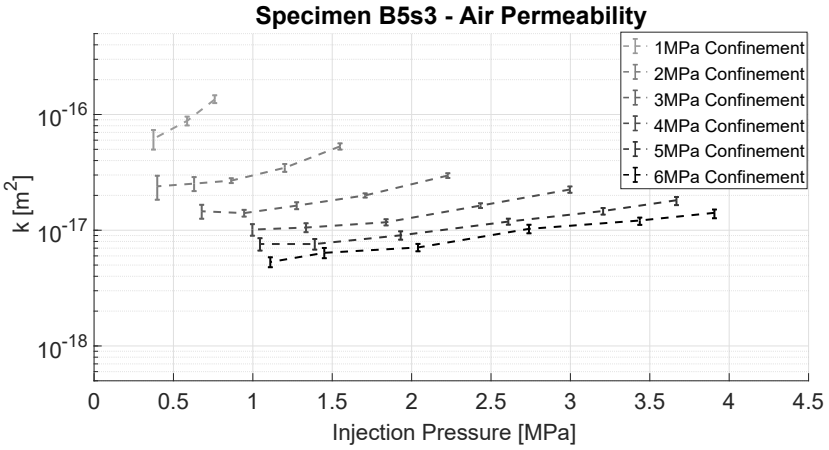

Figure II–41 – Permeability evolution with air pressure for specimen B5s3 (different confinements).

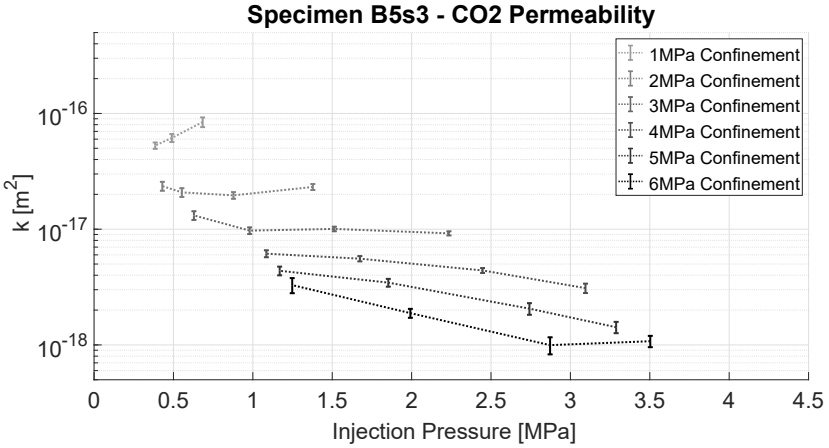

Figure II–42 – Permeability evolution with CO_2 pressure for specimen B5s3 (different confinements).

The first consequence of increasing the confinement is a progressive closure of the cleats, reducing the permeability. Figure II–43 shows how the computed permeability drops as the confinement increases for different CO_2 injection pressures [5].

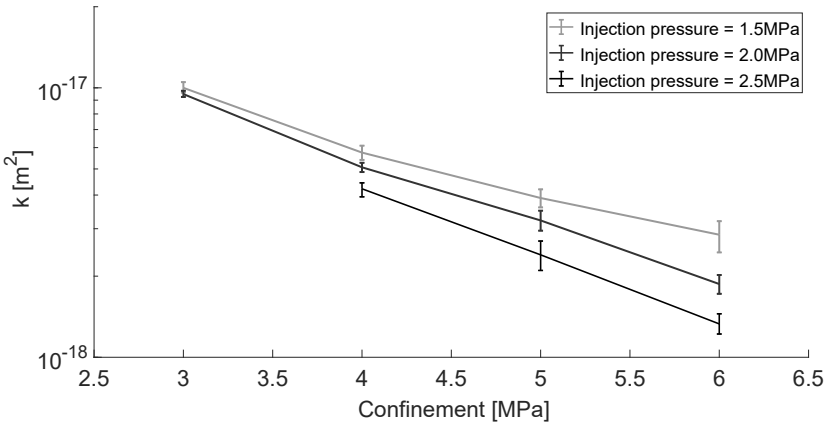

Figure II–43 – CO_2 permeability evolution with the applied confinement.

5. Values were interpolated as experimental data were not measured for the same injection pressures but only the same confinements.

Moreover, the lower the confinement and the easier the total volume can increase with the injection pressure, what contributes to increase the permeability with the injection pressure. A smaller confinement also implies that an increase of the injection pressure leads to a larger decrease of the effective stress than for a larger confinement. The permeability increases with the decrease of the effective stress.

When using air as an injected gas, it was observed that increasing the injection pressure results in an augmentation of permeability, which is explained by an opening of the cleats. Indeed, air is a weakly adsorbing gas like nitrogen [Fitzgerald et al., 2005, Battistutta et al., 2010], and the gas slippage phenomenon (Klinkenberg effect [Klinkenberg et al., 1941]) tends to diminish with an increase in gas pressure. Consequently, the mechanism behind the permeability increase with the air pressure is the effective stress rather than the Klinkenberg effect.

When using carbon dioxide as an injected gas, it was observed that the permeability decreases with the injection pressure. This phenomenon is linked to the adsorption of CO_2 on the coal, which results in swelling of the coal matrix. Because the specimen is confined, swelling is hindered and tends to close the cleats. This closure mechanism prevails over the opening of the cleats due to an increase of effective stress as the injection pressure augments.

Note that the permeability will not indefinitely decrease with the injection pressure. Some experiments conducted by Robertson and Christiansen [Robertson et al., 2007] and Wang *et al* [Wang et al., 2011] showed the permeability decreases at low pore pressure but increases at high pore pressure (larger than 3MPa). Indeed, when tending to the sorption saturation, the impact of the internal swelling is decreasing. In this thesis, a larger range of confinement values was used and it appeared in Figure II–42 that the rebound pressure occurs at lower CO_2 injection pressures for lower confinements.

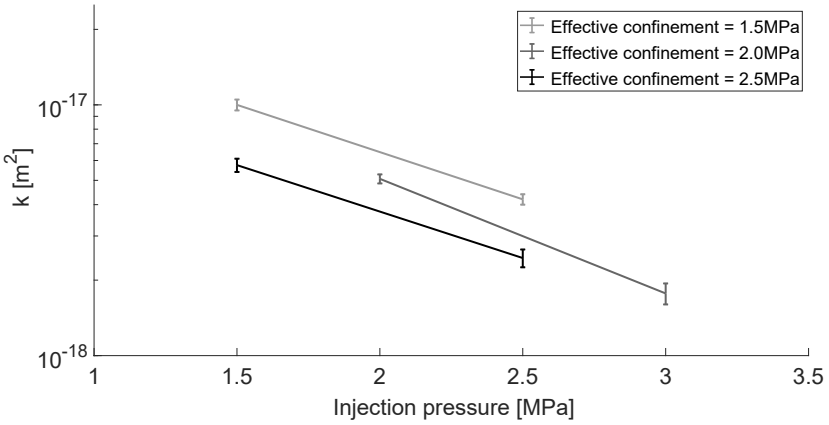

Figure II–44 – CO_2 permeability evolution with the pore pressure for a constant difference pressure.

Combining different confinements and injection pressures, it is possible to obtain permeability values for constant effective confinement (confinement pressure minus injection pressure) and therefore highlight the effect of the swelling (Figure II–44). The magnitude of the decrease is larger than when considering the permeability evolution with the injection pressure for a constant confinement (where the effective stress is thus decreasing and contributes to increase the permeability).

Conclusions Part II

This thesis aims to model gas flow into coalbed. Before the modelling, it was therefore essential to understand the behaviour of the material we are trying to model. In this purpose, few results from the literature were presented to characterize and highlight the hydro-mechanical behaviour of coal. From a structural point of view, tomography imaging carried out on coal shows a geometry of blocks and fractures. Then, injecting gas in the material, a hyperbolic sorption isotherm is measured. Sorption induces a matrix swelling which is often given as a linear relation of the adsorbed quantity despite the actual behaviour generally deviates from this linear model. Finally, we are interested in gas flow, the most important phenomenon observed is that the swelling affects permeability.

This part of the thesis was not limited to a literature review, an experimental study was also carried out to highlight the hydro-mechanical couplings in coal with an emphasis on cleat permeability changes due to the variation of the adsorbed gas content in the matrix and the variation of the fluid pressure in the cleats. To do so, the material was also characterized via a suite of mechanical tests and sorption isotherm measurements. The cleat spacing of the specimens was also investigated with a tomography imaging and some thin sections. However, it was not possible to identify a clear fracture network in the samples.

The permeability was estimated from a gas pressure decay test. The tests carried out with air show that the permeability augments with injection pressure which is explained by an effective stress effect opening the cleats, regardless of the degree of confinement. In contrast, the evolution of permeability when injecting CO_2 depends on the degree of confinement. Under low confinement, the same effective stress prevails and the permeability increases as the injection pressure increases. However, under higher degrees of confinement (i.e. past 3MPa), the permeability decreases with the injection pressure as a result of matrix swelling closing the cleats. This swelling behaviour was evidenced by a specific swelling test where the volumetric strain following CO_2 injection was recorded.

The task now is to develop a hydro-mechanical model that takes into account the observed phenomena. Different scales are investigated in the following parts of the thesis.

Acknowledgements

I thank Glendell coal mine for providing the studied material. Laboratory staff from the University of Newcastle (Australia), the University of Liège (Belgium), the Monash University of Melbourne (Australia) and the University of Mons (Belgium) are also thanked for their technical support.

Part III

Macroscale

Introduction Part III

Most coal seams hold important quantities of methane which is recognized as a valuable energy resource. Coal reservoir is considered not conventional because methane is held adsorbed on the coal surface. Coal is naturally fractured, it is a dual-porosity system made of matrix blocks and cleats (i.e fractures). In general, cleats are initially water saturated with the hydrostatic pressure maintaining the gas adsorbed in the coal matrix. Production of coalbed methane (CBM) first requires the mobilization of water in the cleats to reduce the reservoir pressure. Changes of coal properties during methane production are a critical issue in coalbed methane recovery. Indeed, any change of the cleat network will likely translate into modifications of the reservoir permeability.

This part presents a consistent hydro-mechanical model at the macroscale for the modelling of multiphase flow in coalbeds. However, due to the particular structure of coal, the model is based on a dual-continuum approach to enrich the macroscale with microscale considerations. Shape factors are employed to take into account the geometry of the matrix blocks in the mass exchange between matrix and fractures (Figure III–1). The hydro-mechanical model is fully coupled. For example, it captures the sorption-induced volumetric strain or the dependence of permeability on fracture aperture, which evolves with the stress state.

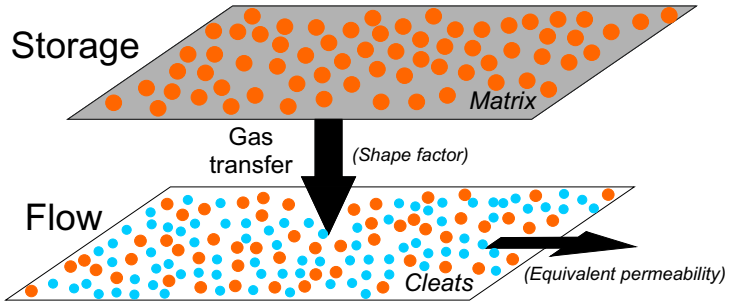

Figure III–1 – Dual-continuum approach for the hydraulic modelling.

This part consists in four sections. The first one presents some general concepts used for the modelling of geomaterials. Then, the hydro-mechanical model is presented detailing the mechanics, the hydraulic and the hydro-mechanical couplings. This model is formulated in a finite element method. Finally, the last section presents the application of the model to coalbed methane production.

5. General framework for geomaterials

The objective of this section is to present some general concepts used to model the hydro-mechanical behaviour of coalbed. The adopted representation of the porous medium allows the application of continuum mechanics. A referential has also to be defined. Finally, the balance equations are established.

5.1 Porous medium representation

The structure of geomaterials is complex, it is an assembly of solid grains forming a solid skeleton with fluids filling the porous space between the grains (Figure III–2). The full description of this system is almost impossible. For this reason, relying on a mixture theory, the real discontinuous porous medium may be modelled by superimposed continua [Bowen, 1980, Coussy, 1995].

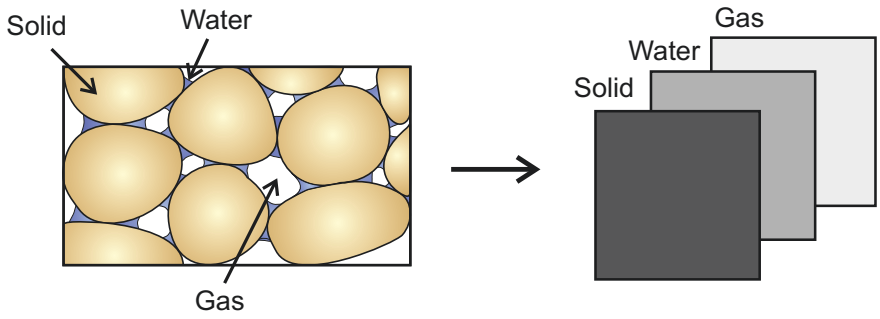

Figure III–2 – Porous medium and superimposed continua.

The concept of volume fractions is used to create some homogenized continua of reduced densities, allowing the application of continuum mechanics. Indeed, every point of the idealized system consists of a mixture of phases because all phases are assumed to occupy the same region of space simultaneously.

The volume fraction of the phase is defined as

— (III–1)

where is the volume of the phase and is the total volume of the control space. The sum of the different volume fractions of all phases is 1. The following volume fractions are defined:

$_s$ 1 ; $_l$ S_r ; $_g$ 1 S_r (III–2)

where s, l and g denote the solid, the liquid and the gas phases respectively, is the total porosity defined as the ratio between the total void volume $_v$ and the total volume :

$\frac{v}{}$ $\frac{v}{s \quad v}$ $\frac{l \quad g}{s \quad l \quad g}$ 0 1 (III–3)

and S_r is the water saturation degree, defined as the ratio between the volume of the liquid phase $_l$ and the porous volume $_v$:

S_r $\frac{l}{v}$ (III–4)

5.2 Continuum mechanics

Let us consider a force vector whose components are F_i in an orthogonal coordinate system. This force is acting on a surface element of area A of a given body. This surface is not necessarily a part of the exterior of the body. Imagining a cross section, it is a purely conceptual surface anywhere inside this body (Figure III–3).

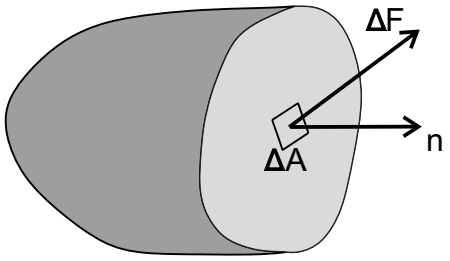

Figure III–3 – Cross section on a body with an internal force F acting on a surface A.

Under the assumption of continuity, we can define the limiting value of the ratio of force over area, it is

$$t_i \quad \lim_{A \to 0} \frac{F_i}{A} \quad \frac{\mathrm{d}F_i}{\mathrm{d}A} \tag{III–5}$$

where t_i is called the traction vector, or stress vector. This stress vector, which is associated to the surface characterized by an unit-length normal vector n_j, is related to a stress tensor σ_{ij} through [1]

$$t_i \quad \sigma_{ij} n_j \tag{III–6}$$

In three dimensions, the 9 components of the stress tensor σ_{ij} may be visualized on a tetrahedron made up three triangles parallel to the orthogonal coordinate planes and a fourth triangle whose orientation is defined by n_j (Figure III–4). The stress tensor is actually symmetric, $\sigma_{ij} \quad \sigma_{ji}$.

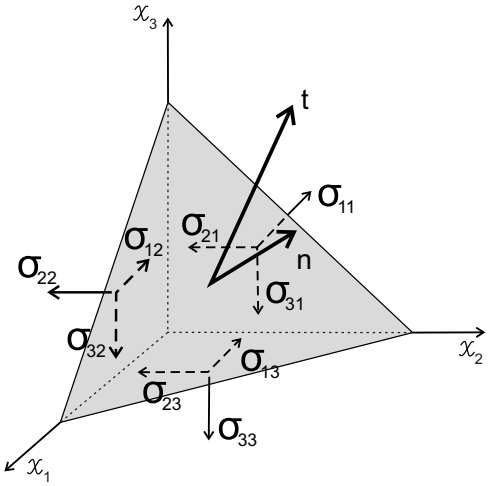

Figure III–4 – Tetrahedral portion of material with a traction vector t_i acting on a surface characterized by a normal n_j.

The true stress is the force per unit area in the current, deformed, configuration. It is called the Cauchy stress [2] to distinguish it from other stress tensors.

1. Einsiten indicial notation is adopted so that summation over repeated indices is assumed. $i \ j \quad 1 \ 2$ for two-dimensional analysis and $i \ j \quad 1 \ 3$ for three-dimensional analysis.

2. Named after Augustin Louis Cauchy who described the notion of internal stress in solids [Cauchy, 1823] following Navier's work on the bending of planes [Navier, 1820].

5.3 Referential definition

The kinematics of the material must be described using an appropriate referential. There is roughly the choice between two families, using either an Eulerian or a Lagrangian referential [Malvern, 1969]. In the Eulerian description, the movement of particles is described through a spatially fixed referential frame while the Lagrangian frame is linked to the material points and moves with it.

In this work, an updated Lagrangian formulation is chosen for the solid mechanics description. Such formulation allows large deformation problems for which a distinction is realised between the deformed and the initial configurations. On a finite element point of view, it means that the reference configuration evolves at every step (Figure III–5).

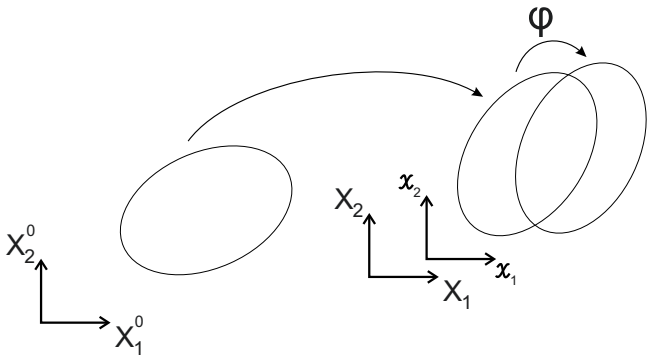

Figure III–5 – Updated Lagrangian formulation: $X_1^0;X_2^0$ is the initial basis relative to the initial configuration, $X_1;X_2$ is the updated reference basis relative to the reference configuration, and $x_1;x_2$ is the current basis relative to the deformed configuration. is the mapping that associates a material point of the reference configuration with its current position x_i X_i .

The transformation from the reference to the current configuration is characterised by a deformation gradient whose components in indicial notation are

$$F_{ij} \quad \frac{x_i}{X_j} \tag{III–7}$$

The velocity of a material point in the current configuration is given by

$$v_i \quad \frac{\mathrm{d}x_i}{\mathrm{d}t} \quad \dot{u}_i \tag{III–8}$$

where t denotes time and u_i is the displacement vector.

The velocity gradient field in the current configuration reads

$$L_{ij} \quad \frac{v_i}{x_j} \tag{III–9}$$

which can be decomposed in its symmetrical and anti-symmetrical parts.

The Cauchy strain rate is given as the symmetrical part of this velocity gradient:

$$\dot{}_{ij} \quad \frac{1}{2} L_{ij} \quad L_{ji} \tag{III–10}$$

and the anti-symmetric part corresponds to the spin rate tensor:

$$w_{ij} \quad \frac{1}{2} L_{ij} \quad L_{ji} \tag{III–11}$$

5.4 Balance equations

The balance equations of the hydro-mechanical problem consist of the mass balance equations of the solid and the fluids and the balance of momentum of the mixture.

5.4.1 Mass balance equations

Let us consider a control volume Ω to establish the general balance equation for a quantity $M(t)$, such as the mass of a species. The control volume is delimited by a surface A and the outflow through this surface is given by the dot product between the surface flux f_i and the normal vector n_i (Figure III–6).

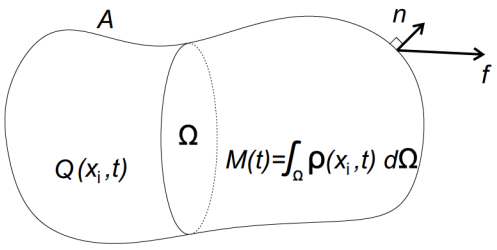

Figure III–6 – Balance on a control volume Ω.

Defining the intensive property ρ as the quantity M per unit volume (such as the density of the species), then:

$$M(t) = \int_{\Omega} \rho(x_i,t)\, d\Omega \tag{III–12}$$

Applying Leibniz's rule, the temporal change of M is:

$$\frac{\partial M}{\partial t} = \frac{\partial}{\partial t}\int_{\Omega} \rho\, d\Omega = \int_{\Omega} \frac{\partial \rho}{\partial t} d\Omega \tag{III–13}$$

Reynolds transport theorem [3] states that the sum of the changes of an intensive property defined over a control volume must be equal to what is lost/gained through the boundaries of the volume plus what is created/consumed by sources and sinks inside this volume.

It writes as:

$$\int_{\Omega} \frac{\partial \rho}{\partial t} d\Omega = \int_{A} -(n_i \cdot f_i)\, dA + \int_{\Omega} Q\, d\Omega \tag{III–14}$$

where Q is the source term.

Changing the integral over the boundary A into a volume integral using Gauss's divergence theorem [4], we have:

$$\int_{\Omega} \left(\frac{\partial \rho}{\partial t} + \frac{\partial f_i}{\partial x_i} - Q \right) d\Omega = 0 \tag{III–15}$$

Finally this balance must be independent of the volume since it is arbitrary, we obtain therefore the following general balance equation in differential form:

$$\frac{\partial \rho}{\partial t} + \frac{\partial f_i}{\partial x_i} - Q = 0 \tag{III–16}$$

where the first term is the storage term, Q is the source term and the divergence of the fluxes f_i expresses the difference between the input and the output fluxes of the given volume.

3. [Reynolds et al., 1903].
4. Or sometimes called Ostrogradsky's theorem.

Mass balance equations are established following a compositional approach [Panday and Corapcioglu, 1989, Olivella et al., 1994, Collin, 2003] which consists of balancing species rather than phases. In this way, exchange terms between the phases are canceled out. The model is developed for a single gas species which refers therefore to methane in the case of coal seam gas recovery. Thanks to a Lagrangian description, the referential follows the solid skeleton which is deforming. Inside this solid framework, the description of the fluid is Eulerian.

5.4.1.1 Solid mass balance equation

As the reference system used follows the solid phase, there is necessarily the conservation of the solid mass, it writes:

$$\frac{\partial}{\partial t}(\rho_s(1-\phi_f)\Omega) = 0 \tag{III–17}$$

with ρ_s the coal matrix density and ϕ_f the porosity from the fractures ($\phi_f = \dfrac{\Omega_f}{\Omega}$ with Ω_f the volume of the fractures).

5.4.1.2 Water mass balance equation

As mobile water is assumed only present in the fracture system, the following single water mass balance equation is written:

$$\underbrace{\frac{\partial}{\partial t}(\rho_w S_r \phi_f) + \frac{\partial}{\partial x_i}(\rho_w\, q_{l\,i})}_{\text{Liquid water}} + \underbrace{\frac{\partial}{\partial t}(\rho_v(1-S_r)\phi_f) + \frac{\partial}{\partial x_i}\left(\rho_v\, q_{g\,i} + (1-S_r)\, J^w_{g\,i}\right)}_{\text{Water in gas phase}} = 0 \tag{III–18}$$

where ρ_w and ρ_v are the water and water vapour densities, $q_{l\,i}$ and $q_{g\,i}$ are the liquid and gas advective flows, and $J^w_{g\,i}$ is the diffusive mass flux of water vapour. Terms relative to vapour are presented for the sake of generalization. Evaporation may occur in the late-life of the reservoir at low pressure but the impact of this phenomenon on the production curve is not considered as a major issue, it will therefore not be considered in numerical simulations.

5.4.1.3 Gas mass balance equation

For gas, present in cleats and matrix, a dual-porosity approach is adopted [Barenblatt et al., 1960]. This concept, introduced by Barenblatt, requires to define a pressure for both fractures and matrix. The difference in pressure between the cleats and the matrix is responsible for a mass exchange E between the two systems, it is a source for one and a sink for the other. This exchange is determined using shape factors (section 6.2.3). The gas mass balance equations, the first equation being relative to the cleats and the second one to the matrix, are:

$$\underbrace{\frac{\partial}{\partial t}\left(\rho_{g,f}\,(1-S_r)\phi_f\right) + \frac{\partial}{\partial x_i}\left(\rho_{g,f}\, q_{g\,i} + (1-S_r)\, J^g_{g\,i}\right)}_{\text{Gas phase}} + \underbrace{\frac{\partial}{\partial t}\left(\rho^d_{g,f}\, S_r \phi_f\right) + \frac{\partial}{\partial x_i}\left(\rho^d_{g,f}\, q_{l\,i} + S_r\, J^g_{l\,i}\right)}_{\text{Dissolved gas in water phase}} = E \tag{III–19}$$

$$\text{and} \qquad \frac{\partial}{\partial t}\left(\rho^{Ad}_g\right) = -E \tag{III–20}$$

where $\rho_{g,f}$, $\rho^{d}_{g,f}$ and ρ^{Ad}_{g} are respectively the densities of the gas in the cleats, the dissolved gas in the water and the gas adsorbed on the matrix. $J^{g}_{g\,i}$ and $J^{g}_{l\,i}$ represent the diffusive flows of the gas species in the gas phase (only if water vapour is considered) and the dissolved gas in the liquid phase. Equation (III–19) is relative to the cleats, the first brace refers to the dry gas phase while the second one refers to the dissolved gas in water. Indeed, as gas may be dissolved in water, it is transported with the water flow and may also diffuse in water. Finally, Equation (III–20), relative to the matrix, indicates that rate of gas storage equals the mass transfer E with the cleats. This rate is the variation of the amount of gas adsorbed within the matrix.

5.4.2 Momentum balance equation

The equation of motion [5] states that the rate of change of momentum for a continuum volume is equal to the resultant force F_i:

$$F_i = \int_{\Omega} \rho \frac{\partial v_i}{\partial t}\, d\Omega \tag{III–21}$$

There are two types of forces: the contact force t_i and the gravity volume force ρg_i with g_i the gravity acceleration vector and ρ the specific mass of the mixture. Thence, the balance of linear momentum writes

$$\int_{A} t_i\, dA + \int_{\Omega} \rho g_i\, d\Omega = \int_{\Omega} \rho \frac{\partial v_i}{\partial t}\, d\Omega \tag{III–22}$$

Introducing Cauchy's Equation (III–6) and applying the divergence theorem, the balance of momentum gives

$$\int_{\Omega} \left(\frac{\partial \sigma_{ij}}{\partial x_j} + \rho g_i \right) d\Omega = \int_{\Omega} \rho \frac{\partial v_i}{\partial t}\, d\Omega \tag{III–23}$$

For quasi-static loading, the second term vanishes and the balance of momentum of the mixture in the local form is

$$\frac{\partial \sigma_{ij}}{\partial x_j} + \rho g_i = 0 \tag{III–24}$$

For our applications, the thickness of the coal seam is considered very small compared to the depth of the seam, the gravity may be neglected:

$$\frac{\partial \sigma_{ij}}{\partial x_j} = 0 \tag{III–25}$$

This total stress tensor σ_{ij} is related to the strains through the mechanical constitutive model discussed immediately here after (section 6.1).

5. Euler's first law [Euler, 1749]. It is the equivalent of Newton's second law [Newton, 1687], today written as $\mathbf{F} = m\mathbf{a}$, used for objects idealised as single point masses.

6. Hydro-mechanical model

This section presents the hydro-mechanical macroscale model developed to take into account the hydro-mechanical couplings observed with pressure variation in coalbeds and which affect the permeability during CBM production or CCS. To achieve this, an equivalent continuum approach is adopted to model the mechanical behaviour of the fractured medium and a double porosity approach using shape factors is used for the modelling of the hydraulic part. Different models and approaches available in the literature have therefore been merged to develop a new consistent macroscale model. It is detailed first for the mechanical part and then the hydraulics. The choice to start with one or the other is not trivial because of the couplings that are discussed right after.

6.1 Mechanical part

Coal is an elasto-brittle geomaterial and an elastic constitutive law is therefore assumed effective for describing the stress-strain relationship of coal before failure. The elastic constitutive model relates stress and strain increments through the elastic stiffness tensor C_{ijkl} or inversely with the elastic compliance D_{ijkl}:

$$\tilde{}_{ij} \quad C_{ijkl} \dot{}_{kl} \qquad \dot{}_{ij} \quad D_{ijkl} \tilde{}_{kl} \tag{III–26}$$

where $\dot{}_{ij}$ is the Cauchy strain rate and $\tilde{}_{ij}$ is the Jaumann stress rate.

The Jaumann objective stress rate [Jaumann, 1911] is adopted so that any rigid-body motion does not induce modification of stress within the material, it is defined by

$$\tilde{}_{ij} \quad \dot{}_{ij} \quad w_{ij} \quad {}_{ij} \quad {}_{ij} \, w_{ij} \tag{III–27}$$

where $\dot{}_{ij}$ is the Cauchy stress rate. As will be seen in section 6.3.1.1, it is actually an effective stress rate.

For modelling purpose, the complex structure of coal is reduced to a collection of matrix blocks of simple geometries (e.g. slides, matches, parallelepiped, cubes or spheres) separated by fracture voids. The size and shape of the blocks depend on the fracture density and the number of fractures sets [Reiss, 1980, van Golf-Racht, 1982]. Figure III–7 represents the geometry model with three sets of cleats. Each set of fracture is defined by an aperture h_i and a spacing w_i.

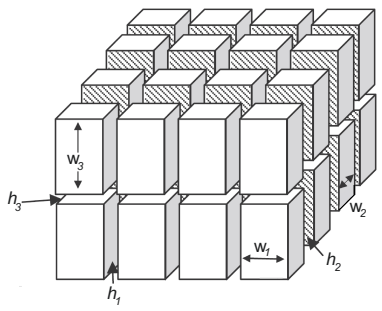

Figure III–7 – Geometry model with three sets of cleats. *After* [Reiss, 1980].

The fractured rock is therefore a dual system. The mechanical behaviour of the fractured rock is analogous to a series of two springs (Figure III–8). The spring standing for the fractures is non-linear and initially the softest. When the system is compressed, the soft spring will undergo the first deformations. Then, once fractures are nearly closed, the stiffness tends to the one of the matrix.

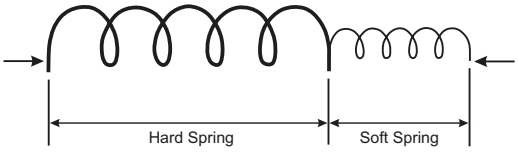

Figure III–8 – Analogy with two springs in series. *After* [Liu et al., 2009].

6.1.1 Matrix

The coal matrix is considered isotropic. Therefore, only two independent elastic parameters are required to define the elastic constitutive tensor, e.g. the Young's modulus of the matrix E_m and the Poisson's ratio $_m$ or the shear modulus G_m and the bulk modulus K_m.

$$G_m \quad \frac{E_m}{2\ 1\quad _m} \tag{III–28}$$

$$K_m \quad \frac{E_m}{3\ 1\quad 2\ _m} \tag{III–29}$$

Some authors mentioned orthotropy or transverse isotropy after mechanical tests on small coal cubes [Szwilski, 1984, Espinoza et al., 2013]. This may be caused by the presence of fractures at a lower scale or be inherited from the sedimentation. It does not significantly change the understanding of the model while more parameters should be defined. In this work, the mechanical behaviour of the matrix is kept as simple as possible with an isotropic law and the global orthrotropy of the material is induced by the presence of different sets of fractures.

6.1.2 Fractures

A fracture is a discontinuity described by a shear and a normal stiffness, respectively K_s and K_n [Goodman, 1976, Fossum, 1985]. These properties depend on the geometry of the asperities of contact between the two rough walls. Due to the rearrangement of these asperities, the normal stiffness increases with the decrease of the normal fracture aperture. The change of normal stiffness for a given mated [1] fracture is evaluated using the empirical model proposed by Bandis [Bandis et al., 1983]:

$$K_n \quad \frac{K_n^0}{1 \quad \frac{u_n}{u_n^{max}}\ ^2} \tag{III–30}$$

where $u_n \quad h_0 \quad h$ is the normal displacement with h_0 and h respectively the initial and the current fracture apertures. K_n^0 is the normal stiffness corresponding to a zero displacement. The maximal displacement u_n^{max} is a given ratio of the initial aperture. From Equation (III–30), the stiffness is increasing rapidly when the normal displacement tends to the maximal displacement allowed.

1. *i.e.* no offset between the fracture walls. Most cleats are probably mated fractures because of being an opening mode [Gu and Chalaturnyk, 2010].

6.1.3 Equivalent continuum

Globally, combining some isotropic matrix blocks with three orthogonal sets of fractures, the material behaviour is orthotropic. In this case, there are 9 independent elastic parameters: E_1, E_2, E_3, ν_{12}, ν_{13}, ν_{23}, G_{12}, G_{13} and G_{23} [Lekhnitskii, 1963, Graham and Houlsby, 1983]. The compliance tensor (written in the form of a matrix with the stress and the strain in the form of vectors) is then given in the axes of orthotropy by:

$$\begin{bmatrix} \frac{1}{E_1} & -\frac{\nu_{21}}{E_2} & -\frac{\nu_{31}}{E_3} & 0 & 0 & 0 \\ -\frac{\nu_{12}}{E_1} & \frac{1}{E_2} & -\frac{\nu_{32}}{E_3} & 0 & 0 & 0 \\ -\frac{\nu_{13}}{E_1} & -\frac{\nu_{23}}{E_2} & \frac{1}{E_3} & 0 & 0 & 0 \\ 0 & 0 & 0 & \frac{1}{2G_{12}} & 0 & 0 \\ 0 & 0 & 0 & 0 & \frac{1}{2G_{13}} & 0 \\ 0 & 0 & 0 & 0 & 0 & \frac{1}{2G_{23}} \end{bmatrix} \tag{III–31}$$

Due to thermodynamic requirements, this tensor must be symmetric [Love, 1927]. The symmetry involves the following equalities [2]:

$$\frac{\nu_{ij}}{E_i} = \frac{\nu_{ji}}{E_j} \tag{III–32}$$

The elastic stiffness tensor can be deduced by inverting the compliance tensor:

$$\begin{bmatrix} \frac{1-\nu_{23}\nu_{32}}{E_2E_3\Upsilon} & \frac{\nu_{21}+\nu_{31}\nu_{23}}{E_2E_3\Upsilon} & \frac{\nu_{31}+\nu_{21}\nu_{32}}{E_2E_3\Upsilon} & 0 & 0 & 0 \\ \frac{\nu_{12}+\nu_{13}\nu_{32}}{E_1E_3\Upsilon} & \frac{1-\nu_{13}\nu_{31}}{E_1E_3\Upsilon} & \frac{\nu_{32}+\nu_{12}\nu_{31}}{E_1E_3\Upsilon} & 0 & 0 & 0 \\ \frac{\nu_{13}+\nu_{12}\nu_{23}}{E_1E_2\Upsilon} & \frac{\nu_{23}+\nu_{21}\nu_{13}}{E_1E_2\Upsilon} & \frac{1-\nu_{12}\nu_{21}}{E_1E_2\Upsilon} & 0 & 0 & 0 \\ 0 & 0 & 0 & 2G_{12} & 0 & 0 \\ 0 & 0 & 0 & 0 & 2G_{13} & 0 \\ 0 & 0 & 0 & 0 & 0 & 2G_{23} \end{bmatrix} \tag{III–33}$$

with

$$\Upsilon = \frac{1-\nu_{12}\nu_{21}-\nu_{13}\nu_{31}-\nu_{23}\nu_{32}-2\nu_{12}\nu_{23}\nu_{31}}{E_1E_2E_3}$$

Orthotropic coordinate axes may not correspond to the global coordinate axes. In this case, because the constitutive law is formulated in the orthotropic axes, a change of coordinate reference system has to be computed using a rotation matrix R_{ij} which depends on three angles (e.g. Euler's angles) corresponding to rotations relative to the three global axes. To obtain the elastic strain tensor rate in the orthotropic axes ($^\diamond$) from the one expressed in the global axes, the change of reference system is then defined as

$$^\diamond\dot{\varepsilon}_{ij} = R_{ik}R_{jl}\dot{\varepsilon}_{kl} \tag{III–34}$$

2. Einstein summation notation is not used in this equation, *i.e* repeated indices do not have to be summed.

Once the stress state is calculated in the orthotropic axes, it is reformulated in the global axes by reversing the rotation:

$$\tilde{\sigma}_{kl} = R_{ki} R_{lj} {}^{\diamond}\tilde{\sigma}_{ij} \tag{III–35}$$

Elastic parameters mentioned in Equation (III–31) are determined based on the concept of equivalent continuum medium [Amadei and Goodman, 1981]. By analogy with two springs in series, the Young's modulus of the fractured rock in the direction i is calculated as follows [2] [Gu and Chalaturnyk, 2010]:

$$\frac{1}{E_{(i)}} = \frac{1}{E_m} + \frac{1}{(K_n)_{(i)} \cdot w_{(i)}} \tag{III–36}$$

where i may be any of the three directions of the fractures sets.

The equivalent Poisson's ratios are obtained by:

$$\nu_{ij} = \frac{E_i}{E_m} \cdot \nu_m \tag{III–37}$$

There are therefore 3 independent Poisson's ratios since Equation (III–37) gives the same value for ν_{12} and ν_{13}, ν_{21} and ν_{23}, and ν_{31} and ν_{32}. Finally, the equivalent shear modulus in the plane defined by the directions i and j is estimated by [2]:

$$\frac{1}{G_{(ij)}} = \frac{1}{G_m} + \frac{1}{(K_s)_{(i)} \cdot w_{(i)}} + \frac{1}{(K_s)_{(j)} \cdot w_{(j)}} \tag{III–38}$$

The applicability of the equivalent deformation model to coal was validated by [Gu et al., 2006] by matching some experimental results.

In fact, as these elastic parameters depend on the non-constant normal stiffness of the fractures and/or the widths of the matrix blocks, the elastic law is non-linear. The change of cleat aperture h in the direction [3] i due to the change of normal stress in this direction ($\tilde{\sigma}_{(ii)}$) is the normal displacement estimated with [2]

$$\dot{h}_{(i)} = \frac{\tilde{\sigma}_{(ii)}}{(K_n)_{(i)}} \tag{III–39}$$

where stresses are positive in traction. Without considering the possibility of dilatancy, the shear displacement does not modify the cleat aperture. The total change of cleat aperture is then simply given by Equation (III–39). The total change of the width of one unit including one matrix block and one cleat is the sum of the cleat aperture and the block width changes [2]:

$$\dot{w}_{(i)} + \dot{h}_{(i)} = (w_{(i)} + h_{(i)}) \cdot \dot{\varepsilon}_{(ii)} \tag{III–40}$$

Therefore, the change of the matrix width appearing in Equations (III–36) and (III–38) is given by [2]:

$$\dot{w}_{(i)} = (w_{(i)} + h_{(i)}) \cdot \dot{\varepsilon}_{(ii)} - \dot{h}_{(i)} \tag{III–41}$$

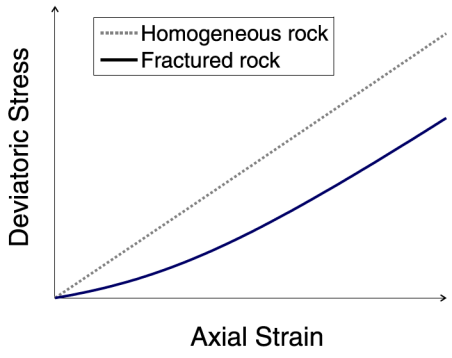

Figure III–9 – Comparison between homogeneous and equivalent continua.

3. This direction i belongs to the orthotropic axes. Orthotropy is a consequence of the presence of different sets of fractures.

Figure III–9 compares the numerical results of a triaxial test performed on homogeneous and fractured rocks. The homogeneous rock is modelled with constant elastic moduli corresponding to the matrix blocks of the fractured rock. The deviatoric stress evolution with the strain is obviously linear. For the fractured rock, modelled by the equivalent continuum, the initial stiffness is initially lower because of the fractures. Then, while the fractures are closing, the stiffness of the rock tends to the one of the intact rock. The deviatoric stress evolutions are then parallel.

6.2 Hydraulic part

Usually, coal deposits are aquifers and the methane is maintained adsorbed within the coal matrix by the hydrostatic pressure. The CBM production consists therefore to generate a pressure drop by dewatering the cleats network [Harpalani and Schraufnagel, 1990]. Then, gas molecules diffuse in the matrix to reach the cleats which are preferential pathways [Mitra et al., 2012].

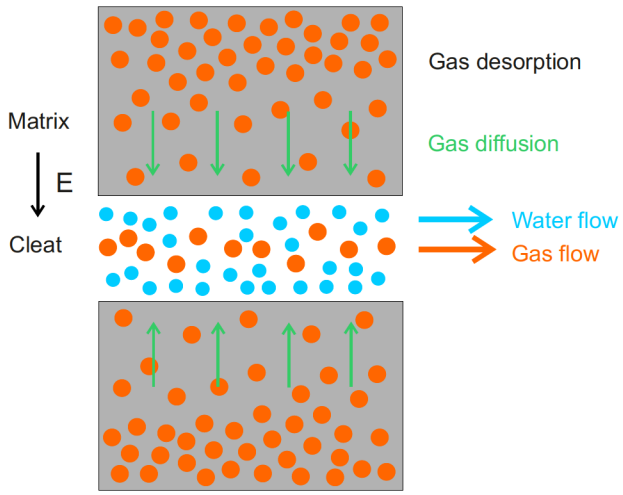

Figure III–10 – Conceptual hydraulic model.

This section presents a hydraulic model for the modelling of CBM production. The mass balance equations written above involve different variables which are linked to the main variables of the problem through some constitutive and equilibrium equations. Similarly to the mechanical problem, the macroscopic hydraulic model is enriched from the microscale. In this purpose, a dual-porosity approach is adopted, requiring a mass transfer between the matrix and the cleats as presented in the gas mass balance Equations (III–19) and (III–20). The model is developed for a single gas species, enhanced coalbed methane modelling is therefore out of the scope of this work.

6.2.1 Constitutive equations

Different variables such as densities, degrees of saturation or fluid flows appear in the balance equations presented above. All these variables depend on the main variables of the problem, the water pressure and the gas pressure.

6.2.1.1 Liquid density variation

If the compressibility of the liquid phase is not neglected, its density ρ_w varies with pressure p_w. The liquid water bulk density evolves according to:

$$\rho_w = \rho_{w_0}\left(1 + \frac{p_w - p_{w_0}}{\chi_w}\right) \tag{III–42}$$

where $_{w0}$ is the liquid density at the pressure p_{w0} and 1 $_{w}$ is the liquid compressibility. At 20°*C*, 1 $_{w}$ 5 10 ^{10}Pa ^{1}.

6.2.1.2 Gas density variation

The classical ideal [4] gas equation of state is used to write the gas densities as

$$_{g} \quad \frac{M_{m_g}}{RT} p_g \tag{III–43}$$

where R is the universal gas constant (8 3143 J mol K), T is the absolute temperature, M_{m_g} is the molecular mass of the gas (0 016 kg mol for methane) and p_g is the gas pressure either in the fractures ($p_{g\,f}$) or in the matrix ($p_{g\,m}$).

6.2.1.3 Multiphase flow model

In porous media, flow occurs in the pore spaces between the solid skeleton. However, the pore-scale representation is not suitable to simulate flow over large domains. Instead of direct modelling, a phenomenological continuum approach is preferred (Figure III–11).

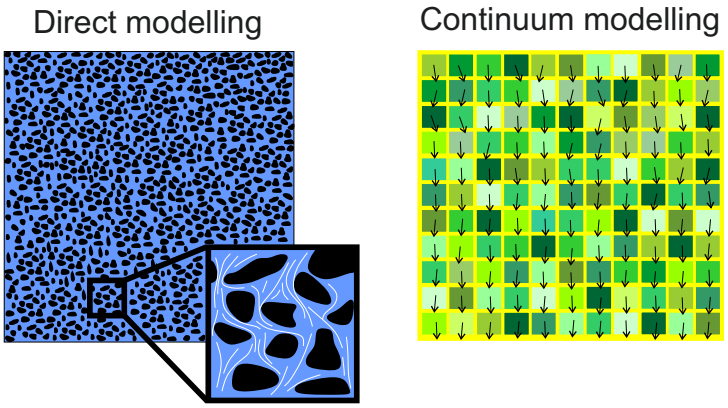

Figure III–11 – Two representations of flow in porous media: direct modelling (Navier Stokes) *versus* continuum modelling (e.g. Darcy).

Modelling the hydraulic behaviour of coal, it is assumed advective flows take place within a representative regular macroporosity, the fractures network. Darcy's equation is therefore employed using a permeability coefficient which is function of the apertures of the fractures and the widths of the blocks. Within the microporosity of the matrix blocks, diffusive flows are computed with a Fick's law and a diffusive coefficient.

Advective flows in the cleats for saturated conditions

From the experiments performed by Darcy on a column of sand [Darcy, 1856], it follows that the flow q m s through a porous medium is proportional to the total pressure drop. This law is valid only for a slow and viscous flow, *i.e.* at small Reynolds numbers (Stokes' flow). In one dimension (s is the distance in the one-dimension system), it writes:

$$q \quad \frac{k}{\mu} \frac{\mathrm{d}p}{\mathrm{d}s} \tag{III–44}$$

4. It is not very restrictive for methane. However, the formulation could be improved with a Z compressibility factor for carbon dioxide to account for the non-linearity evolution of the density with pressure at a given temperature. Another equation of state [Span and Wagner, 1996] has to be applied for deeper seams where the carbon dioxide is not in the gas state.

where the linear coefficient $k[m^2]$ is called the *intrinsic* or *absolute permeability* of the porous medium. The complex geometry of the porous medium can be therefore replaced by a permeability parameter, what makes Darcy's law very suitable for a continuum macroscopic modelling. In the case of fractured rocks, the permeability may be determined theoretically as a function of the fracture aperture. The permeability through a set of parallel fractures of equal aperture, oriented parallel to flow direction, is given by [van Golf-Racht, 1982, Bear et al., 1993]:

$$k = \frac{h_b^3}{12w} \tag{III–45}$$

where h_b is the hydraulic aperture and w is the fracture spacing (Figure III–12). In fact, this results can be obtained from the Navier-Stokes Equations [Neuman, 1977]. Indeed, the flow through a single fracture represented by two plates is [5]:

$$q_f = -\frac{h_b^2}{12} \cdot \frac{1}{\mu} \frac{\mathrm{d}p}{\mathrm{d}s} \tag{III–46}$$

Thus, the total flow $Q[m^3/s]$ between the two plates is:

$$Q = q_f \cdot h_b \cdot w = -\frac{h_b^3 w}{12} \frac{1}{\mu} \frac{\mathrm{d}p}{\mathrm{d}s} \tag{III–47}$$

Considering a section A with n fractures, the permeability through the section is:

$$k = \frac{n}{A} \cdot \frac{h_b^3 w}{12} \tag{III–48}$$

where $A = n \cdot (w + h_b)^2 \simeq nw^2$ as $w \gg h_b$. Substituting this value in Equation (III–48), the permeability through the fractured medium is, as announced, given by Equation (III–45).

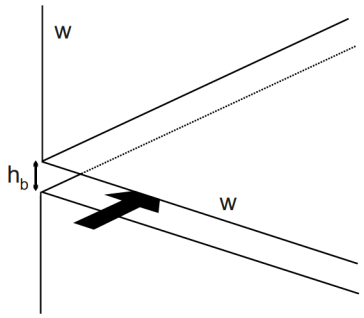

Figure III–12 – Fluid flow through a cleat. *Modified from* [Reiss, 1980].

Superposing the different sets of cleats, the anisotropic permeability tensor in the axes of these three sets is:

$$k_{ij} = \begin{bmatrix} \frac{1}{12}\left(\frac{h_{b_2}^3}{w_2} + \frac{h_{b_3}^3}{w_3}\right) & 0 & 0 \\ 0 & \frac{1}{12}\left(\frac{h_{b_1}^3}{w_1} + \frac{h_{b_3}^3}{w_3}\right) & 0 \\ 0 & 0 & \frac{1}{12}\left(\frac{h_{b_1}^3}{w_1} + \frac{h_{b_2}^3}{w_2}\right) \end{bmatrix} \tag{III–49}$$

The apertures of cleats may be either determined from direct or indirect measurements. The apertures from direct measurements are mechanical apertures while the apertures deduced from the permeability

5. It will be demonstrated for the microscale model in Part IV.

are hydraulic apertures. Barton presented an empirical relationship between hydraulic apertures h_b and mechanical apertures h [Barton et al., 1985]:

$$h_b = \begin{cases} \dfrac{h^2}{JRC^{2.5}}, & \text{if } h \geqslant h_b \text{ and } JRC > 0. \\ h, & \text{otherwise.} \end{cases} \tag{III–50}$$

where the unit of apertures is micron and JRC is the Joint Roughness Coefficient [Barton and Choubey, 1977]. A zero JRC represents smooth plane surfaces, in this case the hydraulic aperture is the mechanical one.

Furthermore, the porosity from the fractures can be written as [Pan and Connell, 2012]:

$$\phi_f = \frac{h_1}{w_1} + \frac{h_2}{w_2} + \frac{h_3}{w_3} \tag{III–51}$$

Under isotropic conditions, the porosity is therefore $\phi_f = \dfrac{3h}{w}$. Assuming smooth fractures, this porosity is substituted in Equation (III–45) to give:

$$k = \frac{1}{96} w^2 \phi_f^3 \tag{III–52}$$

Thence, the permeability change with respect to a reference state (subscript 0) writes:

$$\left(\frac{k}{k_0}\right) = \left(\frac{w}{w_0}\right)^2 \left(\frac{\phi_f}{\phi_{f_0}}\right)^3 \tag{III–53}$$

Considering the matrix size change as negligible compared to porosity change ($w \approx w_0$), then Equation (III–53) can be simplified as:

$$\left(\frac{k}{k_0}\right) = \left(\frac{\phi_f}{\phi_{f_0}}\right)^3 \tag{III–54}$$

This relationship is commonly used and widely accepted in petroleum industry to describe the permeability change with respect to porosity variation [Palmer et al., 1996, Cui and Bustin, 2005]. It is supported by experimental results on fractured rocks [Jones Jr et al., 1975]. However, since the porosity is a scalar variable, the anisotropy vanishes in the absolute permeability evolution. Moreover, some experimental results have shown Equation (III–54) may not be applicable for most coalbeds [Somerton et al., 1975]. For this reason, it is preferable to keep a direct relation between the permeability and the cleats apertures. Therefore, contrary to many permeability models described in the literature, Equation (III–54) is not used in this thesis to model coalbed methane flows.

Advective flows in the cleats for unsaturated conditions

Generally, gas and water flows are simultaneously encountered in the cleats and it is therefore necessary to extend the model to unsaturated conditions. To this purpose, the widely-used concept of *relative permeability* k_r is introduced to account for the reduction in permeability between partially and fully saturated conditions:

$$k_r = \frac{k_e}{k} \tag{III–55}$$

where k is the absolute permeability and k_e is the *effective permeability* of the phase considered. It allows to rewrite the flow equation in the following form:

$$q_i = -\frac{k_r \cdot k_{ij}}{\mu} \frac{\partial p}{\partial x_j} \tag{III–56}$$

In petroleum engineering, the relative permeabilities of the wetting phase (k_{rw}) and the non-wetting phase (k_{rnw}) are often expressed as power law functions of the saturation (S_r), known as Corey functions [Corey, 1954]. These functions were originally developed for the case of two-phase flow of oil and gas through conventional sedimentary sand rocks. The model was derived on the assumption of a bundle of capillary tubes with various radii in the porous medium (Figure III–13). It is well known that the height of the wetting fluid in a capillary tube is inversely proportional to the tube's radius [6].

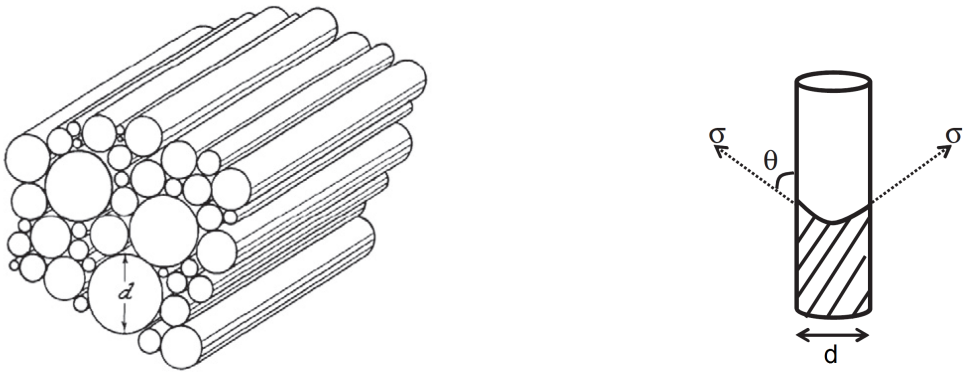

Figure III–13 – Bundle of capillary tubes model. *After* [Gates et al., 1950] *and* [Chen et al., 2013].

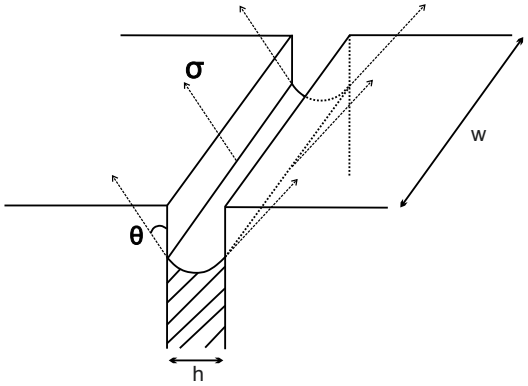

Figure III–14 – Capillary pressure in a cleat. *Modified from* [Chen et al., 2013].

In fact, the same mathematical expressions can be developed considering a flow between parallel plates instead of capillary tubes (Figure III–14). Indeed, from Young-Laplace equilibrium [7], the mechanical balance in the cleat between the capillary pressure p_c and the interfacial tension is:

$$p_c \quad h_b \quad w \quad 2w \quad \cos \qquad p_c \quad \frac{2 \quad \cos}{h_b} \tag{III–57}$$

where is the contact angle of the liquid or gas phase and the solid phase (Figure III–14), a wetting fluid presents a contact angle lower than 90°. The capillary pressure p_c (or suction) is defined as:

$$p_c \quad p_{nw} \quad p_w \tag{III–58}$$

where p_w is the wetting phase pressure and p_{nw} is the non-wetting phase pressure. The general rule is water-wet reservoir in petroleum engineering [Selley and Sonnenberg, 2014]. For coal, it is known to be hydrophobic [8] but the contact angles appear to be largely in the range 60-90° for the coal-water-air system at atmospheric pressure (Figure III–15) [Keller Jr, 1987]. In the following, water is therefore

6. Known as Jurin's law [Jurin, 1718].
7. After [Young, 1805] and [Laplace, 1806].
8. Coal hydrophobicity depends on coal rank, see section 3.1.

considered as the wetting phase and gas the non-wetting phase. However, it should be mentioned that [Siemons et al., 2006] reported a water contact angle larger than 90° for an anthracite-water-CO_2 system with pressures larger than few bars (contact angles were measured using the captive bubble technique with different water pressures in the cell).

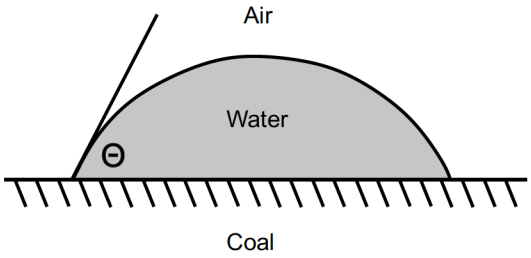

Figure III–15 – Wettability of coal as observed by [Bailey and Gray, 1958] with a air and water.

Equation (III–57) indicates that capillary pressure is inversely proportional to the fracture aperture. It is assumed that σ and θ remain constant while the capillary pressure p_c is linked to the saturation S_r of the wetting phase. Substituting Equation (III–57) in Equation (III–46), we have the following flow rate through the cleat:

$$q = -\frac{(\sigma\cos\theta)^2}{3}\cdot\frac{1}{\mu}\frac{\mathrm{d}p}{\mathrm{d}s}\cdot\frac{1}{(p_c(S_r))^2} \tag{III–59}$$

Considering now a flow occurring through a large number of N parallel cleats of equal length but of different apertures, the total flow rate through the medium is:

$$q_N = -\frac{(\sigma\cos\theta)^2\cdot\Phi}{3}\cdot\frac{1}{\mu}\frac{\mathrm{d}p}{\mathrm{d}s}\cdot\sum_{i=1}^{N}\frac{V_i}{(p_c(S_r))_i^2} \tag{III–60}$$

where V_i is the ratio of each cleat volume to the total cleat volume and Φ represents the ratio of the total cleat volume to the total volume. Comparing Equation (III–60) with Equation (III–44), the following effective permeability in the unsaturated fractured medium is found:

$$k_e(S_r) = \frac{(\sigma\cos\theta)^2\cdot\Phi}{3}\cdot\sum_{i=1}^{N}\frac{V_i}{(p_c(S_r))_i^2} \tag{III–61}$$

In fact, a change in saturation ΔS_r occurs when the pressure is increased from p_{c1} to p_{c2}. This change in saturation is a result of liquid either entering (non-wetting liquid) or receding (wetting liquid) from all the fractures having capillary pressure between p_{c1} and p_{c2}. All fractures in this interval are treated as if they exhibited some intermediate average capillary pressure $(p_c)_{av}$ comprised between p_{c1} and p_{c2}. Choosing a number r of such intervals where n_j is the number of fractures concerned by the j$^{\text{th}}$ interval, we have [Purcell et al., 1949]:

$$\sum_{i=1}^{n_j}\frac{V_i}{(p_c(S_r))_i^2} \approx \left[\frac{\Delta S_r}{(p_c(S_r))_{av}^2}\right]_j \tag{III–62}$$

and

$$\sum_{i=1}^{N}\frac{V_i}{(p_c(S_r))_i^2} = \sum_{j=1}^{r}\sum_{i=1}^{n_j}\frac{V_i}{(p_c(S_r))_i^2} \approx \sum_{j=1}^{r}\left[\frac{\Delta S_r}{(p_c(S_r))_{av}^2}\right]_j \tag{III–63}$$

Then, with infinitesimal intervals, we have exactly:

$$\sum_{i=1}^{N}\frac{V_i}{(p_c(S_r))_i^2} = \int_0^{S_r}\frac{dS_r}{(p_c(S_r))^2} \tag{III–64}$$

Hence, introducing Equation (III–64) in Equation (III–61), the effective permeability of the wetting phase in the medium is given by

$$k_{ew} = \frac{(\sigma \cos\theta)^2 \cdot \Phi}{3} \cdot \int_0^{S_r} \frac{dS_r}{(p_c(S_r))^2} \tag{III–65}$$

and the absolute permeability by

$$k = \frac{(\sigma \cos\theta)^2 \cdot \Phi}{3} \cdot \int_0^{1} \frac{dS_r}{(p_c(S_r))^2} \tag{III–66}$$

Relative permeabilities are then computed for the wetting phase (water) and the non-wetting phase (gas) as follows:

$$k_{rw} = \frac{k_{ew}}{k} = \frac{\int_0^{S_r} \frac{dS_r}{(p_c(S_r))^2}}{\int_0^{1} \frac{dS_r}{(p_c(S_r))^2}} \tag{III–67}$$

$$k_{rg} = \frac{k_{eg}}{k} = \frac{\int_{S_r}^{1} \frac{dS_r}{(p_c(S_r))^2}}{\int_0^{1} \frac{dS_r}{(p_c(S_r))^2}} \tag{III–68}$$

Some analytical expressions of the relatives permeabilities may be therefore obtained from the expression of the capillary pressure. Among the capillary pressure models, we can cite the Brooks–Corey model [Brooks and Corey, 1964] and the van Genuchten model [Van Genuchten, 1980]. Brooks and Corey have proposed empirically the following function:

$$p_c(S_r) = p_e \cdot (S_r^*)^{\frac{-1}{\lambda}} \tag{III–69}$$

where p_e is the entry pressure [9], λ is the cleat size distribution index which decreases with the increase of the heterogeneity, and S_r^* is the normalized wetting phase saturation:

$$S_r^* = \frac{S_r - S_{r,res}}{1 - S_{r,res} - S_{r_g,res}} \tag{III–70}$$

with $S_{r,res}$ and $S_{r_g,res}$ the residual water and gas saturations. If the residual water and gas contents are considered constant while the porosity evolves, the mass conservation of these residual fluids implies

$$S_r^* = \frac{S_r - S_{r,res_0} \left(\frac{\phi}{\phi_0}\right)^{-1} \left(\frac{\rho_w}{\rho_{w_0}}\right)^{-1}}{1 - S_{r,res_0} \left(\frac{\phi}{\phi_0}\right)^{-1} \left(\frac{\rho_w}{\rho_{w_0}}\right)^{-1} - S_{r_g,res_0} \left(\frac{\phi}{\phi_0}\right)^{-1} \left(\frac{\rho_g}{\rho_{g_0}}\right)^{-1}} \tag{III–71}$$

As the material is deformable, the pore size varies. In fact, the total amount of residual contents may change with the porosity as a result of pore size variation. To represent experimental data, the residual saturations expressions are improved by introducing some exponents n_{rw} and n_{rg} [Chen et al., 2013]:

$$S_{r,res} = S_{r,res_0} \left(\frac{\phi}{\phi_0}\right)^{-n_{wr}} \left(\frac{\rho_w}{\rho_{w_0}}\right)^{-1} \tag{III–72}$$

$$S_{r_g,res} = S_{r_g,res_0} \left(\frac{\phi}{\phi_0}\right)^{-n_{gr}} \left(\frac{\rho_g}{\rho_{g_0}}\right)^{-1} \tag{III–73}$$

Besides, the shape of the capillary pressure function may also changes as a result of porosity change. This can be taken into account in Equation (III–69) by replacing the parameters λ (distribution index) and p_e (entry value) with functions of the porosity instead of constant values. It is not further investigated in this work due to the lack of data on this aspect for coal.

9. Minimum pressure required before the non-wetting phase can invade the pore structure.

Substituting the Equation (III–69) in Equations (III–67) and (III–68), one can obtain the following relationships to compute the water and the gas phase relative permeabilities:

$$k_{rw} = (S_r^*)^{\frac{2+3\lambda}{\lambda}} \qquad \text{(III–74)} \qquad k_{rg} = 1 - (S_r^*)^{\frac{2+3\lambda}{\lambda}} \qquad \text{(III–75)}$$

The water relative permeability increases with the increment of the cleats aperture distribution index and, in the opposite, the gas relative permeability decreases.

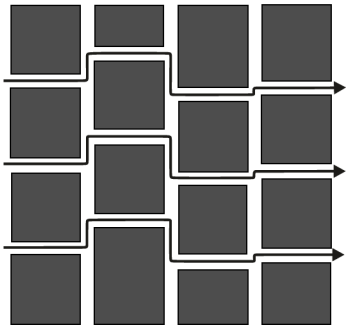

Figure III–16 – Effect of tortuosity. *Modified from* [Chen et al., 2013].

In order to improve equations (III–67) and (III–68), a tortuosity parameter can be introduced. Indeed, there are two sets of cleats: the face and the butt cleats. The face cleats are almost continuous; hence, the flows is more or less straightforward in this direction and this case not requires a tortuosity parameter. On the opposite, the butt cleats are less continuous and the flow in this direction is not straightforward (Figure III–16); tortuosity should be taken into account. As can be observed, the tortuosity not only depends on the geometry but also relies on the flow main direction.

A tortuosity parameter ζ can be applied as follows [Mualem, 1976]:

$$k_{rw} = (S_r^*)^{\zeta} \frac{\int_0^{S_r} \frac{dS_r}{p_c^2}}{\int_0^1 \frac{dS_r}{p_c^2}} \qquad \text{(III–76)} \qquad k_{rg} = (1 - S_r^*)^{\zeta} \frac{\int_{S_r}^1 \frac{dS_r}{p_c^2}}{\int_0^1 \frac{dS_r}{p_c^2}} \qquad \text{(III–77)}$$

In the particular case where ζ [10] equals 2, equations (III–76) and (III–77) reduce to the equations presented by Burdine [Burdine et al., 1953]. Substituting Equation (III–69) in Equations (III–76) and (III–77), the relative permeabilities for a fractured reservoir can be expressed this time as

$$k_{rw} = (S_r^*)^{\zeta+1+\frac{2}{\lambda}} \qquad \text{(III–78)} \qquad k_{rg} = (1 - S_r^*)^{\zeta} \cdot \left[1 - (S_r^*)^{1+\frac{2}{\lambda}}\right] \qquad \text{(III–79)}$$

Relative permeabilities are represented in Figure III–17 for different values of ζ and λ. For instance, coal cleats become more tortuous with the increase of ζ and the relative permeabilities for both water and gas phases decrease. When ζ equals to 0, the effect of tortuosity is not considered.

10. This tortuosity parameter is not defined as usually as the ratio between the straight line distance and the effective length covered by the particles. It may be larger than 1.

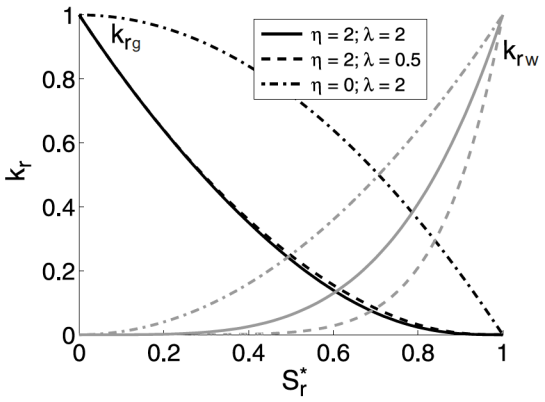

Figure III–17 – Effect of tortuosity and cleat size distribution index on relative permeability curves.

Finally, advective flows of liquid and gas phases are respectively

$$q_{l_i} = -\frac{k_{rw} \cdot k_{ij}}{\mu} \frac{\partial p_w}{\partial x_j} \tag{III–80}$$

and

$$q_{g_i} = -\frac{k_{rg} \cdot k_{ij}}{\mu} \frac{\partial p_g}{\partial x_j} \tag{III–81}$$

Diffusive flows

Fick's law [Fick, 1855] is the most popular approach to evaluate diffusive flow. It states the flow is directly proportional to the concentration gradient. The flow in the direction i for the species α is given by:

$$J_{\alpha i} = -D_\alpha \frac{\partial C_\alpha}{\partial x_i} \tag{III–82}$$

Equation III–82 is known as the Fick's first law. In this equation, the determination of the phenomenological coefficient D_α $[m^2/s]$ is naturally the most critical part of the equation. Fick's second law can be derived from Fick's first law and mass conservation, this law is written as follows:

$$\frac{\partial C_\alpha}{\partial t} = D_\alpha \frac{\partial^2 C_\alpha}{\partial x_i^2} \tag{III–83}$$

In porous media, as real pores are generally of various diameters and twisted, the path for diffusion of the molecules within the pores is tortuous. A reasonable approximation for the effective diffusion coefficient of the species α through β, is given by [Mason and Malinauskas, 1983]:

$$D_\beta^{\alpha *} = \phi \, \Lambda \, D_\beta^\alpha \tag{III–84}$$

in which ϕ is the porosity of the medium and Λ is the tortuosity defined as the square of the ratio between the straight line distance and the effective length covered by the molecule. It is therefore an obstruction factor lower or equal to one which attempts to account for the longer distance traversed in the pores.

Fick's law will be used in the dual-porosity approach (section 6.2.3) to account in the gas transfer between matrix and cleats that desorption is not instantaneous. Fick's law is also used to express the diffusive flow in the cleats of the dissolved gas in water and possibly the diffusive flow of water vapour through the gas species:

$$J_{l_i}^g = -D_l^{g *} \, \rho_w \, \frac{\partial}{\partial x_i} \left(\frac{\rho_g^d}{\rho_w} \right) \tag{III–85}$$

$$J_{gi}^{w} = D_{g}^{w\,*}\,\rho_g\,\frac{\partial}{\partial x_i}\left(\frac{\rho_v}{\rho_g}\right) = -J_{gi}^{g} \tag{III–86}$$

For methane dissolved in water, the diffusion coefficient is 1.84E-9 m^2/s. All flows appearing in the mass balance Equations (III–18) to (III–19) are therefore now defined.

6.2.2 Equilibrium equations

For closure of the mass balance equations, some restrictions are also required to link the different phases of each species (Figure III–18).

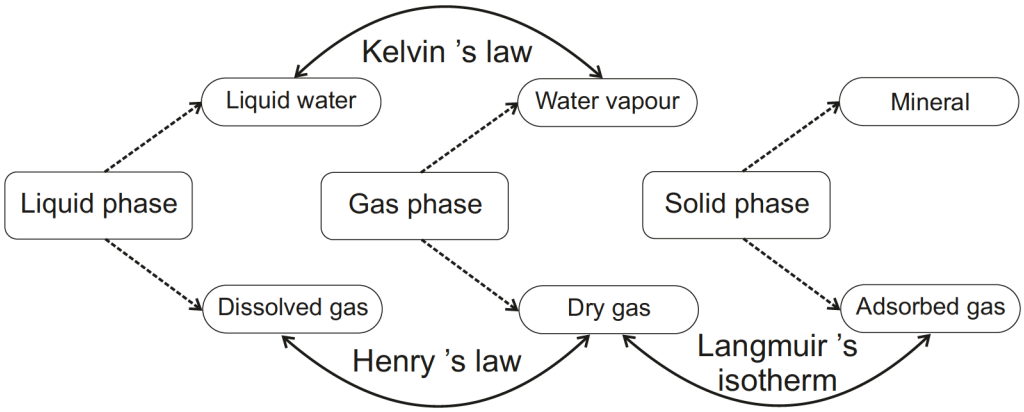

Figure III–18 – Phases, species and equilibrium restrictions.

6.2.2.1 Kelvin's law

If water vapour is considered, an equilibrium restriction is necessary to link the concentration of water vapour with liquid water. Assuming a thermodynamic equilibrium between the two phases, it is given by the Kelvin's law:

$$\rho_v = \rho_v^0 \exp\left(\frac{-p_c\,M_{m_w}}{RT\rho_w}\right) \tag{III–87}$$

where ρ_v^0 is the density of saturated water vapour, it is a constant for a given temperature [Garrels and Christ, 1965, Ewen and Thomas, 1989]. M_{m_w} is the molecular mass of water. This law is only given for the sake of generality.

6.2.2.2 Henry's law

Assuming a thermodynamic equilibrium between the dissolved gas and the dry gas, the density of the dissolved gas may be obtained with the Henry's law [Lide, 2004]:

$$\rho_{g,f}^{d} = H_g \rho_{g,f} \tag{III–88}$$

Hence, Henry's coefficient H_g allows determining the dissolved gas volume in the water. Its value depends on gas type and temperature. For methane dissolved in water at standard conditions, $H_g = 0.0347$ [Sander, 2015].

6.2.2.3 Langmuir's isotherm

The Langmuir model relates the maximal quantity of adsorbed gas to gas pressure at a given temperature. The Langmuir model is a special form of the multilayer Brunnauer-Emmet-Teller (BET) model for which each adsorbate molecule in the first layer serves as an adsorption site for an adsorbate molecule

into the second layer, the second layer for the third layer, and so on [Brunauer et al., 1938]. The Langmuir's isotherm may be derived considering an equilibrium equation between the gas phase molecules, the vacant surface sites and the species adsorbed on the surface (see section 3.3). It is therefore a physically-based equation where the total adsorbed volume V_g^{Ad} depends on the pressure p as:

$$V_g^{Ad} \quad \frac{V_L \ p}{P_L \quad p} \tag{III–89}$$

where P_L is the Langmuir pressure corresponding to $\frac{1}{2}V_L$. These two parameters, P_L and V_L, are used to control the shape of the curve to best fit some experimental data, as shown in the previous part of the thesis (Table II–9). V_g^{Ad} and V_L are not strictly volumes but volumes of stored gas at standard conditions per unit of mass of coal. The density of the gas adsorbed on the coal matrix is therefore evaluated as

$$\begin{matrix} Ad \\ g \end{matrix} \qquad _{g\ std} \quad _c \ V_g^{Ad} \tag{III–90}$$

where $_{g\ std}$ is the gas density at standard conditions and $_c$ is the coal density. To define a gas pressure in the matrix, Equation (III–89) is introduced in Equation (III–90) and rearranged with the gas equation of state (Equation III–43).

Following the depletion of the reservoir, the adsorbed gas pressure in the matrix must therefore tend to:

$$p_{g\ m}^{lim} \quad \frac{RT}{M_{m_g}} \quad _{g\ std} \quad _c \frac{V_L \ p_{res}}{P_L \quad p_{res}} \tag{III–91}$$

where the reservoir pressure is evaluated with the following equivalent pressure:

$$p_{res} \quad S_r p_w \quad 1 \quad S_r \ p_{g\ f} \tag{III–92}$$

Due to diffusion in the matrix, the adsorbed gas pressure is not instantaneously in equilibrium with this limit pressure. It is taken into account in the following section thanks to the dual-porosity approach. Note that the adsorbed gas pressure is actually a pseudo-pressure. It is simply the translation of the adsorbed gas density through the gas equation of state (despite the adsorbed gas is not subject to this familiar gas law). The Langmuir's equilibrium could have been written in term of adsorbed density but the original dual-porosity approach which initiated our model is written for a difference of pressure between the fractures and the matrix. Moreover, nodal unknowns in the finite element code Lagamine are usually pressures. The most important is the mass balance is ensured regardless of the definition of the intermediate variable used to write the equilibrium between the cleat and the matrix.

6.2.3 Dual-porosity approach

Naturally-fractured reservoirs may be treated as dual-porosity media. The drainage rate per unit bulk volume from matrix to fractures was idealized by Barenblatt and later by Warren and Root as [Barenblatt et al., 1960, Warren et al., 1963]:

$$E \qquad \frac{k}{\mu} \ p_m \quad p_f \tag{III–93}$$

where the parameter is a shape factor with the dimension of reciprocal area, μ is the dynamic viscosity and p_m and p_f are respectively the matrix and fracture pressures. In the case of coal, adsorption isotherm has to be considered in the equation. Indeed, the motor of the transfer is the difference between the matrix pressure and the limit matrix pressure (Figure III–19). This limit matrix pressure is the pressure towards which the pressure tends given the pressure in the fractures, it is determined *via* Equation (III–91).

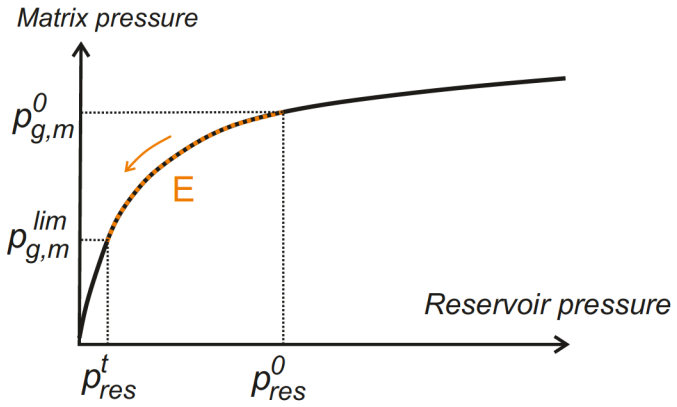

Figure III–19 – Mass exchange process between cleats and matrix.

As the drainage rate results from a diffusion process, a Fickian form is employed to give

$$E = \Psi D^g_m M_{m_g} (C_{g,m} - C^{lim}_{g,m}) \quad \text{(III–94)}$$

$$= \Psi D^g_m \frac{M_{m_g}}{RT} (p_{g,m} - p^{lim}_{g,m}) \quad \text{(III–95)}$$

The gas law of state is applied to obtain the mass flow given the definition of the adsorbed gas pressure. The shape factor Ψ aims to take into account the geometry of the matrix block in the release of gas (Figure III–20).

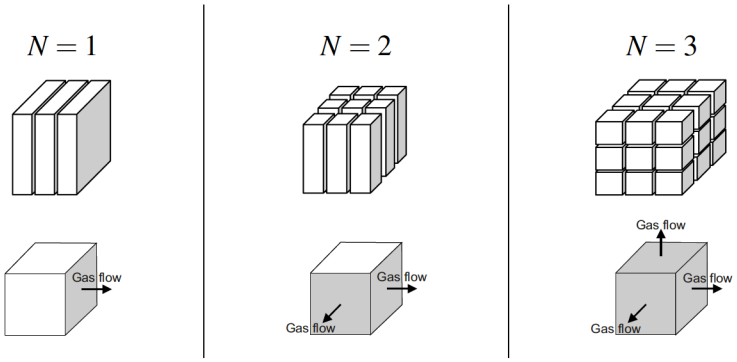

Figure III–20 – Influence of the geometry on the release process.

Warren and Root obtained the following expression of the shape factor:

$$\Psi = \frac{4N(N+2)}{w^2} \quad \text{(III–96)}$$

where N is the number of sets of fractures (1, 2 or 3) and w is the fracture spacing. According to Kazemi, the shape factor should be evaluated as [Kazemi et al., 1976]:

$$\Psi = 4\left(\frac{1}{w_1^2} + \frac{1}{w_2^2} + \frac{1}{w_3^2}\right) \quad \text{(III–97)}$$

Kazemi's formula is perhaps the most used in commercial reservoir simulators such as Eclipse [Mora et al., 2009]. However, this shape factor probably does not represent the most realistic pressure distribution in the matrix. Observations were made in the literature on the need to multiply the Kazemi's shape factor by a factor 2 or 3 to correspond to experimental results [Ueda et al., 1989]. Actually, Warren and Root's model and Kazemi's one are two extreme bounds, others authors derived intermediate rates of change flow [Coats et al., 1989, Chang, 1993, Zimmerman et al., 1993, Quintard and Whitaker,

1996, Lim and Aziz, 1995]. For example, based on a Fourier finite sine transform and integration, Coats derived a shape factor doubled compared to Kazemi [Coats et al., 1989]. Based on the same method, Lim and Aziz developed a shape factor formula assuming the flow obeys Darcy's law in the matrix with constant fracture pressure [Lim and Aziz, 1995].

In order to understand the assumptions under the use of a shape factor, the procedure is shortly developed assuming the flow obeys Fick's first law (Equation III–82) in the matrix. From Fick's second law (Equation III–83), the concentration distribution satisfies in one dimension:

$$\frac{\partial C}{\partial t} = D_m^g \frac{\partial^2 C}{\partial x^2} \tag{III–98}$$

The following boundary conditions ($N = 1$) are considered:

- At $t = 0$, we have $C = C^0$ for $-\frac{w}{2} \leqslant x \leqslant \frac{w}{2}$
- For $t > 0$, we have $C = C^{lim}$ for $x = -\frac{w}{2}$ and $x = \frac{w}{2}$

If the matrix is initially at a uniform concentration C^0 and the concentration at the boundary is maintained constant at C^{lim}, solution of Equation (III–98) is expressed by the Crank analytical solution [Crank, 1979]:

$$\frac{\bar{C}_m - C^0}{C^{lim} - C^0} = 1 - \sum_{n=0}^{\infty} \frac{8}{(2n+1)^2\pi^2} \exp\left(\frac{-(2n+1)^2\pi^2 D_m^g\, t}{w^2}\right) \tag{III–99}$$

where $\bar{C}_m$ is the average concentration in the matrix at time t. Taking the first term in the infinite summation series, Equation (III–99) is approximated by:

$$\frac{\bar{C}_m - C^0}{C^{lim} - C^0} = 1 - 0.81 \exp\left(\frac{-\pi^2 D_m^g\, t}{w^2}\right) \tag{III–100}$$

Differentiating this equation with respect to time yields to

$$\frac{1}{C^{lim} - C^0} \frac{\partial \bar{C}_m}{\partial t} = \frac{\pi^2 D_m^g}{w^2} 0.81 \exp\left(\frac{-\pi^2 D_m^g\, t}{w^2}\right) \tag{III–101}$$

$$= \frac{\pi^2 D_m^g}{w^2} \left[1 - \frac{\bar{C}_m - C^0}{C^{lim} - C^0}\right] \tag{III–102}$$

where Equation (III–102) is not time-dependent. The time dependence is eliminated using only the first term of the series. Figure III–21 shows the approximate solution is in good agreement with the analytical solution except in the first dimensionless times.

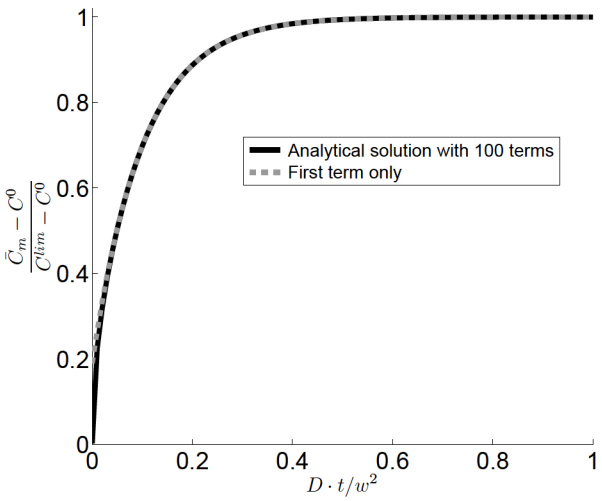

Figure III–21 – Crank solution for diffusion (D coefficient) in a plane (width w) and its approximation.

Thence, we can write:

$$\frac{\partial \bar{C}_m}{\partial t} = \frac{\pi^2 D_m^g}{w^2}(C^{lim} - \bar{C}_m) \tag{III–103}$$

The rate of the matrix-fracture transfer can be related to the rate of mass accumulation in the matrix as follows:

$$E = -M_{m_g} \frac{\partial \bar{C}_m}{\partial t} \tag{III–104}$$

Substituting Equation (III–103) in Equation (III–104) and comparing with Equation (III–94), we finally find a shape factor of $\frac{\pi^2}{w^2}$ for $N = 1$. For the 3D case, similar developments yields to [Lim and Aziz, 1995]:

$$\Psi = \pi^2 \left(\frac{1}{w_1^2} + \frac{1}{w_2^2} + \frac{1}{w_3^2} \right) \tag{III–105}$$

	$N=1$	$N=2$	$N=3$
Warren and Root	12	32	60
Kazemi	4	8	12
Coats	8	16	24
Lim and Aziz	π^2	$2\pi^2$	$3\pi^2$

Table III–1 – Dimensionless shape factor values ($\Psi\, w^2$) from different authors.

Table III–1 compares different shape factors from different authors. Values of the shape factors depend on the block geometry which is assumed. A regular microscale configuration has to be considered when evaluating macroscopically the transfer between the two porosity systems. Moreover, Equation (III–99) suggests differentiation with respect to time will not eliminate the dependence from time in the actual shape factor, as approximated by all the authors referred in Table III–1 considering a pseudo-steady state [11]. As a result, the mass transfer between cleat and matrix is approximated for the transient period before the establishment of the pseudo-steady state, as illustrated by the Figure III–21.

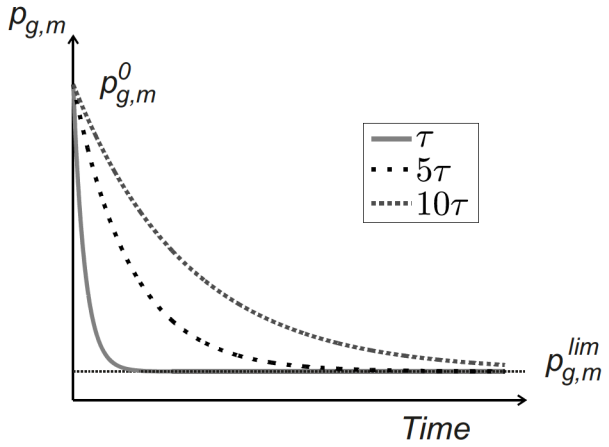

Figure III–22 – Comparison of the matrix gas pressure evolutions for different $\mathcal{T}$.

Finally, the differential equation governing the matrix gas pressure evolution is

$$\dot{p}_{g,m}(t) = -\Psi D_g^m \cdot \left(p_{g,m}(t) - p_{g,m}^{lim}(t) \right) \tag{III–106}$$

11. Change in the rate of pressure over time is constant at every point.

Given an initial gas matrix pressure $p^0_{g,m}$ and assuming a constant fracture pressure, the mathematical solution of this equation is a decreasing exponential function in the form:

$$p_{g,m}(t) = \left(p^0_{g,m} - p^{lim}_{g,m}\right) \cdot \exp\left(\frac{-t}{\mathcal{T}}\right) + p^{lim}_{g,m} \tag{III–107}$$

where

$$\mathcal{T} = \frac{1}{\Psi D^m_g} \tag{III–108}$$

is the sorption time. It allows to account for the combined impacts of cleat spacing and gas diffusion in coal matrix on gas flow. This sorption time corresponds to the time required to desorb 63.2% of the gas which can be produced following a given pressure drop in the fractures. Indeed, the part of the gas already released at any time t is given by:

$$1 - \exp\left(\frac{-t}{\mathcal{T}}\right) \tag{III–109}$$

Thence, replacing t with $\mathcal{T}$ leads to $1 - \exp(-1) = 63.2\%$.

Figure III–22 compares the evolution of the matrix pressure for different values of the sorption time. The lower is the sorption time and the faster the gas is desorbed.

6.3 Hydro-mechanical couplings

The mechanical and the hydraulic laws presented above should not be treated separately because of couplings, this is especially true for coalbed methane production. Indeed, the reservoir depletion compacts the rock and decreases the permeability. However, matrix shrinkage following the gas desorption from the coal matrix may increase the cleat aperture and thus the permeability [Gray et al., 1987].

6.3.1 Hydraulic - mechanical coupling

The influence of the hydraulic problem on the mechanical one is of two kinds. First, the mechanical behaviour of porous media is not entirely controlled by the total stress, it is also influenced by the presence of fluids in the pores. In this purpose, the concept of effective stress [Nuth and Laloui, 2008] is introduced. Secondly, sorption or desorption induces a swelling or a shrinkage of the matrix.

6.3.1.1 Effective stress approach

Terzaghi was the first to notice the role of the pore fluid pressure in rock and soil deformation [Terzaghi, 1936]. After experiments with sand, clay and concrete, he concluded that the change in bulk volume was only influenced by the difference between the confining pressure and the pore pressure, *i.e. effective stress*. This stress represents the stresses acting effectively between the solid grains. For porous materials fully saturated with water, Terzaghi postulated the following definition [12] of the effective stress field σ'_{ij}:

$$\sigma'_{ij} = \sigma_{ij} - p_w\, \delta_{ij} \tag{III–110}$$

where δ_{ij} is the Kronecker symbol [13].

In order to introduce the material compressibility in the effective stress definition, Biot proposed to scale down the effect of p_w in Equation (III–110). Biot's expression of the effective stress reads [Biot, 1941]:

$$\sigma'_{ij} = \sigma_{ij} - b\; p_w\, \delta_{ij} \tag{III–111}$$

12. Definition with soil mechanics convention in which compressive stress is positive.
13. $\delta_{ii} = 1$ and $\delta_{i \neq j} = 0$.

where the b, the Biot's coefficient, represents the compressibility of the solid grains relative to the skeleton compressibility. For isotropic materials, it is defined as

$$b = 1 - \frac{K}{K_s} \tag{III–112}$$

where K is the drained bulk modulus of the material and K_s is the bulk modulus of the solid grains. If the bulk modulus of the porous material is low in comparison to the solid bulk modulus, e.g. unconsolidated material, b is close to 1. Considering the general case of anisotropy, b is actually a tensor b_{ij}.

The principle of effective stress has also been investigated by [Tuncay and Corapcioglu, 1995] for saturated fractured media. Based on the double porosity model, they expressed the effective stress in terms of the total stress, the pore and fracture fluid pressures and bulk moduli of nonfractured porous blocks, fractured porous medium and solid grains. In the case where the pore fluid pressure is equal to the fracture fluid pressure, they recovered the same expression obtained by Biot.

For partially saturated conditions, Bishop extended Terzaghi's definition of the effective stress by combining both liquid and gas pressures. The effective stress is expressed as [Bishop, 1959]:

$$\sigma'_{ij} = \sigma_{ij} - p_g\ \delta_{ij} + \chi(p_g - p_w)\ \delta_{ij} \tag{III–113}$$

where χ is the Bishop's stress parameter. This parameters varies from 0 in dry state to 1 in saturated state, recovering Terzaghi's definition. An elementary relationship is [Schrefler, 1984]:

$$\chi = S_r \tag{III–114}$$

Note an important deviation from this commonly used choice can appear for relatively high plasticity soils [Pereira et al., 2010]. But under this assumption, Equation (III–113) is rewritten in the following form:

$$\sigma'_{ij} = \sigma_{ij} - [S_r\ p_w + (1 - S_r)\ p_g]\ \delta_{ij} \tag{III–115}$$

Compared with Terzaghi's definition, the water pressure in Equation (III–110) is replaced by an average fluid pressure composed of the pressures of each fluid weighted by their degree of saturation. In this way, models developed for saturated conditions are straightforwardly extended to unsaturated conditions by redefining the effective stress. Presuming that partial saturation and compressibility effects can be considered together, the Biot's effective stress is formulated under unsaturated conditions as follows:

$$\sigma'_{ij} = \sigma_{ij} - b_{ij}\ [S_r\ p_w + (1 - S_r)\ p_g]\ \delta_{ij} \tag{III–116}$$

This expression is kept as the effective stress definition for the double porosity model with the water and gas pressures in the fractures. Biot's coefficients depend on the elastic moduli of the fractured medium and the nonfractured blocks, their expressions are:

$$b_{ij} = \delta_{ij} - \frac{C_{ijkk}}{3K_m} \tag{III–117}$$

where K_m is the bulk modulus of the matrix blocks.

6.3.1.2 Swelling/shrinkage

Sorption or desorption induces structural rearrangements within the structure of the coal matrix [Karacan, 2003]. As a consequence, a volumetric strain is induced. Figure II–37 in the experimental observations part presented data from different CO_2 injection experiments. It appears these data could be modelled fairly accurately using the same mathematical form as the Langmuir's Equation ([Levine,

1996]). Moreover, the volumetric sorption-induced strain ε_{vs} is approximately proportional to the volume of adsorbed gas [Cui and Bustin, 2005] [14]:

$$\varepsilon_{vs} = \beta_\varepsilon \cdot V_g^{Ad} \tag{III–118}$$

where β_ε is the volumetric strain coefficient. Assuming an isotropic swelling/shrinkage of the matrix, the linear strain in the direction i due to gas adsorption/desorption can be estimated from [2]:

$$\varepsilon_{(ii)_s} = \alpha_\varepsilon \cdot V_g^{Ad} \cong \frac{1}{3}\beta_\varepsilon \cdot V_g^{Ad} = \frac{1}{3} \cdot \varepsilon_{vs} \tag{III–119}$$

where α_ε is the linear strain coefficient. Indeed [2], $\varepsilon_v = (1+\varepsilon_{(ii)})^3 - 1 \cong 3\varepsilon_{(ii)}$ for small strains. Actually, the linear strain coefficient could be different in every direction. A larger expansion may occur in the direction perpendicular to the bedding plane [Ceglarska-Stefaríska, 1994]. However, isotropic conditions have to be assumed in the absence of more information.

6.3.2 Mechanical - hydraulic coupling

The constitutive mechanical model relates effective stress and strain according to

$$\tilde{\sigma}'_{ij} = C_{ijkl}\ \dot{\varepsilon}_{kl} \quad \Leftrightarrow \quad \dot{\varepsilon}_{ij} = D_{ijkl}\ \tilde{\sigma}'_{kl} \tag{III–120}$$

where $\tilde{\sigma}'_{ij}$ is the Jaumann objective effective stress rate and $\dot{\varepsilon}_{ij}$ takes into account sorption-induced strain analogously to thermal expansion of rocks [Palmer et al., 1996]. In practice, based on the principle of superposition, the total linear strain is due to the changes in effective stress and adsorbed gas swelling. In the axes of orthotropy, it writes:

$$^{\diamond}\dot{\varepsilon}_{ij} = \dot{\varepsilon}_{ij} + \dot{\varepsilon}_{ij_s}\delta_{ij} \tag{III–121}$$

Thence, the strain rate used in Equation (III–120) must be

$$\dot{\varepsilon}_{ij} = {}^{\diamond}\dot{\varepsilon}_{ij} - \dot{\varepsilon}_{ij_s}\delta_{ij} \tag{III–122}$$

Thereby, if the displacement imposed by the boundary conditions is null, the swelling strain is totally converted into internal stresses, which are partly traduced in fracture aperture change according to the following equation written for the direction i [2]:

$$\dot{h}_{(i)} = \frac{\tilde{\sigma}'_{(ii)}}{(K_n)_{(i)}} \tag{III–123}$$

As permeability evolves with the cleat aperture (Equation III–49), the influence of the mechanical aspects on the hydraulic problem is a critical issue. A review of the analytical models used in the literature for the coal permeability evolution with the stress state may be found in [Pan and Connell, 2012], where around twenty others models are presented. In fact, many of them are based on the relationship between permeability and porosity presented above (Equation III–54). The porosity evolution is deduced from poromechanics [Nikoosokhan et al., 2012].

Reservations were expressed here when linking the evolution of the permeability tensor to a scalar variable. In our model, by introducing Equation (III–123) in Equation (III–49), it is not the case.

14. In the following, material mechanical convention with positive tensile stress and strain is adopted to be in accordance with the convention of the finite element code.

7. Finite element formulation

The hydromechanical model previously presented is formulated as a series of balance equations which are local equilibria expressed in a differential form. In addition to the balance equations, initial and boundary conditions are necessary to obtain a well-posed problem (section 7.1). To address problems over large domains with a finite element analysis, balance equations must be written in a weak form (section 7.2). Then, the numerical formulation requires to convert continuous time and space into finite time steps and finite elements (section 7.3). Finally, the system of linear equations is solved to give the global solution of the problem (section 7.4). Since the method is extensively developed in many books (see for instance [Zienkiewicz and Taylor, 2000]), it is not completely detailed here.

7.1 Initial and boundary conditions

While the balance equations represent the equilibrium of the material elementary volume Ω, the boundary conditions are the equilibrium at the external surface of the domain Γ. Initial conditions are also necessary for model closure, it describes the entire fields of displacements, water pressures and gas pressures to start from. A state variable defining the adsorbed gas pressure is also initialized.

The initial adsorbed gas pressure is defined based on the initial reservoir pressure. The maximum pressure is

$$p_{g,m}^{max} = \frac{RT}{M_{m_g}} \cdot \rho_{g,std} \cdot \rho_c \cdot \frac{V_L \cdot p_{res}^0}{P_L + p_{res}^0} = 1.897\ MPa \tag{III–124}$$

where p_{res}^0 is the initial water pressure for the saturated reservoir. It can also be chosen to define the initial adsorbed gas as a fraction of this maximum storage (adsorbed pressure under the isotherm):

$$p_{g,m}^0 = \mathcal{A} \cdot p_{g,m}^{max} \tag{III–125}$$

If $\mathcal{A}$ is lower than 1, the initial gas content is under the isotherm and the first drop of pressure does not lead to desorption. Gas pressure in the matrix remains constant. Desorption starts once the Langmuir's isotherm is reached (Figure I–6), *i.e.* at the critical reservoir pressure p_{res}^{crit}:

$$p_{res}^{crit} = \frac{p_{g,m}^0 \cdot P_L}{\left(\frac{RT}{M_{m_g}} \cdot \rho_{g,std} \cdot \rho_c \cdot V_L - p_{g,m}^0\right)} \tag{III–126}$$

Concerning the boundary conditions, the external traction force per unit area acting on a part of the external surface reads

$$\bar{t}_i = \sigma_{ij} \cdot n_j \tag{III–127}$$

where n_i is the unit vector normal to the boundary. Similarly, the conditions for prescribed water and gas fluxes are

$$q_w + f_{w_i} \cdot n_i = 0, \text{ and } q_g + f_{g_i} \cdot n_i = 0 \tag{III–128}$$

where q_w and q_g are the input water and gas masses (positive for inflow) and f_{w_i} and f_{g_i} are internal total fluxes of water and gas species in both liquid and gas phases:

$$f_{w_i} = \rho_w\, q_{l_i} \quad \left(+\, \rho_v\, q_{g_i} + (1 - S_r)\, J_{g_i}^w\right) \tag{III–129}$$

$$f_{g_i} = \rho_{g,f}\, q_{g_i} + \rho^d_{g,f}\, q_{l_i} + S_r\, J^g_{l_i} \quad \left(+ (1-S_r)\, J^g_{g_i}\right) \tag{III–130}$$

with the flows q_{l_i}, q_{g_i}, $J^w_{g_i}$, $J^g_{g_i}$ and $J^g_{l_i}$ defined by Equations (III–80), (III–81), (III–85) and (III–86).

7.2 Weak form of the balance equations

A weak form of the local momentum balance Equation (III–24) can be obtained considering an admissible virtual velocity field v^*_i, *i.e.* which respects the solid continuity and the boundary conditions. The principle of virtual power implies that, for any admissible virtual velocity, the solid is in equilibrium if internal virtual power $\dot{W}^*_I$ is equal to external one $\dot{W}^*_E$:

$$\underbrace{\int_\Omega \sigma_{ij}\, \frac{1}{2}\left(\frac{\partial v^*_j}{\partial x_i} + \frac{\partial v^*_i}{\partial x_j}\right) d\Omega}_{\dot{W}^*_I} = \underbrace{\int_\Omega \rho g_i\, v^*_i\, d\Omega + \int_\Gamma \bar{t}_i\, v^*_i\, d\Gamma}_{\dot{W}^*_E} \tag{III–131}$$

Using the fact that the double contraction of a symmetric tensor and a skew-symmetric one is zero, it also reads:

$$\underbrace{\int_\Omega \sigma_{ij}\, \frac{\partial v^*_i}{\partial x_j}\, d\Omega}_{\dot{W}^*_I} = \underbrace{\int_\Omega \rho g_i\, v^*_i\, d\Omega + \int_\Gamma \bar{t}_i\, v^*_i\, d\Gamma}_{\dot{W}^*_E} \tag{III–132}$$

As this principle holds for any v^*_i, the momentum balance Equation (III–24) and the boundary condition (III–127) are thus deduced inside the domain Ω and for any point on the boundary Γ.

In the same way, the fluids mass balance equations may be written in a weak form considering some kinematically admissible virtual fluid pressure fields. With p^*_w the virtual water pressure field, the water mass balance equation reads

$$\underbrace{\int_\Omega \left[\dot{M}_w p^*_w - f_{w_i}\frac{\partial p^*_w}{\partial x_i}\right] d\Omega}_{\dot{W}^*_I} = \underbrace{\int_\Omega Q_w p^*_w\, d\Omega - \int_\Gamma \bar{q}_w\, p^*_w\, d\Gamma}_{\dot{W}^*_E} \tag{III–133}$$

where Q_w is the water source term and M_w is the total mass of water:

$$M_w = \rho_w\, S_r\, \phi_f + \rho_v\, (1-S_r)\, \phi_f \tag{III–134}$$

Similarly with p^*_g the virtual gas pressure field, the gas mass balance equation is

$$\underbrace{\int_\Omega \left[\dot{M}_g \delta p^*_g - f_{g_i}\frac{\partial p^*_g}{\partial x_i}\right] d\Omega}_{\dot{W}^*_I} = \underbrace{\int_\Omega Q_g p^*_g\, d\Omega - \int_\Gamma \bar{q}_g\, p^*_g\, d\Gamma}_{\dot{W}^*_E} \tag{III–135}$$

where Q_g is the gas source term and M_g is the total mass of gas:

$$M_g = \rho_{g,f}\, (1-S_r)\, \phi_f + \rho^d_{g,f}\, S_r\, \phi_f + \rho^{Ad}_g \tag{III–136}$$

7.3 Discretization

7.3.1 Time

All the balance equations should be verified at any time t. However, the continuous time has to be descritized into finite time steps Δt in order to solve the boundary value problem numerically. Time

derivatives of the displacement, water pressure and gas pressure fields are defined using a fully implicit difference scheme:

$$\dot{u}_i^{t+\Delta t} = \frac{u_i^{t+\Delta t} - u_i^t}{\Delta t} \tag{III–137}$$

$$\dot{p}_w^{t+\Delta t} = \frac{p_w^{t+\Delta t} - p_w^t}{\Delta t} \tag{III–138}$$

$$\dot{p}_{g,f}^{t+\Delta t} = \frac{p_{g,f}^{t+\Delta t} - p_{g,f}^t}{\Delta t} \tag{III–139}$$

In fact, the current step Δt of the global time discretization may be subdivided in many sub-steps δt for the integration of the constitutive laws:

$$\delta t = \frac{\Delta t}{nsteps} \tag{III–140}$$

with $nsteps$ the number of sub-intervals used to reach Δt.

In particular, this sub-stepping procedure is applied to evaluate accurately the value of the adsorbed gas pressure at the end of the time step Δt. From Equation (III–106), the evolution of the gas pressure in the matrix is given by

$$p_{g,m}(t) = p_{g,m}(t-\Delta t) + \frac{1}{\mathcal{T}}\left(p_{g,m}^{lim} - p_{g,m}(t-\Delta t)\right)\Delta t \tag{III–141}$$

where $p_{g,m}^{lim}$ is given by Equation (III–91). The number of sub-intervals $nsteps$ to reach Δt with the sub-steps δt is based on the characteristic time of the process, *i.e.* the sorption time $\mathcal{T}$. The sub-interval value is chosen to be one thousandth of the sorption time but limited to a minimum value of 1 (to avoid a sub-interval greater than the interval) and a maximum value of 1000 (to avoid an excessive computation):

$$nsteps = \max\left(\max\left(1,\ ceil\left(\frac{\Delta t}{\frac{\mathcal{T}}{1000}}\right)\right), 1000\right) \tag{III–142}$$

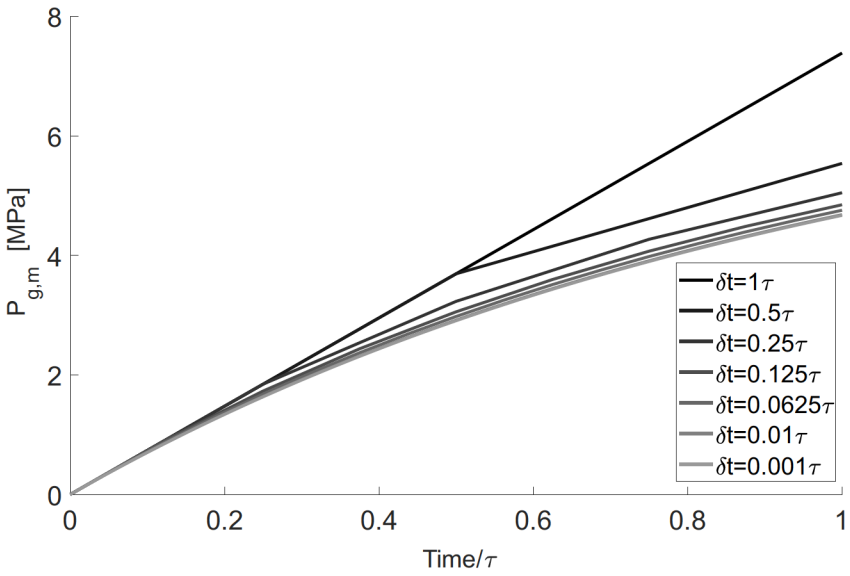

Figure III–23 – Illustration of the interest to subdivide the time step in smaller intervals for the computation of the adsorbed gas pressure.

Figure III–23 illustrates the computation of the adsorbed gas pressure for different numbers of sub-intervals. The initial adsorbed CO_2 pressure is null and the injection pressure is set to $5MPa$ from the

initial time. Using some given Langmuir's parameters ($V_L = 0.054 m^3/kg$ and $P_L = 1 MPa$), the adsorbed gas pressure will tend to 7.4MPa. From Equation (V–54), the adsorbed gas pressure will be directly equal to 7.4MPa at the end of the time step Δt if this step is equal to the sorption time, e.g. one day. The time step should be smaller than the characteristic time to correctly determine the evolution of the adsorbed gas pressure.

7.3.2 Space

The continuum medium is discretised by n_e finite elements of volume Ω_e such that it is approximated by:

$$\Omega = \bigcup_{e=1}^{n_e} \Omega_e \tag{III–143}$$

A coupled finite element is used to model solid bodies [Collin, 2003]. It is an isoparametric element with eight nodes and four integration points (Figure III–24).

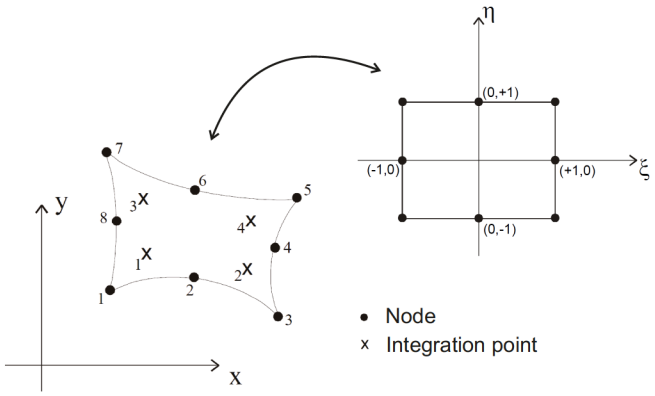

Figure III–24 – Two-dimensional finite isoparametric element.

The Jacobian matrix J_{ij} of the transformation from the global coordinates (x_1, x_2) to the local coordinates (ξ, η) is defined by:

$$J_{ij} = \begin{bmatrix} \dfrac{\partial x_1}{\partial \xi} & \dfrac{\partial x_1}{\partial \eta} \\ \dfrac{\partial x_2}{\partial \xi} & \dfrac{\partial x_2}{\partial \eta} \end{bmatrix} \tag{III–144}$$

Primary unknowns are the nodal coordinates u_{l_k}, each node k has l degrees of freedom, e.g. the two spatial coordinates, the water and fracture gas pressures, and temperature [1]. Note the adsorbed gas pressure is not considered as a nodal variable but as a state variable, it is computed from the fracture pressures. Coordinates $u_l^e(\xi, \eta)$ and displacements $\Delta u_l^e(\xi, \eta)$ are interpolated over the parent element using shape functions $\mathcal{N}^{(k)}(\xi, \eta)$:

$$u_l^e(\xi, \eta) = \sum_{k=1}^{8} \mathcal{N}^{(k)}(\xi, \eta)\, u_{l_k} \quad \text{and} \quad \Delta u_l^e(\xi, \eta) = \sum_{k=1}^{8} \mathcal{N}^{(k)}(\xi, \eta)\, \Delta u_{l_k} \tag{III–145}$$

Following Equation (III–132) and writing $v_i^{*\Omega_e}$ the vector of velocities from the i^{th} direction of the nodes composing the single element Ω_e, the mechanical part of the virtual internal power for that element

1. This work is restricted to isothermal conditions. The interested reader may found in [Collin, 2003] the energy balance equation required to solve non-isothermal problems.

is

$$\begin{aligned} \dot{W}_I^{*\Omega_e} &= \int_{\Omega_e} \sigma_{ij} \frac{\partial v_{i_k}^{*\Omega_e}}{\partial x_j} \, d\Omega_e \\ &= \sum_{k=1}^{8} \left[\int_{\Omega_e} \sigma_{ij} \frac{\partial N^{(k)}}{\partial x_j} \, d\Omega_e \right] v_{i_k}^{*\Omega_e} \\ &= \sum_{k=1}^{8} \left[F_{I,i_k}^{\Omega_e} \right]^T v_{i_k}^{*\Omega_e} \end{aligned} \tag{III–146}$$

The integration of $F_{I,i_k}^{\Omega_e}$ over the deformed element is carried out numerically using Gauss integration scheme:

$$\int_{\Omega_e} \sigma_{ij} \frac{\partial \mathcal{N}^{(k)}}{\partial x_j} \, d\Omega_e = \sum_{IP} \left[\sigma_{ij} \frac{\partial \mathcal{N}^{(k)}}{\partial x_j} \right]_{IP} \det(J_{ij}) \, W_G \tag{III–147}$$

where IP is the number of integration points and W_G is the Gauss weight corresponding to the integration point IP.

Equation (III–147) only defines the mechanical internal nodal forces. Similarly, hydraulic nodal forces can be derived considering the expressions of internal virtual work Equations (III–133) and (III–135). Then, hydraulic and mechanical nodal forces can be gathered in the same vector $F_{I,l_k}^{\Omega_e}$, a generalised equivalent nodal forces both from mechanics and hydraulics. $F_{I,l_k}^{\Omega_e}$ is the vector of internal energetically equivalent nodal forces associated to node k of the element Ω_e. The global discretized body being composed of n_e elements, they must be assembled together according to Equation (III–143). Thence, the global vector of the nodal forces reads

$$F_{I,l_k} = \bigcup_{e=1}^{n_e} F_{I,l_k}^{\Omega_e} \tag{III–148}$$

In the same way, external energetically equivalent nodal forces F_{E,l_k} are derived from external virtual power.

7.4 Global solution of the problem

The solution is found when the equilibrium between the energetically equivalent internal nodal forces F_{I,l_k} and the external ones F_{E,l_k} is reached. However, due to the evolution of the loading and transient effects, it is likely these nodal forces are not balanced at the beginning of any time step. Therefore, generalised degrees of freedom must be corrected to verify the equilibrium. To this purpose, the system of non-linear Equations (III–131) to (III–135) is transformed into an auxiliary linear problem and solved numerically with a Newton-Raphson scheme.

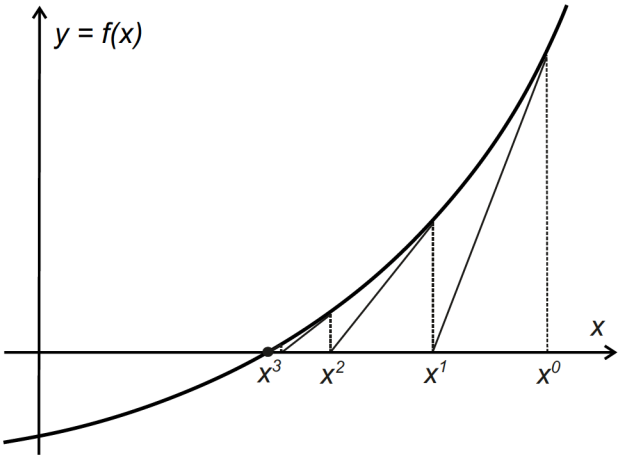

Figure III–25 – Illustration of the Newton-Raphson iterative scheme for a one-variable function.

A measurement of the imbalance within the system is given by the out of balance forces which are defined by:

$$F_{OB,l_k} = F_{E,l_k} - F_{I,l_k} \tag{III–149}$$

A numerical criterion has to be adopted in order to decide if the equilibrium is reached or not. Indeed, the out-of-balance forces will most probably not be exactly null. Expanding this out-of-balance forces in a Taylor series limited to the first order gives

$$F^{t+\Delta t}_{OB,l_k} \approx F^{t}_{OB,l_k} + \frac{\partial F^{t}_{OB,l_k}}{\partial u_{m_n}} \Delta u_{m_n} \tag{III–150}$$

where the derivative is the variation of the nodal force relative to the degree of freedom l at node k, F^{t}_{OB,l_k}, due to a variation of the coordinate m at node n, u_{m_n}.

The equilibrium is reached at time $t+\Delta t$ in the case the out-of-balance forces are equal to zero:

$$F^{t+\Delta t}_{OB,l_k} = 0 \tag{III–151}$$

Therefore, generalised degrees of freedom are iteratively corrected by:

$$\Delta u_{m_n} = -\left[\frac{\partial F^{t}_{OB,l_k}}{\partial u_{m_n}}\right]^{-1} F^{t}_{OB,l_k} = -\left[K^{t}_{l_k m_n}\right]^{-1} F^{t}_{OB,l_k} \tag{III–152}$$

where $K^{t}_{l_k m_n}$ is the stiffness matrix at time step t. Components of this matrix are computed at each iteration of the Newton-Raphson procedure as the variation of the equivalent nodal forces due to a variation of the generalised coordinates:

$$K^{t}_{l_k m_n} = \frac{\partial F^{t}_{OB,l_k}}{\partial u_{m_n}} \tag{III–153}$$

The off-diagonal terms contain the multi-physical coupling terms, it means a monolithic (fully coupled) procedure is adopted.

A simple way to compute the stiffness matrix is to approximate Equation (III–153) by the following finite difference:

$$K^{t}_{l_k m_n} \approx \frac{F^{t}_{OB,l_k}(u_{m_n} + \varepsilon) - F^{t}_{OB,l_k}}{\varepsilon} \tag{III–154}$$

where ε is a small perturbation and $F_{OB,l_k}(u_{m_n}+\varepsilon)$ is the out-of-balance response after perturbing the u_{m_n} coordinates with ε. The size of this numerical perturbation has to be small enough to actually compute a derivative and large enough not to be influenced by the numerical imprecision of the constitutive relation. Although the inverse operation of the stiffness matrix in Equation (III–152) is generally the most CPU time consuming operation, the numerical perturbation can also have a non-negligible impact as it requires the response to a certain load increment to be computed several additional times. As the analytical solution is available here for Equation (III–153), it is preferred to the perturbations method which was only used to check the implementation of the analytical method.

Finally, once the stiffness matrix is known, the new generalized coordinates are computed as follows

$$u^{t+\Delta t}_{l_k} = u^{t}_{l_k} + \Delta u_{l_k} \tag{III–155}$$

to find a new configuration closer to the equilibrium. As the problem has been linearized, the scheme is iterative (Figure III–25).

7.5 Implementation in the Lagamine code

In the Lagamine code, the coupled finite element used to model the solid bodies is the MWAT element [Collin, 2003]. This already existing element has been adapted to be used with the new mechanical and hydraulic routines. The mechanical part of the model has been implemented under the routine name ELADUA and the hydraulic part under the name WADUA.

8. Reservoir modelling

First, in order to illustrate the applicability of the model, a production scenario is tested on a hypothetical cylindrical CBM reservoir. This synthetic simulation allows us to choose a simple history of the well pressure drop in order to highlight the physical phenomena. The reference case is presented and then a parametric and couplings analysis is performed to highlight the influence of the hydro-mechanical couplings and some key parameters on the production profiles. Finally, the model is applied to represent production data obtained from a real production well.

8.1 Synthetic reference case

The reservoir is horizontal with initial homogeneous properties. The radius of the reservoir is $400m$ while the uniform thickness of the coal seam is $5m$. The reservoir is modelled in 2D axisymmetric conditions with 3000 (10x300 [1]) coupled finite elements. Both water and gas pressures are initially set to $2MPa$ in the fracture system, the reservoir is water saturated. In the matrix system, the gas pressure is set on the Langmuir's isotherm. Isothermal conditions are considered. The water vapour is not considered. Concerning the boundary conditions, all boundaries are impermeable to gas except at the well where the pressure P_{well} is decreased from 2 to 0 $5MPa$ in 10 days. The differences between this pressure and the proximate water and gas pressures in the reservoir are responsible for water and gas production rates.

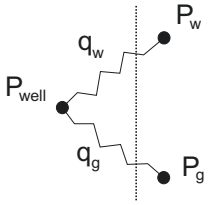

The mass production rates are computed at the boundary as follows [Peaceman et al., 1978]:

$$q_{w_{well}} \quad T_{well} \quad w \quad \frac{k_{rw}}{\mu_w} \quad p_w \quad P_{well}$$

$$q_{g_{well}} \quad T_{well} \quad g \quad \frac{k_{rg}}{\mu_g} \quad p_{g\,f} \quad P_{well} \quad H_g \quad g \frac{f_w}{w}$$

where $T_{well}\ m^3$ is a transmissibility factor taking into account the characteristics of the well: the borehole radius and the skin factor. Note the dissolved gas is taken into account thanks to the Henry coefficient H_g. The outer boundary is not assumed totally impermeable to water, the income water flow is computed according to

$$q_{w_{ob}} \quad ob \quad p_{w_0} \quad p_w \tag{III–156}$$

where $_{ob}\ kg \quad m^2 \ s \ Pa$ is a penalty coefficient. The value of this coefficient is chosen in order to ensure the water flow at the well is never null, to be closer to real conditions.

1. The computation could have been restricted to 1x300.

Concerning mechanical boundary conditions, lateral displacements on the lateral boundaries are null, vertical displacement on the lower boundary is null and there is an overburden pressure of $5MPa$ at the top of the coal seam. All others parameters used for the simulation are listed in Table III–2. The shape factor is evaluated according to Lim and Aziz's formula (Equation III–105). Based on the cleat aperture and the matrix width, the porosity due to fractures is calculated with Equation (III–51), $_f$ 0 3%. Then, the initial permeability is calculated with Equation (III–49), k 6 667E-14 m^2. Note the permeability is initially isotropic but evolves anisotropically. The Young's modulus and the Poisson's ratio of the equivalent continuum are, from equations III–36 and III–37, E 1 429GPa and 0 086. Finally, the initial Biot's coefficient is equal to 0 86, it is initially isotropic since the stiffness and the aperture of the fractures are equal in the three directions. Then, following Equation (III–117), it evolves anisotropically.

Parameters	Values
Seam thickness (m)	5
Reservoir radius (m)	400
Temperature (K)	303
Overburden pressure (Pa)	5E6
Well transmissibility T (m^3)	1E-12
Penalty coefficient (m^2 s kg Pa)	1 5E-19
Coal density $_c$ (kg m^3)	1500
Matrix Young's modulus E_m (Pa)	5E9
Matrix Poisson's ratio $_m$	0 3
Matrix width w (m)	0 02
Cleat aperture h (m)	2E-5
Cleat normal stiffness K_n (Pa m)	100E9
Cleat shear stiffness K_s (Pa m)	25E9
Maximum cleat closure ratio	0 5
Joint Roughness coefficient JRC	0
Sorption time $\mathcal{T}$ (days)	3
Langmuir volume V_L (m^3 kg)	0 02
Langmuir pressure P_L (Pa)	1 5E6
Matrix shrinkage coefficient (kg m^3)	0 4
Entry capillary pressure p_e (Pa)	10000
Cleat size distribution index	0 25
Tortuosity coefficient	1
Initial residual water saturation $S_{r\,res_0}$	0 1
Residual water saturation exponent, n_{wr}	0 5
Residual gas saturation	0 0

Table III–2 – Reservoir and well parameters used in the reference case.

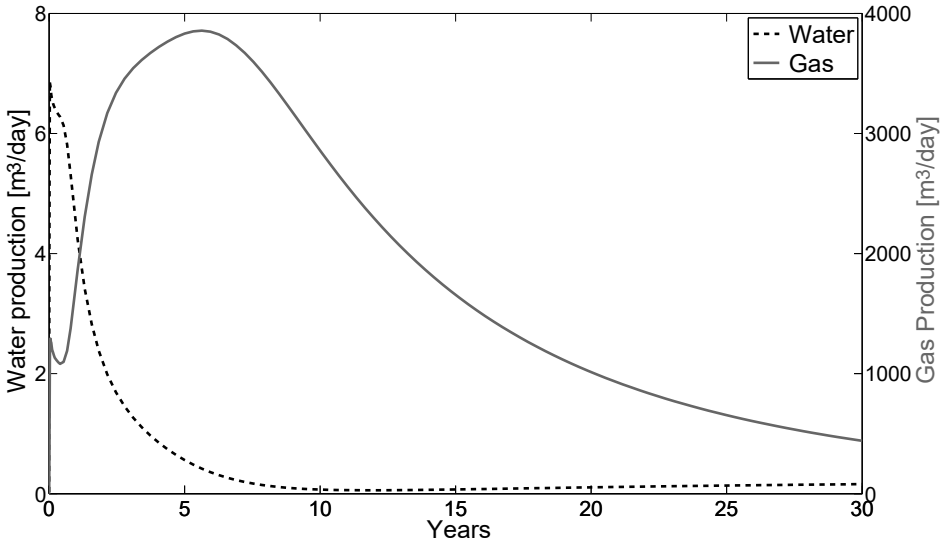

Figure III–26 – Reference case: water and gas production profiles.

The water and gas production profiles are plotted for 30 years from the start of the production in Figure III–26. The peak of water production occurs soon after the beginning of the production. The water production is close to zero after the 10^{th} year but it is never null since the outer boundary is not assumed totally impermeable to water (Equation III–156). For gas, relative permeabilities play an important role. While the production of water decreases, the gas production increases. Of course, as the gas tank is a closed volume, it can not indefinitely increases. A peak in the gas production is experienced after the 6^{th} year, at this time, the gas rate is about 3850 standard $m^3 \ day$. Then, after the peak is observed, the gas production exponentially declines. In Figure III–27, it results in a straight line on a semi-log plot of gas rate versus time [Salmachi and Yarmohammadtooski, 2015].

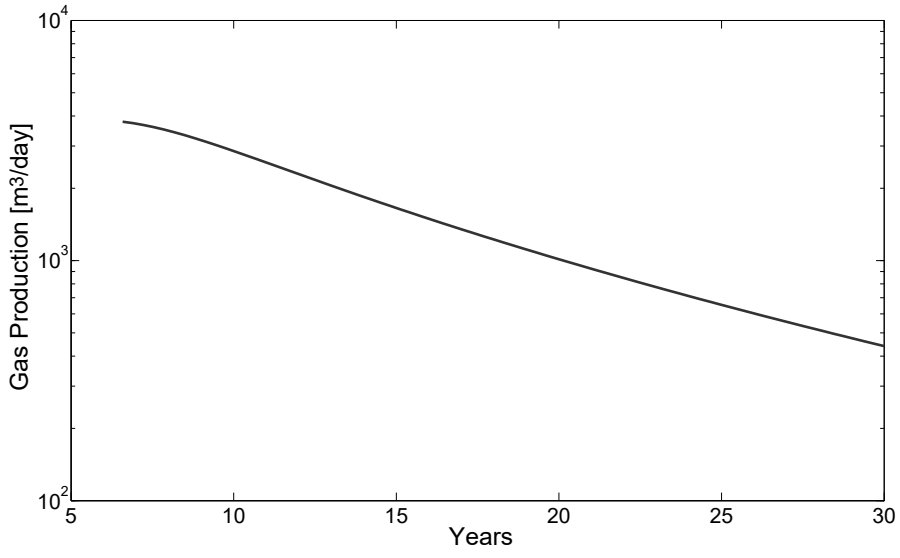

Figure III–27 – Reference case: gas production profile after peak in a semi-log plot.

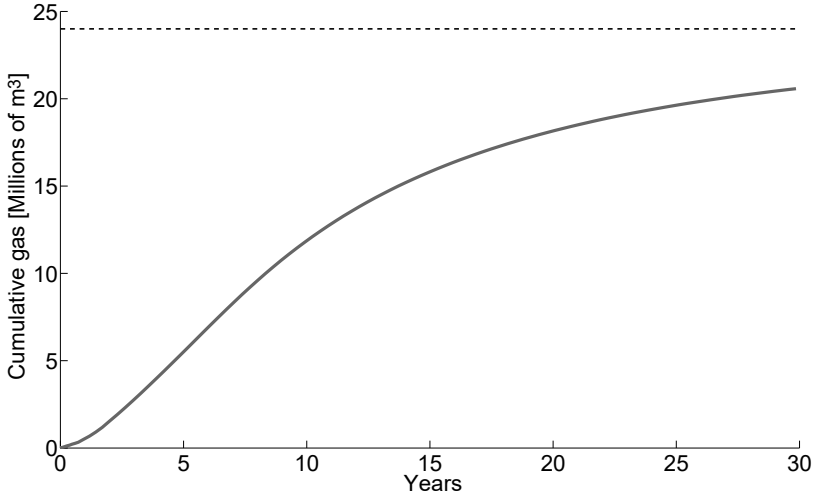

Figure III–28 – Reference case: cumulative gas.

After 30 years, the cumulative quantity of gas produced is more than 20 millions cubic meters (Figure III–28). Knowing the volume of the reservoir and the Langmuir's parameters, the total amount of gas adsorbed at $2MPa$ is 43 millions of cubic meters. As the minimal borehole pressure is 0 $5MPa$, it means 19 millions of cubic meters cannot be produced. Thence, 24 millions of cubic meters could be released.

8.2 Parametric and couplings analysis

The proposed model considers both the evolutions of permeability and porosity during the production. The permeability and porosity evolutions result from a competition between the increase of effective stress due to the reservoir depletion and the desorption strain following the gas production. Figure III–29 compares gas production profiles from the synthetic reference simulation with cases where the couplings are limited. One simulation is performed with a constant aperture of the fractures, *i.e.* constant permeability and porosity, a second one where only the permeability is constant and a third one where only the porosity is constant.

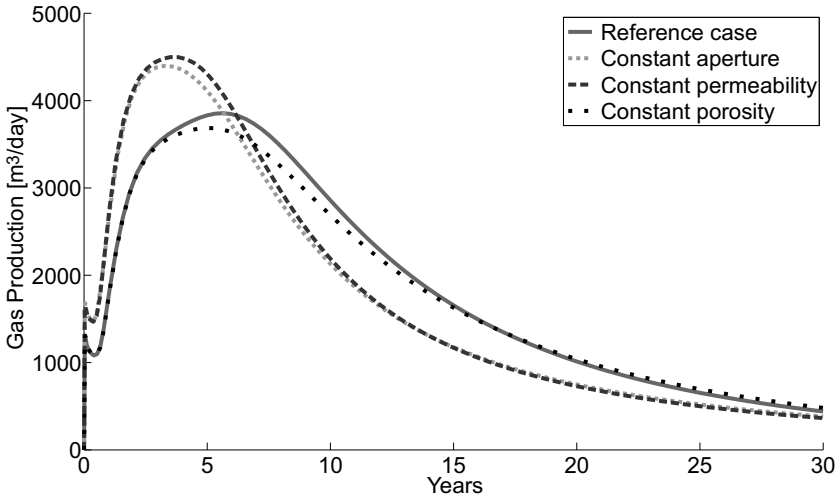

Figure III–29 – Gas production curves.

Figures III–30 and III–31 show respectively the corresponding evolutions of the porosity and the

permeability in the direction perpendicular to the well, plotted at 50*cm* from the well and mid-thickness of the seam. Figure III–29 shows permeability and porosity evolutions impact the kinetics of the production. It appears the production peak occurs earlier and higher for cases where the permeability is kept constant. Indeed, when the permeability evolution is allowed, Figure III–31 shows the permeability first decreases due to the reservoir depletion and many years are required to recover the initial permeability due to desorption. In fact, the decrease of the permeability following the increase of effective stress occurs directly after the pressure drop while the increase of the permeability due to the matrix shrinkage is not immediate. The peak is also slightly higher when the porosity is not constant.

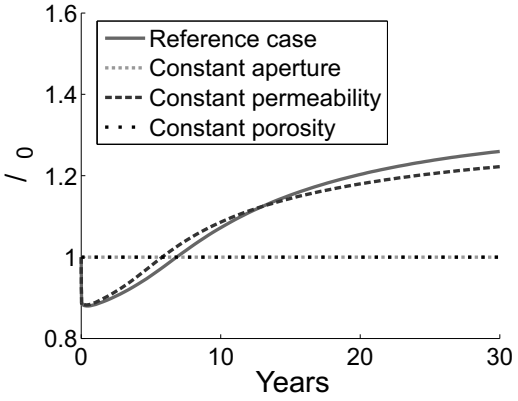

Figure III–30 – Porosity evolution at 50*cm* from the well.

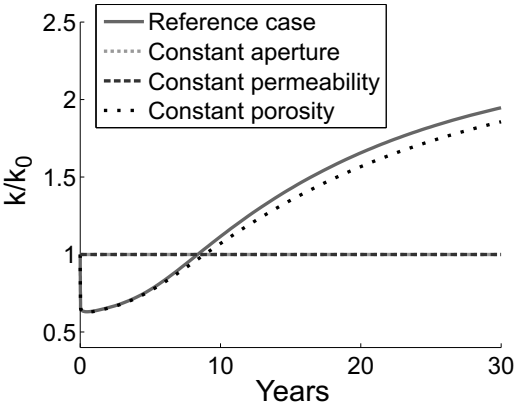

Figure III–31 – Radial permeability evolution at 50*cm* from the well.

Figure III–32 shows that the water pressure is decreased faster when the porosity increases, more space being available for the fluids. On the first hand, gas permeability is increased faster thanks to the faster decrease of the water saturation. On the other hand, gas desorption increases with the decrease of the water pressure. These phenomena are responsible for an increase in gas production.

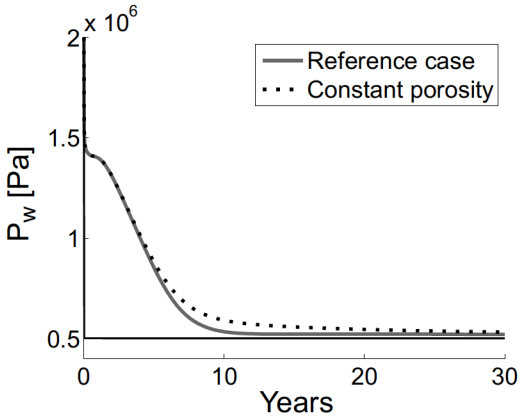

Figure III–32 – Water pressure evolution at 50cm from the well.

Figure III–33 shows the radial permeability next to the well for different sorption time factors. The longer is the sorption time factor, the later the inversion of permeability curve. However, at the time scale of the life of the well, the desorption time has a minor impact on the gas production profile which is controlled by Darcy flow when this characteristic time is about few days [Seidle, 2011].

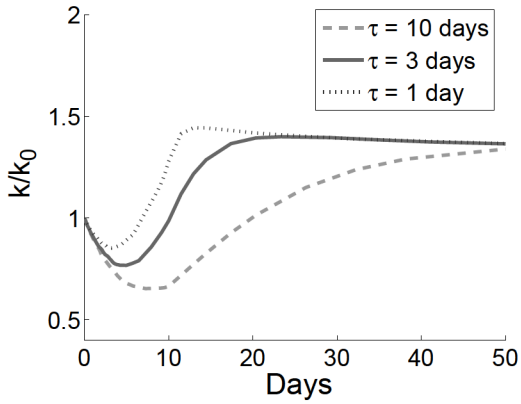

Figure III–33 – Radial permeability right next to the well.

The desorption strain coefficient is a very significant parameter. Obviously, if the desorption strain is neglected ($\beta = 0\ kg/m^3$), the permeability never increases after the decrease due to the depletion. The peak production is therefore lower. Figures III–34 and III–35 present also an intermediate case.

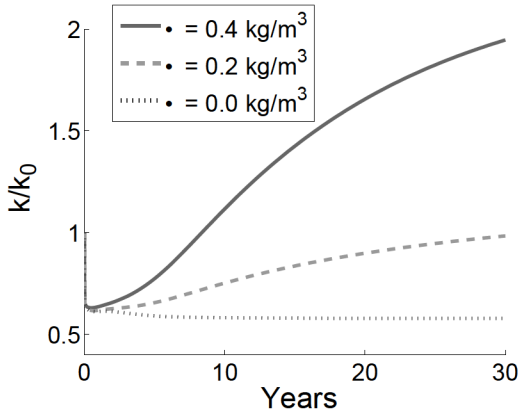

Figure III–34 – Influence of the desorption strain on the radial permeability at 50cm from the well.

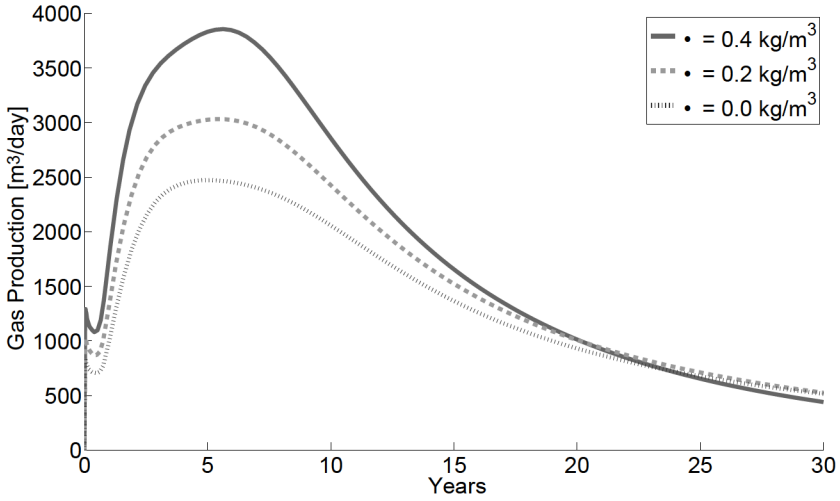

Figure III–35 – Influence of the desorption strain on the gas production curve.

The depletion rate influences also the permeability evolution. Indeed, the pressure drop set in 10 days does not let enough time for desorption strain to counterbalance immediately the increase of effective stress. This time, the pressure well is decreased from 2 to $0.5MPa$ in 5 years. In this case, the dotted permeability evolution in Figure III–36 has a less lower minima than the reference case. The gas production peak is delayed but it is slightly higher (Figure III–37). It appears also when the pressure drop at the well is less abrupt there is not a brief decrease in the gas production right after the pressure is maintained constant.

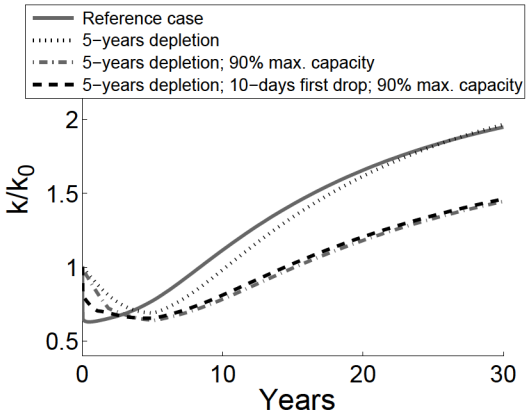

Figure III–36 – Influence of the depletion rate and gas content on the radial permeability at $50cm$ from the well.

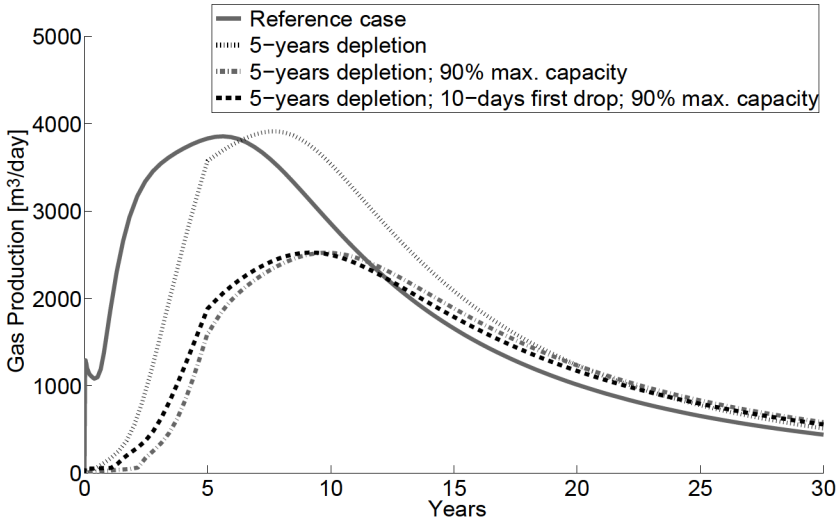

Figure III–37 – Influence of the depletion rate and gas content on the gas production profile.

Previously, the gas content in the matrix was assumed equal to the maximum capacity, *i.e.* on the Langmuir's isotherm. For the pressure of the reservoir equal to $2MPa$, the maximum adsorbed gas pressure is

$$p_{g,m}^{max} = \frac{RT}{M_{m_g}} \cdot \rho_{g,std} \cdot \rho_c \cdot \frac{V_L \cdot p_{res}^0}{P_L + p_{res}^0} = 1.897\ MPa \tag{III–157}$$

The fact that the adsorbed gas pressure is on the isotherm means the desorption mechanism is activated right after the decrease of the reservoir pressure. Now, let assume only 90% of the maximal capacity is adsorbed in the matrix. Then, the desorption starts from a critical pressure equal to

$$p_{res}^{crit} = \frac{0.9 \cdot p_{g,m}^{max} \cdot P_L}{\left(\frac{RT}{M_{m_g}} \cdot \rho_{g,std} \cdot \rho_c \cdot V_L - 0.9 \cdot p_{g,m}^{max}\right)} = 1.588\ MPa \tag{III–158}$$

Thence, any gas is desorbed until the pressure of $1.588\ MPa$ is reached in the reservoir. The production peaks therefore later. It is also lower since there is less gas in the reservoir. In fact, it is better to drop the pressure from $2MPa$ to $1.588MPa$ as soon as possible. Indeed, whatever the depletion rate chosen, no favourable permeability change can occur during this period. The last production scenario considers a pressure drop from $2MPa$ to $1.588MPa$ in 10 days and then the pressure is decreased to reach $0.5MPa$ after 5 years. This production scenario does not lower the minimal radial permeability and the production peak is earlier.

8.3 Horseshoe Canyon case

In this section, pressure and gas rate data presented by Gerami *et al.* [Gerami et al., 2007] for a well drilled in the Horseshoe Canyon coals from the Western Canadian Sedimentary Basin are used for a history matching exercise in order to test the permeability model. As this well does not produce water, this exercise is simplified since relative permeabilities do not play a role in the production behaviour. Reservoir properties provided by Gerami *et al.* are listed in Table III–3. As part of their analysis, they also estimated a total initial gas-in-place of 6.36 millions of standard cubic meters. Other parameters, such as matrix shrinkage coefficient, were not reported.

Given the Langmuir's parameters and the reservoir pressure, the maximal amount of adsorbed gas is 2.14E-03 m^3/kg (Equation III–89). Assuming 90% of this maximum capacity is actually stored, there are 2.83 of standard cubic meters of gas per cubic meter of coal. Therefore, the volume of 6.36 millions of standard cubic meters of gas is stored in a reservoir volume of 2.25 millions of cubic meters. Given

Parameters	Values
Initial reservoir pressure (Pa)	1 416E6
Temperature (K)	289
Coal density ($kg\ m^3$)	1468
Seam thickness (m)	8 99
Porosity $_f$	0 005
Langmuir volume V_L ($m^3\ kg$)	0 0092
Langmuir pressure P_L (Pa)	4 652E6

Table III–3 – Reservoir parameters for Horseshoe Canyon coals [Gerami et al., 2007].

the thickness of the seam, the radius of the cylindrical reservoir is $282m$. From the porosity of 0 5%, many combinations of the fracture aperture and the block width may be considered (Equation III–51), giving different values of the permeability. It takes part in the calibration process. Reservoir parameters used to calibrate the model are listed in Table III–4. The block matrix width and the fracture aperture used in the calibration to meet a porosity of 0 5% are respectively $8mm$ and $0\ 01333mm$, it corresponds to a permeability k 4 935E-14 m^2.

Parameters	Values
Reservoir radius (m)	282
Overburden pressure (Pa)	5E6
Matrix Young's modulus E_m (Pa)	5E9
Matrix Poisson's ratio $_m$	0 3
Matrix width w (m)	0 008
Cleat aperture h (m)	1 333E-5
Cleat normal stiffness K_n ($Pa\ m$)	100E9
Cleat shear stiffness K_s ($Pa\ m$)	2 5E9
Maximum cleat closure ratio	0 5
Sorption time $\mathcal{T}$ (hours)	1000
Matrix shrinkage coefficient ($kg\ m^3$)	0 5

Table III–4 – Reservoir parameters used to calibrate the model for the Horseshoe Canyon case.

Figure III–38 presents and compares data from Gerami *et al.* [Gerami et al., 2007] with results of the simulation performed with parameters provided in Tables III–3 and III–4. The pressure at the well is given as input to the model and the production rate is observed as the response of the model to this loading. Parameters obtained in Table III–4 by reverse analysis are one set of parameters which relatively accurately represent the production data. Of course, the solution is non-unique and it can not be asserted the taken values are physically accurate. More experimental data and information would be required to ensure this. However, it proves the model is able to represent production data from a real case. Compared to the model presented by Gerami *et al.* [Gerami et al., 2007], gas desorption is not considered instantaneous since the kinetics of diffusion is taken into account thanks to the shape factor. Moreover, compaction is not neglected, the hydro-mechanical couplings are considered to account for the permeability evolution.

An interesting output occurs at around 170 days, whereas the well pressure increases, the gas production decreases and later, when the well pressure rapidly decreases, the gas rate increases. Indeed, the model answers to a variation of the well pressure with an opposite variation in the production. It could not be shown with the synthetic reference case since a simpler loading was carried out.

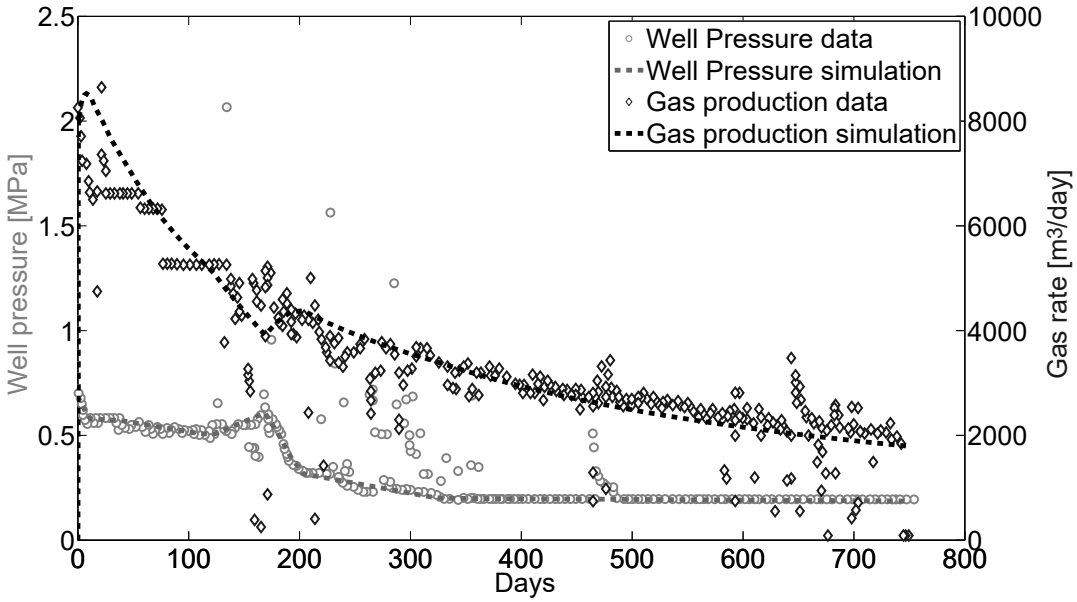

Figure III–38 – Production history matching. Horseshoe Canyon data from [Gerami et al., 2007].

Conclusions Part III

This part presented a first hydro-mechanical model useful for the modelling of coalbed methane production. This first model was developed with a macroscale framework as currently followed in the literature. The objective of this part was therefore to introduce the existing framework by formulating a consistent hydro-mechanical model.

This model takes into account the permeability evolution resulting from the reservoir pressure depletion. Indeed, coalbed methane production is a highly coupled problem. It requires to enrich the macroscale with microscale aspects. A novelty is to consider simultaneously a dual-continuum approach for both mechanical and hydraulic behaviours in order to, contrary to many models in the literature, directly link the permeability evolution to the fracture aperture instead of the porosity evolution. A remarkable feature of the model is that it does not consider desorption strain is necessarily fully converted into a fracture opening. Moreover, the model was developed for multiphase flows in the fractures. Beside advective flows in the cleats, the model considers, thanks to shape factors, the influence of the kinetics of diffusion on the mass transfer between the matrix and the fractures. The Langmuir's isotherm is used to evaluate the gas content in the matrix. It appears in the mass transfer equation between the matrix and cleats, it is not usual.

This model was applied to the modelling of the CBM production at the scale of one well. Simulations on a hypothetical reservoir showed it is interesting not to drop the pressure at the well too fast in order to reduce the closure of the fracture due to the increase of effective stress. However, in the case the reservoir does not store the maximal adsorbed gas capacity, it is advisable to apply a first pressure drop until the desorption mechanism is activated. This pressure can be estimated if the adsorbed gas content and the Langmuir's parameters of the coal reservoir are known. The model was also applied to a real production well in the Horseshoe Canyon coals. This dry reservoir presents a different production profile from a water saturated reservoir. However, it allows to simplify the history matching production data exercise since the relative permeability parameters do not have to be calibrated. This exercise showed the model is also suitable for the modelling of this particular kind of coal reservoir.

Part IV

Microscale

Introduction Part IV

Many models taking into account the coal permeability evolution with the gas pressure have been developed over the past few decades [Somerton et al., 1975, Schwerer et al., 1984, Seidle et al., 1992, Gilman and Beckie, 2000, Pan and Connell, 2007, Pan and Connell, 2012, Shi et al., 2014, Peng et al., 2017, Bertrand et al., 2017]. However, these models are either analytical formulations or macroscopic models. In this part of the thesis, a hydro-mechanical model is formulated at the scale of the coal constituents, *i.e.* cleats and matrix blocks, and then implemented into the numerical code Lagamine developed by the University of Liège [Charlier, 1987, Habraken, 1989]. At this scale, a channel flow model is directly derived from Navier-Stokes equations and cleats are modelled thanks to interface elements. It means the permeability evolution is not based on a porosity model and the use of shape factor is not required since the geometry is explicitly represented (Figure IV–1).

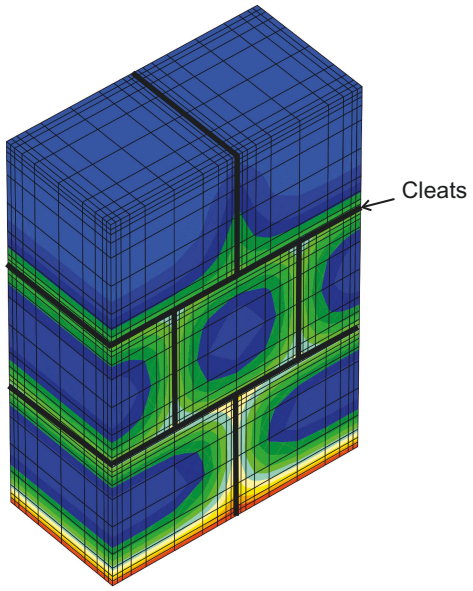

Figure IV–1 – Example of direct modelling: Adsorbed gas pressure in the matrix.

Methane is mainly stored in the coal matrix as adsorbed gas [Gray et al., 1987] but once the pressure is decreased in the cleats, the coal becomes less capable of retaining the methane and gas molecules diffuse through the matrix the reach the cleats. In the following, the hydro-mechanical model for both the matrix and the cleats is presented in details. The sorption isotherm is included in the formulation of the gas transfer between the matrix and the cleats to account for the change of state. The implementation in the finite element code is briefly presented with a special attention paid to the interface elements. Then, the implementation of the model is validated by comparison with analytical models. Finally, the numerical model is used for the modelling on a representative elementary volume. Note the model can be used for both gas production and gas injection. The permeability alteration due to CO_2 is modelled for different boundary conditions.

9. Hydro-mechanical model

During gas production or storage, flows are advective in the cleats while it is diffusive in the matrix since micropores are small compared to the gas mean free path. Gas molecules are therefore firstly adsorbed or desorbed at the coal matrix-cleat interface, what establishes a gas concentration gradient which is a driving force for the gas migration in the matrix (IV–2).

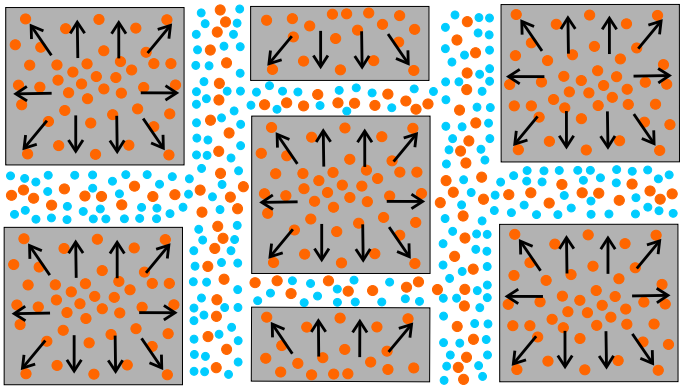

Figure IV–2 – Conceptual hydraulic microscale model

In the context of CBM or CCS, we are certainly interested in the modelling of this fluid flow problem. However, since it is highly coupled, it can not be treated apart from the mechanical problem. The hydro-mechanical model is presented hereafter first for the matrix and then for the cleats.

9.1 Matrix

9.1.1 Mechanical problem

The matrix bodies verify the classic mechanical equilibrium Equation (III–24). Neglecting the gravity term, this equation reads

$$\frac{\partial \sigma_{ij}}{\partial x_j} = 0 \tag{IV–1}$$

with σ_{ij} the Cauchy stress tensor.

An elastic constitutive law is assumed effective for describing the stress-strain relationship of the coal matrix before failure. The elastic constitutive model relates stress and strain increments through the elastic stiffness tensor C_{ijkl} or inversely with the elastic compliance D_{ijkl}:

$$\tilde{\sigma}_{ij} = C_{ijkl}\,\dot{\varepsilon}_{kl} \qquad \dot{\varepsilon}_{ij} = D_{ijkl}\,\tilde{\sigma}_{kl} \tag{IV–2}$$

where $\dot{\varepsilon}_{ij}$ is the Cauchy strain rate and $\tilde{\sigma}_{ij}$ is the Jaumann stress rate.

Considering an isotropic medium, the elastic constitutive tensors are defined by two independent parameters, e.g. the Young's modulus E_m and the Poisson's ratio ν_m. The elastic compliance writes

$$\frac{1}{E}\cdot\begin{bmatrix} 1 & -\nu_m & -\nu_m & 0 & 0 & 0 \\ -\nu_m & 1 & -\nu_m & 0 & 0 & 0 \\ -\nu_m & -\nu_m & 1 & 0 & 0 & 0 \\ 0 & 0 & 0 & (1+\nu_m) & 0 & 0 \\ 0 & 0 & 0 & 0 & (1+\nu_m) & 0 \\ 0 & 0 & 0 & 0 & 0 & (1+\nu_m) \end{bmatrix} \tag{IV–3}$$

The elastic stiffness tensor C_{ijkl} may be determined by calculating the inverse of the elastic compliance D_{ijkl}. This mechanical constitutive relation is written in total stress for the matrix part of model (grains).

9.1.2 Hydraulic problem

9.1.2.1 Mass balance equation

Gas is the only mobile fluid considered in the matrix. On a unit volume, the mass balance equation of the gas in the matrix is:

$$\frac{\partial}{\partial t}\left(\rho_g^{Ad}\right) + \frac{\partial}{\partial x_i}\left(J_{mi}^g\right) = 0 \tag{IV–4}$$

where the first term is related to the mass variation of the adsorbed gas and the second term is related to the gas diffusion. These two quantities are considered in the following paragraphs.

9.1.2.2 Density variation

The classical ideal gas equation of state is used to write the adsorbed gas density as

$$\rho_g^{Ad} = \frac{M_{m_g}}{RT} p_g^{Ad} \tag{IV–5}$$

where R is the universal gas constant ($8.3143\ J/mol\cdot K$), $T[K]$ is the absolute temperature, M_{m_g} is the molecular mass of the gas ($0.016\ kg/mol$ for methane and $0.044\ kg/mol$ for carbon dioxide) and p_g^{Ad} is the gas pressure in the matrix, *i.e.* an adsorbed gas pressure [1].

9.1.2.3 Diffusive flows

Due to its simplicity, Fick's law [Fick, 1855] is the most popular approach to evaluate diffusive flows. It states the flux in the direction i for the species g diffusing in the matrix (m) is directly proportional to the concentration gradient in that direction:

$$J_{mi}^g = -D_m^g \frac{\partial C_g}{\partial x_i} \tag{IV–6}$$

In this equation, the determination of the phenomenological coefficient D_m^g is naturally the most critical part of the equation. Rigorously, the thermodynamically correct driving force for diffusion is the

1. The remark written for the macroscale model still holds here, the adsorbed gas pressure p_g^{Ad} has no other physical meaning than the application of the gas law of state between the real density and this fictive pressure. The model is formulated in terms of pressures since the nodal unknowns are pressures in the finite element formulation. The adsorbed pressure will be obtained from the translation of the adsorbed gas density determined with the Langmuir's isotherm through the gas equation of state, see Equation (III–91) in the macroscale model. This time, as will be seen in section 9.2.2.4, the Langmuir's equilibrium is only written at the interface between the cleat and the matrix to define the gas transfer between the two and control the diffusion inside the matrix. All the gas mass extracted from the material makes sense since the gas must go through the cleat to get out.

chemical potential gradient. Indeed, diffusion is a spontaneous process reducing the total free energy. As the chemical potential generally increases with increasing concentration, it is convenient to express diffusion in term of concentration or mass density.

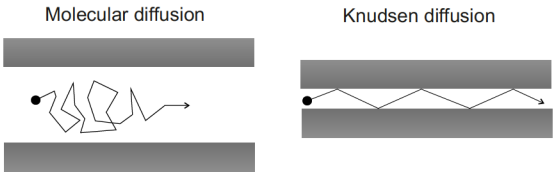

Figure IV–3 – Different types of diffusion.

When the pores are very narrow, diffusing molecules collide with the walls much more frequently than with other molecules. It results in a sliding of the gas molecules along the internal walls of the porous network, it is the Knudsen diffusion (Figure IV–3). The Knudsen number serves to distinguish which type of diffusion is predominant in the transport process, it is defined as follows [Cussler, 2009]:

$$\kappa_n = \frac{\bar{l}}{d_p} \tag{IV–7}$$

where $\bar{l}$ is the gas mean free path and d_p is a characteristic length such as the mean pore diameter of the porous media. Molecular diffusion (molecule-molecule collisions) prevails when the pore diameter is greater than ten times the mean free path (*i.e.* κ_n lower than 0.1). But if the mean free path is greater than ten times the pore diameter (κ_n greater than 10), Knudsen diffusion (molecule-wall collisions) may be assumed. In the intermediate, Knudsen diffusion and molecular diffusion compete with one another. For liquids, the Knudsen number is generally small because the mean free path is a few angstroms. For gas, the mean free path can be estimated as [Cussler, 2009]:

$$\bar{l} = \frac{4k_B T}{\pi\, d_g^2 p_g} \tag{IV–8}$$

where d_g is the collision diameter of the gas molecule (3.3Å for CO_2 and 3.8Å for CH_4 [Ismail et al., 2015]), k_B is the Boltzmann constant, $T[K]$ is the temperature and $p_g[Pa]$ is the pressure of the gas. For any given adsorbent and adsorbate, there is therefore a transition from molecular diffusion at high pressures to Knudsen flow at low pressures. For methane and coal, it has been estimated that the mean free path of the methane molecule at standard conditions is about $50nm$, it is substantially lower in deep coal seams where higher pressure is encountered [Shi and Durucan, 2003]. However, gas diffusion in the coal matrix is more controlled by Knudsen diffusion due the extremely small size of the pores of the matrix (lower than $2nm$).

The Knudsen diffusion coefficient may be estimated by analogy of the kinetic theory of rigid spheres that predicts [Cussler, 2009]:

$$D^g_{mK} = \frac{1}{3} d_p v_g \tag{IV–9}$$

where v_g is the gas molecular velocity. From the kinetic energy theory of molecules, we have:

$$\frac{1}{2} M_g v_g^2 = k_B T \tag{IV–10}$$

The Knudsen diffusion coefficient is then:

$$D^g_{mK} = \frac{d_p}{3}\sqrt{\frac{2k_B T}{M_g}} \tag{IV–11}$$

Actually, in fine micropores (lower than $1nm$), the diffusing molecules never really escape the potential field of the adsorbing surface. Therefore, their transport is an activated process consisting by jumps from one adsorption site to the other [Shi and Durucan, 2003]. This transport process is thus more similar to surface diffusion (Figure IV–4) involving a diffusion coefficient $D^g_{mS}[m^2/s]$ which is proportional to the mean-square jump distance $[m^2]$ and the jump frequency $[s^{-1}]$. The contribution of surface transport to gas diffusion in coals varies from one coal to another. On one side, Thimons and Kissell [Thimons and Kissell, 1973] studied methane and helium diffusion in U.S. coals by gas flow through a narrow disk of coal and reported that surface diffusion in adsorbed methane film is negligible compared to gas transport in pores. On the other side, Sevenster [Sevenster, 1959] conducted similar experiments on British coals and concluded that surface transport has a large contribution to gas diffusion in coals.

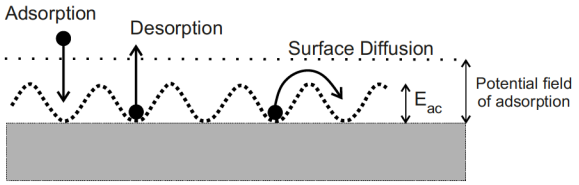

Figure IV–4 – Schematic diagram of surface diffusion. *Modified from* [Wu et al., 2015].

As different mechanisms may be combined, the diffusion process is a complex physical phenomenon. It is assumed it may be represented by a global phenomenological parameter $D^g_m[m^2/s]$ to evaluate the diffusive flux J^g_{mi} with Equation (IV–6) in which the concentration C_g is replaced by the density ρ^{Ad}_g. J^g_{mi} becomes therefore a mass flux.

9.1.3 Hydro-mechanical coupling

A structural rearrangement of the matrix is induced by the variation of the adsorbed gas pressure [Karacan, 2003]. As a consequence, the matrix swells or shrinks. The variation of the volumetric sorption-induced strain $\dot{\varepsilon}_{v_s}$ is approximately proportional to the variation of the adsorbed gas content [2]:

$$\dot{\varepsilon}_{v_s} = \beta_\varepsilon \frac{M_{m_g}}{RT} \frac{1}{\rho_{g,std}\,\rho_c} \frac{\partial p^{Ad}_g}{\partial t} \tag{IV–12}$$

where $\beta_\varepsilon[kg/m^3]$ is the volumetric strain coefficient and $\rho_{g,std}$ and ρ_c are respectively the gas density at standard conditions and the coal density. Assuming an isotropic swelling/shrinkage of the matrix, the mechanical constitutive equation becomes [2]:

$$\tilde{\sigma}_{ij} = C_{ijkl}\left(\dot{\varepsilon}_{kl} - \frac{1}{3}\dot{\varepsilon}_{v_s}\delta_{ij}\right) \tag{IV–13}$$

with δ_{ij} the Kronecker's symbol.

Note the swelling may, to some extent, deviates from a linear relationship with the gas content. However, given its wider and easier applicability, the linear law is often chosen [Cui and Bustin, 2005]. Using a non-linear model would not modify the understanding on the hydro-mechanical behaviour of the material.

There is no other coupling to consider in the matrix. The effective stress is only required in the cleats.

9.2 Cleats

Considering a matchstick geometry [Seidle et al., 1992], coal is defined by some matrix blocks of width w separated by cleats (Figure IV–5). The mechanical aperture of the cleats is h. However, a

2. Positive tensile strain and stress.

hydraulic aperture h_b is considered for the hydraulic problem. In 3D, the fracture is defined by the plane (x_1, x_3).

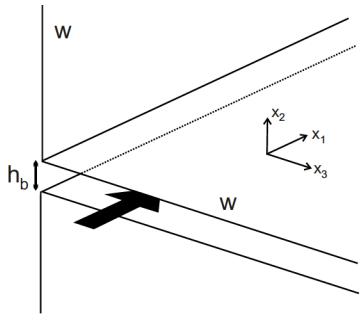

Figure IV–5 – Definition of the geometry of the cleat with a flow along x_1. *Modified from* [Reiss, 1980].

9.2.1 Mechanical problem

The relation between the normal stress rate $\dot{\sigma}$ and the fracture closure $\dot{h}$ is defined via the normal stiffness K_n [2]:

$$\dot{\sigma} = K_n \cdot \dot{h} \tag{IV–14}$$

Due to the deforming asperities, this relation should be non-linear [Gens et al., 1990] (Figure IV–6). A hyperbolic law is used to account for the evolution of the stiffness with the fracture closure [Goodman, 1976, Bandis et al., 1983]:

$$K_n = \frac{K_n^0}{\left(1 + \frac{\Delta h}{h_0}\right)^2} \tag{IV–15}$$

where K_n^0 is the stiffness corresponding to the aperture h_0 and $\Delta h = h - h_0$.

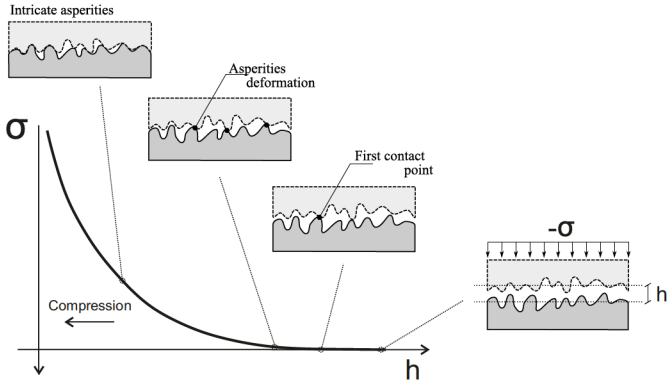

Figure IV–6 – Constitutive law describing the normal behaviour of a rough rock joint. *Modified from* [Cerfontaine et al., 2015].

For the tangential behaviour of the fracture, two states can be distinguished: the stick and the slip states. In the first state, two points in contact are stuck together. In the second state, there is a relative tangential displacement in the plane of the fracture. The tangential variation of displacement in the direction i (1 and 3), $\dot{s}_i$, is related to the shear stress in that direction, $\dot{\tau}_i$, as [2]

$$\dot{\tau}_i = K_s \cdot \dot{s}_i \tag{IV–16}$$

where K_s is the shear stiffness of the fracture.

The two states can be distinguished by a constitutive criterion. One of the most basic is probably the Mohr-Coulomb criterion. Using a single variable μ_f representing a friction coefficient, the criterion reads

$$f = ||\tau|| - \mu_f \cdot \sigma \tag{IV–17}$$

where $||\tau||$ is the norm of the shear stresses. The criterion is represented in Figure IV–7.

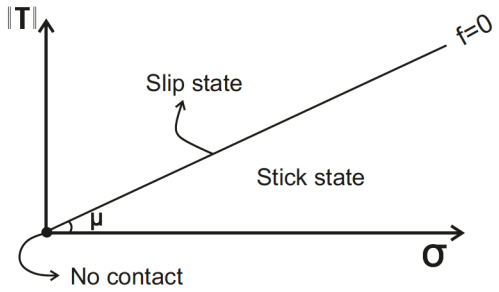

Figure IV–7 – Mohr-Coulomb criterion.

When the combination of tangential and normal stresses lies below the criterion ($f < 0$), it is a tangential stick state. It can be compared to an elastic state. In this case, the incremental relation between stresses and displacements reads

$$\begin{Bmatrix} \dot{\tau}_1 \\ \dot{\sigma} \\ \dot{\tau}_3 \end{Bmatrix} = \begin{bmatrix} K_s & 0 & 0 \\ 0 & K_n & 0 \\ 0 & 0 & K_s \end{bmatrix} \begin{Bmatrix} \dot{s}_1 \\ \dot{h} \\ \dot{s}_3 \end{Bmatrix} \tag{IV–18}$$

If the stress state lies on the criterion ($f = 0$), then it is a slip state. Once this state is reached, the elastoplastic constitutive relation is then

$$\begin{Bmatrix} \dot{\tau}_1 \\ \dot{\sigma} \\ \dot{\tau}_3 \end{Bmatrix} = \begin{bmatrix} K_s \left(1 - \frac{(\tau_1)^2}{||\tau||^2}\right) & -\mu_f K_n \frac{\tau_1}{||\tau||} & -\mu_f K_s \frac{\tau_1 \tau_3}{||\tau||^2} \\ 0 & K_n & 0 \\ -\mu_f K_s \frac{\tau_1 \tau_3}{||\tau||^2} & -\mu_f K_n \frac{\tau 3}{||\tau||} & K_s \left(1 - \frac{(\tau_3)^2}{||\tau||^2}\right) \end{bmatrix} \begin{Bmatrix} \dot{s}_1 \\ \dot{h} \\ \dot{s}_3 \end{Bmatrix} \tag{IV–19}$$

The cohesion c can be used as second parameter to define the general Mohr-Coulomb criterion. Note that many others constitutive laws also exist, taking into more complex behaviours of fractures with damage for instance, but it is not of primary interest in the context of gas flow modelling.

9.2.2 Hydraulic problem

Two kinds of flow are distinguished in the cleats, transverse and longitudinal flows (Figure IV–8). Transverse flows q_T represent the gas transfer between the cleats and the matrix while the longitudinal multiphase flows q_L occur in between the fracture walls. The longitudinal flow of the gas species consists of the flow of the dry gas and the flow of the dissolved gas in the water phase. For the sake of simplicity, the hydraulic problem described in the following is written considering only a longitudinal flow along x_1 and not x_3.

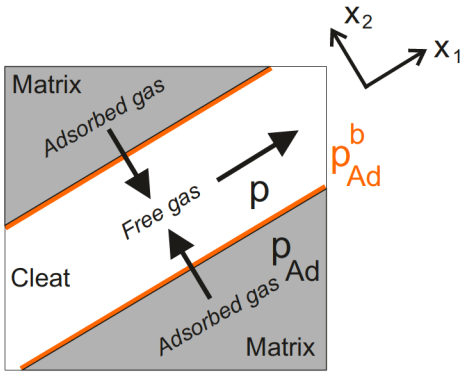

Figure IV–8 – Cleats flow model.

9.2.2.1 Mass balance equations

The unsaturated model considers both gas and water in the cleats. The mass balance equation for water is:

$$\frac{\partial}{\partial t}(\rho_w\, S_r\, h_b) + \frac{\partial}{\partial x_1}(\rho_w\, h_b\, q_{l_L}) = 0 \tag{IV–20}$$

where ρ_w is the water density, S_r is the degree of saturation, h_b is the hydraulic aperture and q_{l_L} the liquid advective flows along the fracture. A second longitudinal flow should appear in the equation when 3D conditions are considered. There is no transverse flow since water is not considered in the matrix. Note the cleat is considered as an entirely void volume and no porosity therefore appears in this equation. Moreover, the water vapour is not considered.

Concerning the mass balance equation for gas, it reads:

$$\begin{aligned} &\frac{\partial}{\partial t}\left(\rho_{g,f}\,(1-S_r)\,h_b\right) \\ &\underbrace{+\frac{\partial}{\partial x_1}\left(\rho_{g,f}\,h_b\,q_{g_L}\right) + \frac{\partial}{\partial x_2}\left(\rho_{g,f}\,h_b\,(q^1_{g_T} - q^2_{g_T})\right)}_{\text{Gas phase}} \\ &\underbrace{+\frac{\partial}{\partial t}\left(\rho^d_{g,f}\,S_r\,h_b\right) + \frac{\partial}{\partial x_1}\left(\rho^d_{g,f}\,h_b\,q_{l_L} + S_r\,h_b\,J^g_{l\,L}\right)}_{\text{Dissolved gas in water phase}} = 0 \end{aligned} \tag{IV–21}$$

where $\rho_{g,f}$ and $\rho^d_{g,f}$ are respectively the densities of the gas and the dissolved gas in the water. $J^g_{l\,L}$ represents the diffusive flows of the dissolved gas in the liquid phase, it is determined with a Fick's law. q_{g_L} represents the longitudinal flow and $q^1_{g_T}$ and $q^2_{g_T}$ the two transverse flows. The formulations of these advective flows are described hereafter.

9.2.2.2 Thermodynamic equilibrium

The density of the dissolved gas is obtained with the Henry's law assuming a thermodynamic equilibrium between the dissolved gas and the dry gas [Lide, 2004]:

$$\rho^d_{g,f} = H_g \rho_{g,f} \tag{IV–22}$$

where H_g is the so-called Henry's coefficient ($H_g = 0.0347$ for methane and $H_g = 0.8317$ for carbon dioxide).

9.2.2.3 Density variations

The density ρ_w of the liquid phase evolves with the pressure p_w according to:

$$\rho_w = \rho_{w_0}\left(1 + \frac{p_w - p_{w_0}}{\chi_w}\right) \tag{IV–23}$$

where ρ_{w_0} is the liquid density at the pressure p_{w_0} and $1/\chi_w$ is the liquid compressibility. At $20°C$, $1/\chi_w = 5 \cdot 10^{-10} Pa^{-1}$.

The classical ideal gas equation of state is used to write the gas density in the fractures as

$$\rho_{g,f} = \frac{M_{m_g}}{RT} p_{g,f} \tag{IV–24}$$

where $p_{g,f}$ is the gas pressure in the fractures.

9.2.2.4 Gas transfer

The quantity of gas stored in the matrix in function of the pressure in the cleats depends on the Langmuir's isotherm. Thence, in order to evaluate the gas transfer between the matrix and the fractures, the fracture pressure is translated with the isotherm into an adsorbed gas pressure. Given a pressure p in the cleat, the gas pressure in the matrix must tend (from its boundary) to:

$$p_g^{Adb} = \frac{RT}{M_{m_g}} \cdot \rho_{g,std} \cdot \rho_c \frac{V_L \cdot p}{P_L + p} \tag{IV–25}$$

where the pressure in the cleat can be evaluated by weighting the water and gas pressures by the saturation of each phase:

$$p = S_r p_w + (1 - S_r) p_{g,f} \tag{IV–26}$$

Then, the gas transfer from the matrix to the cleat is proportional to the difference between the adsorbed gas pressure at the boundary of the matrix p_g^{Adm} (initially defined) and the limit pressure on the boundary p_g^{Adb} :

$$q_{gT} = -T_t \cdot (p_g^{Adb} - p_g^{Adm}) \tag{IV–27}$$

where T_t $[m/(Pa \cdot s)]$ is the gas transverse transmissivity of the fracture. If p_g^{Adb} is lower than p_g^{Adm}, there is desorption for any saturation condition. If p_g^{Adb} is greater than p_g^{Adm}, there is obviously adsorption in gas saturated conditions. For unsaturated conditions, it should be verified that gas is available for adsorption. Indeed, water pressure is part of the reservoir pressure translated with the Langmuir's isotherm to determine the gas transfer. A simple criterion is to allow a gas transfer only if the adsorbed gas pressure p_g^{Adb} calculated with the gas pressure $p_{g,f}$ is itself greater than adsorbed pressure on the matrix boundary p_g^{Adm}.

9.2.2.5 Channel flow model

Saturated conditions

The motion of compressible Newtonian fluids is described by the Navier-Stokes equations. These equations result from the application of the Reynolds transport theorem to the fluid density ρ and the momentum ρv_i. Considering a constant density and if there is no source or sink of mass, the conservation of mass reduces to conservation of volume:

$$\frac{\partial v_i}{\partial x_i} = 0 \tag{IV–28}$$

According to Cauchy momentum equation, the source term in the balance of the momentum may be decomposed into the surface forces (normal and shear stresses) and the body forces, such as gravity. Considering Equation (IV–28), the conservation of momentum gives the following formulation of the Navier-Stokes equations:

$$\rho\left(\frac{\partial v_i}{\partial t}+v_j\frac{\partial v_i}{\partial x_j}\right)=-\frac{\partial p}{\partial x_i}+\mu\frac{\partial^2 v_i}{\partial x_j^2}+f_i \tag{IV–29}$$

where ρ is the fluid density, v_i are the components of the fluid velocity, t is the time, p is the pressure, μ is the dynamic viscosity and f_i is an external body force.

Under the assumption the cleats are two closely-space parallel plates separated by an aperture h_b (Figure IV–5), the geometry is known and we can derive the constitutive flow law directly from Navier-Stokes. This channel flow model is straightforward, it allows to directly link the fluid velocity with the fracture aperture.

Assuming laminar flow $\left(v_j\frac{\partial v_i}{\partial x_j}=0\right)$ and steady state conditions $\left(\frac{\partial v_i}{\partial t}=0\right)$, the momentum Equation (IV–29) reduces to Equation (IV–30) when no body force is considered.

$$\frac{\partial^2 v_i}{\partial x_j^2}=\frac{1}{\mu}\frac{\partial p}{\partial x_i} \tag{IV–30}$$

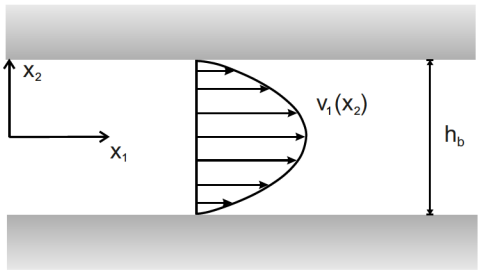

Figure IV–9 – Laminar fluid flow profile between two parallel plates.

The following non-slip boundary conditions are considered at the walls:

$$v\left(x_2=\pm\frac{h}{2}\right)=0$$

Moreover, the flow is only carried by the x_1 component: $\frac{\partial p}{\partial x_2}=0$. It leads to the following parabolic profile where the maximum velocity is reached in the middle of the channel:

$$v_1(x_2)=-\frac{1}{2\mu}\left(\left(\frac{h_b}{2}\right)^2-x_2^2\right)\frac{\mathrm{d}p}{\mathrm{d}x_1} \tag{IV–31}$$

Then, averaging the velocity over the thickness h leads to:

$$q=\langle v_1\rangle=\frac{1}{h_b}\int_{-\frac{h_b}{2}}^{\frac{h_b}{2}}v_1 dx_2=-\frac{h_b^2}{12}\cdot\frac{1}{\mu}\frac{\mathrm{d}p}{\mathrm{d}x_1} \tag{IV–32}$$

This channel flow Equation (IV–32) is known as the Hele-Shaw relation [Gustafsson and Vasil'ev, 2006]. Using the distance s along the channel to generalize the example, we can write

$$q=-\frac{h_b^2}{12}\cdot\frac{1}{\mu}\frac{\mathrm{d}p}{\mathrm{d}s} \tag{IV–33}$$

It is equivalent to the Darcy's equation with a permeability equal to $k = \frac{h_b^2}{12}$ [Darcy, 1856, Witherspoon et al., 1980], it is function of the fracture aperture.

The channel flow model has been derived with no-slip boundary conditions. However, it may be not the case for gas flow. If the Knudsen number (κ_n) is less than 0.01, then viscous flow dominates: the fluid is immobile at the pore wall and Equation (IV–33) can be applied. If κ_n is comprised between 0.01 and 0.1, slip flow regime occurs and our flow model should be modified to account this effect. For higher values of κ_n, equations of diffusive flows are employed.

The problem of gas slippage in capillary tubes and its effect on permeability in porous media was first addressed by Klinkenberg [Klinkenberg et al., 1941]. We derive hereafter a model for the flow between two parallel plates. Kundt and Warburg showed that the velocity at the wall is proportional to the velocity gradient at the wall [Kundt and Warburg, 1875]:

$$v_1\left(\frac{h_b}{2}\right) = -c\,\bar{l}\,\left.\frac{\mathrm{d}v_1}{\mathrm{d}x_2}\right]_{x_2=\frac{h_b}{2}} \tag{IV–34}$$

where c is a constant with a value slightly less than 1 according to Kundt and Warburg and $\bar{l}$ is the mean free path of the gas molecules at the mean pressure. The velocity gradient is obtained by integrating equation (IV–30), it gives:

$$\frac{\mathrm{d}v_1}{\mathrm{d}x_2} = \frac{x_2}{\mu}\frac{\mathrm{d}p}{\mathrm{d}x_1} + C \tag{IV–35}$$

To ensure an extremum value in the center ($x_2 = 0$), the constant C must be zero. Thence, the velocity at the walls is:

$$v_1\left(\frac{h_b}{2}\right) = -\frac{c\,\bar{l}\,h_b}{2\mu}\frac{\mathrm{d}p}{\mathrm{d}x_1} \tag{IV–36}$$

These boundary conditions allows to find the following velocity profile:

$$v_1(x_2) = -\frac{1}{2\mu}\left(c\,\bar{l}\,h_b + \left(\frac{h_b}{2}\right)^2 - x_2^2\right)\frac{\mathrm{d}p}{\mathrm{d}x_1} \tag{IV–37}$$

Averaging this velocity over the aperture, we find:

$$q = \langle v_1 \rangle = \frac{1}{h_b}\int_{-\frac{h_b}{2}}^{\frac{h}{2}} v_1 dx_2 = -\frac{h_b^2}{12}\left(1 + \frac{6c\bar{l}}{h_b}\right)\cdot\frac{1}{\mu}\frac{\mathrm{d}p}{\mathrm{d}x_1} \tag{IV–38}$$

In comparison with equation (IV–33), one can observe that the permeability is increased of a dimensionless correction factor f_c given by:

$$f_c = \left(1 + \frac{b_g}{\bar{p}}\right) \qquad \text{with} \quad \frac{b_g}{\bar{p}} = \frac{6\,c\,\bar{l}}{h_b} = 6\,c\,\kappa_n, \tag{IV–39}$$

where $c \approx 1$, $\bar{p}$ is the mean gas pressure and b_g is the Klinkenberg number. For a capillary tube, it has been found that $\frac{b}{\bar{p}} = \frac{4\,c\,\bar{l}}{r}$ with r the effective pore radius [Klinkenberg et al., 1941]. Note that the gas permeability is a function of the mean free path $\bar{l}$ of the gas molecules, it depends therefore on the pressure, the temperature and the nature of the gas. Considering a fracture aperture of few micrometers, the correction factor at reservoir temperature conditions is less than 1% for a CO_2 or CH_4 pressure of 1MPa. In these conditions of gas flow, Klinkenberg effect can be disregarded.

Unsaturated conditions

Finally, if gas and water flows are simultaneously considered in the cleats, it is necessary to extend the model to unsaturated conditions. In this purpose, relative permeability k_r may be introduced as a measure of the reduction in permeability of a given phase that occurs between partially and fully saturated conditions. In petroleum engineering, the relative permeabilities of the wetting phase (k_{rw}) and the non-wetting phase (k_{rnw}) in porous media are often expressed as power law functions of saturation (S_r), known as Corey functions [Corey, 1954]. Equations (III–78) and (III–79) were derived from a macroscopic approach and were interesting in this perspective. This time, it is considered two phases are simultaneously flowing in a single cleat. Logically, the space occupied by one phase is not available for the flow of the other phase. Based on the work of Romm, a simple model consists to equalize the relative permeabilities to the phases saturations, it is known as the X curves [Romm, 1966]:

$$k_{rw} \quad S_r \qquad \text{(IV–40)} \qquad\qquad k_{rg} \quad S_g \quad 1 \quad S_r \qquad \text{(IV–41)}$$

As can be noticed, the sum of k_{rw} and k_{rg} equals 1 in the X model, which means each phase flows in its own path without impeding the flow of the other, the interference between the phases is not considered.

Through a real fracture, the X model may no longer be valid if the interference is significant. In order to characterize the deviation from the X model, Chen and Horne proposed the following expressions [Chen et al., 2004]:

$$k_{rw} \quad \frac{S_r}{c\,w} \qquad \text{(IV–42)} \qquad\qquad k_{rg} \quad \frac{1 \quad S_r}{c\,g} \qquad \text{(IV–43)}$$

where $_{c\,w}$ and $_{c\,g}$ are the channel tortuosities of the two phases. These coefficients, varying between 1 and the infinity, quantify the shear stress at the interface between the two fluids. Chen and Horne evaluate the tortuosity coefficients analysing the structure flow by digital image processing techniques. Unfortunately, a model that predicts the flow structure in a fracture does not exist. It is therefore impossible to evaluate $_{c\,w}$ and $_{c\,g}$ without resorting to experiments. However, assuming a simple flow structure, it is possible to derive a model which takes into account the interference between the two phases through viscous considerations. Yuster used co-axial flows in a single circular cylinder to infer a viscosity ratio dependence of the relative permeabilities [Yuster et al., 1951]. This viscous coupling model can also be applied to a two-phase flow between two plates [Fourar et al., 1998]. We consider two fluids flowing simultaneously with a planar interface. Water is the wetting fluid and therefore is in contact with the walls, and gas (non-wetting) flows in between (Figure IV–10).

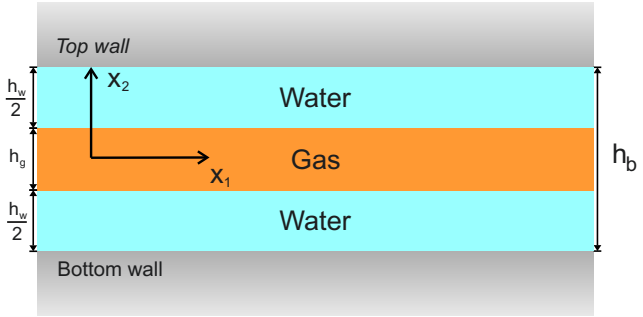

Figure IV–10 – Gas flow in between of water flows in a fracture space.

The viscous coupling between the fluids is derived by integrating Stokes' equation in each stratum. The velocity of each phase is the same at the interface, the shear force on the two phases is therefore the

same at the interface:

$$L \cdot w \cdot \mu_w \left(\frac{\mathrm{d}v_1}{\mathrm{d}x_2}\right)_w = L \cdot w \cdot \mu_g \left(\frac{\mathrm{d}v_1}{\mathrm{d}x_2}\right)_g \quad \Rightarrow \quad \mu_w \left(\frac{\mathrm{d}v_1}{\mathrm{d}x_2}\right)_w = \mu_g \left(\frac{\mathrm{d}v_1}{\mathrm{d}x_2}\right)_g \tag{IV–44}$$

where the area $L \cdot w$ vanishes out.

Equations of the form given by equation (IV–35) for the two phases at the interface $\left(x_2 = \frac{h_g}{2}\right)$ are:

$$\left(\frac{\mathrm{d}v_1}{\mathrm{d}x_2}\right)_w = \frac{h_g}{2\mu_w}\frac{\mathrm{d}p}{\mathrm{d}x_1} + C_w \tag{IV–45}$$

$$\left(\frac{\mathrm{d}v_1}{\mathrm{d}x_2}\right)_g = \frac{h_g}{2\mu_g}\frac{\mathrm{d}p}{\mathrm{d}x_1} + C_g \tag{IV–46}$$

Due to symmetry, the derivative of the velocity equals zero in the center of the fracture ($x_2 = 0$); it means that $C_g = 0$. Moreover, to satisfy Equation (IV–44), we have:

$$\mu_w \cdot C_w = \mu_g \cdot C_g \tag{IV–47}$$

It follows that $C_w = 0$. Therefore, the generalized expression for the velocity gradient perpendicular to the direction of flow is:

$$\frac{\mathrm{d}v_1}{\mathrm{d}x_2} = \frac{x_2}{\mu}\frac{\mathrm{d}p}{\mathrm{d}x_1} \tag{IV–48}$$

Integrating Equation (IV–48) to give the velocity profile perpendicular to the direction of flow leads to:

$$v_1 = \frac{x_2^2}{2\mu}\frac{\mathrm{d}p}{\mathrm{d}x_1} + \mathcal{Z} \tag{IV–49}$$

Applying this to the water phase, when $x_2 = \frac{h_b}{2}$, then $v_1 = 0$ and we find Equation (IV–31):

$$v_{1w} = -\frac{1}{2\mu_w}\left(\left(\frac{h_b}{2}\right)^2 - x_2^2\right)\frac{\mathrm{d}p_w}{\mathrm{d}x_1} \tag{IV–50}$$

Thence, the velocity at the interface is:

$$v_{1i} = -\frac{1}{2\mu_w}\left(\left(\frac{h_b}{2}\right)^2 - \left(\frac{h_g}{2}\right)^2\right)\frac{\mathrm{d}p}{\mathrm{d}x_1} \tag{IV–51}$$

For the gas phase, the velocity distribution is:

$$v_{1g} = \frac{x_2^2}{2\mu_g}\frac{\mathrm{d}p_g}{\mathrm{d}x_1} + \mathcal{Z}_g \tag{IV–52}$$

And at the interface:

$$v_{1i} = \frac{1}{2\mu_g}\left(\frac{h_g}{2}\right)^2\frac{\mathrm{d}p}{\mathrm{d}x_1} + \mathcal{Z}_g \tag{IV–53}$$

Since the velocity of the two phases at the interface has been assumed to be the same, then equations (IV–51) and (IV–53) may be equated to find $\mathcal{Z}_g$. Thence, from equation (IV–52), we obtain the following velocity profile in the gas phase:

$$v_{1g} = -\frac{1}{2}\left[\frac{1}{\mu_w}\left(\left(\frac{h_b}{2}\right)^2 - \left(\frac{h_g}{2}\right)^2\right) + \frac{1}{\mu_g}\left(\left(\frac{h_g}{2}\right)^2 - x_2^2\right)\right]\frac{\mathrm{d}p_g}{\mathrm{d}x_1} \tag{IV–54}$$

Equations (IV–50) and (IV–54) give the velocity profile in the water and gas phases respectively. To derive the relative permeabilities, it is necessary to calculate the average velocity of each phase over the aperture. For the liquid phase, it gives:

$$\begin{aligned} q_{lL} &= \frac{2}{h_b}\int_{\frac{h_g}{2}}^{\frac{h_b}{2}} v_{1w}\, dx_2 \\ &= -\frac{h_b^2}{12}\left(1-\frac{3}{2}\frac{h_g}{h_b}+\frac{1}{2}\left(\frac{h_g}{h_b}\right)^3\right)\frac{1}{\mu_w}\frac{\mathrm{d}p_w}{\mathrm{d}x_1} \end{aligned} \tag{IV–55}$$

Knowing that $\frac{h_g}{h_b} = \frac{h_b - h_w}{h_b} = 1 - S_r$, we have

$$q_{lL} = -\frac{h_b^2}{12}\left(\frac{S_r^2}{2}(3-S_r)\right)\frac{1}{\mu_w}\frac{\mathrm{d}p_w}{\mathrm{d}x_1} \tag{IV–56}$$

And for the gas phase, we have:

$$\begin{aligned} q_{gL} &= \frac{2}{h_b}\int_0^{\frac{h_g}{2}} v_{1g}\, dx_2 \\ &= -\frac{h_b^2}{12}\left(\frac{\mu_g}{\mu_w}\frac{3}{2}\left(\frac{h_g}{h_b}\right)\left(1-\frac{h_g}{h_b}\right)^2+\left(\frac{h_g}{h_b}\right)^3\right)\frac{1}{\mu_g}\frac{\mathrm{d}p_g}{\mathrm{d}x_1} \\ &= -\frac{h_b^2}{12}\left(\frac{3}{2}\mu_r S_r(1-S_r)(2-S_r)+(1-S_r)^3\right)\frac{1}{\mu_g}\frac{\mathrm{d}p_g}{\mathrm{d}x_1} \end{aligned} \tag{IV–57}$$

where $\mu_r = \frac{\mu_g}{\mu_w}$ is the viscosity ratio. So, the longitudinal flows are

$$q_{lL} = -k_{rw}\,\frac{h_b^2}{12}\,\frac{1}{\mu_w}\frac{\partial p_w}{\partial x_1} \tag{IV–58}$$

and

$$q_{gL} = -k_{rg}\,\frac{h_b^2}{12}\,\frac{1}{\mu_g}\frac{\partial p_g}{\partial x_1} \tag{IV–59}$$

with the following relative permeabilities:

$$k_{rw} = \frac{S_r^2}{2}(3-S_r) \tag{IV–60}$$

$$k_{rg} = (1-S_r)^3 + \frac{3}{2}\mu_r S_r(1-S_r)(2-S_r) \tag{IV–61}$$

Note if μ_r is larger than one, the relative permeability of the non-wetting phase is also larger than unity (lubrication effect). For μ_r equal to one, the sum of the k_r is also equal to one; however, k_r is not equal to saturation as for the X model. In fact, for gas and water two-phase flows, the viscosity ratio is largely lower than one and the second term on the right-hand side of Equation (IV–61) is negligible.

The relative permeability is not equal to the saturation but it is however a function of this variable. A retention curve is therefore required to derive the saturation degree from the primary unknowns of the problem, the water and gas pressures. In the previous part, at the macroscale, the use of the retention curve implies a distribution in the size of the fractures (or capillary tubes). Depending on the capillary pressure, all the fractures are filled with water under a certain size and filled with gas above this size. At the microscale, we are interested in developing a capillary pressure model taking into account a multiphase flow in a single fracture. For this purpose, we take advantage of the natural irregular shape of the fracture wall. Realizing many natural structures are constituted of irregular objects appearing in

a similar way when observed at different scales, a fractal technique [Mandelbrot and Pignoni, 1983] is applied to describe the geometry of the fracture wall.

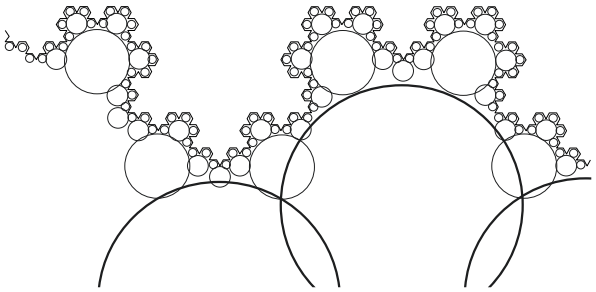

Figure IV–11 – A fracture wall seen as a fractal object with a distribution of open capillary tubes.

Assuming the fracture wall is a fractal object, the space between two walls can be filled by a fractal distribution of capillary tubes with smaller tubes at the walls and larger tubes in the middle (Figure IV–11). Note these tubes are actually open. However, it is not an issue since capillary forces are also able to raise water into narrow open channels or V-shaped grooves [Terzaghi et al., 1996]. This fact was demonstrated by Terzarghi with the apparatus shown in Figure IV–12. *If the highest point of the groove is located below the level to which the surface tension can lift the water, the capillary forces will pull the water into the descending part of the groove and will slowly empty the vessel. This process is known as capillary siphoning* [Terzaghi et al., 1996].

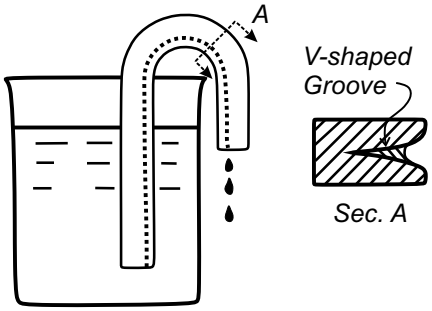

Figure IV–12 – Capillary flow through V-shaped groove. *From* [Terzaghi et al., 1996].

For a tube with a radius r, the capillary pressure is expressed as:

$$p_c \quad \frac{2 \ \cos}{r} \tag{IV–62}$$

where p_c is the capillary pressure, is the surface tension and is the contact angle.

Mathematically, the number of units whose radius is larger than r is represented by a power-law function [Kewen et al., 2004]:

$$r \quad a \ r^{\ D_f} \tag{IV–63}$$

where D_f is the fractal dimension and a a constant of proportionality. Defining the volume of the unit equal to $r^2 l_u$, the number of the units invaded by the non-wetting phase is

$$r \quad \frac{g}{r^2 l_u} \tag{IV–64}$$

Combining Equations (IV–63) and (IV–64):

$$_g \quad a \quad l_u \, r^{\,2 \ D_f} \tag{IV–65}$$

Substituting Equation (IV–62) in Equation (IV–65), the saturation of the non-wetting phase is then:

$$S_{r_g} = \frac{\Omega_g}{\Omega_v} = a' \cdot p_c^{-(2-D_f)} \tag{IV–66}$$

with a' a constant of proportionality. Differentiating Equation (IV–66):

$$\frac{dS_{r_g}}{dp_c} = a'' \cdot p_c^{-(3-D_f)} \tag{IV–67}$$

with a'' a constant of proportionality. Then, assuming p_c tends to p_e when $S_{r_g} = 0$ and p_c approaches infinity when $S_{r_g} = 1 - S_{r,res} - S_{r_g,res}$, we have by integrating Equation (IV–67):

$$\frac{\int_0^{1-S_r-S_{r_g,res}} dS_r}{\int_0^{1-S_{r,res}-S_{r_g,res}} dS_r} = \frac{\int_{p_e}^{p_c} p_c^{-(3-D_f)}}{\int_{p_e}^{+\infty} p_c^{-(3-D_f)}} \tag{IV–68}$$

$$\frac{1-S_r-S_{r_g,res}}{1-S_{r,res}-S_{r_g,res}} = \frac{p_c^{-(2-D_f)} - p_e^{-(2-D_f)}}{p_e^{-(2-D_f)}} \tag{IV–69}$$

$$= 1 - \left(\frac{p_c}{p_e}\right)^{-(2-D_f)} \tag{IV–70}$$

Equation (IV–70) is obtained considering the fractal dimension is lower than 2. Reducing this equation leads to:

$$p_c = p_e \cdot (S_r^*)^{-\frac{1}{2-D_f}} \tag{IV–71}$$

where S_r^* is the normalized saturation. As can be observed, Equation (IV–71) is the same form as the Brooks-Corey equation:

$$p_c = p_e \cdot (S_r^*)^{-\frac{1}{\lambda}} \tag{IV–72}$$

where p_e is the entry capillary pressure and λ is an index representing the size distribution of the capillary tubes. Actually, it is possible these parameters vary with the closure of the fracture. For instance, it is likely the entry capillary pressure decreases with the opening of the fracture. Hence aperture can be used to scale the entry value as

$$p_e = p_{e_0} \cdot \left(\frac{h_{b_0}}{h_b}\right)^m \tag{IV–73}$$

where p_{e_0} is the entry pressure value defined for the aperture h_{b_0} and m is the material parameter of the power law [3].

9.2.3 Hydro-mechanical couplings

The first coupling is the direct dependency of the permeability on the fracture aperture, which is stress-dependent. To take into account the non-smoothness of the fracture walls, an hydraulic aperture is considered rather than a mechanical one. The hydraulic aperture h_b is derived from the mechanical one h according to the following linear relation:

$$h_b = h^{min} + h \tag{IV–74}$$

3. $m = 0$ is equivalent to take a constant entry value while there is a direct relation between the entry value and the inverse of aperture ratio evolution with $m = 1$. Based on experimental results [Seiphoori et al., 2014], Dieudonné found that the power law parameter (linking void ratio and air entry value) was about 3.3 for a given bentonite [Dieudonné, 2016]. This parameter is not further investigated for coal in this work, a constant entry value is used.

It means a fracture which is mechanically closed ($h = 0$) still allows a flow to circulate between the asperities if a non-zero minimal hydraulic aperture h^{min} is defined (Figure IV–13). Actually, an exponential law could also be applied to relate the hydraulic aperture to the mechanical aperture (and the JRC) [Barton et al., 1985, Olsson and Barton, 2001].

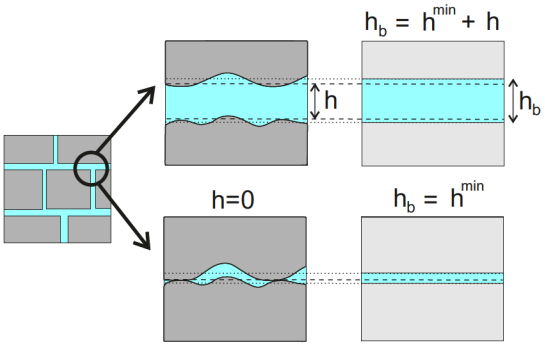

Figure IV–13 – Relation between the hydraulic and the mechanical aperture. *Modified from* [Marinelli et al., 2016].

A second coupling is created by the storage component. Indeed, the variations of the total masses of water $\dot{M}_w$ and gas stored $\dot{M}_g$ in the cleat come from a rheological part, *i.e* the variations of the fluid densities and the saturation of each phase, but also from a geometric part, *i.e* the opening/closure of the gap and the variation of the surface of the discontinuity:

$$\dot{M}_w = \dot{\rho}_w\, S_r\, h_b\, \Gamma + \rho_w\, \dot{S}_r\, h_b\, \Gamma + \underbrace{\rho_w\, S_r\, \dot{h}_b\, \Gamma + \rho_w\, S_r\, h_b\, \dot{\Gamma}}_{\text{Hydro-mechanical coupling}} \tag{IV–75}$$

and

$$\begin{aligned}\dot{M}_g = {} & (\dot{\rho}_{g,f}\,(1-S_r) + \dot{\rho}^d_{g,f}\, S_r + \rho_{g,f}\,(1-\dot{S}_r) + \rho^d_{g,f}\,\dot{S}_r)\, h_b\, \Gamma \\ & + \underbrace{(\rho_{g,f}\,(1-S_r) + \rho^d_{g,f}\, S_r)\,(\dot{h}_b\, \Gamma + h_b\, \dot{\Gamma})}_{\text{Hydro-mechanical coupling}}\end{aligned} \tag{IV–76}$$

where Γ is the surface of the discontinuity.

Inversely, the fluid flow within the cleat also influences its mechanical behaviour. The total pressure σ acting on each side of the fracture can be decomposed into an effective mechanical pressure σ' and a fluid pressure p in the fracture defined by Equation (IV–26). Then, the mechanical constitutive law defined in section 9.2.1 must be treated with reference to the effective stress [2]:

$$\sigma' = \sigma + p \tag{IV–77}$$

rather than the total pressure σ. Note that the application of the effective stress concept at the fracture scale has the advantage that a biot coefficient is not required contrary to Equation (III–112) used in the macroscopic model.

9.3 Continuum formulation

9.3.1 Mechanical problem

For the mechanical problem, let consider two media Ω^1 and Ω^2 representing for instance two matrix blocks (Figure IV–14). Their boundaries are termed Γ^1 and Γ^2 with Γ^1_c and Γ^2_c denoting parts of the boundaries where contact is likely to happen.

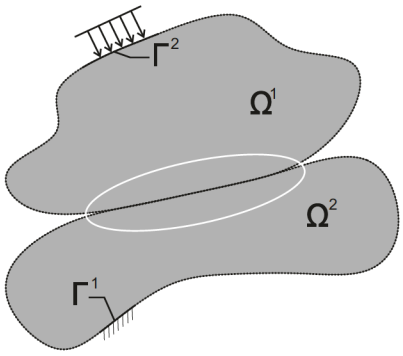

Figure IV–14 – Definition of the mechanical problem.

Each of these solids verifies the mechanical equilibrium Equation (IV–1). Solving the mechanical problem consists in finding the field of displacement verifying the equilibrium under the constraint of a non-zero pressure along the contact zone Γ_c. In this purpose, the weak formulation is obtained considering an admissible virtual velocity field v_i^*. The virtual power principle reads

$$\sum_{k=1}^{2}\left[\int_{\Omega^k}\sigma_{ij}\,\frac{\partial v_i^*}{\partial x_j}\,d\Omega\right]=\sum_{k=1}^{2}\left[\int_{\Gamma^k_{\bar{t}_i}}\bar{t}_i\,v_i^*\,d\Gamma+\int_{\Gamma^k_c}T_i^k\,v_i^*\,d\Gamma\right] \tag{IV–78}$$

where $\bar{t}_i$ are the imposed tractions and T_i^k is the projection of the local stress tensor in global coordinates.

9.3.2 Hydraulic problem

The hydraulic problem considers the presence of the third volume Ω^3 to represent the discontinuity creating a preferential pathway for the fluid flow (Figure IV–15). This volume Ω^3 is bounded by the boundaries $\Gamma^1_{\tilde{q}}$ and $\Gamma^2_{\tilde{q}}$ corresponding to the regions where Ω^1 and Ω^2 are close from each other. The fluid flows between Ω^3 and the solid bodies Ω^1 and Ω^2 are non-classical boundary conditions for these bodies since neither the flow nor the pressure is imposed. Elsewhere, imposed flux boundaries on Ω^1 and Ω^2 are denoted by $\Gamma^k_{\bar{q}}$ with $k=1,2$.

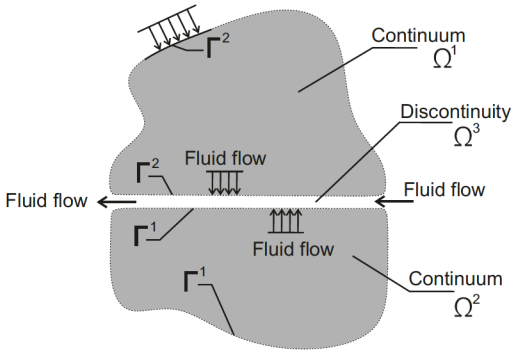

Figure IV–15 – Definition of the flow problem.

For gas, these three volumes verify the hydraulic equilibrium Equations (IV–4) and (IV–21) with a non-classical boundary given by Equation (IV–27). Considering a field of admissible virtual gas pressure p_g^*, the weak form of the virtual power principle is

$$\begin{aligned}&\sum_{k=1}^{3}\left[\int_{\Omega^k}\dot{S}_g\,p_g^*-f^k_{g_i}\frac{\partial p_g^*}{\partial x_i}\,d\Omega\right]=\\&\sum_{k=1}^{3}-\left[\int_{\Gamma^k_{\bar{q}_g}}\bar{q}_g\,p_g^*\,d\Gamma+\int_{\Gamma^k_{\tilde{q}_g}}\tilde{q}_g\,p_g^*\,d\Gamma\right]\end{aligned} \tag{IV–79}$$

where $k = 1,2$ corresponds to the matrix blocks in contact and $k = 3$ to the volume of the cleat. For Ω^1 and Ω^2, the storage term $\dot{S}_g$ is the variation of the adsorbed gas mass. For Ω^3, it is the mass variation given by Equation (IV–76) over a unit surface of discontinuity. $f_{g_i}^k$ is the gas flux, advective or diffusive, inside Ω^k. $\overline{q}_g$ and $\tilde{q}_g$ are the fluid flows along the different boundaries.

The integral over Ω^3 may be transformed into a surface integral over $\Gamma^1_{\tilde{q}_g}$ assuming the inner pressure is constant over the fracture aperture. The flux $f_{g_i}^k$ is replaced by the longitudinal flux f_{g_L} and the flux $\tilde{q}_g$ is replaced by the transverse fluxes $f_{g\,T}^k$. The integral over Ω^3 reads

$$\int_{\Gamma^1_{\tilde{q}_g}} \left[\dot{S}_g \; p_g^* - f_{g_L} \frac{\partial p_g^*}{\partial x_1} \right] \; h_b \; d\Gamma = - \int_{\Gamma^1_{\tilde{q}_g}} \left(f_{g\,T}^1 - f_{g\,T}^2 \right) \; p_g^* \; d\Gamma \tag{IV–80}$$

where the internal longitudinal flux of the gas species f_{g_L} is given by (along x_1):

$$f_{g_L} = \rho_{g,f} \; q_{g_L} + \rho_{g,f}^d \; q_{l_L} + S_r \; J_{l_L}^g \tag{IV–81}$$

and the two transverse fluxes $f_{g\,T}^1$ and $f_{g\,T}^2$ are (along x_2):

$$f_{g\,T}^k = \rho_{g,f} \; q_{gT}^k \tag{IV–82}$$

Similarly for water, equilibrium Equation (IV–20) has to be verified. Considering a field of admissible virtual water pressure p_w^*, and as water transfers are not allowed between the cleat and the matrix, we finally have

$$\int_{\Gamma^1_{\tilde{q}_w}} \left[\dot{S}_w \; p_w^* - f_{w_L} \frac{\partial p_w^*}{\partial x_1} \right] \; h_b \; d\Gamma = 0 \tag{IV–83}$$

where the storage term $\dot{S}_w$ is the mass variation $\dot{M}_w$ over a unit surface of discontinuity and $f_{w_L} = \rho_w \; q_{l_L}$.

The final step is the discretization of these governing equations with finite elements.

10. Finite element formulation

The hydro-mechanical model presented in the previous section is implemented with finite elements for gas saturated conditions in 3D and gas saturated and unsaturated conditions in 2D. The finite element method is extensively described in the literature (see for instance [Zienkiewicz and Taylor, 2000]). It is certainly the case for the continuum elements used to discretize the matrix. Cleats are discretized with elements of zero-thickness which are probably less usual. A particular attention is therefore given to the interface elements. The elements which served as a basis for the cleat discretization are described for water saturated conditions in [Cerfontaine et al., 2015]. This section is mainly focused on the specificities of the formulation of the new model.

10.1 Space and pressure discretization

The governing equations are discretized based on a segment-to-segment approach. A three-node formulation is adopted to described the fluid flow through and within the interface. In 3D, it means twelve nodes are required for the complete representation of the interface (Figure IV–16). There are four nodes with three mechanical degrees of freedom (coordinates x y z) and at least one fluid degree of freedom per node. For the two sides of the interface, this fluid degree of freedom is the adsorbed gas pressure p_g^{Ad} while it is the gas pressure $p_{g\,f}$ for the inner nodes.

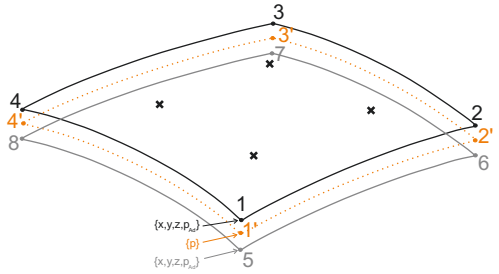

Figure IV–16 – A 3D interface element defined by 12 nodes.

For the matrix, 8-nodes 3D elements are used to match the 3D interface element presented above. The mechanical and hydraulic degrees of freedom are gathered into a vector u_{m_n} of generalised coordinates with m the number of degrees of freedom of the node n. These coordinates are continuously interpolated over the element with classical linear interpolation functions $\mathcal{N}^n$.

10.2 Energetically equivalent nodal forces

10.2.1 External forces

The energetically equivalent nodal associated to the node n are computed numerically for a single interface element from Equation (IV–78) using a Gauss-scheme. The mechanical nodal forces acting on

the boundary of one of the elements are computed as

$$F^{\Omega_e}_{E,m_n} = \sum_{IP} \left[t_m \, \mathcal{N}^{(n)} \, \det(J_{ij}) \, W_G \right]_{IP} \tag{IV–84}$$

with $m = 1,2,3$ the mechanical degrees of freedom and $n = 1,2,3,4$ or $n = 5,6,7,8$ the nodes used to compute the mechanical forces on the first side of the interface Γ_c^1 or the other side Γ_c^2. In both cases, the imposed traction t_m and the components of the Jacobian matrix J_{ij} of the transformation to the isoparametric system are computed with respect to the local system of coordinates of Γ_c^1. W_G is the Gauss weight corresponding to the integration point IP.

For the flow problem, transverse flows involve energetically equivalent external forces related to gas degrees of freedom. For water, it is not considered but for gas, the contribution of the interface to the external virtual power is derived from Equation (IV–80). It is numerically computed on the boundary of Ω^1 according to

$$F^{\Omega_e}_{E,4_n} = \sum_{IP} \left[(f^1_{g\,T} - f^2_{g\,T}) \, \mathcal{N}^{(n)} \, \det(J_{ij}) \, W_G \right]_{IP} \tag{IV–85}$$

with $f^1_{g\,T}$ and $f^2_{g\,T}$ defined by Equation (IV–82) instead of the classical definition based on a difference between the interface inner node and the solid node.

10.2.2 Internal forces

The energetically equivalent internal forces due to the gas flows along the interface are derived from Equation (IV–80) adapted in 3D. It is numerically computed according to

$$F^{\Omega_e}_{I,4_n} = \sum_{IP} \left[\left(\dot{S}_g \, \mathcal{N}^{(n)} - f_{gL\,1} \frac{\partial \mathcal{N}^{(n)}}{\partial x_1} - f_{gL\,2} \frac{\partial \mathcal{N}^{(n)}}{\partial x_2} \right) \det(J_{ij}) \, W_G \right]_{IP} \tag{IV–86}$$

Similarly for water, the energetically equivalent internal forces due to the longitudinal water flows inside the interface f_{w_L} is derived from Equation (IV–83).

10.2.3 Out of balance forces

Internal and external nodal forces are gathered together to compute the global vectors F_{I,m_n} and F_{E,m_n}. Solving the numerical problem consists to obtain the equality between these two vectors. The out of balance forces vector is computed as

$$F_{OB,m_n} = F_{E,m_n} - F_{I,m_n} \tag{IV–87}$$

In order to obtain $F_{OB,m_n} = 0$, generalised coordinates Δu_{m_n} are iteratively corrected by:

$$\Delta u_{m_n} = - \left[\frac{\partial F^t_{OB,l_k}}{\partial u_{m_n}} \right]^{-1} F^t_{OB,l_k} = - \left[K^t_{l_k m_n} \right]^{-1} F^t_{OB,l_k} \tag{IV–88}$$

where $K^t_{l_k m_n}$ is the stiffness matrix at time step t.

Note the fluid flow problem is naturally time-dependent and requires the discretization of time. It is assumed the media in contact are initially in equilibrium at a given time t ($F_{OB,m_n} = 0$) and the equilibrium of the discretized system is then written at $t + \Delta t$ with an implicit scheme.

10.3 Stiffness matrix

The stiffness matrix $K_{l_k m_n}$ is computed analytically by derivation of out of balance forces:

$$K_{l_k m_n} = \frac{\partial F_{OB,l_k}}{\partial u_{m_n}} \tag{IV–89}$$

A description of the components of the stiffness matrix for the interface elements may be found in [Cerfontaine et al., 2015], it was adapted to gas degrees of freedom by taking into account the gas equation of state (IV–24).

Finally, for the continuum elements discretizing the matrix, the shrinkage/swelling due to the adsorbed gas pressure evolution is taken into account like it would be done for thermal dilatation in the code. Thence, from the constitutive Equation (IV–13), the couplings terms of the stiffness matrix accounting for the influence of the adsorbed gas on the mechanics read

$$\frac{\partial F_{OB,i_k}}{\partial p_g^{Ad}{}_n} = \sum_{IP} \left[\frac{1}{3} \beta_\varepsilon \frac{M_{m_g}}{RT} \frac{1}{\rho_{g,std}\, \rho_c} \frac{(1-\nu_m)\, E}{(1+\nu_m)(1-2\nu_m)} \frac{\partial N^{(k)}}{\partial x_i} \det(J_{ij})\, W_G \right] \tag{IV–90}$$

with $i = 1,2,3$ the three mechanical degrees of freedom.

10.4 Implementation in the Lagamine code

For the 3D case, only gas saturated conditions are considered. The coupled finite elements to be used to model the solid bodies and the interface are respectively the CSOL3 and the FAIN3 elements. For the solid bodies, the mechanical part of the model is implemented in the law ELA3G and the hydraulic part in WADG3. These two laws have been created to deal with the swelling behaviour of the matrix blocks due to sorption. For the interfaces, the mechanical law is implemented in the routine INTME3 and the hydraulic law in CLEAT3F1. The routine CLEAT3F1 is created to manage the transfer of the gas from the adsorbed state in the matrix to a free state in the cleats.

The user can employ CSOL2 and the FAIN2 elements to model the same gas saturated conditions in the 2D case. Then, the laws to be used are ELA2G, WADG2, INTME2 and CLEAT2F1. For unsaturated conditions in the cleats, the new elements MWAD2 and CLE22 have to be used respectively for the matrix and for the interfaces. The hydraulic law CLEAT2F2 is then used instead of CLEAT2F1 for the interfaces. The saturation curve and the relative permeability curves are implemented in the routine FKRSAT.

11. Analytical verification

In order to validate the implementation of the model in the finite element code, basic simulations are completed to compare the numerical results to analytical solutions. Actually, many different analytical models were developed in the literature to take into account the hydro-mechanical couplings influencing the permeability evolution [Pan and Connell, 2012]. Most of these models are based on the cleat porosity evolution. The typical model found in the literature is an exponential equation.

11.1 Exponential model

From Equation (IV–33), the permeability governing the fracture flow in Darcy's equation is [1]

$$k_{cleat} = \frac{h^2}{12} \tag{IV–91}$$

Considering a fractured rock with a spacing w between a set of parallel fractures, the equivalent permeability of this set is

$$k = k_{cleat} \cdot \frac{h}{w} = \frac{h^3}{12w} \tag{IV–92}$$

From this cubic law, the permeability evolution may be approximated as [Seidle et al., 1992]:

$$k = k_0 \left(\frac{\phi}{\phi_0} \right)^3 \tag{IV–93}$$

where k is the permeability and ϕ the fracture porosity. The index 0 denotes a reference state.

Furthermore, the porosity evolution is generally expressed in terms of pore and bulk strains, respectively ε_p and ε_b [Cui and Bustin, 2005]:

$$\frac{\mathrm{d}\phi}{\phi_0} = \mathrm{d}\varepsilon_b - \mathrm{d}\varepsilon_p \tag{IV–94}$$

These strains increments may be decomposed into mechanistic and swelling strains increments. Then, the mechanistic strains increments are expressed in terms of stiffness or compressibility and pressure increments (confining and pore pressures) [Zimmerman et al., 1986]. Neglecting the cleat stiffness in comparison to the bulk stiffness and, under the approximation of constant cleat stiffness, Equations (IV–93) and (IV–94) finally give (rock mechanics convention) [Cui and Bustin, 2005, Connell et al., 2010]:

$$\begin{aligned} k = k_0 \cdot \exp \Bigg[-3 \Bigg(& \frac{1}{K_p} \left((\sigma - \sigma_0) - (p - p_0) \right) \\ & + (\varepsilon_{p_s} - \varepsilon_{p_{s0}}) - (\varepsilon_{bs} - \varepsilon_{bs0}) \Bigg) \Bigg] \end{aligned} \tag{IV–95}$$

1. For the sake of simplicity, the hydraulic aperture was assimilated to the mechanical aperture h in these developments.

where k_0 is the reference permeability for the reference stress σ_0 and the reference pore pressure p_0, and K_p is the cleat stiffness [2]. The stress σ includes the boundary conditions and the model may be expanded for different boundaries. The subscript s denotes swelling quantities. In practice, the pore swelling strain ε_{p_s} is difficult to measure and it is sometimes assumed it is equal to the bulk swelling strain ε_{bs} [Cui and Bustin, 2005]. For instance, for reservoir boundary conditions, this assumption leads to the model developed by Shi and Durucan [Shi and Durucan, 2004, Cui and Bustin, 2005]:

$$k = k_0 \cdot \exp\left[\frac{3}{K_p}\left(\frac{\nu_m}{1-\nu_m}(p-p_0) - \frac{E_m}{3(1-\nu_m)}(\varepsilon_{v_s} - \varepsilon_{v_{s_0}})\right)\right] \tag{IV–96}$$

However, Connell *et al* [Connell et al., 2010] suggested the magnitude of ε_{p_s} is higher than ε_{bs} and related the two quantities through a fitting parameter γ:

$$\varepsilon_{p_s} = \gamma \cdot \varepsilon_{bs} \tag{IV–97}$$

More recently, some authors linked the relationship between ε_{p_s} and ε_{bs} to the fracture porosity [Lu et al., 2016, Peng et al., 2017], but it still requires some fitting parameters. In the following, the analytical solution is determined based on the equilibrium between the matrix block and the fracture instead of the bulk volume.

11.2 Analytical solution

Due to the evolution of the pressure in the fracture or the swelling of the matrix, the fracture aperture is not constant:

$$h = h_0 + \Delta h \tag{IV–98}$$

where the subscript 0 denotes the initial configuration and Δ the increment. So, from Equation (IV–92), the permeability evolution is given by:

$$\boxed{k = \frac{(h_0 + \Delta h)^3}{12w}} \tag{IV–99}$$

The fracture aperture is stress-dependent and it is determined stating a stress equilibrium between the fracture and the matrix.

For the fracture, the evolution of the normal effective stress (rock mechanics convention) reads

$$(\sigma - p_{g,f}) = (\sigma_0 - p_{g,f_0}) + \Delta(\sigma - p_{g,f}) \tag{IV–100}$$

where σ is the normal total stress and $p_{g,f}$ is the gas pressure in the fracture. As stated by Equation (IV–14), the variation of the normal effective stress is related to the variation of the fracture aperture through

$$\mathrm{d}(\sigma - p_{g,f}) = -K_n \cdot \mathrm{d}h \tag{IV–101}$$

where K_n is the normal stiffness of the fracture.

For the matrix, the stress evolution reads

$$\sigma_{ij} = \sigma_{ij_0} + \Delta\sigma_{ij} \tag{IV–102}$$

where $\Delta\sigma_{ij}$ is given by the Hooke's mechanical law taking into account the swelling behaviour:

$$\Delta\sigma_{ij} = 2G_m\Delta\varepsilon_{ij} + \lambda_m\Delta\bar{\varepsilon}\,\delta_{ij} + K_m\Delta\varepsilon_{v_s}\delta_{ij} \tag{IV–103}$$

2. The dimension of this stiffness differs from the stiffness used in Equation (IV–14), there are related by $K_p = h \cdot K_n$.

where ε_{ij} is the strain tensor, $\bar{\varepsilon} = \varepsilon_{ij}\delta_{ij}$ with δ_{ij} the Kronecker's symbol, $\Delta\varepsilon_{v_s}$ is the volumetric sorption-induced strain, G_m is the Coulomb's modulus, λ_m is the first Lamé parameter and K_m is the bulk modulus of the matrix. All these elastic moduli may also be replaced by E_m and ν_m, respectively the Young's modulus and the Poisson's ratio:

$$G_m = \frac{E_m}{2(1+\nu_m)} \tag{IV–104}$$

$$\lambda_m = \frac{E_m \nu_m}{(1+\nu_m)(1-2\nu_m)} \tag{IV–105}$$

$$K_m = \frac{E_m}{3(1-2\nu_m)} \tag{IV–106}$$

Thence, Equation (IV–103) can also be written as

$$\begin{aligned}\Delta\sigma_{ij} = &\frac{E_m}{1+\nu_m}\Delta\varepsilon_{ij} + \frac{E_m\nu_m}{(1+\nu_m)(1-2\nu_m)}\Delta\bar{\varepsilon}\,\delta_{ij} \\ &+ \frac{E_m}{3(1-2\nu_m)}\Delta\varepsilon_{v_s}\delta_{ij}\end{aligned} \tag{IV–107}$$

At equilibrium between the fracture and the matrix pressure, the sorption-induced strain $\Delta\varepsilon_{v_s}$ may be expressed in term of pressure in the fracture. For instance, it can be linearly linked to the Langmuir's isotherm:

$$\Delta\varepsilon_{v_s} = \beta_\varepsilon \left(\frac{V_L \cdot p_{g,f}}{P_L + p_{g,f}} - \frac{V_L \cdot p_{g,f_0}}{P_L + p_{g,f_0}} \right) \tag{IV–108}$$

where β_ε is a linear coefficient, and V_L and P_L are the Langmuir's parameters. The analytical solution is not restricted to any particular relationship between the sorption-induced strain. A linear relationship is chosen like it was implemented in the finite element code.

11.2.1 Constant fracture stiffness

First, if a constant normal stiffness is considered for the fracture, then there is a linear relationship between the fracture closure and the normal stress given by Equation (IV–101). Thence, Equation (IV–100) gives

$$\sigma = \sigma_0 + \Delta p_{g,f} - K_n \cdot \Delta h \tag{IV–109}$$

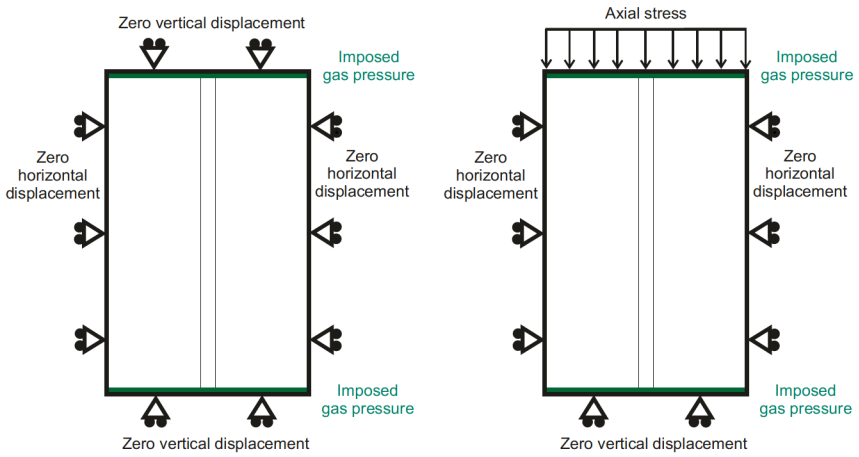

(a) Full rigid boundaries. (b) Reservoir conditions.

Figure IV–17 – One vertical fracture delimited by two half blocks and boundary conditions considered.

Considering a vertical fracture delimited by two half matrix blocks, from Equations (IV–102) and (IV–109), the horizontal equilibrium reads

$$p_{g\,f} \quad K_n \quad h \qquad _{xx} \tag{IV–110}$$

Finally, h is found by solving Equation (IV–110) where $_{xx}$ depends on h through the boundary conditions introduced in Equation (IV–107). Two types are considered, full rigid boundaries and *in situ* reservoir conditions.

11.2.1.1 Full rigid boundaries

With full rigid boundary conditions, the strains in the matrix are $_{xx} \quad \frac{h}{w_0}$ and $_{yy} \qquad _{zz} \quad 0$. Introducing these conditions in Equation (IV–107) directly gives

$$_{xx} \qquad \frac{E_m \;\; 1 \quad _m}{1 \quad _m \;\; 1 \quad 2 \;\; _m} \frac{h}{w_0} \quad \frac{E_m}{3 \;\; 1 \quad 2 \;\; _m} \quad _{v_s} \tag{IV–111}$$

$$M_m \frac{h}{w_0} \quad K_m \quad _{v_s} \tag{IV–112}$$

where $M_m \quad \frac{E_m \;\; 1 \quad _m}{1 \quad _m \;\; 1 \quad 2 \;\; _m}$ is the P-wave modulus of the matrix. Introducing this stress increment into Equation (IV–110), the closure is finally given by

$$\boxed{h \quad w_0 \quad \frac{p_{g\,f} \quad K_m \quad _{v_s}}{K_n \;\; w_0 \quad M_m}} \tag{IV–113}$$

The model for the permeability evolution is finally obtained introducing this equation into Equation (IV–99).

11.2.1.2 Reservoir boundaries

In situ, rigid boundaries should be considered only horizontally: $_{xx} \quad \frac{h}{w_0}$ and $_{yy} \quad 0$, while vertically we have $_{zz} \quad 0$. From these boundary conditions, we can write

$$\begin{aligned} &\frac{1}{E_m} \quad _{xx} \quad \frac{_m}{E_m} \quad _{yy} \quad \frac{1}{3} \quad _{v_s} \quad \frac{h}{w_0} \\ &\frac{1}{E_m} \quad _{yy} \quad \frac{_m}{E_m} \quad _{xx} \quad \frac{1}{3} \quad _{v_s} \quad 0 \end{aligned} \tag{IV–114}$$

Then, by solving this system of equations, we find the following stress increment:

$$_{xx} \quad \frac{E_m}{1 \quad \frac{2}{m}} \frac{h}{w_0} \quad \frac{E_m}{3 \;\; 1 \quad _m} \quad _{v_s} \tag{IV–115}$$

Hence, introducing this stress increment in Equation (IV–110), the closure is given by

$$\boxed{h \quad w_0 \quad \frac{p_{g\,f} \quad \frac{E_m}{3 \;\; 1 \quad _m} \quad _{v_s}}{K_n \;\; w_0 \quad \frac{E_m}{1 \quad \frac{2}{m}}}} \tag{IV–116}$$

The case of a horizontal fracture with vertical stresses is like introducing a zero stress change in Equation (IV–110) to write the vertical equilibrium. As a result, the fracture aperture variation is directly $h \quad \frac{p_{g\,f}}{K_n}$. It means this fracture is not impacted by the swelling but only the variation of fluid pressure.

11.2.2 Hyperbolic fracture stiffness

The evolution of the normal stiffness with the fracture closure given by Equation (IV–15) is now considered. Then, integrating Equation (IV–101) gives this time

$$\Delta(\sigma - p_{g,f}) = -\int_{h_0}^{h} \frac{K_n^0}{\left(1+\frac{h-h_0}{h_0}\right)^2}\,\mathrm{d}h = -\frac{K_n^0\, h_0}{h}\cdot\Delta h \tag{IV–117}$$

Then, the following equation has to be solved:

$$\Delta p_{g,f} - \frac{K_n^0\, h_0}{h}\cdot\Delta h = \Delta\sigma_{xx} \tag{IV–118}$$

Considering full rigid boundaries, Equation (IV–112) is introduced in Equation (IV–118) and the second order equation to solve to find Δh is

$$\Delta p_{g,f} - \frac{K_n^0\, h_0}{h_0+\Delta h}\cdot\Delta h = M_m\frac{\Delta h}{w_0} + K_m\Delta\varepsilon_{v_s} \tag{IV–119}$$

Considering reservoir boundaries conditions as described above, Equation (IV–115) is introduced in Equation (IV–118), it gives

$$\Delta p_{g,f} - \frac{K_n^0\, h_0}{h_0+\Delta h}\cdot\Delta h = \frac{E_m}{(1-\nu_m^2)}\frac{\Delta h}{w_0} + \frac{E_m}{3(1-\nu_m)}\Delta\varepsilon_{v_s} \tag{IV–120}$$

The permeability models for the two types of boundaries are obtained introducing the solutions of these second degree equations into Equation (IV–99) and keeping the positive permeability. It is plotted in the following section for a given set of parameters.

11.3 Analysis and validation

In this section, the analytical solution of the permeability evolution developed above is compared to the numerical simulation to verify the implementation of the model. But first, the evolution of the internal swelling stress with injection pressure obtained numerically under constant volume conditions is compared to the expected evolution. Finally, the transient behaviour is also investigated comparing the evolution of the average pressure in the matrix with a shape factor solution (section 6.2.3).

11.3.1 Internal swelling stress

If the matrix is considered alone with full rigid boundary conditions, the internal stress induced by the constrained swelling is, from Equation (IV–112), given by

$$\Delta\sigma = K_m\,\Delta\varepsilon_{v_s} \tag{IV–121}$$

with $\Delta\varepsilon_{v_s}$ determined with Equation (IV–108).

Parameter		Value	
Young's modulus	E_m	1.21	GPa
Poisson's ratio	ν_m	0.16	
Langmuir's volume	V_L	0.054	m^3/kg
Langmuir's pressure	P_L	1	MPa
Swelling strain coefficient	β_ε	0.8	kg/m^3

Table IV–1 – Model parameters used for the comparison between the numerical and analytical solutions.

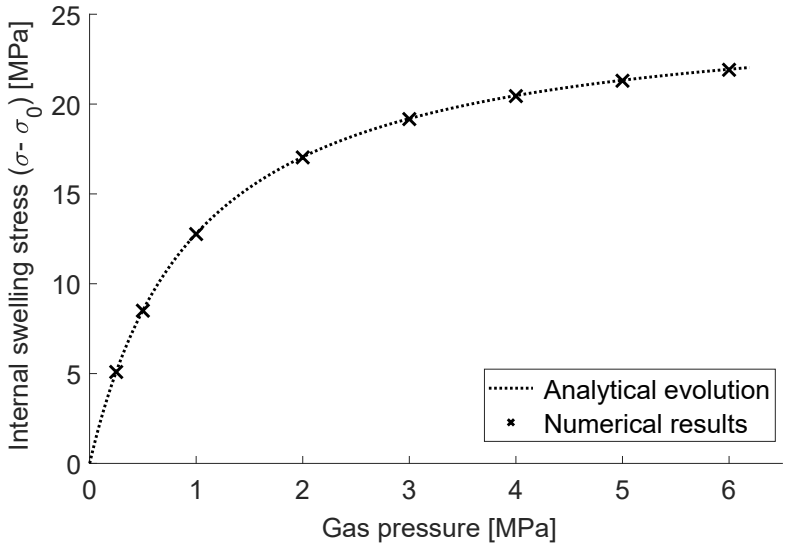

Figure IV–18 – Evolution of the internal swelling stress in the matrix with the gas pressure.

Figure IV–18 compares the evolution of the analytical evolution of the internal swelling stress with numerical results computed for different injection pressures. The numerical model reproduces the expected behaviour. The parameters used for this comparison are given in Table IV–1, the sorption and mechanical parameters of the matrix come from the experimental study carried out in laboratory.

Now considering fractures, the swelling stresses of the matrix are partially converted into fracture closure affecting the permeability.

11.3.2 Permeability evolution

The geometry shown in Figure IV–17 with some matrix blocks separated by a fracture is considered to illustrate the permeability evolution for constant volume and reservoir boundary conditions. Using the parameters given in Tables IV–1 and IV–2, Figures IV–19 and IV–20, considering respectively a constant fracture stiffness and a hyperbolic variation of the stiffness, present these permeability evolutions obtained for the two different boundary conditions The decrease of the permeability is logically more important with the full rigid boundaries than when the displacement is allowed vertically.

Parameter		Value	
Matrix block width	w_0	0 003	m
Cleat aperture	h_0	18 10 ^{6}	m
Cleat normal stiffness	K_n^0	1 66 10^6	MPa.m ^{1}

Table IV–2 – Geometry and fractures parameters used for the comparison between the numerical and the analytical solutions.

The numerical results (stabilized permeability) are compared to the analytical solutions to validate the implementation of our model. Each numerical result represents the stabilized permeability after the diffusion of the gas in the matrix from the increase of the pressure in the fracture, what induces the swelling gradually. This transient aspect is discussed in the next section.

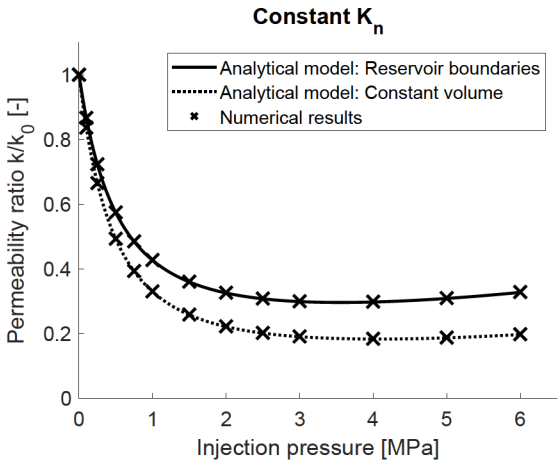

Figure IV–19 – Constant fracture stiffness: Numerical results *versus* analytical model.

For the hyperbolic evolution of the fracture stiffness in Figure IV–20, the initial fracture aperture and stiffness were taken the same as the constant case. As the stiffness increases with the closure of the fracture, the permeability is less decreased compared to the results obtained with the constant stiffness behaviour in Figure IV–19.

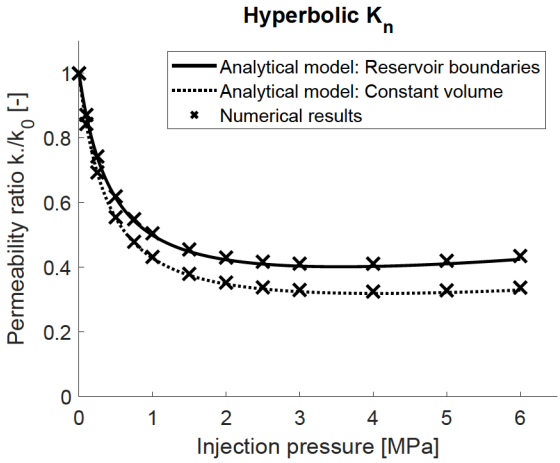

Figure IV–20 – Hyperbolic fracture stiffness: Numerical results *versus* analytical model.

At low injection pressures, the aperture evolution is more impacted by the swelling than the effective stress in the fracture. It is interesting to observe the permeability evolution presents then a minimum before the permeability rebounds. Indeed, the rate of the swelling increment is decreasing since a Langmuir-like equation is considered. The rebound pressure can be estimated differentiating the analytical model and equalizing to zero. For the constant stiffness, the rebound pressure for the full rigid boundaries is given by

$$p_{rb} = \sqrt{K_m \cdot \beta_\varepsilon \cdot V_L \cdot P_L} - P_L \tag{IV–122}$$

which is 4.06MPa in Figure IV–19. For the reservoir boundary conditions in Figure IV–20, it is

$$p_{rb} = \sqrt{\frac{E_m}{3(1-\nu_m)} \cdot \beta_\varepsilon \cdot V_L \cdot P_L} - P_L \tag{IV–123}$$

which is 3.55MPa with the parameters used in Figure IV–19.

Finally, Figure IV–21 compares the constant fracture stiffness model for reservoir conditions with the Shi & Durucan SD-model given by Equation (IV–96) for the same conditions. In this equation, the

stiffness K_p is taken to be $K_n \cdot h_0$. The exponential law from Shi & Durucan is close to the analytical solution presented above.

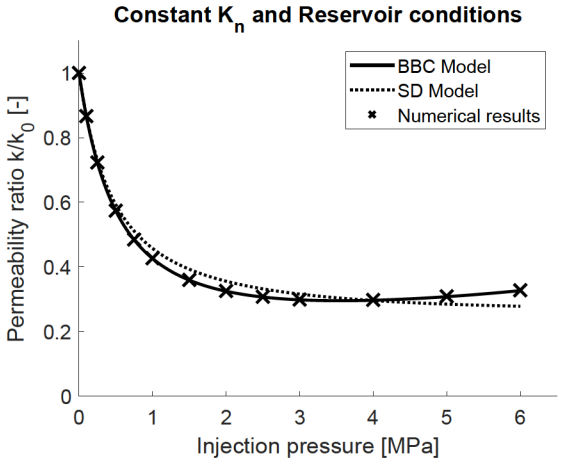

Figure IV–21 – Constant fracture stiffness and reservoir boundary conditions: Comparison with the model from Shi & Durucan (Equation IV–96 with $K_p = h_0 \cdot K_n$).

11.3.3 Transient behaviour

As stated in section 6.2.3, the differential equation governing the evolution of the mean gas pressure in the matrix is

$$\dot{p}_g^{Ad}(t) = -\frac{1}{\mathcal{T}} \cdot \left(p_g^{Ad}(t) - p_g^{Ad^{lim}}(t) \right) \tag{IV–124}$$

where $\mathcal{T}$ is a sorption time which depends on the size of the matrix blocks and the diffusion coefficient. This equation assumes that the variation in the pressure rate over time is constant at all points, *i.e.* pseudo-steady state conditions.

The solution for a constant $p_g^{Ad^{lim}}$ is the following function:

$$p_g^{Ad}(t) = \left(p_g^{Ad}{}_0 - p_g^{Ad^{lim}} \right) \cdot \exp\left(\frac{-t}{\mathcal{T}} \right) + p_g^{Ad^{lim}} \tag{IV–125}$$

As it is more likely that the loading is not applied instantaneously, the solution for a linear evolution of $p_g^{Ad^{lim}}$ with a slope a is also given below:

$$p_g^{Ad}(t) = -a\,\mathcal{T}\,\exp\left(\frac{-t}{\mathcal{T}} \right) + a\,(\mathcal{T} - t) + p_g^{Ad}{}_0 \tag{IV–126}$$

Figure IV–22 compares the two functions given by Equations (IV–125) and (IV–126). Switching from constant to linear loading induces an inflection point in the mean gas pressure evolution.

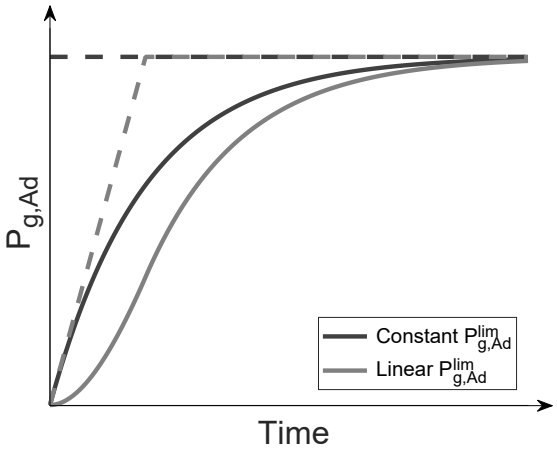

Figure IV–22 – Analytical homogenous evolution of the adsorbed gas pressure for a constant and a linear limit pressure.

Actually, the loading we want to carry out numerically is a linear variation of the fracture pressure, it corresponds therefore to a hyperbolic evolution of $p_g^{Ad^{lim}}$ due the form of the sorption isotherm. Figure IV–23 compares the linear loading with the hyperbolic loading. The solution of this second loading is a piecewise function obtained by interpolating the hyperbolic variation in linear increments over a large number of intervals.

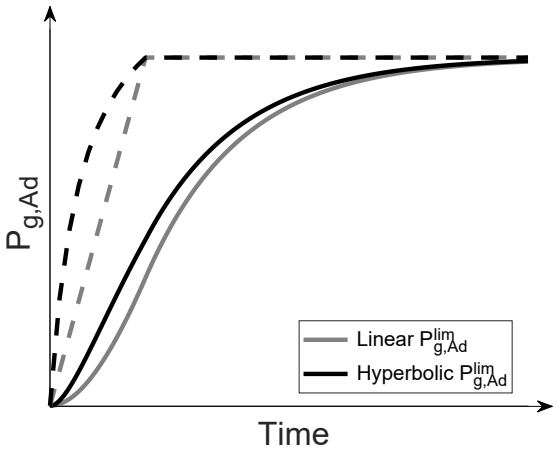

Figure IV–23 – Analytical homogenous evolution of the adsorbed gas pressure for a linear and a hyperbolic limit pressure.

A purely hydraulic simulation is performed on $1cm$ blocks with a diffusion coefficient of $2\ 10^{-11} m^2\ s$. With these parameters, Kazemi [Kazemi et al., 1976] predicts a sorption time of 2 9 days while it is 7 2 days according to Lim and Aziz [Lim and Aziz, 1995]. Figure IV–24 presents the solutions with these two sorption times for an increase of the fracture pressure until $3MPa$ in 10 days using the Langmuir's parameters from Table IV–1. After 10 days, the limit pressure imposed is thus $p_g^{Ad^{lim}}$ 6 $5MPa$. The results from the numerical simulation is presented in the same figure. The numerical values are obtained averaging the gas pressure distribution over the block as the pressure does not evolve homogeneously in the block. Figure IV–25 shows for instance the distribution after 5 days. It appears in this case that the evolution of the mean gas pressure in the blocks lies between the solutions given by the two sorption times mentioned above. The median sorption time of 5 05 days fits fairly well the numerical results. The slight difference is explained by the fact we compare an average evolution with an analytical solution describing the homogeneous gas pressure evolution in the matrix block characterized by a given sorption time parameter and assuming pseudo-steady state conditions.

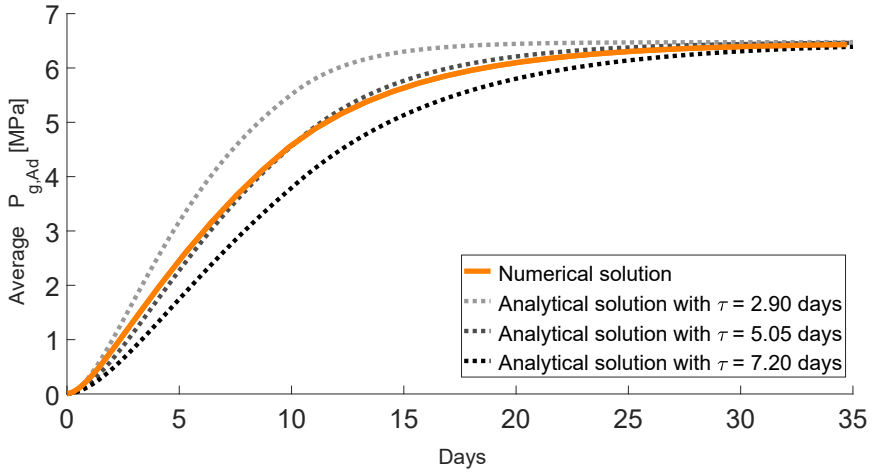

Figure IV–24 – Comparison of the mean gas pressure evolution with the analytical homogenous evolution with different sorption times.

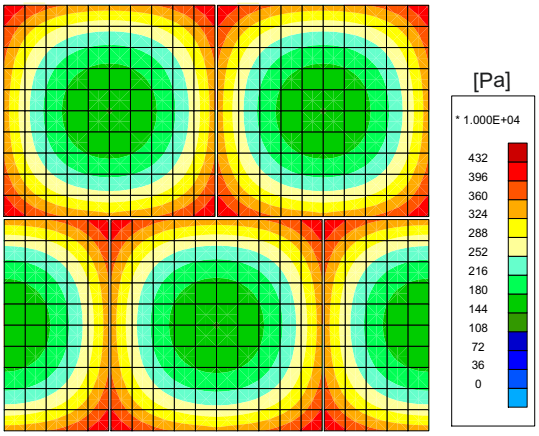

Figure IV–25 – Adsorbed gas pressure in the matrix after 5 days.

12. REV modelling

The interest of the numerical model is that it can be used on complex geometries and it easily takes into account the anisotropy coming from the material and the boundary conditions. Moreover, the transient behaviour is also modelled.

In the following, a purely mechanical test is first modelled to reproduce the non-linear behaviour experimentally observed for fractured media. Then, a coupled test is carried out by modelling the injection of carbon dioxide in the material. The permeability evolution with the gas pressure is computed for different boundary conditions.

12.1 Mechanical modelling

The first numerical test carried out is a compression test. For the geometry, a quarter cylinder with a 5 3cm diameter and a 7 7cm height is meshed. Three horizontal cleats define four regular blocks (Figure IV–26). Concerning the boundary conditions, normal zero-displacements are imposed at the bottom and inner boundaries while there are free displacements at the outer boundaries. At the top boundary, a vertical strain rate of 10E-6 s is imposed. The confinement is 10kPa.

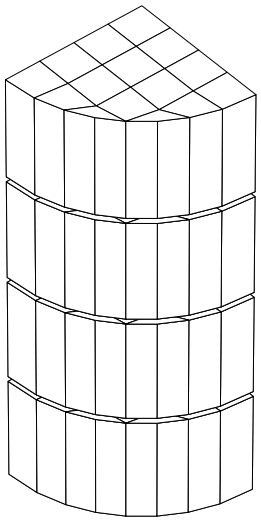

Figure IV–26 – Geometry of the sample for the mechanical test.

Figures IV–27a and IV–27b represent the decrease of the aperture of the middle horizontal fracture and the corresponding increase of the normal stiffness during the test. This leads to the non-linear stress-strain curve represented in Figure IV–28, the behaviour is elastic as the state of the fractures is stick for this test. Mechanical parameters used for the simulation are defined in Table IV–3. The normal stiffness of the fracture and the Young's modulus were chosen to fit the experimental data obtained with the $B5s2$ test (Part II).

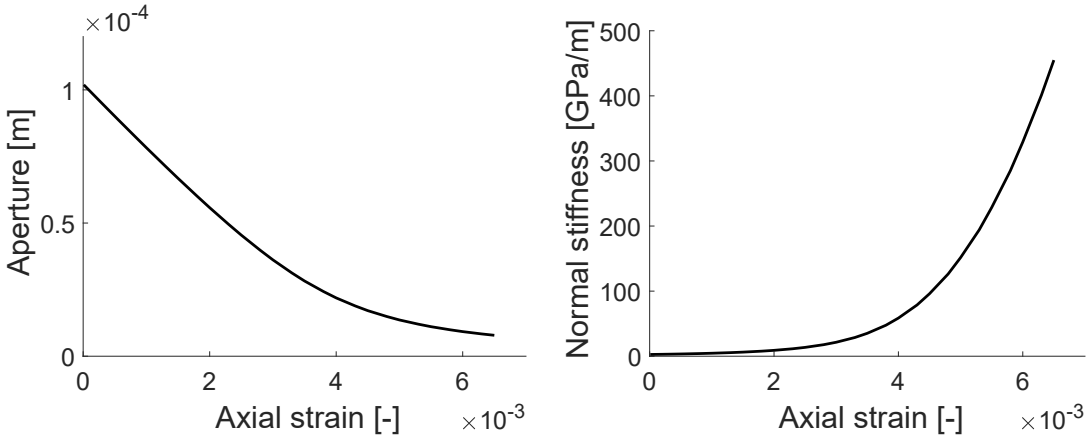

(a) Fracture aperture evolution (b) Normal stiffness evolution.

Figure IV–27 – Evolutions of remarkable variables during the mechanical test.

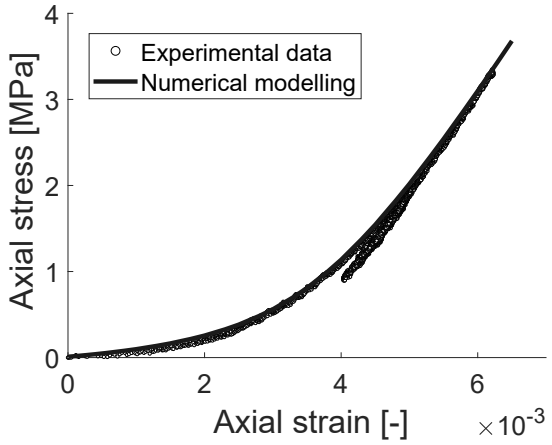

Figure IV–28 – Stress-strain curve 10kPa confinement: Simulation *versus* experimental data.

Parameter		Value	
Matrix			
Young's modulus	E_m	1 3E9	Pa
Poisson's ratio	$_m$	0 13	
Width (vertical)	w	0 07679 4	m
Cleat			
Initial normal stiffness	K_n^0	2 5E9	$Pa\ m$
Initial mechanical aperture	h_0	106E-6	m

Table IV–3 – Mechanical parameters used to fit the $B5s2$ triaxial tests.

Note that the geometry with 3 fractures was arbitrarily chosen. The set of parameters which properly fit the data is therefore not unique since more fractures with a smaller aperture could give the same result. The initial aperture is determined observing that the non-linear axial strain (due to fractures in the model) is about 3 5 10 ^{3}, the total closure of the fractures should be therefore around 270μm, *i.e.* 90μm per fracture. Then, the normal stiffness is chosen to best fit the curvature of the strain-stress curve. Given

the confinement of $10kPa$, the actual initial aperture and normal stiffness are given Table IV–4. This set of parameters is also confronted to data obtained with different confinements in Figure IV–29.

$\sigma' = 0MPa$	$\sigma' = 10kPa$	$\sigma' = 500kPa$	$\sigma' = 1MPa$	$\sigma' = 2MPa$
$h = 106\mu m$	$h = 102\mu m$	$h = 37\mu m$	$h = 22\mu m$	$h = 12\mu m$
$K_n = 2.5GPa/m$	$K_n = 2.7GPa/m$	$K_n = 20.8GPa/m$	$K_n = 57.0GPa/m$	$K_n = 182.6GPa/m$

Table IV–4 – Initial apertures and normal stiffnesses for different confinements.

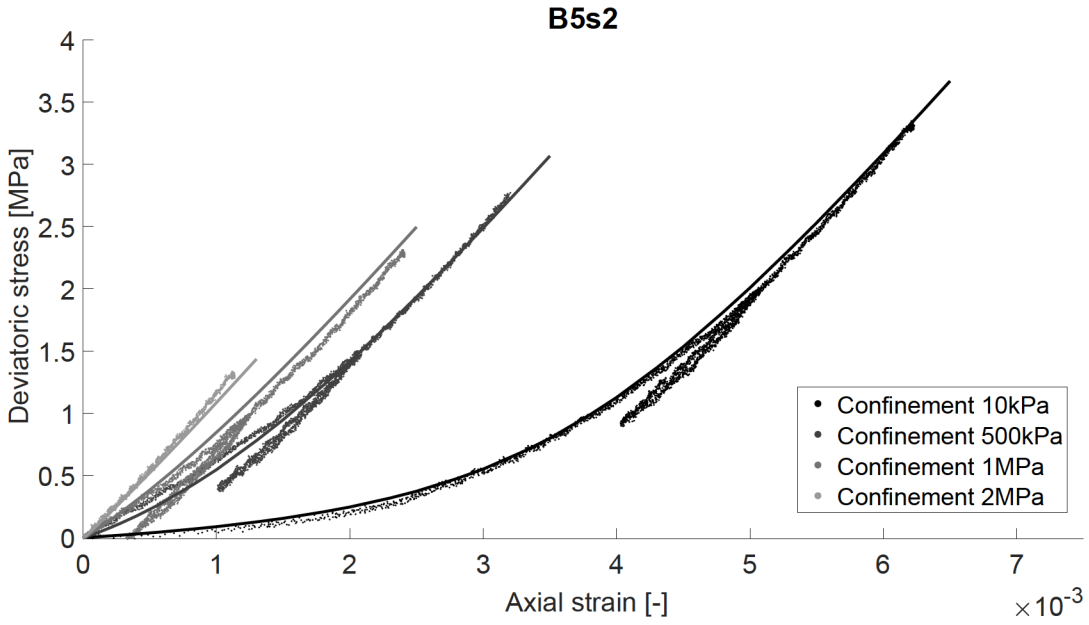

Figure IV–29 – Stress-strain curves: Simulations *versus* experimental data.

12.2 Hydro-mechanical modelling

Figure IV–30 presents the geometry and the boundary conditions considered for the numerical modelling of the permeability evolution. A representative elementary volume (REV) made up of five blocks and two half-blocks arranged in three rows is meshed. The width of the blocks is 3mm. The axial stress applied for the reservoir boundary conditions is 4MPa. In both cases, the initial internal stress in the material is 4MPa. The parameters used for the numerical modelling are the ones given in Table IV–1. In addition, a diffusion coefficient of $10^{-10}m^2/s$ is considered. For this modelling, the gas pressure is increased in few hours to the wanted injection pressure at the end of every fracture on the boundaries (Figure IV–30).

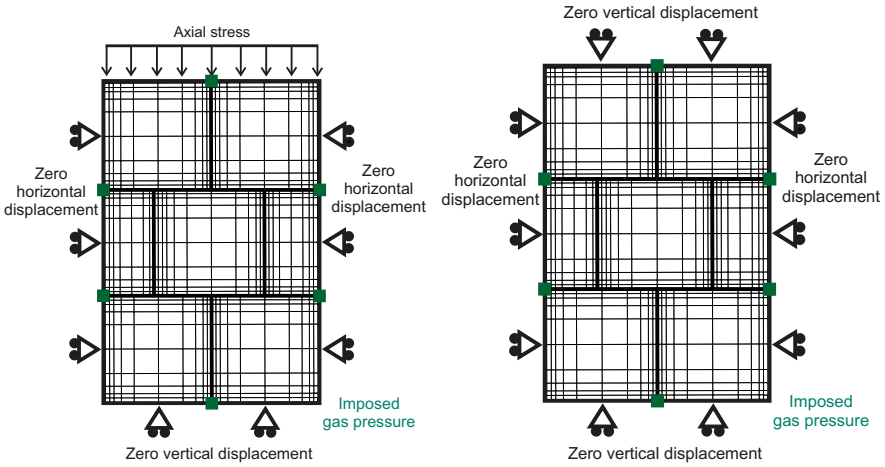

(a) Reservoir conditions. (b) Full rigid boundaries.

Figure IV–30 – REV geometry and boundary conditions considered for the modelling.

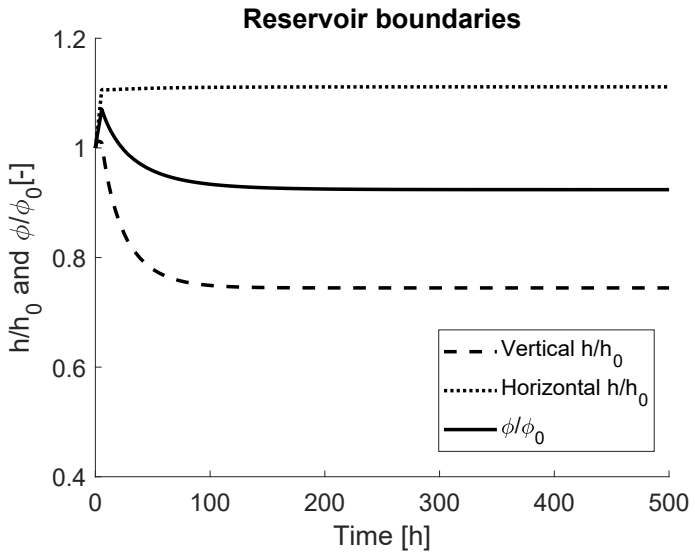

Figure IV–31 – Vertical and horizontal fracture aperture evolution with time (injection pressure: 3MPa).

As the reservoir boundary conditions are anisotropic, the response of the horizontal fractures differs from the vertical fractures. Figure IV–31 presents the fracture aperture evolution with time of the vertical and horizontal fractures. The injection pressure was increased to 3MPa and then maintained constant. An initial opening of the fractures is observed horizontally and vertically during the loading phase, it is the effect of the effective stress decrease. Then, as the material is constrained horizontally, the vertical fractures are closing with the swelling. In contrast, the material is not constrained vertically and the horizontal fractures are opening. The global porosity evolution lies between the vertical and horizontal aperture evolutions.

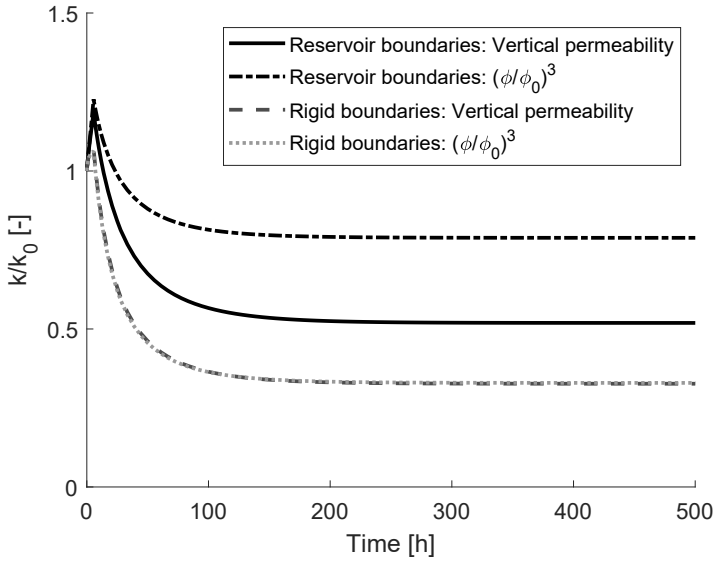

Figure IV–32 – Equivalent vertical permeability evolution with time compared to the porosity model (injection pressure: 3MPa).

From the curves in Figure IV–31, one can understand an analytical model based on the porosity evolution is not able to correctly represent the permeability evolution for both the vertical and horizontal fractures. Indeed, the porosity is a scalar variable while the permeability may be anisotropic, it is a tensor. Figure IV–32 represents the evolution of the vertical permeability of the REV. This permeability was computed using a weighted harmonic average following the path of the fluid in the vertical and horizontal fractures to flow from the bottom to the top of the REV. As expected, the permeability evolution based on the porosity evolution largely deviates when anisotropic boundaries are considered. However, in the case of full rigid boundaries, the vertical and horizontal apertures are closing in the same way and the porosity model perfectly fit the permeability evolution.

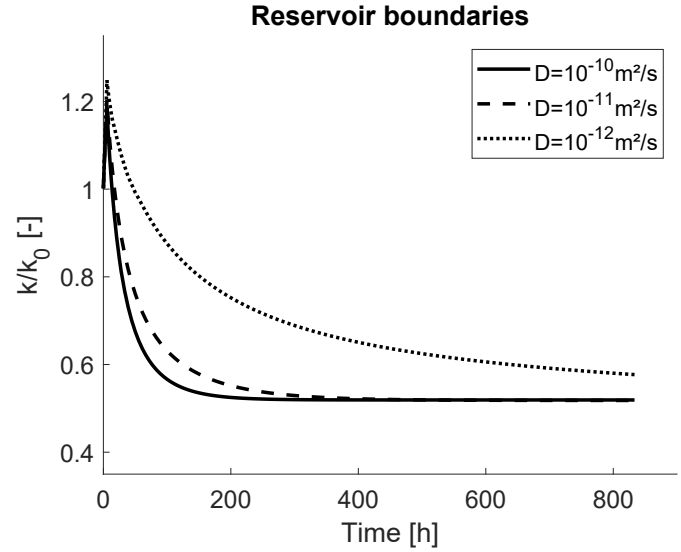

Figure IV–33 – Equivalent vertical permeability evolution with time for different diffusion coefficients (injection pressure: 3MPa).

The previous figures are presenting the evolution of the permeability evolution with time. This transient behaviour depends actually on the diffusion coefficient in the matrix. For lower values of this

coefficient, the swelling occurs more slowly and the permeability decreases more slowly (Figure IV–33). It tends towards the same stabilized permeability value.

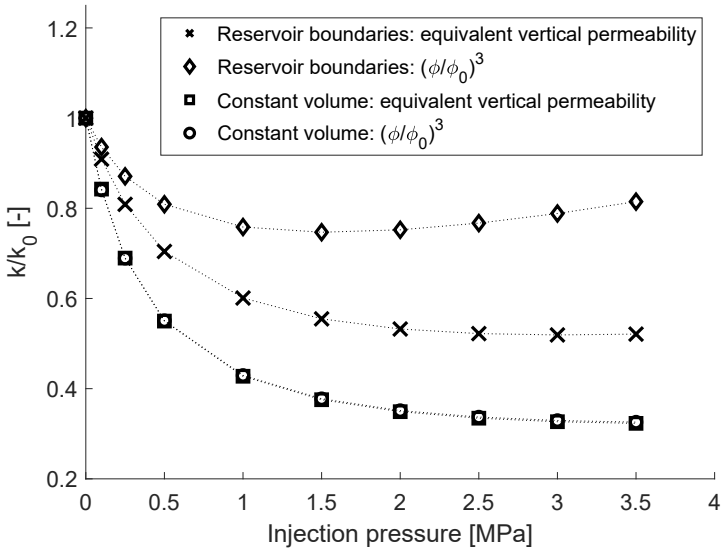

Figure IV–34 – Permeability evolution with the pore pressure.

Figure IV–34 represents the (stabilized) permeability evolution with the pore pressure. Each result was obtained simulating the permeability evolution with the swelling for different injection pressures. The gas slippage phenomenon was not considered in these simulations in order to only highlight the effects of the swelling and the effective stress. As already noticed, the porosity model is not adequate to represent the permeability evolution in reservoir boundary conditions, it underestimates the decrease of the vertical permeability since the porosity integrates the opening of the horizontal fractures, what predicts a rebound pressure happening already at low pressure. It is therefore wiser to consider full rigid boundaries when applying a porosity model. The use of the numerical model avoids this problem for any geometry.

Conclusions Part IV

A hydro-mechanical model is developed at the scale of the coal constituents to distinguish the hydro-mechanical behaviour of the matrix and the cleats. For the matrix, a simple isotropic linear elastic law is used for the mechanical behaviour and a diffusion law is considered for the gas flow. The swelling/shrinkage of the matrix is linked to its gas content and, depending on the boundary conditions, this sorption-induced strain may impact the fracture aperture. It is considered that the normal stiffness evolves with the fracture closure. This closure modifies the permeability of the fracture and impacts the fluid flow in the fracture. As a multi-phase flow may be encountered in the cleats in the context of coalbed methane recovery, a full model was presented for unsaturated conditions. The Langmuir's isotherm is innovatively included in the gas transfer between the cleats and the matrix.

The implementation of the model was verified by comparison between some stabilized permeability values obtained numerically for different CO_2 injection pressures and the analytical solution of the problem. The analytical model traduces the physics and the experimental observations, it is solely based on a matchstick model, the Hooke's law, a sorption-induced strain law and the effective stresses concept. The analytical solution was developed for different boundary conditions and for different expressions of the normal stiffness of the fracture. The constant stiffness case is also compared to a classical exponential model derived in the literature from the bulk deformation of the material.

The reader may be surprised the model is not confronted with the evolution of the permeability obtained in the laboratory (Part II) when a laboratory scale model was just presented. Actually, there are several reasons why this exercise in not performed. The aim of the tomography imaging was to reveal the cleat network of the material, but it appeared some fractures were mineralized. Only 2D sections were available to observe a complex structure of opened fractures and it makes impossible to validate the model in a deterministic way. Then, the type of boundary conditions used in laboratory also makes it difficult to reproduce the observed relationship between the gas pressure and the permeability. Indeed, with independent matrix blocks under confinement, the model does not predict a fracture closure with the swelling of the blocks but an increase of the total volume. The decrease in permeability actually happens since the blocks are not clearly separated in the real 3D sample. Attaching the blocks at some points in the modelling allows to reproduce a decrease of the permeability but it introduces an unknown parameter. Last but not least, considering zero vertical displacement with lateral confinement, horizontal fractures are highly affected by the swelling of the matrix. Since matrix blocks are likely to be staggered, the vertical permeability evolution may paradoxically be more dependent on the horizontal fractures than the vertical ones with this combination of boundaries. The experimental part of the thesis has been useful to question our understanding of the model but for the reasons mentioned above, the numerical permeability results are only compared with an analytical solution of the permeability evolution.

Finally, the model was used for the modelling of a representative elementary volume made up few blocks. This REV combines horizontal and vertical fractures that impacts differently the permeability evolution if anisotropic boundaries conditions are encountered. In this case, it was shown that models based on the porosity evolution largely deviates from the direct fracture aperture model, such it is supposed to be in the reservoir. Note the computational cost of the direct modelling of the full microstructure would be highly expensive at the scale of the reservoir. However, the model presented in this work is very useful for the modelling of the representative elementary volume which, using homogenization

techniques, would define the macroscale behaviour of the material [Marinelli et al., 2016, Argilaga et al., 2016]. This microscale model has therefore now to be integrated into a multi-scale approach to be able to model gas flows at the reservoir scale.

Part V

Multiscale

Introduction Part V

A constitutive microscale model has been extensively described in the previous part of the thesis. For the mechanical behaviour, a simple linear elastic constitutive law was introduced for the matrix blocks (section 9.1.1) while a non-linear stress-strain relationship was used for the interfaces (section 9.2.1). Concerning the hydraulic behaviour, gas diffusive fluxes were considered and modelled by a Fick's law in the matrix (section 9.1.2) while a channel flow based on the Navier-Stokes equations was used for the multiphase flow in the cleats (section 9.2.2). This microscale model has now to be integrated into a multiscale approach to be able to model a production or storage scenario at the reservoir scale. The microscale model is used for the REV boundary value problem (Figure V–1) and the homogenization from the microscale to the macroscale avoids the use of some constitutive laws at this scale.

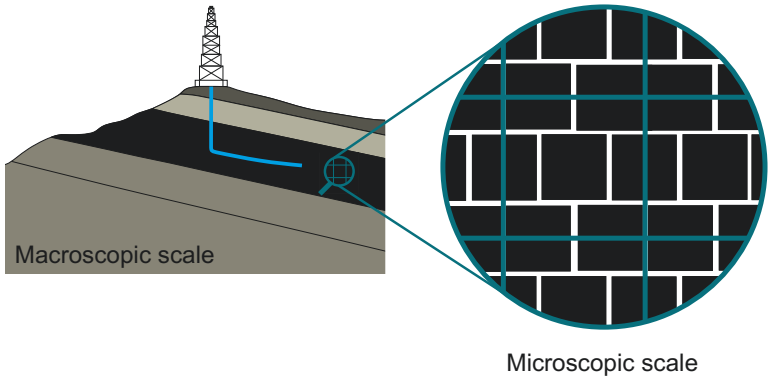

Figure V–1 – Multiscale approach.

The first section outlines the Finite Element Square Method. This method is then applied to develop a hydro-mechanical model with multiphase flows in a coal reservoir. In order to integrate the microscale model in the doublescale scheme and compute a consistent stiffness matrix for the macroscale, some adaptions of the microscale model are required. For instance, the REV boundary value problem is formulated under steady-state conditions given the separation of the scales between the microscale and the macroscale. Thus, a double porosity effect is not directly taken into account by the modelling of diffusive flows in he matrix but by introducing a sorption time coefficient in the macroscopic storage term. Finally, 2D-axisymmetric conditions are used for the modelling of a well production scenario.

13. The Finite Element Square Method

13.1 A multiscale modelling approach

Different scale-approaches can be adopted for modelling heterogeneous media such as geomaterials or composite materials:

1. A macroscopic approach: the medium is treated as homogeneous on a coarse scale (denoted by L) with constitutive laws developed to represent the whole behaviour of the material.

In the case of geomaterials, the mixture theory [Bowen, 1980], for instance, can be used to take into account the presence of one or several fluids percolating inside the solid skeleton, which influences the behaviour of the mixture. Using a finite element method, one only needs to model the macroscopic scale. This approach was followed at the beginning of this thesis. It is quite easy to use but it is more difficult to precisely take into account the interactions between the phases and the microscopic constituents, especially when the microstructure plays a major role.

2. A microscopic approach: the whole structure, including the heterogeneities, is represented and directly modelled. The microscopic constituents (with a characteristic length l) are described by their own constitutive equations.

This approach, used in the previous part of the thesis, relies on a brute computational force. However, the ratio $l \ll L$ is typically very small and modelling sizeable problems entirely on the microscale is not realistic since it leads to giant computations. As direct computation is often not possible with a reasonable amount of time, several homogenization techniques have been created to insert the microscopic constitutive model at the macroscopic level. It is the multiscale approach, which is followed in the present part of the thesis.

3. A multiscale approach: the macroscopic response is not based on closed-form constitutive equations but is derived from the local description of the material using homogenization techniques.

The mathematical homogenization theory [Bensoussan et al., 1978] is one of the suitable frameworks for the resolution of two-scale problems. It is based on a double-scale asymptotic expansion of the variable field on the ratio $l \ll L$. Then, variational principles are used to bridge the gap between the two scales. It is assumed the microstructure is locally formed by the spatial repetition of a suitable very small part of the whole microstructure and the material properties are periodic functions of the microscopic spacial parametrization [Fish and Wagiman, 1993, Schröder, 2014]. Fundamentals of this theory is documented in [Bensoussan et al., 1978, Sanchez-Palencia and Zaoui, 1985]. In practise, the analytical homogenization is usually restricted to very simple microscopic geometries.

An alternative method to analytical homogenization is numerical homogenization [Kouznetsova et al., 2001]. The material behaviour at the macroscale results from the modelling of a representative elementary volume (REV) which contains a detailed model of the material microstructure. The macroscopic phenomenological constitutive law is replaced by suitable averages over the REV. Indeed, the global response of the REV to the deformation, dictated by the macroscale local deformation, serves as a numerical constitutive law for the macroscale.

The analysis on the REV level can be realised using different methods: the finite element method [Terada and Kikuchi, 1995, Smit et al., 1998, Miehe et al., 1999, Feyel and Chaboche, 2000, Kouznetsova et al., 2001, Massart, 2003, Özdemir et al., 2008, Larsson et al., 2010b, Su et al., 2011, Frey et al., 2013] , the discrete element method (DEM) [Nitka et al., 2011, Nguyen et al., 2014], the Voronoi cell method [Ghosh et al., 1995] or the Fourier series approach [Moulinec and Suquet, 1998]. When finite elements are used at both scales, the method is called the finite element square method (FE^2), method used in this thesis to develop a double-scale model describing the coal behaviour.

The numerical double-scale procedure is based on the following consecutive steps:

1. Macro-to-micro: Localization of the macroscale deformations to the microscale
2. Resolution of the boundary value problem on the microscale
3. Micro-to-macro: Homogenization of the microscale stresses to compute the macroscopic quantity
4. Resolution of the boundary value problem on the macroscale

These steps are repeated for each Gauss point until the convergence is obtained on both scales. Despite the method is computationally rather expensive, it is far less than the brute force approach. Moreover, a parallel computation may be used [Kouznetsova et al., 2002]. In the context of multi-physics and coupling phenomena, the FE^2 method was first applied to deal with heat conduction problems [Özdemir et al., 2008]. Then, it was used for the modelling of saturated porous media [Su et al., 2011, Van den Eijnden, 2015]. In the context of CBM recovery, the method has to be extended to partially saturated media. In the present section, the important concepts underlying the FE^2 method are presented for the mechanical problem. The application of this method to multiphase flow in a fractured medium will be discussed in more detail in the next section.

13.2 Macro–to-micro scale transition (Localization)

The double-scale modelling approach distinguishes a microscale and a macroscale [1]. Given a point $\hat{\mathcal{P}}$ with a displacement $u_i^M\ \hat{\mathcal{P}}$, the microkinematics $u_i^m\ \hat{\mathcal{P}}$ is identical. For a point $\mathcal{P}$ close to $\hat{\mathcal{P}}$, the displacement can be defined with a Taylor expansion:

$$u_i\ \mathcal{P} \quad u_i\ \hat{\mathcal{P}} \quad \frac{u_i\ \hat{\mathcal{P}}}{x_j}\ x_j \quad \hat{x}_j \quad \frac{1}{2}\frac{^2u_i\ \hat{\mathcal{P}}}{x_j\ x_k}\ x_j \quad \hat{x}_j \quad x_k \quad \hat{x}_k \tag{V–1}$$

where x_j and $\hat{x}_j$ are respectively the j$^{\text{th}}$ coordinates of $\mathcal{P}$ and $\hat{\mathcal{P}}$.

In the macroscale continuum, higher-order terms of the expansion can be neglected. So, the macromechanical displacement field $u_i^M\ \mathcal{P}$ is approximately equal to:

$$u_i^M\ \mathcal{P} \quad u_i^M\ \hat{\mathcal{P}} \quad \frac{u_i^M\ \hat{\mathcal{P}}}{x_j}\ x_j \quad \hat{x}_j \tag{V–2}$$

For the microscale, higher-order terms can not be neglected because the continuity of the displacement field is not ensured. The micromechanical displacement field $u_i^m\ \mathcal{P}$ is therefore decomposed in the macromechanical field $u_i^M\ \mathcal{P}$ and a fluctuation displacement field $u_i^f\ \mathcal{P}$ replacing higher order terms:

$$u_i^m\ \mathcal{P} \quad u_i^M\ \hat{\mathcal{P}} \quad \frac{u_i^M\ \hat{\mathcal{P}}}{x_j}\ x_j \quad \hat{x}_j \quad u_i^f\ \hat{\mathcal{P}} \tag{V–3}$$

This fluctuation field results of the variations in material properties within the REV. It represents therefore the fine scale deviations with respect to the average fields.

1. The superscript m is used to refer to the microscale while the capital letter M denotes macroscopic quantities.

13.2.1 Deformation averaging

An important characteristic of the scale transition between the micro and the macro level is the transfer of deformation gradients $F_{ij} = \dfrac{\partial x_i}{\partial X_j}$. In computational homogenization, the micro-to-macro is achieved by imposing a volumetric averaging of a microscale property. This volumetric averaging of the deformation gradient taken with respect to the reference microstructural configuration reads

$$F_{ij}^M = \frac{1}{\Omega_0}\int_{\Omega_0} F_{ij}^m \, d\Omega_0 = \frac{1}{\Omega_0}\int_{\Gamma_0} x_i \, N_j \, d\Gamma_0 \tag{V–4}$$

where Ω_0 denotes the reference volume of the REV and Γ_0 is its external reference surface. The integral over the surface Γ_0 is obtained from the integral over the volume Ω_0 using the divergence theorem. x_i is the position vector and N_j is the unit vector normal to Γ_0.

As the microscopic deformation gradient may be split in a constant (macro) and a fluctuation contributions, Equation (V–4) also means that

$$\int_{\Gamma_0} u_i^f \, N_j \, d\Gamma_0 = 0 \tag{V–5}$$

It can be satisfied by different sets of boundary conditions imposed at the micro level [Kouznetsova et al., 2001, Özdemir et al., 2008].

13.2.2 Separation of scales

As the statement $u_i^m(\hat{\mathcal{P}}) = u_i^M(\hat{\mathcal{P}})$ has to hold for any point of the macroscale, it follows that

$$\frac{\partial u_i^M(\hat{\mathcal{P}})}{\partial x_j}(x_j - \hat{x}_j) + u_i^f(\hat{\mathcal{P}}) \ll u_i^M(\hat{\mathcal{P}}) \tag{V–6}$$

The validity of the approach is therefore theoretically restricted to situations in which the scale of variation of the macroscopic fields is large compared to the microstructure and its REV. It is the concept of separation of scales [Kouznetsova et al., 2002]. Simply written, the microscopic characteristic length l_c has to be much smaller than the characteristic fluctuation length L_c of the macroscopic deformation fields:

$$l_c \ll L_c \tag{V–7}$$

If this assumption holds, the boundary conditions of the microscale boundary value problem (BVP) can be properly dictated by the local macroscale deformation gradient. If the macroscopic field varies considerably in critical regions of high gradient, the assumption of scale separation may not hold. Large spatial gradients are observed, for instance, with strain localization problems [Geers et al., 2010]. In this case, a higher-order homogenization technique should be applied [Schröder, 2014]. It means the Taylor expansion of the displacement field is not troncated before the second-order term [Kouznetsova et al., 2002].

This work is limited to the application of the first-order computational homogenization. It supposes therefore a separation of scales.

13.3 Microscale boundary value problem

13.3.1 Choice of the REV

The physical and geometrical properties of the microstructure are embedded on a representative elementary volume (REV). This one must be selected such that it is large enough to represent the microstructure and small enough so that the principle of scale separation is not violated. Figure V–2 (thought experiment) illustrates the explanation of the representativeness of the elementary volume applied to porosity.

As the volume decreases, the porosity fluctuates and the volume is not representative of the medium [Bear, 1972, Lake and Srinivasan, 2004].

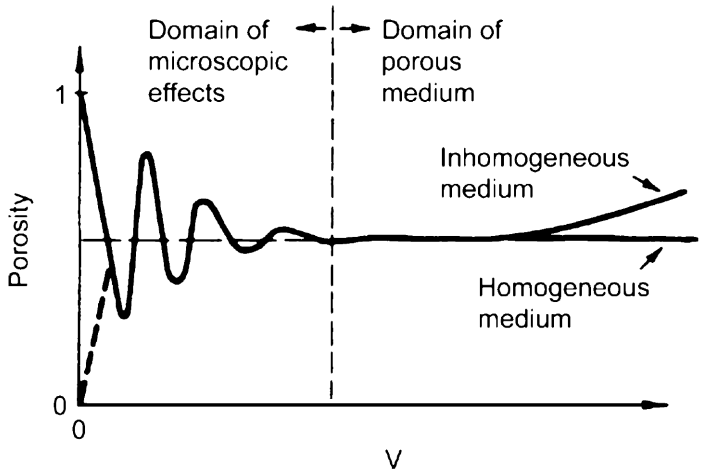

Figure V–2 – Representativity of the REV applied to the concept of porosity. *From* [Lake and Srinivasan, 2004] *adapted from* [Bear, 1972].

It is usually a delicate task to identify the REV. For now, it is assumed the appropriate REV has been already selected such that we can directly consider the boundary value problem (BVP).

13.3.2 Boundary conditions

The macroscopic deformation enters the microscale BVP through the boundary conditions [Geers et al., 2010]. Different types of boundary conditions can be chosen to translate the macroscale deformation to the microscale. The three canonical types are:

Uniform strain boundary condition: displacements are prescribed, it corresponds to a Dirichlet boundary condition.

Uniform stress boundary condition: tractions are prescribed, it corresponds to a Neumann boundary condition.

Periodic boundary conditions: relative displacements between opposite boundaries are enforced and boundary tractions on opposite boundaries are antisymmetric.

Actually, Dirichlet and Neumann boundary conditions provide an upper and lower bound solution, the former tend to overestimate and the latter to underestimate the equivalent material strength when the REV is not large enough to be fully representative [Suquet, 1987]. The periodic boundary conditions, giving a result between these two bounds, are therefore adopted for their efficiency to transfer the macroscale deformation to the microscale REV. This choice has been justified by different authors [Van der Sluis et al., 2000, Terada et al., 2000]. Note that the application of periodic boundary conditions does not actually requires a periodic material. For instance, these boundary conditions may be applied for a granular material. However, it is a natural course of action for periodic media such as coal since these boundary conditions enforce the local periodicity of the microscale material behaviour [Van den Eijnden, 2015].

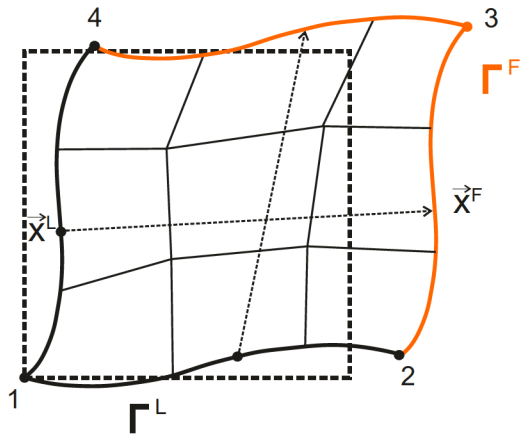

Figure V–3 – Periodic boundary conditions

For the definition of the boundary value problem on the REV, different periodic frames can be chosen [Anthoine, 1995]. It is convenient to choose a periodic frame with a simple geometry and the most straightforward is certainly a rectangular frame aligned along the coordinate axes. The boundary Γ enclosing the REV being periodic, it can be subdivided in two parts: the lead part Γ^L and the follow part Γ^F. The kinematics of any point x^F on the follow boundary Γ^F depends obviously on the kinematics of its homologous x^L on the lead boundary Γ^L. The periodicity conditions for the microstructural REV are written using the global deformation gradient tensor as

$$\begin{aligned} x_i^F &= x_i^L + \frac{\partial x_i^M}{\partial X_j}\,(X_j{}^F - X_j{}^L) \\ &= x_i^L + F_{ij}^M\,(X_j{}^F - X_j{}^L) \end{aligned} \tag{V–8}$$

where the capital letter X_j refers to the vector of coordinates in the reference configuration. In terms of displacements, it can be written as

$$u_i^F = u_i^L + \frac{\partial u_i^M}{\partial X_j}\,(X_j{}^F - X_j{}^L) \tag{V–9}$$

Then, the micro fluctuation displacement between the lead and the follow must be zero:

$$u_i^{f\,F} - u_i^{f\,L} = 0 \tag{V–10}$$

One point on the lead boundary is fixed to prevent rigid body motion, for instance the lower left corner in Figure V–3.

We can verify that the use of these periodic boundary conditions satisfies Equation (V–4):

$$\begin{aligned} F_{ij}^M &= \frac{1}{\Omega_0}\int_{\Gamma_0} x_i\,N_j\,d\Gamma_0 \\ &= \frac{1}{\Omega_0}\left(\int_{\Gamma_0^F} x_i^F\,N_j{}^F\,d\Gamma_0 + \int_{\Gamma_0^L} x_i^L\,N_j{}^L\,d\Gamma_0\right) \\ &= \frac{1}{\Omega_0}\int_{\Gamma_0^F} (x_i^F - x_i^L)\,N_j{}^F\,d\Gamma_0 \\ &= \frac{1}{\Omega_0}F_{ik}^M\int_{\Gamma_0^F} (X_k^F - X_k^L)\,N_j^F\,d\Gamma_0 \\ &= \frac{1}{\Omega_0}F_{ik}^M\int_{\Gamma_0} X_k\,N_j\,d\Gamma_0 \\ &= \frac{1}{\Omega_0}F_{ik}^M\int_{\Omega_0} \delta_{kj}\,d\Omega_0 \\ &= F_{ij}^M \end{aligned} \tag{V–11}$$

13.3.3 Balance equation

The REV is in equilibrium. As it is small, the body forces can be neglected and the equilibrium written in terms of the first Piola-Kirchhoff [2] stress tensor P^m_{ij} reads:

$$\frac{\partial P^m_{ij}}{\partial X_j} = 0 \tag{V–12}$$

13.3.4 Constitutive behaviour

Each microstructural constituent present in the REV is described by its constitutive laws specifying the stress-strain relationship. The constitutive relation between the stress rate $\dot{P}_{ij}$ and the strain rate $\dot{F}_{ij}$ can be written in a general incremental form as

$$\dot{P}^m_{ij} = f(\dot{F}^m_{ij}, P^m_{ij}, \mathcal{K}) \tag{V–13}$$

where κ represents some internal variables of the law which are not discussed in this section. A priori, it is possible to introduce any continuous incremental constitutive relation.

13.3.5 Weak form of the balance equation

A weak form of the local momentum balance Equation (V–12) can be obtained considering an admissible virtual velocity field v^{*m}_i. The principle of virtual power implies that, for any admissible virtual velocity, the solid is in equilibrium if internal virtual power $\dot{W}^*_I$ is equal to external one $\dot{W}^*_E$:

$$\underbrace{\int_\Omega P^m_{ij}\, \dot{F}^{*m}_{ij}\, d\Omega}_{\dot{W}^*_I} = \underbrace{\int_\Gamma \bar{t}_i\, v^{*m}_i\, d\Gamma}_{\dot{W}^*_E} \tag{V–14}$$

where $\bar{t}_i$ is the boundary traction on any boundary Γ. The periodic boundary conditions also imply the antisymmetry of the boundary traction:

$$\bar{t}^F_i + \bar{t}^L_i = 0 \tag{V–15}$$

13.3.6 Solution of the problem

In the FE^2 method, the boundary value problem is solved by discretizing the REV with finite elements. Coordinates and displacements are interpolated over the element using shape functions. In general, the balance Equation (V–14) is non-linear and has to be solved with a Newton-Raphson incremental-iterative scheme. The incremental relation between the nodal displacement components $\{u^m\}$ and nodal force components $\{f^m\}$ is governed by the global stiffness matrix $[K^m]$:

$$[K^m]\, \{\delta u^m\} = \{\delta f^m\} \tag{V–16}$$

$[K^m]$ is obtained from the linearization of the nodal force equilibrium around the updated configuration. As classical constitutive relations are used at the microscale, a closed-form analytical solution exists for the partial derivatives of the constitutive equations and the components of $[K^m]$ can usually be determined analytically. Computations to solve Equation (V–16) related to all the REVs take most of the global computation time. Actually, these computations are highly suitable for parallelization and an important gain in efficiency can be obtained by solving multiple REV boundary value problems in parallel.

2. Piola-Kirchhoff stress relates the force acting in the current configuration to the surface element in the reference configuration.

13.4 Micro–to-macro scale transition (Homogenization)

13.4.1 Stress averaging

Similarly to the deformation, the volume average of the first Piola-Kirchhoff stress tensor P_{ij} is established as

$$P_{ij}^M \equiv \frac{1}{\Omega_0}\int_{\Omega_0} P_{ij}^m \, d\Omega_0 = \frac{1}{\Omega_0}\int_{\Gamma_0} \bar{t}_i \, X_j \, d\Gamma_0 \tag{V–17}$$

As the REV boundary value problem is solved using a FE discretization, this boundary integral can be approximated by a sum over the nodal forces f_i^m. Using the periodicity conditions on a finite element discretization of the 2D REV depicted in Figure V–3, the only contribution to the boundary integral is offered by the nodal reaction forces at the three prescribed corner nodes:

$$P_{ij}^M = \frac{1}{\Omega_0}\sum_{k=1,2,4} f_i^m{}_k X_{j_k} \tag{V–18}$$

Actually, the first Piola-Kirchhoff stress tensor is used in this section since it has been advocated by Hill to be a more consistent way of taking into account the macro-homogeneity. The actual macroscopic Cauchy stresses can be obtained from the first Piola-Kirchhoff stress tensor by the standard relation

$$\sigma_{ij}^{M\star} = \frac{1}{\det(F_{kj}^M)} P_{ik}^M F_{kj}^M \tag{V–19}$$

However, formulating the microscale problem under a small strain assumption, the averaging relation for the microscopic Cauchy stress tensor σ_{ij} over the current REV is directly given by

$$\sigma_{ij}^M \equiv \frac{1}{\Omega}\int_{\Omega} \sigma_{ij}^m \, d\Omega = \frac{1}{\Omega}\int_{\Gamma} \bar{t}_i \, x_j \, d\Gamma = \frac{1}{\Omega}\sum_{k=1,2,4} f_i^m{}_k x_{j_k} \tag{V–20}$$

13.4.2 Macro-homogeneity condition

The macro-homogeneity condition, also known as the Hill-Mandel condition [Hill, 1965, Mandel, 1972] requires that the local variation of the work on the macroscale is equal to the volume average of the variation of work on the REV:

$$\delta W^M \equiv \frac{1}{\Omega_0}\int_{\Omega_0} \delta W^m \, d\Omega_0 \tag{V–21}$$

Formulating in terms of the work conjugate pair P_{ij} and F_{ij}, this principle which establishes the energy rate consistency between the micro and the macro scale reads

$$P_{ij}^M \, \delta F_{ij}^M \equiv \frac{1}{\Omega_0}\int_{\Omega_0} P_{ij}^m \, \delta F_{ij}^m \, d\Omega_0 \; = \frac{1}{\Omega_0}\int_{\Gamma_0} \bar{t}_i \, \delta x_i \, d\Gamma_0 \tag{V–22}$$

We can verify that the boundary conditions adopted satisfy the Hill-Mandel condition if the averaging relations defined above for the deformation gradient tensor (V–4) and the first Piola-Kirchhoff stress tensor (V–17) are employed.

$$\begin{aligned}
\frac{1}{\Omega_0}\int_{\Omega_0} \delta W^m \, d\Omega_0 &= \frac{1}{\Omega_0}\left(\int_{\Gamma_0^F} \bar{t}_i^F \, \delta x_i^F \, d\Gamma_0 + \int_{\Gamma_0^L} \bar{t}_i^L \, \delta x_i^L \, d\Gamma_0\right) \\
&= \frac{1}{\Omega_0}\int_{\Gamma_0^F} \bar{t}_i^F \, (\delta x_i^F - \delta x_i^L) \, d\Gamma_0 \\
&= \frac{1}{\Omega_0}\int_{\Gamma_0} \bar{t}_i^F \, (X_j^F - X_j^L) \, d\Gamma_0 \quad \delta F_{ji}^M \\
&= \frac{1}{\Omega_0}\int_{\Gamma_0} \bar{t}_i \, X_j \, d\Gamma_0 \quad \delta F_{ij}^M \\
&= P_{ij}^M \, \delta F_{ij}^M \\
&= \delta W^M
\end{aligned} \tag{V–23}$$

13.5 Macroscale boundary value problem

The macroscopic structure to be analyzed is assumed to be macroscopically homogeneous and is discretized by finite elements. The macroscopic non-linear system of equations is solved by a standard iterative manner. However, there is no specific constitutive behaviour defined on the macrolevel. The macroscale constitutive relation

$$\dot{\sigma}_{ij}^{M} = C_{ijkl}^{M}\,\dot{\varepsilon}_{kl}^{M} \tag{V–24}$$

is obtained by assigning a discretized periodic REV to each Gauss point of the macroscopic mesh. Indeed, the local macroscopic deformation tensor is transmitted to the REV through the boundary conditions and the local macroscopic stress is returned to the macroscopic integration point by the microscale analysis. Thence, the stiffness matrix required at every macroscopic integration point by the Newton-Raphson scheme has to be determined numerically from the relation between variations of the macroscopic stress and variations of the macroscopic deformation at this point. It can be obtained by numerical perturbation [Miehe, 1996] or by static condensation [Kouznetsova et al., 2001].

13.5.1 Consistent stiffness matrix by numerical perturbation

This method is not restricted to multi-scale computations, it has already been presented in section 7.4 dedicated to the macroscale model. Although the linearization by numerical perturbation is a simple method to obtain the stiffness matrix, it requires the response to a certain load increment to be computed several additional times and, particularly for a multi-scale model, this can have a major impact on the total computational expense. Actually, the computational costs of obtaining the response from the incremental loading of the microstructure quickly exceeds the costs of the global computation at the macroscale. A possible alternative is the computation of the stiffness matrix by static condensation.

13.5.2 Consistent stiffness matrix by static condensation

Computational homogenization by static condensation [Kouznetsova et al., 2001] avoids to solve many additional BVPs. The method consists to condense the microscale stiffness by reducing the REV system of equations to the relation between the forces acting on the retained vertices of the boundary and the displacements of these vertices. To this purpose, the linear system of equations (V–16) is extended with the macroscale strain $\{\delta\varepsilon^{M}\}$:

$$\begin{bmatrix} [0] & [0] \\ [0] & [K^{m}] \end{bmatrix} \begin{Bmatrix} \{\delta\varepsilon^{M}\} \\ \{\delta u^{m}\} \end{Bmatrix} = \begin{Bmatrix} \{0\} \\ \{\delta f^{m}\} \end{Bmatrix} \tag{V–25}$$

This system can be reduced to a well-posed problem using the definition of the averaged stress (V–20) and the boundary conditions (V–9) and (V–15). It leads to the following system [Van den Eijnden, 2015]:

$$\begin{bmatrix} [K^{\diamond pp}] & [K^{\diamond pi}] \\ [K^{\diamond ip}] & [K^{\diamond ii}] \end{bmatrix} \begin{Bmatrix} \{\delta\varepsilon^{M}\} \\ \{\delta u^{\diamond m}\} \end{Bmatrix} = \begin{Bmatrix} \{\delta\sigma^{M}\} \\ \{0\} \end{Bmatrix} \tag{V–26}$$

where $[K^{\diamond pp}]$, $[K^{\diamond pi}]$, $[K^{\diamond ip}]$ and $[K^{\diamond ii}]$ are the partitions of the stiffness matrix deduced from the elimination procedure and $\{\delta u^{\diamond m}\}$ is the remaining displacement variations. Then, the static condensation of the system of equations (V–26) on $\{\delta\varepsilon^{M}\}$ allows us to determine the stiffness matrix $[C^{M}]$ from

$$[C^{M}]\{\delta\varepsilon^{M}\} = \{\delta\sigma^{M}\} \tag{V–27}$$

as

$$[C^{M}] = [K^{\diamond pp}] - [K^{\diamond pi}] \cdot [K^{\diamond ii}]^{-1} \cdot [K^{\diamond ip}] \tag{V–28}$$

13.6 Algorithm of the FE^2 method

To conclude this section, the FE^2 method can be summarized by the following subsequent steps [Kouznetsova et al., 2001]:

1. The macrostructure is discretized by finite elements. An incremental procedure is used to apply the external load with increments associated with discrete time steps.
2. The macroscopic deformation gradient tensor is computed for each macroscopic integration point from the estimation of the macroscopic nodal displacements relative to the external load. During the initialization step, zero deformation is assumed throughout the macroscopic structure.
3. A periodic REV, representing the microstructure morphology of the material, is assigned to each macroscopic integration point. The appropriate displacements are applied to the prescribed corner nodes of each REV based on the local macroscopic deformation tensor.
4. The resulting stress and deformation distributions on the microscale are computed by solving the REV boundary value problems using a separate finite element discretisation.
5. The REV averaged stress is computed with the REV vertex forces and returned as the local macroscopic stress to the macroscopic integration point. The REV global stiffness matrix is also computed.
6. The macroscopic internal nodal forces are computed based on the stresses obtained for each integration point. If these forces are in balance with the external load, then incremental convergence is achieved and the next time increment can be evaluated. Otherwise, the procedure is continued updating the estimation of the macroscopic nodal displacements.
7. The consistent macroscopic matrix is computed for each macroscopic integration point from the REV global stiffness matrix. An updated estimation of the macroscopic displacement field is produced.

14. Hydro-mechanical model

Based on the general steps of the FE^2 method presented in the previous section, the method is used to develop a doublescale hydro-mechanical model for partially saturated conditions in coalbeds.

14.1 Background and proposed developments

The starting point of the developments described hereafter is the hydro-mechanical doublescale model implemented in the Lagamine code by [Marinelli, 2013] and [Van den Eijnden, 2015], which are based on the work of [Frey, 2010], preceded by [Bilbie, 2007].

With respect to the previous developments, a new fluid degree of freedom has been added. The presence of gas implies the implementation of the microscale hydraulic constitutive model for partially saturated conditions. In particular, based on the model presented in the previous part of the thesis, the following contributions are proposed:

Definition of a retention curve for the interface elements.

Introduction of some relative permeabilities curves to compute the advective fluxes.

Use of equilibrium equations between the phases.

Moreover, the particular case of coal, with sorption properties, requires the following developments:

Computation of the gas storage term taking into account the Langmuir's isotherm and a sorption time.

Hydro-mechanical coupling in the solid bodies to account for the swelling/shrinkage due to the sorption/desorption.

Finally, the reservoir modelling requires the following considerations:

Variable REV length scale.

Introduction of some initial stresses.

2D-axisymmetric conditions around the wellbore.

14.2 REV and unit cell

The REV is built with solid matrix blocks separated by interfaces. Figure V–4 represents this kind of structure. The REV needs to contain enough blocks to be a good statistical representation of the random microstructure. A numerical analysis of the variation of the macroscale response with the size of the REV should be therefore carried out to assess the representativeness of the chosen REV.

In the case of materials with a specifically built periodic microstructure, one can simply choose a periodic unit cell as REV. The choice of this cell is non-unique (Figure V–5) but it is convenient to choose a rectangular frame (Figure V–6). Unit cells are extensively used for the modelling of human-made materials such as masonry walls [Anthoine, 1995, Massart, 2003]. It is more questionable for natural materials. However, coal is generally described as a periodic material in the literature. The multiscale method is however not restricted to periodic materials and one can prefer a classical REV.

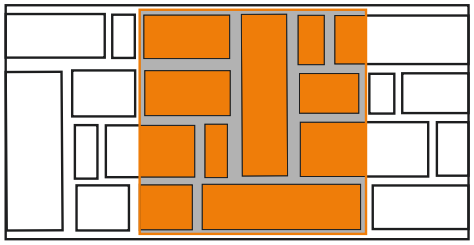

Figure V–4 – Example of REV.

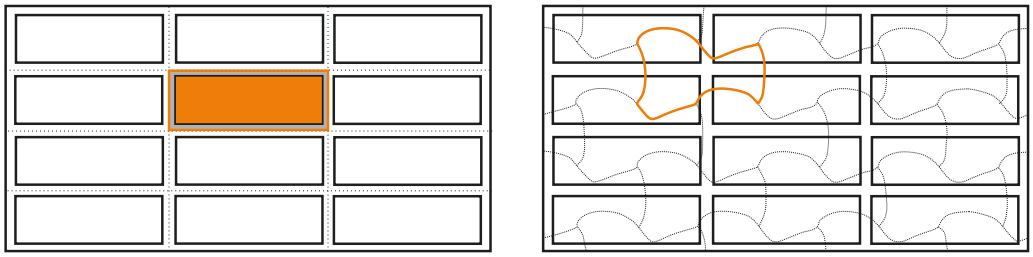

Figure V–5 – Convenience in the choice of the unit cell. *Modified from* [Anthoine, 1995].

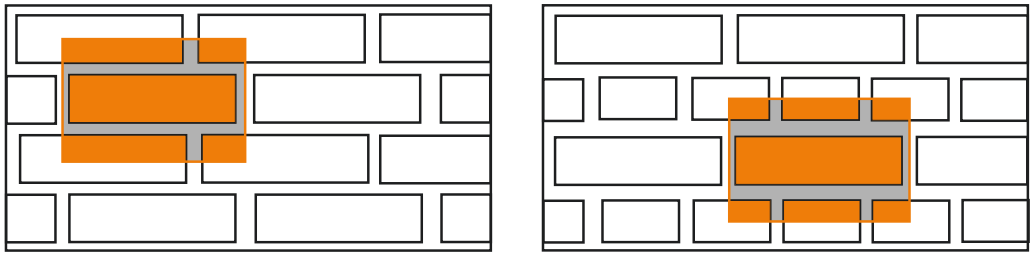

Figure V–6 – Examples of rectangular unit cells. *Modified from* [Anthoine, 1995].

For the sake of simplicity, it is chosen not to use a REV border along a fracture. The kind of REV that may be used with our model is represented in Figure V–7. The REV is actually constituted of three parts: the solid matrix, the mechanical interfaces between the grains, and the fluid network.

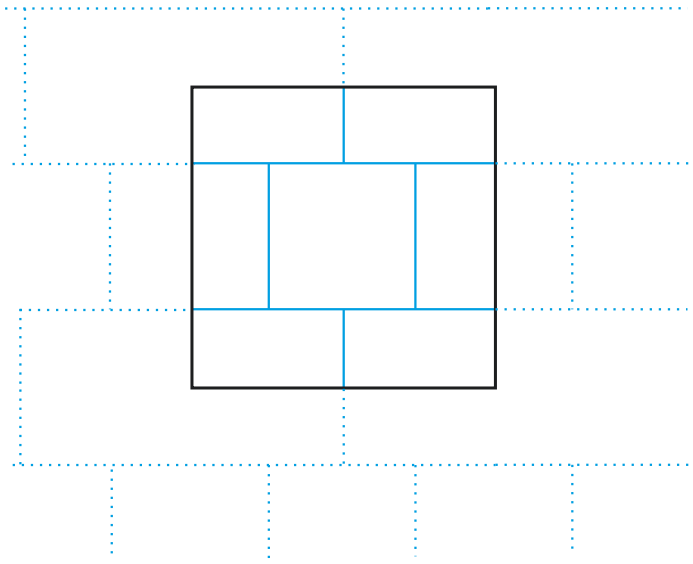

Figure V–7 – Microstructure with REV borders through the matrix.

Note that, from a mechanical point of view, it is not necessary to define a REV size. However, the dimensionless fracture apertures of the REV/unit cell has to be converted using a conversion parameter with a length dimension to obtain a meaningful permeability tensor. In a practical way, the REV is defined with a size of one by one and, the macroscopic scale being expressed in meters, the factor defining the REV length (unit or fraction of a unit) is used for the conversion in the localization and homogenization steps.

14.3 Decomposition of the microkinematics

In order to develop the hydro-mechanical problem for partially saturated conditions, the water pressure p_w and gas pressure p_g are introduced. The number of degrees of freedom is thus augmented by 2 with respect to the purely mechanical problem. As for the microscale displacements, the microscale pressure fields of water and gas can be decomposed into macroscale components and microkinematical fluctuations:

$$p_w^m(\mathcal{P}) = p_w^M(\hat{\mathcal{P}}) + \frac{\partial p_w^M(\hat{\mathcal{P}})}{\partial x_j}(x_j - \hat{x}_j) + p_w^f(\mathcal{P}) \tag{V–29}$$

and

$$p_g^m(\mathcal{P}) = p_g^M(\hat{\mathcal{P}}) + \frac{\partial p_g^M(\hat{\mathcal{P}})}{\partial x_j}(x_j - \hat{x}_j) + p_g^f(\mathcal{P}) \tag{V–30}$$

The requirement of separation of scales implies that

$$\frac{\partial p_w^M(\hat{\mathcal{P}})}{\partial x_j}(x_j - \hat{x}_j) + p_w^f(\mathcal{P}) \ll p_w^M(\hat{\mathcal{P}}) \tag{V–31}$$

and

$$\frac{\partial p_g^M(\hat{\mathcal{P}})}{\partial x_j}(x_j - \hat{x}_j) + p_g^f(\mathcal{P}) \ll p_g^M(\hat{\mathcal{P}}) \tag{V–32}$$

Section 14.5 will present the practical way to verify these requirements on the boundary conditions.

14.4 Periodic boundary conditions

For small strains, the mechanical part of the periodic boundary conditions for the REV is defined through the relation

$$u_i^F = u_i^L + \varepsilon_{ij}^M \, ({x_j}^F - {x_j}^L) \tag{V–33}$$

In the same way, the boundary conditions for water and gas pressures are given by

$$p_w^F = p_w^L + \frac{\partial p_w^M}{\partial x_j} \, ({x_j}^F - {x_j}^L) \tag{V–34}$$

and

$$p_g^F = p_g^L + \frac{\partial p_g^M}{\partial x_j} \, ({x_j}^F - {x_j}^L) \tag{V–35}$$

Moreover, the periodic boundary conditions lead to the requirement of the antisymmetry of the boundary traction:

$$\overline{t}_i^F + \overline{t}_i^L = 0 \tag{V–36}$$

And anti-symmetric boundary fluxes:

$$\overline{q}_w^F + \overline{q}_w^L = 0 \tag{V–37}$$

and

$$\overline{q}_g^F + \overline{q}_g^L = 0 \tag{V–38}$$

14.5 Separation of scales

As stated above with Equation (V–7), the microscopic characteristic length has to be much smaller than the characteristic fluctuation length of the macroscopic deformation fields. Applying the macroscopic deformation fields on the boundaries, the microscopic characteristic length is reasonably the length between these boundaries (${x_j}^F - {x_j}^L$), i.e. the REV size l_{REV}. Then, the macroscopic length depends in part on the load applied on the REV, i.e. the macroscopic gradient of fluid pressure $\frac{\partial p^M}{\partial x_j}$ (or written ∇p^M) for the hydraulic part. Moreover, it is rational to consider that a pressure gradient of $1MPa/m$ does not lead to the same characteristic length if the macroscopic pressure is $1MPa$ or $10MPa$. We define the wanted macroscopic length as the ratio of the pressure over the pressure gradient. We have therefore to verify that

$$l_{REV} \ll \frac{p^M}{\nabla p^M} \tag{V–39}$$

to satisfy the separation of scales. It is formulated here for the fluid pressure and pressure gradient (gas or water) since the objective of the thesis is to model a pressure drop at a production well. It is therefore the most critical quantity.

Moreover, as the size of the REV/unit cell should be very small compared to the macroscale, it is generally consistent to assume the hydraulic flow at the micro level is insensitive to the time variations of the fluid storage at this level. In other words, the microscale problem may be solved under steady-state conditions. It means that boundary conditions dictate the instantaneous pressure changes at the micro level. However, in some cases, it is sometimes necessary to take into account transient effects. For instance, there may be a double porosity effect due to the diffusive flows in the matrix. An instantaneous equilibrium between the pressure and the matrix should only be considered if

$$\mathcal{T} \ll \frac{p^M}{\dot{p}^M} \tag{V–40}$$

where $\mathcal{T}$ is the characteristic time at the microscale, it is the sorption time in this case. It depends on the diffusion coefficient and the size of the matrix block (see Equation III–108). The right-hand term refers to the macroscopic characteric time.

If condition (V–40) is not ensured, a transient computational homogenization could be used to take into account micro-structural inertia effects at the macroscopic level. For instance, [Larsson et al., 2010a, Larsson et al., 2010b] avoided the steady state assumption for heat flow at the microscale considering higher order terms in the homogenization procedure. An appropriate scale transition has been presented by [Pham et al., 2013] for the dynamic modelling of a heterogeneous medium subjected to a pulse loading. This transient scheme is not developed in this work as the loading is likely less extreme in the context of reservoir modelling. However, to model more adequately cases where the sorption time is close to the loading characteristic time, it is interesting to introduce the sorption time coefficient in the adsorbed gas pressure evolution computed under pseudo-steady state conditions. This approach has already been used to develop the macroscale model (Part III) and section 14.7.1.2 explains its integration into the multiscale model.

14.6 Balance equations

Neglecting the body forces, the equilibrium of the REV means the Cauchy stress tensor σ^m_{ij} has to satisfy:

$$\frac{\partial \sigma^m_{ij}}{\partial x_j} = 0 \tag{V–41}$$

The weak form of the local momentum balance Equation (V–41) is obtained applying the principle of virtual power considering the admissible virtual velocity field v_i^{*m}, it reads

$$\int_\Omega \sigma_{ij}^m \frac{\partial v_i^{*m}}{\partial x_j}\, d\Omega = \int_\Gamma \bar{t}_i\, v_i^{*m}\, d\Gamma \tag{V–42}$$

As the REV is constituted of blocks and interfaces, the boundary Γ in Equation (V–42) can be divided in external boundaries Γ^{ext} (the periodic REV boundaries) and internal boundaries Γ^{int} (the interfaces). The integral over the external boundary is zero given the periodic boundary conditions. Writing $T_i^{+/-}$ the global components of the cohesive or frictional interface forces acting on the upper/lower part of the interface and $\Gamma^{int,+}$ and $\Gamma^{int,-}$ the opposite interface boundaries, it gives

$$\int_\Omega \sigma_{ij}^m \frac{\partial v_i^{*m}}{\partial x_j}\, d\Omega = \int_{\Gamma^{int,+}} T_i^+\, v_i^{*m}\, d\Gamma + \int_{\Gamma^{int,-}} T_i^-\, v_i^{*m}\, d\Gamma \tag{V–43}$$

In addition to the mechanical equilibrium, the mass balance equations for water and gas are

$$\dot{M}_w^m + \frac{\partial f_{w_i}^m}{\partial x_i} = 0 \tag{V–44}$$

and

$$\dot{M}_g^m + \frac{\partial f_{g_i}^m}{\partial x_i} = 0 \tag{V–45}$$

where $f_{w_i}^m$ and $f_{g_i}^m$ are the internal total fluxes of water and gas, and $\dot{M}_w^m$ and $\dot{M}_g^m$ represent the variations of the fluid contents. Under the assumption of steady state at the microscale, these latter terms will vanish out. Considering some kinematically admissible virtual fluid pressure fields p_w^{*m} and p_g^{*m}, the fluids mass balance equations may be written in the following weak forms:

$$\int_\Omega \left[\cancel{\dot{M}_w^m p_w^{*m}} - f_{w_i}^m \frac{\partial p_w^{*m}}{\partial x_i} \right] d\Omega = -\int_\Gamma \overline{q}_w^m\, p_w^{*m}\, d\Gamma \tag{V–46}$$

$$\int_\Omega \left[\cancel{\dot{M}_g^m p_g^{*m}} - f_{g_i}^m \frac{\partial p_g^{*m}}{\partial x_i} \right] d\Omega = -\int_\Gamma \overline{q}_g^m\, p_g^{*m}\, d\Gamma \tag{V–47}$$

14.7 Constitutive laws

The constitutive microscale model is constituted of some mechanical laws for the matrix and the fracture, the fluid density variation law and the multiphase flow model. The multiscale framework presented in this section is not restricted to some particular constitutive laws. Based on the developments in the previous part of the thesis, the laws used for the coalbed modelling are shortly presented hereafter.

14.7.1 Matrix

14.7.1.1 Solid constitutive law

It is assumed the sophistication of the material behaviour is obtained from the assembly of different constituents. It is thus not unreasonable to consider an isotropic linear elastic relation for the matrix:

$$\Delta\sigma_{ij} = 2G_m \Delta\varepsilon_{ij} + \lambda_m \Delta\bar{\varepsilon}\, \delta_{ij} \tag{V–48}$$

where ε_{ij} is the small-strain tensor [1] given by $\frac{1}{2}\left(\frac{\partial u_i}{\partial x_j} + \frac{\partial u_j}{\partial x_i}\right)$, $\bar{\varepsilon} = \varepsilon_{ij}\delta_{ij}$ with δ_{ij} the Kronecker's symbol, G_m is the Coulomb's modulus and λ_m is the first Lamé parameter. Note that effective and total

1. The change from a large deformation formulation to small strain assumption at the microscale was introduced in the code by [Van den Eijnden, 2015]. Through this assumption, the Piola-Kirchhoff stress and the Cauchy stress tensors can be assumed approximately equal, as the deformation gradient tensor is assumed to be approximately equal to identity matrix.

stresses are equal in the matrix.

In order to model a wellbore, note that axisymmetric conditions are applied on the macroscale. Compared to previous implementations, true 2D conditions at the microscale are not enough. Axisymmetric conditions require that stresses are known in the off-plane direction.

In addition, the reservoir conditions require the presence of initial stresses σ_{ij_0}. The stress tensor at a given time is then

$$\sigma_{ij} = \sigma_{ij_0} + \Delta\sigma_{ij} \tag{V–49}$$

where $\Delta\sigma_{ij}$ represents the increment of stress between the initial and current stresses. Indeed, it was chosen to implement the microscale mechanical constitutive laws of the multiscale approach with increments from the initial state and not from the previous time step. Using elastic mechanical laws, there is no reason to store in memory the current REV configuration for the computation at the next time step.

Equation (V–48) only gives the stress increment if the swelling/shrinkage is not considered. Modelling gas sorption in coalbed, sorption-induced strain has to be considered and the elastic law writes

$$\Delta\sigma_{ij} = 2G_m\Delta\varepsilon_{ij} + \lambda_m\Delta\bar{\varepsilon}\,\delta_{ij} + K_m\Delta\varepsilon_{v_s}\delta_{ij} \tag{V–50}$$

where K_m is the bulk modulus of the matrix and $\Delta\varepsilon_{v_s}$ is the volumetric sorption-induced strain. This sorption-induced strain depends on the adsorbed gas content $V_g^{Ad}[m^3/kg]$ and a linear coefficient $\beta_\varepsilon[kg/m^3]$:

$$\Delta\varepsilon_{v_s} = \beta_\varepsilon\Delta V_g^{Ad} = \beta_\varepsilon\,\frac{M_{m_g}}{RT}\,\frac{1}{\rho_{g,std}\rho_c}\,\Delta p_g^{Ad} \tag{V–51}$$

where R is the universal gas constant ($8.3143\ J/mol\cdot K$), $T[K]$ is the absolute temperature, M_{m_g} is the molecular mass of the gas ($0.016\ kg/mol$ for methane and $0.044\ kg/mol$ for carbon dioxide), $\rho_{g,std}$ is the gas density at standard conditions, ρ_c is the coal density, and p_g^{Ad} is the adsorbed gas pressure in the matrix.

14.7.1.2 Adsorbed gas pressure evolution

At equilibrium, the adsorbed gas pseudo-pressure is given by

$$p_g^{Ad} = \frac{RT}{M_{m_g}}\,\rho_{g,std}\,\rho_c\,\frac{V_L\cdot p}{P_L + p} \tag{V–52}$$

where V_L and P_L are the Langmuir's parameters, and p depends on the macroscopic fluid pressures (which is consistent with the separation of scales):

$$p = \max(p_w^M, p_g^M) \tag{V–53}$$

If the hypothesis of an instantaneous equilibrium between the pressure in the cleats and the adsorbed gas content in the matrix is too restrictive, it is interesting to introduce a sorption time $\mathcal{T}$ to take into account the delay imposed by the diffusion process into the matrix. The average adsorbed gas pressure p_g^{Ad} is then given by

$$p_g^{Ad}(t) = p_g^{Ad}(t-\Delta t) + \frac{1}{\mathcal{T}}\left(p_g^{Ad,lim} - p_g^{Ad}(t-\Delta t)\right)\Delta t \tag{V–54}$$

with $p_g^{Ad,lim}$ evaluated with Equation (V–52). The value of the adsorbed gas pressure p_g^{Ad} at the end of the time step is more accurately determined following a sub-stepping procedure by replacing Δt with δt as explained in section 7.3.1.

14.7.2 Cleats

14.7.2.1 Interface mechanical law

The mechanical law for the interfaces is defined by two parameters, the normal stiffness K_n and tangential stiffness K_s, which define the relation between the stresses and the fracture displacements. The tangential stiffness is considered constant, $K_s = K_s^0$, while a Bandis-type law is used for the normal stiffness [Goodman, 1976, Bandis et al., 1983]:

$$K_n = \frac{K_n^0}{\left(1 + \frac{h-h_0}{h_0}\right)^2} \tag{V–55}$$

where K_n^0 is the stiffness corresponding to the initial aperture h_0. This initial aperture is actually defined for a null stress. Thus, when considering some initial stresses, the initial normal closure is given by [2]

$$\Delta h_0 = \frac{-\sigma_0' \, h_0}{K_n^0 \, h_0 + \sigma_0'} \tag{V–56}$$

where σ_0' is the normal effective stress.

Since the tangential stiffness is constant, the initial tangential closure is directly:

$$\Delta s_0 = \frac{\tau_0}{K_s^0} \tag{V–57}$$

where τ_0 is the initial tangential stress. Given the initial stresses σ_{xx_0} and σ_{yy_0}, and the orientation θ of the fracture with the horizontal, the normal and tangential stresses are computed as

$$\sigma_0 = \sigma_{xx_0} \cos^2(\theta) + \sigma_{yy_0} \sin^2(\theta) \tag{V–58}$$

$$\tau_0 = \frac{1}{2}(\sigma_{yy_0} - \sigma_{xx_0}) \sin(2\theta) \tag{V–59}$$

Finally, the relations between stresses and displacements are:

$$\sigma_0' + \Delta\sigma' = \frac{K_n^0 \, h_0}{h} \, (\Delta h_0 + \Delta h) \tag{V–60}$$

$$\tau_0 + \Delta\tau = K_s^0 \, (\Delta s_0 + \Delta s) \tag{V–61}$$

The mechanical behaviour of the fracture is supposed to remain stick. Note a second mechanical law, considering damage, is implemented in the Lagamine code. This law is based on the shear-tensile cohesive model proposed by [Camacho and Ortiz, 1996]. This model is characterized by three parameters: the maximum cohesion, the history of relative displacement between the interface boundaries and the critical relative displacement corresponding to a complete decohesion. The interested reader may find an extensive description on the implementation of this damage law in the following theses [Bilbie, 2007], [Frey, 2010], [Marinelli, 2013] and [Van den Eijnden, 2015].

As it was defined in the microscale model in the previous part of the thesis, the effective stress in the fracture (appearing in Equation V–56) does not require a Biot's coefficient as usually used in macroscale constitutive laws for homogenized medium. Besides, a one-dimensional consolidation problem was studied by [Marinelli et al., 2016] to compare the results of the water saturated multiscale model with the analytical solution from the classical Biot poromechanics theory [Biot, 1941].

2. Applying Equation (IV–117).

14.7.2.2 Channel flow model

From the constitutive microscale model, the interface mass flux of water is given by

$$\omega_w = -\rho_w\, h_b\, k_{rw}\, \frac{h_b^2}{12}\, \frac{1}{\mu_w} \frac{dp_w^m}{ds} = -\rho_w\, \frac{k_{rw}}{\mu_w}\, \kappa(s) \frac{dp_w^m}{ds} \tag{V–62}$$

where $\kappa(s)$ is the geometric transmissivity function along the channel with s the coordinate along this channel. This equation provides the relation between the water pressure gradient along the channel and the channel water mass flux. The steady state flow condition at the microscale implies that the mass flux ω_w is constant over the length of the channel. Moreover, considering the scale separability, the fluid pressure variation is very small compared to the REV size and has a negligible effect on the fluid density ρ_w. The density is thus considered to be constant throughout the REV [3]. Under isothermal conditions, the water density is only dependent on the macroscale water pressure. In the same way, the relative permeability k_{rw} is only dependent on the macroscale fluid pressures.

The density ρ_w of the liquid phase evolves with the macroscale pressure p_w^M according to:

$$\rho_w = \rho_{w_0} \left(1 + \frac{p_w^M - p_{w_0}^M}{\chi_w}\right) \tag{V–63}$$

where ρ_{w_0} is the liquid density at the pressure $p_{w_0}^M$ and $1/\chi_w$ is the liquid compressibility. At $20°C$, $1/\chi_w = 5 \cdot 10^{-10} Pa^{-1}$.

Then, we can write the mass fluxes over the channel between s_1 and s_2 as

$$\begin{aligned} \omega_w^l &= [p_w^m(s_2) - p_w^m(s_1)]\, \frac{\rho_w(p_w^M)\, k_{rw}(p_w^M, p_{g,f}^M)}{\mu_w} \left(\int_{s_1}^{s_2} \frac{1}{\kappa(s)} ds\right)^{-1} \\ &= [p_w^m(s_2) - p_w^m(s_1)]\, \frac{\rho_w(p_w^M)\, k_{rw}(p_w^M, p_{g,f}^M)}{\mu_w}\, \Phi^l \end{aligned} \tag{V–64}$$

where Φ^l is the geometric transmissivity of the channel.

For gas, the interface mass flux is:

$$\begin{aligned} \omega_g &= -\rho_g\, h_b\, k_{rg}\, \frac{h_b^2}{12}\, \frac{1}{\mu_g} \frac{dp_g^m}{ds} - H_g\, \rho_g\, h_b\, k_{rw}\, \frac{h_b^2}{12}\, \frac{1}{\mu_w} \frac{dp_w^m}{ds} \\ &= -\frac{\rho_g\, k_{rg}}{\mu_g}\, \kappa\, \frac{dp_g^m}{ds} - H_g\, \frac{\rho_g\, k_{rw}}{\mu_w}\, \kappa\, \frac{dp_w^m}{ds} \end{aligned} \tag{V–65}$$

The classical ideal gas equation of state is used to write the gas density in the fractures as

$$\rho_g = \frac{M_{m_g}}{RT} p_g^M \tag{V–66}$$

where p_g^M is the macroscale gas pressure.

Note that, to be consistent with the scale separability and the negligible effect of the variations of the fluid pressures in the REV on the fluid densities, diffusive flows are not considered in the fractures. Over

3. This modification was introduced by [Van den Eijnden, 2015] and it is justified if the separation of scales is respected. In addition to this conceptual point of view, this modification has a numerical advantage compared to the original model: since the variations of the fluid densities are only dependent on the local fluid pressures, the resulting hydraulic system of equations becomes linear and is much easier to solve (see section 14.8.2).

the channel, the gas mass flux is then evaluated by:

$$\begin{aligned}\omega_g^l = & \left[p_g^m(s_2) - p_g^m(s_1)\right] \frac{\rho_g\, k_{rg}}{\mu_g} \left(\int_{s_1}^{s_2} \frac{1}{\kappa(s)} ds\right)^{-1} \\ & + \left[p_w^m(s_2) - p_w^m(s_1)\right] H_g\, \rho_g \frac{k_{rw}}{\mu_w} \left(\int_{s_1}^{s_2} \frac{1}{\kappa_w(s)} ds\right)^{-1} \\ = & \left[p_g^m(s_2) - p_g^m(s_1)\right] \frac{\rho_g\, k_{rg}}{\mu_g} \Phi^l + \left[p_w^m(s_2) - p_w^m(s_1)\right] H_g\, \rho_g \frac{k_{rw}}{\mu_w} \Phi^l\end{aligned} \tag{V–67}$$

In this work, no flow is directly considered in the matrix [4]. The fluxes $\overline{q}_w$ and $\overline{q}_g$ appearing in the balance equations and boundary conditions are therefore given by the fluxes in the interfaces, ω_w^l and ω_g^l.

14.8 Numerical solution

The problem is solved iteratively in two parts, starting with the mechanical problem and then finding the different flows for the given fracture apertures. The sequence is repeated until convergence.

14.8.1 Mechanical part

The system of field Equation (V–43) governing the microscale BVP is solved numerically using a full Newton-Raphson scheme. Knowing the configuration at time t in equilibrium with the boundary conditions, the objective is to find the configuration in equilibrium at the end of the time step. An updated configuration is first guessed, for which it is likely the equilibrium is not met. Residuals therefore appear in the balance equations and the aim is to find a new configuration for which the residuals vanish. In this purpose, the boundary volume is discretized with finite elements.

14.8.1.1 Continuum (Matrix)

For the matrix, a 4-node element [5] with 4 integration points is adopted for the spatial discretization. The coordinate system $[\xi, \eta]$ with nodal coordinates $[\pm 1, \pm 1]$ is used for the parent element (Figure V–8).

Between the nodal values, a bilinear interpolation may be applied using the following functions:

$$\begin{aligned}\mathcal{N}^{(1)} &= \frac{1}{4}(1-\xi)\cdot(1-\eta) & \mathcal{N}^{(2)} &= \frac{1}{4}(1+\xi)\cdot(1-\eta) \\ \mathcal{N}^{(3)} &= \frac{1}{4}(1+\xi)\cdot(1+\eta) & \mathcal{N}^{(4)} &= \frac{1}{4}(1-\xi)\cdot(1+\eta)\end{aligned} \tag{V–68}$$

4. Diffusive flows in the matrix are indirectly considered using a sorption time coefficient to compute the mean adsorbed gas pressure evolution with Equation (V–54).

5. In classical poromechanical computations, these elements are known to introduce oscillations in the numerical results of transient problems. The problem does not arise here. As the microscale computation is restricted to steady-state conditions, diffusive flows are not modelled in the matrix and the hydraulic problem given by the hydraulic network is solved separately.

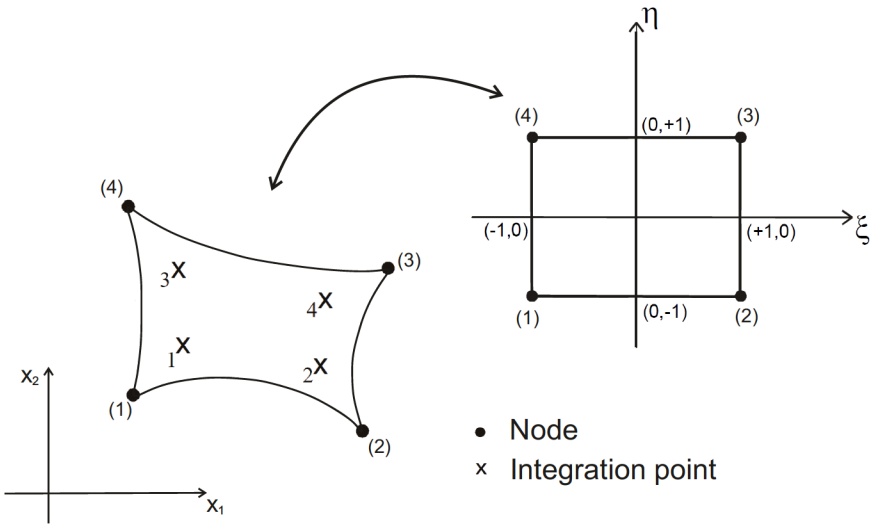

Figure V–8 – Two-dimensional 4-node element.

The column vectors of the nodal positions, displacements and velocities in global coordinates are denoted by $\{X^{Node}\}$, $\{U^{Node}\}$ and $\{V^{Node}\}$:

$$\{X^{Node}\} = \begin{Bmatrix} x_1^{(1)} \\ x_2^{(1)} \\ x_1^{(2)} \\ x_2^{(2)} \\ x_1^{(3)} \\ x_2^{(3)} \\ x_1^{(4)} \\ x_2^{(4)} \end{Bmatrix} \qquad \{U^{Node}\} = \begin{Bmatrix} u_1^{(1)} \\ u_2^{(1)} \\ u_1^{(2)} \\ u_2^{(2)} \\ u_1^{(3)} \\ u_2^{(3)} \\ u_1^{(4)} \\ u_2^{(4)} \end{Bmatrix} \qquad \{V^{Node}\} = \begin{Bmatrix} v_1^{(1)} \\ v_2^{(1)} \\ v_1^{(2)} \\ v_2^{(2)} \\ v_1^{(3)} \\ v_2^{(3)} \\ v_1^{(4)} \\ v_2^{(4)} \end{Bmatrix} = \{\dot{U}^{Node}\} \tag{V–69}$$

In order to express the strain $\dfrac{\partial u_i}{\partial x_j}$ as a function of its local coordinates and the nodal displacements, the following matrices $[A]$ and $[B]$ of partial derivatives are defined:

$$[A] = \begin{bmatrix} \dfrac{\partial \xi}{\partial x_1} & \dfrac{\partial \eta}{\partial x_1} & 0 & 0 \\ \dfrac{\partial \xi}{\partial x_2} & \dfrac{\partial \eta}{\partial x_2} & 0 & 0 \\ 0 & 0 & \dfrac{\partial \xi}{\partial x_1} & \dfrac{\partial \eta}{\partial x_1} \\ 0 & 0 & \dfrac{\partial \xi}{\partial x_2} & \dfrac{\partial \eta}{\partial x_2} \end{bmatrix} \tag{V–70}$$

$$[B] = \begin{bmatrix} \frac{\partial \mathcal{N}^{(1)}}{\partial \xi} & 0 & \frac{\partial \mathcal{N}^{(2)}}{\partial \xi} & 0 & \frac{\partial \mathcal{N}^{(3)}}{\partial \xi} & 0 & \frac{\partial \mathcal{N}^{(4)}}{\partial \xi} & 0 \\ \frac{\partial \mathcal{N}^{(1)}}{\partial \eta} & 0 & \frac{\partial \mathcal{N}^{(2)}}{\partial \eta} & 0 & \frac{\partial \mathcal{N}^{(3)}}{\partial \eta} & 0 & \frac{\partial \mathcal{N}^{(4)}}{\partial \eta} & 0 \\ 0 & \frac{\partial \mathcal{N}^{(1)}}{\partial \xi} & 0 & \frac{\partial \mathcal{N}^{(2)}}{\partial \xi} & 0 & \frac{\partial \mathcal{N}^{(3)}}{\partial \xi} & 0 & \frac{\partial \mathcal{N}^{(4)}}{\partial \xi} \\ 0 & \frac{\partial \mathcal{N}^{(1)}}{\partial \eta} & 0 & \frac{\partial \mathcal{N}^{(2)}}{\partial \eta} & 0 & \frac{\partial \mathcal{N}^{(3)}}{\partial \eta} & 0 & \frac{\partial \mathcal{N}^{(4)}}{\partial \eta} \end{bmatrix} \tag{V–71}$$

For each continuum element, the components of the left-hand side of the balance Equation (V–43) can now be written as

$$\left\{V^{*Node}\right\}^T \left[\int_{\Omega_e} [B]^T [A]^T [C_{mm}][A][B]\, d\Omega\right] \left\{\delta U^{Node}\right\} \tag{V–72}$$

with $[C_{mm}]$ the mechanical constitutive matrix:

$$\{\delta\sigma^m\} = \begin{Bmatrix} \delta\sigma_{11} \\ \delta\sigma_{12} \\ \delta\sigma_{21} \\ \delta\sigma_{22} \end{Bmatrix} = [C_{mm}]\{\delta U\} = [C_{mm}][A][B]\left\{\delta U^{Node}\right\} \tag{V–73}$$

The element stiffness matrix relating the variation of nodal displacements to the variation of the nodal forces is found as:

$$[K_{mm}]^e = \int_{\Omega^e} [B]^T [A]^T [C_{mm}][A][B]\, d\Omega = \sum_{IP} [B]^T [A]^T [C_{mm}][A][B]\ \det(J_{ij})\ W_G \tag{V–74}$$

where the integral over the element is replaced by a numerical integration on the parent element. J_{ij} is the Jacobian matrix of the transformation and W_G are the weights of the Gauss quadrature.

The column vector of residual forces on the 4 nodes of the element is

$$\{f\}^e = \begin{Bmatrix} f_1^{(1)} \\ f_2^{(1)} \\ f_1^{(2)} \\ f_2^{(2)} \\ f_1^{(3)} \\ f_2^{(3)} \\ f_1^{(4)} \\ f_2^{(4)} \end{Bmatrix} = \int_{\Omega_e} [B]^T [A]^T \{\sigma^m\} = \sum_{IP} \left[[B]^T [A]^T \{\sigma^m\}\right]_{IP} \det(J_{ij})\ W_G \tag{V–75}$$

14.8.1.2 Interfaces (Cleats)

For the discretization of the cleats, one-dimensional elements with 2 integration points are used. The only parent dimension ξ is required. Subject to define $\eta = 0$, the same interpolation functions as in Equation (V–68) can be used for the interface element. This element is constituted of 6 nodes but only 4 nodes present mechanical degrees of freedom (Figure V–9).

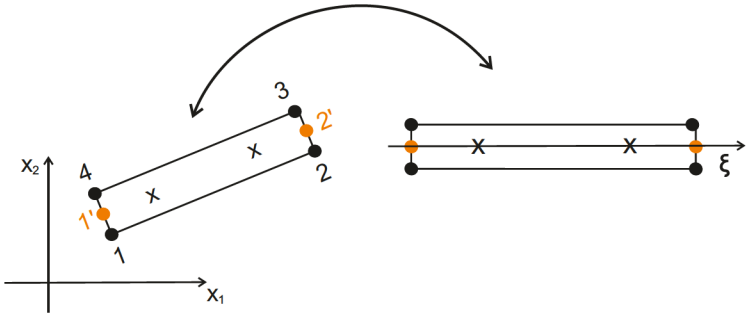

Figure V–9 – One-dimensional element.

In the same way as for the continuum, the column vectors $\{X^{Node}\}$, $\{U^{Node}\}$ and $\{V^{Node}\}$ can be used to denote the nodal positions, displacements and velocities of the 4 mechanical nodes of the interface. The tangential and normal relative opening of the interface, s and h, are computed with:

$$\begin{Bmatrix} s \\ h \end{Bmatrix} = [A^I][B^I]\{U^{Node}\} \tag{V–76}$$

where the matrix $[A^I]$ is

$$[A^I] = \begin{bmatrix} \cos\theta & \sin\theta \\ -\sin\theta & \cos\theta \end{bmatrix} \tag{V–77}$$

where θ is orientation of the interface compared to the global axis. The matrix $[B^I]$ is

$$[B^I] = \begin{bmatrix} -\mathcal{N}^{(1)} & 0 & -\mathcal{N}^{(2)} & 0 & \mathcal{N}^{(3)} & 0 & \mathcal{N}^{(4)} & 0 \\ 0 & -\mathcal{N}^{(1)} & 0 & -\mathcal{N}^{(2)} & 0 & \mathcal{N}^{(3)} & 0 & \mathcal{N}^{(4)} \end{bmatrix} \tag{V–78}$$

It is then now possible to write the two components of the right-hand side of the balance Equation (V–43). For individual elements, it reads

$$\left\{V^{*Node}\right\}^T \left[\int_{I_e^{int}} [B^I]^T [A^I]^T [C^I_{mm}][A^I][B^I] d\Omega\right] \left\{\delta U^{Node}\right\} \tag{V–79}$$

with $[C^I_{mm}]$ a consistent linearization of the interface cohesive/frictional forces:

$$\begin{Bmatrix} \delta T_t \\ \delta T_n \end{Bmatrix} = \begin{bmatrix} C^I_{tt} & C^I_{tn} \\ C^I_{nt} & C^I_{nn} \end{bmatrix} \begin{Bmatrix} \delta s \\ \delta h \end{Bmatrix} \tag{V–80}$$

The element stiffness matrix relating the variation of nodal displacements to the variation of the nodal forces is found as:

$$[K^I_{mm}]^e = \int_{I_e^{int}} [B^I]^T [A^I]^T [C^I_{mm}][A^I][B^I]\, d\Omega = \sum_{IP} [B^I]^T [A^I]^T [C^I_{mm}][A^I][B^I]\ \det\left(J^I_{ij}\right) W_G \tag{V–81}$$

The residual forces on the nodes of the interface elements are

$$\{f^I\}^e = \int_{I_e^{int}} [B^I]^T [A^I]^T \{T\} = \sum_{IP} \left[[B^I]^T [A^I]^T \{T\}\right]_{IP} \det\left(J^I_{ij}\right) W_G \tag{V–82}$$

14.8.1.3 Global assembly

Assembling the element stiffness matrices $[K_{mm}]^e$ and $[K^I_{mm}]^e$ and the element nodal force vectors $\{f\}^e$ and $\{f^I\}^e$, the global stiffness matrix $[K_{mm}]$ yields the incremental relation between the nodal displacement $\{u\}$ and the nodal force $\{f\}$:

$$[K_{mm}]\{\delta u\} = \{\delta f\} \tag{V–83}$$

This relation is valid for constant fluid pressures.

14.8.2 Hydraulic part

The explicit description of the fluid network is solved separately from the mechanical problem in order to find the profiles of the gas and water pressures that respect the boundary conditions and, at the same time, have some average values of the pressure fields equal to the macroscopic water and gas pressures. The particular case of coal involves sorption/desorption mechanisms which are taken into account in the storage term of the macroscale, it is discussed later in section 14.9.3.

The mass conservation along the channel leads to write that, for each node of the hydraulic network, the sum of the input flows must be equal the sum of output flows (Fiqure V–10, Equation V–84).

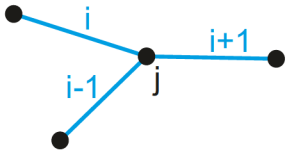

$$\omega^{i-1} + \omega^{i} + \omega^{i+1} = 0 \qquad \text{(V–84)}$$
$$\text{with } \omega^{i} \propto \Phi^{i}(p_j - p_{j-1})$$

Figure V–10 – Mass balance on node j.

For water, the mass balance equations written at each intersection lead to write the following system of equations:

$$[G_{ww}]\{p_w^m\} = 0 \qquad \text{(V–85)}$$

For instance, Figure V–11 gives a basic example of a channel network.

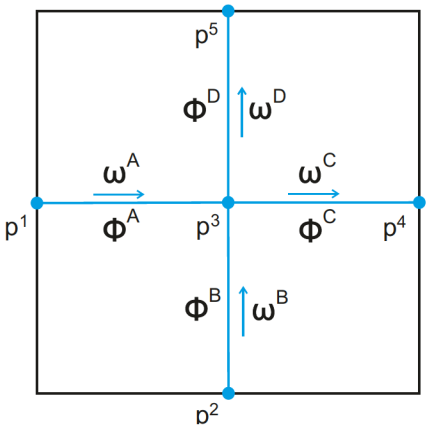

Figure V–11 – Example of a channel network.

For this configuration, taking into account the homologous connectivity of lead and follow node couples over the periodic boundaries, the matrix $[G_{ww}]$ is given by:

$$[G_{ww}] = \frac{\rho_w\, k_{rw}}{\mu_w} \begin{bmatrix} \Phi^A & 0 & -\Phi^A - \Phi^C & \Phi^C & 0 \\ 0 & \Phi^B & -\Phi^B - \Phi^D & 0 & \Phi^D \\ -\Phi^A & -\Phi^B & \Phi^A + \Phi^B + \Phi^C + \Phi^D & -\Phi^C & -\Phi^D \end{bmatrix} \qquad \text{(V–86)}$$

More equations are required to find the 5 unknown nodal pressures. Taking into account the conditions given by the macroscopic pressure gradient (Equation V–34), the system to solve is

$$\begin{bmatrix} \Phi'^A & 0 & -\Phi'^A - \Phi'^C & \Phi'^C & 0 \\ 0 & \Phi'^B & -\Phi'^B - \Phi'^D & 0 & \Phi'^D \\ -\Phi'^A & -\Phi'^B & \Phi'^A + \Phi'^B + \Phi'^C + \Phi'^D & -\Phi'^C & -\Phi'^D \\ -1 & 0 & 0 & 1 & 0 \\ 0 & -1 & 0 & 0 & 1 \end{bmatrix} \begin{pmatrix} p_w^1 \\ p_w^2 \\ p_w^3 \\ p_w^4 \\ p_w^5 \end{pmatrix} = \begin{pmatrix} 0 \\ 0 \\ 0 \\ (\Delta p_w)_x^M \\ (\Delta p_w)_y^M \end{pmatrix} \qquad \text{(V–87)}$$

where $\Phi'^{l} = \dfrac{\rho_w\, k_{rw}}{\mu_w} \cdot \Phi^{l}$. This system is still ill-posed as the third equation is a linear combination of the first and second equations. This is overcome by applying the macroscopic pressure at one of the nodes of the hydraulic network:

$$\begin{bmatrix} \Phi'^{A} & 0 & -\Phi'^{A} - \Phi'^{C} & \Phi'^{C} & 0 \\ 0 & 1 & 0 & 0 & 0 \\ -\Phi'^{A} & -\Phi'^{B} & \Phi'^{A} + \Phi'^{B} + \Phi'^{C} + \Phi'^{D} & -\Phi'^{C} & -\Phi'^{D} \\ -1 & 0 & 0 & 1 & 0 \\ 0 & -1 & 0 & 0 & 1 \end{bmatrix} \begin{pmatrix} p_w^1 \\ p_w^2 \\ p_w^3 \\ p_w^4 \\ p_w^5 \end{pmatrix} = \begin{pmatrix} 0 \\ p_w^M \\ 0 \\ (\Delta p_w)_x^M \\ (\Delta p_w)_y^M \end{pmatrix} \tag{V–88}$$

For gas, as gas dissolved in the water may be considered in the cleats, the advective flows of water implies some gas mass fluxes. The following system of equations can therefore be considered:

$$[G_{gg}]\{p_g^m\} + [G_{gw}]\{p_w^m\} = 0 \tag{V–89}$$

In the same way, the matrix $[G_{gg}]$ for the configuration in Figure V–11 is given by:

$$[G_{gg}] = \frac{\rho_g\, k_{rg}}{\mu_g} \begin{bmatrix} \Phi^{A} & 0 & -\Phi^{A} - \Phi^{C} & \Phi^{C} & 0 \\ 0 & \Phi^{B} & -\Phi^{B} - \Phi^{D} & 0 & \Phi^{D} \\ -\Phi^{A} & -\Phi^{B} & \Phi^{A} + \Phi^{B} + \Phi^{C} + \Phi^{D} & -\Phi^{C} & -\Phi^{D} \end{bmatrix} \tag{V–90}$$

The matrix $[G_{gw}]$ is:

$$[G_{gw}] = \frac{\rho_g^d\, k_{rw}}{\mu_w} \begin{bmatrix} \Phi^{A} & 0 & -\Phi^{A} - \Phi^{C} & \Phi^{C} & 0 \\ 0 & \Phi^{B} & -\Phi^{B} - \Phi^{D} & 0 & \Phi^{D} \\ -\Phi^{A} & -\Phi^{B} & \Phi^{A} + \Phi^{B} + \Phi^{C} + \Phi^{D} & -\Phi^{C} & -\Phi^{D} \end{bmatrix} \tag{V–91}$$

Actually, the system of equations (V–88) for water is solved independently from the microscopic gas pressures [6]. The microscopic water pressures appearing in the system (V–89) are therefore already known before solving the system for gas and it may be written as an independent term on the right side of the equation. Then, applying the macroscopic gas gradient and the macroscopic gas pressure, the system to solve is finally:

$$\begin{aligned} &\begin{bmatrix} \Phi''^{A} & 0 & -\Phi''^{A} - \Phi''^{C} & \Phi''^{C} & 0 \\ 0 & 1 & 0 & 0 & 0 \\ -\Phi''^{A} & -\Phi''^{B} & \Phi''^{A} + \Phi''^{B} + \Phi''^{C} + \Phi''^{D} & -\Phi''^{C} & -\Phi''^{D} \\ -1 & 0 & 0 & 1 & 0 \\ 0 & -1 & 0 & 0 & 1 \end{bmatrix} \begin{pmatrix} p_g^1 \\ p_g^2 \\ p_g^3 \\ p_g^4 \\ p_g^5 \end{pmatrix} \\ &= -\frac{\rho_g^d\, k_{rw}}{\mu_w} \begin{bmatrix} \Phi^{A} & 0 & -\Phi^{A} - \Phi^{C} & \Phi^{C} & 0 \\ 0 & \Phi^{B} & -\Phi^{B} - \Phi^{D} & 0 & \Phi^{D} \\ -\Phi^{A} & -\Phi^{B} & \Phi^{A} + \Phi^{B} + \Phi^{C} + \Phi^{D} & -\Phi^{C} & -\Phi^{D} \end{bmatrix} \begin{pmatrix} p_w^1 \\ p_w^2 \\ p_w^3 \\ p_w^4 \\ p_w^5 \end{pmatrix} + \begin{pmatrix} 0 \\ p_g^M \\ 0 \\ (\Delta p_g)_x^M \\ (\Delta p_g)_y^M \end{pmatrix} \end{aligned} \tag{V–92}$$

where $\Phi''^{l} = \dfrac{\rho_g\, k_{rg}}{\mu_g} \cdot \Phi^{l}$.

14.9 Homogenized macroscale response

The micro-to-macro transition is derived from the Hill-Mandel macro-homogeneity condition which requires the average microscale work to be equal to the macroscale work. As the interfaces introduce discontinuities at the microscale, the computation of the microscale virtual work is not trivial. Moreover, fluid variables must also be homogenized.

6. Densities and relative permeabilities are determined based on the macroscopic fluid pressures.

14.9.1 Stresses

Under the small strain assumption, the macro-homogeneity condition in a virtual work formulation reads

$$\sigma_{ij}^{M}\,\frac{\partial u_i^{*M}}{\partial x_j} \equiv \frac{1}{\Omega}\int_{\Omega} \sigma_{ij}^{m}\,\frac{\partial u_i^{*\jmath m}}{\partial x_j}\,d\Omega \tag{V–93}$$

where an equivalent continuous microscale displacement field $u_i^{\jmath m}$ has to be introduced to overcome the presence of the discontinuities. To define the equivalent strain $\dfrac{\partial u_i^{\jmath m}}{\partial x_j}$, a zone of arbitrary width l is defined around the interface (Figure V–12).

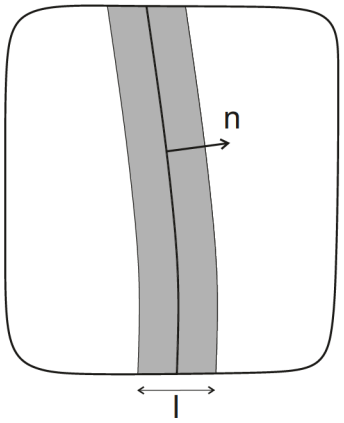

Figure V–12 – Definition of a contact zone of width l around an interface.

Outside the contact zone, the strain remains unchanged: $\dfrac{\partial u_i^{\jmath m}}{\partial x_j} = \dfrac{\partial u_i^{m}}{\partial x_j}$. But inside the contact zone, the equivalent strain can be seen as the sum of the deformation of the contact zone by the strain field $\dfrac{\partial u_i^{m}}{\partial x_j}$ and the interface relative displacement Δu_i:

$$\frac{\partial u_i^{\jmath m}}{\partial x_j} = \frac{1}{l}\left(\int_l \frac{\partial u_i^{m}}{\partial x_j} dl + \Delta u_i\, n_j\right) \tag{V–94}$$

where n_j is the interface normal vector.

This consideration allows to apply Gauss theorem to transform the domain integral over deformation in Equation (V–93) into a boundary integral over displacement:

$$\sigma_{ij}^{M}\,\frac{\partial u_i^{*M}}{\partial x_j} \equiv \frac{1}{\Omega}\int_{\Omega} \sigma_{ij}^{m}\,\frac{\partial u_i^{*\jmath m}}{\partial x_j}\,d\Omega = \frac{1}{\Omega}\int_{\Gamma} \bar{t}_i\, u_i^{*\jmath m}\,d\Gamma \tag{V–95}$$

Using the periodic boundary conditions, this equation reduces to

$$\sigma_{ij}^{M}\,\frac{\partial u_i^{*M}}{\partial x_j} \equiv \frac{1}{\Omega}\,\frac{\partial u_i^{*M}}{\partial x_j}\int_{\Gamma} \bar{t}_i\, x_j\,d\Gamma \tag{V–96}$$

Thence, it means that

$$\begin{aligned}\sigma_{ij}^{M} &= \frac{1}{\Omega}\int_{\Gamma} \bar{t}_i\, x_j\,d\Gamma \\ &= \frac{1}{\Omega}\int_{\Omega} \sigma_{ij}^{m}\,d\Omega\end{aligned} \tag{V–97}$$

14.9.2 Fluid fluxes

The same approach can be followed for the fluid part of the balance equations. This method was used by [Özdemir, 2009] for the homogenization of thermal fluxes and by [Massart and Selvadurai, 2014] for fluid fluxes. The macro-homogeneity condition for water reads:

$$\dot{M}_w^M \; p_w^{*M} - f_{w_i}^M \; \frac{\partial p_w^{*M}}{\partial x_i} = \frac{1}{\Omega} \int_\Omega \left(\dot{M}_w^m \; p_w^{*M} - f_{w_i}^m \; \frac{\partial p_w^{*M}}{\partial x_i} \right) d\Omega \tag{V–98}$$

Under steady-state conditions at the micro-level and then separating the timescales, this reduces temporarily to

$$f_{w_i}^M \; \frac{\partial p_w^{*M}}{\partial x_i} = \frac{1}{\Omega} \int_\Omega f_{w_i}^m \; \frac{\partial p_w^{*M}}{\partial x_i} d\Omega = \frac{1}{\Omega} \int_\Gamma \overline{q}_w^m \; p_w^{*M} \; d\Gamma \tag{V–99}$$

The boundary conditions allow to write:

$$f_{w_i}^M \; \frac{\partial p_w^{*M}}{\partial x_i} = \frac{1}{\Omega} \; \frac{\partial p_w^{*M}}{\partial x_i} \int_\Gamma \overline{q}_w^m \; x_i \; d\Gamma \tag{V–100}$$

Thence, the macroscale fluxes are the integrals of the microscale boundary fluxes:

$$f_{w_i}^M = \frac{1}{\Omega} \int_\Gamma \overline{q}_w^m \; x_i \; d\Gamma \tag{V–101}$$

$$f_{g_i}^M = \frac{1}{\Omega} \int_\Gamma \overline{q}_g^m \; x_i \; d\Gamma \tag{V–102}$$

The macroscale fluxes are therefore the sum of the fluxes on the nodes belonging to the follow boundary.

14.9.3 Fluid masses

The macroscopic fluid contents M_w^M and M_g^M are directly defined as the total amounts of fluid in the REV. As water is assumed only in the fractures, the water content M_w^M is given by (ρ_w is constant over the volume):

$$M_w^M = \frac{1}{\Omega} \int_{\Omega_w^{int}} \rho_w \; d\Omega = \rho_w \; S_r \; \phi_f \tag{V–103}$$

with ρ_w constant over the REV and where S_r is defined as $\dfrac{\Omega_w^{int}}{\Omega^{int}}$ and ϕ_f as $\dfrac{\Omega^{int}}{\Omega}$.

The gas content M_g^M is the amount of gas in the interface (gas phase and dissolved gas in the water) and the adsorbed gas in the matrix for coal.

$$\begin{aligned} M_g^M &= M_{g,f}^g + M_{g,f}^d + M_{g,m}^{Ad} \\ &= \frac{1}{\Omega} \left(\int_{\Omega_g^{int}} \rho_g \; d\Omega + \int_{\Omega_w^{int}} \rho_g^d \; d\Omega + \int_\Omega \rho_g^{Ad} \; d\Omega \right) \\ &= \rho_g \; (1 - S_r) \; \phi_f + \rho_g^d \; S_r \; \phi_f + \rho_g^{Ad} \cdot (1 - \phi_f) \end{aligned} \tag{V–104}$$

with ρ_g constant over the REV. Note ρ_g^{Ad} is directly related to the adsorbed gas pressure p_g^{Ad}. Thus, considering the evolution of p_g^{Ad} taking into account the sorption time (Equation V–54), a pseudo-steady state actually considered for the hydraulic problem.

The fluid mass storage terms $\dot{M}_w^{M,t}$ and $\dot{M}_g^{M,t}$ are obtained with some finite difference approximations over the time interval Δt:

$$\dot{M}_w^{M,t} \approx \frac{M_w^{M,t} - M_w^{M,t-\Delta t}}{\Delta t} \tag{V–105}$$

$$\dot{M}_g^{M,t} \approx \frac{M_g^{M,t} - M_g^{M,t-\Delta t}}{\Delta t} \tag{V–106}$$

14.9.4 Macroscale stiffness matrix

The macroscale computations are governed by:

$$\begin{bmatrix} K^M_{mm}\ {}_{4x4} & K^M_{mw}\ {}_{4x3} & K^M_{mg}\ {}_{4x3} \\ K^M_{wm}\ {}_{3x4} & K^M_{ww}\ {}_{3x3} & K^M_{wg}\ {}_{3x3} \\ K^M_{gm}\ {}_{3x4} & K^M_{gw}\ {}_{3x3} & K^M_{gg}\ {}_{3x3} \end{bmatrix} \begin{matrix} {}^M\ {}_4 \\ p^M_w\ {}_4 \\ p^M_w\ {}_3 \\ p^M_g\ {}_4 \\ p^M_g\ {}_3 \end{matrix} = \begin{matrix} {}^M\ {}_4 \\ f^M_w\ {}_4 \\ \dot{M}^M_w\ {}_3 \\ f^M_g\ {}_4 \\ \dot{M}^M_g\ {}_3 \end{matrix} \tag{V–107}$$

which can be summarized as

$$A^M\ {}_{10x10}\quad U^M\ {}_{10} = {}^M\ {}_{10} \tag{V–108}$$

where A^M is the macroscale stiffness matrix, U^M contains the infinitesimal variations of the macroscale variables and ^{M} is their responses. This stiffness matrix A^M is obtained by numerical perturbations. Developments to obtain the macroscale stiffness matrix by static condensation are given in Appendix A but are not implemented.

14.10 Numerical implementation

The coupled finite element used to mesh the macroscale is the ELEFE2 element. The law to be used for the doublescale computation is FE2WG. It serves to solve the microscale boundary problem and give the homogenized macroscale response.

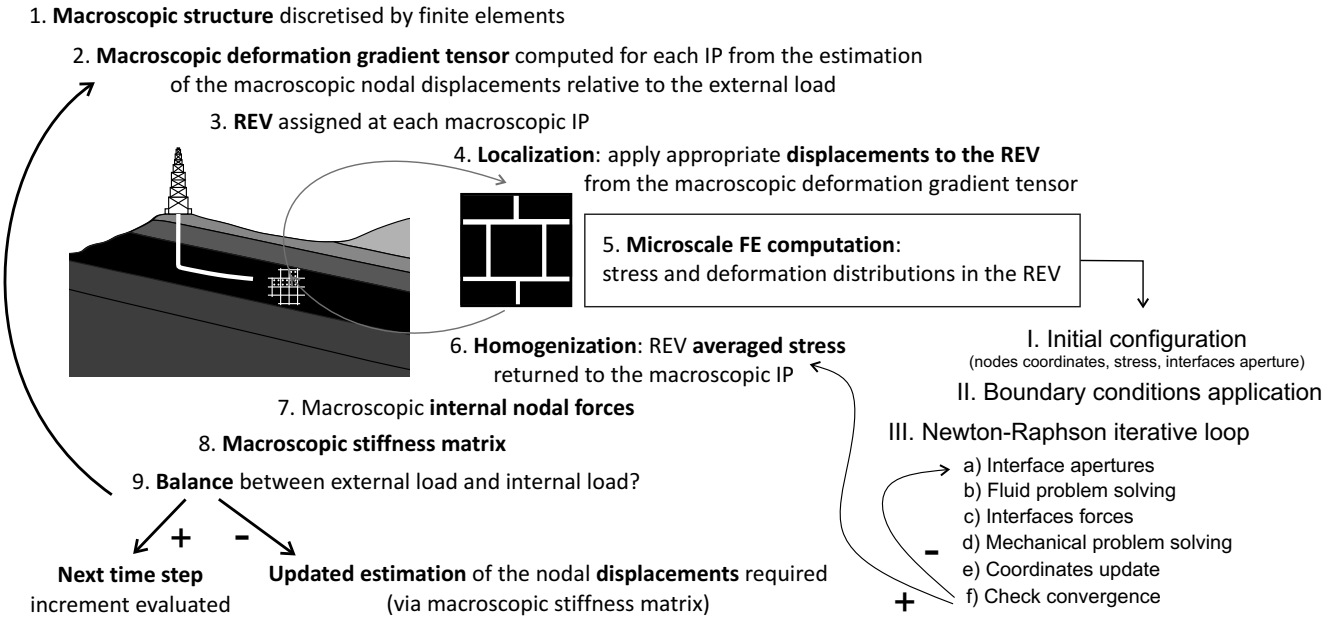

Figure V–13 – Summary of the numerical FE^2 computation.

15. Reservoir modelling

In this last section of the thesis, the multiscale model is applied to the modelling of coalbed methane production from a wellbore. A synthetic production scenario is first considered to perform a sensitivity analysis. Finally, as for the macroscale model in section 8, a real production scenario is considered with the Horseshoe Canyon case.

15.1 Reference case

The macroscale mesh and the geometry of the microstructure considered for the reference simulation is given in Figure V–14. REV is made up few blocks arranged in staggered rows with continuous horizontal cleats. The size of the microstructure is $1cm$ over $1cm$. All the parameters defining the reference case are reported in Table V–1. The seam is $2m$ high and the vertical displacement is blocked on the bottom boundary while a $5MPa$ overburden pressure is applied on the top boundary. Axisymmetric conditions are considered around the well on the left side. The smallest element close to the well is $5cm$ wide. The size of the elements increases with a geometric factor of 1 5, it means 12 elements represent $13m$. The drained volume is approximately $1000m^3$. An actual reservoir is certainly larger but this synthetic reservoir allows us to test very quickly dozens of parameter sets since there are few macroscopic elements (less computation time) and the time to drain the reservoir is not too long to achieve the bell shape of the production curve (less time to simulate). A larger reservoir is modelled with the Horseshoe Canyon case.

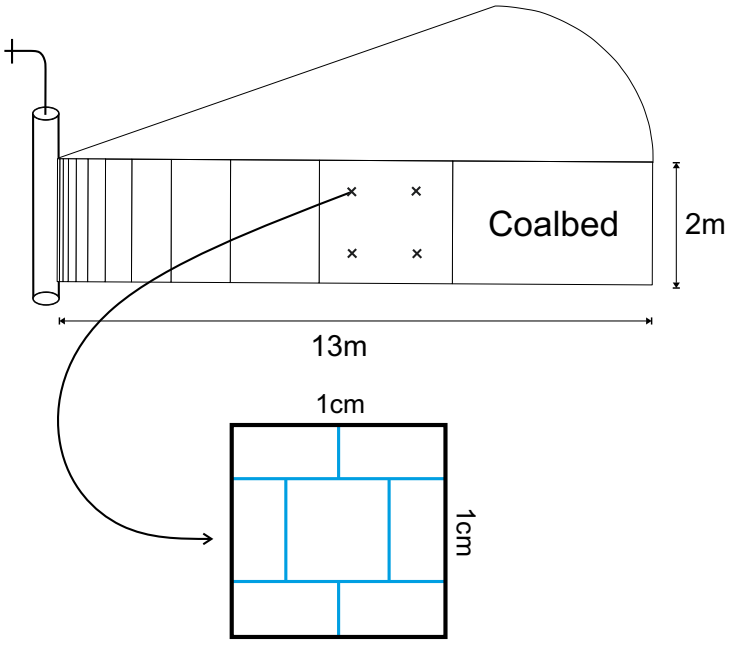

Figure V–14 – Macroscale mesh and REV geometry.

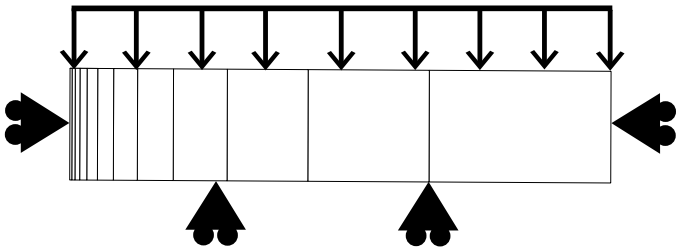

Figure V–15 – Macroscale mechanical boundary conditions.

Parameters	Values
Seam thickness (m)	2
Drainage radius (m)	13
Temperature (K)	293 15
Water pressure (Pa)	3E6
Gas pressure (Pa)	3E6
Overburden pressure (Pa)	5E6
Well transmissibility T (m^3)	1E-10
Coal density $_c$ ($kg\ m^3$)	1500
Matrix Young's modulus E_m (Pa)	1 21E9
Matrix Poisson's ratio $_m$	0 16
Matrix width w (m)	0 005 0 01
Cleat aperture* h (m)	20E-6
Cleat normal stiffness* K_n ($Pa\ m$)	100E9
Cleat shear stiffness K_s ($Pa\ m$)	100E9
Minimum cleat aperture (m)	1E-6
Sorption time $\mathcal{T}$ (hours)	10
Langmuir volume V_L ($m^3\ kg$)	0 02
Langmuir pressure P_L (Pa)	1 5E6
Matrix shrinkage coefficient ($kg\ m^3$)	0 4
Entry capillary pressure p_e (Pa)	1E5
Distribution index	0 25
Residual water saturation $S_{r\,res}$	0 1
Residual gas saturation	0 0

Table V–1 – Parameters defining the reference case. * Aperture and stiffness given for a null stress.

Water and gas pressures are initialized to $3MPa$, the reservoir is water saturated. Given the overburden pressure of $5MPa$, the effective stress in the cleats is $2MPa$. Note the cleat aperture $20\mu m$ in Table V–1 is given for a null stress, as encoded by the user in the Lagamine data file. At the initial effective stress state, the cleat aperture [1] is actually $10\mu m$ and the normal stiffness $225\ \ 10^9\ Pa\ m$. The modelling consists in simulating a drop in the pressure at the well from 3MPa to 1MPa in one day. This pressure drawdown causes the water and gas to flow towards the well. Figure V–16 presents the water pressure profile obtained due to the pumping.

1. Determined using Equation (V–56).

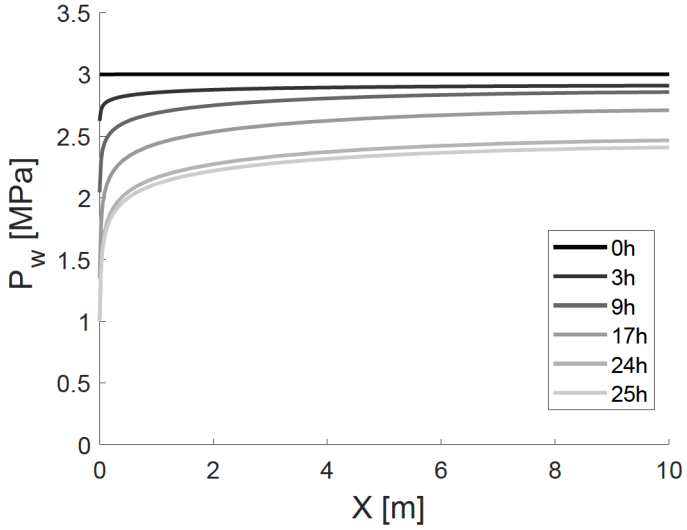

Figure V–16 – Reference case parameters: water pressure drawdown profile for different times.

The most critical water pressure gradient is observed close to the well at the exact time we stop decreasing the well pressure to maintain it at a constant value of $1MPa$, *i.e.* at $24h$ in this case. At this time, the $0.05m$ wide element next to the well shows a water pressure difference of $0.44MPa$ between its left edge ($p_{well} = 1MPa$) and its center ($p_{cent} = 1.44MPa$)[2]. It corresponds to a pressure gradient of $17.6MPa/m$. This results obviously depends on the permeability of the reservoir, it is about $10^{-14}m^2$ ($10mD$) for this simulation. Here, the water pressure profile gives a critical macroscopic characteristic length of $6.9cm$ over the first half of the first element.

$$L_{c_{crit}} = \bar{p} \cdot \frac{\Delta x}{\Delta p} = \frac{p_{cent} + p_{well}}{2} \frac{\Delta x}{p_{cent} - p_{well}} = 0.069m \tag{V–109}$$

Over the second half of this element, the characteristic length is already $22.6cm$, largely greater than the REV size of $1cm$. For comparison, the water pressure gradient in the second half of the 12^{th} element is only $1.9kPa/m$ at the same time. In this area, the separation between the scales is more than 6 orders of magnitude.

For the same pressure drop of $2MPa$, different times of loading are now tested leading to different pressure rates at the well. Figure V–17 shows the evolution of the critical length with the water pressure drop rate. The lower the rate, the larger the characteristic length, the greater the separation between the scales. The minimum characteristic length will be obtained for a pulse loading, this value can be *a priori* determined for the given macroscale mesh. Indeed, the pressure at the well is instantaneously set to the final pressure of $1MPa$ while the pressure at the center of the first element is still the initial pressure of $3MPa$. In this particular case, the mean pressure is equal to the difference of pressure between the well and the center of the first element. Then, the minimum critical characteristic length is directly the length of the half of the first element, *i.e.* $2.5cm$, which is still greater than the size of the REV. Considering an even more critical case where the well pressure is dropped instantaneously to a very small value compared to its initial value ($p_{well} \ll p_{cent}$), then the macroscale characteristic length tends to half of the length of first half-element, $\frac{5cm}{4} > 1cm$. The macroscale mesh has therefore to be chosen with care so that its smallest element is large enough to still ensure the separation of scales and small enough to avoid numerical oscillations (depending also on the permeability and the hydraulic storage). From the discussion above, taking *a priori* the smallest element of the macroscale mesh with a size at least larger than four times the size of the REV ensures the macroscale is larger than the microscale for any pressure drop at any time in any area. Depending how far is the loading compared to a pulse (depending

2. The analysis is performed on the half-element since 8-nodes elements are used for the macroscale mesh.

on the permeability), the macroscopic characteristic length will be very larger than the microscopic characteristic length. This can be verified *a posteriori*.

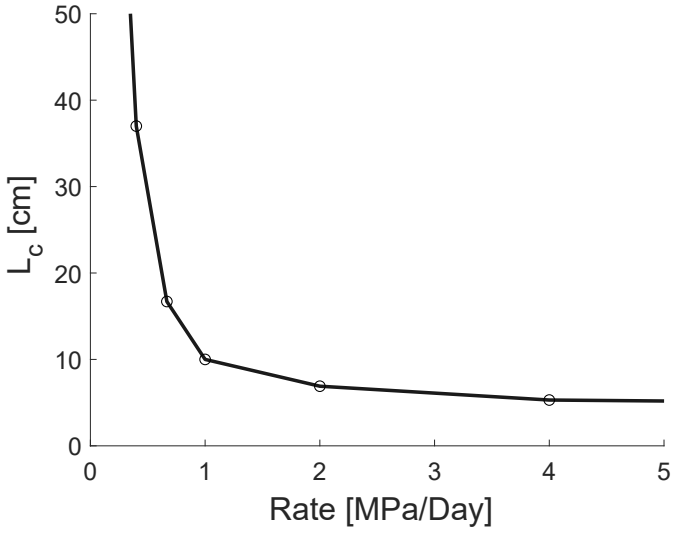

Figure V–17 – Reference case parameters: evolution of the critical characteristic length with the loading rate.

In the early stages, the permeability to gas is lower than the one to water as the reservoir is initially saturated. For the same loading at the well, the pressure gradient in the first element is therefore higher for gas than water. A critical gradient of 39 8$MPa\ \ m$ is obtained in the first half of the first element for the pressure drop of 2MPa in one day, it corresponds to a macroscopic characteristic length of 4 0cm. The minimal characteristic length is the same as water.

From a time point of view, the rate of pressure drop is 2$MPa\ \ day$ at the well. After one day, at the time the well pressure reaches its minimum of 1MPa, the macroscopic characteristic time is therefore 0 5 day. This characteristic time is therefore lower than the sorption time set to 1 day. As a double porosity effect is not negligible at the most critical time close to the well for a concevable sorption time, it was therefore desirable to take into account the sorption time to compute the adsorbed gas pressure evolution in the matrix (microscale). This adsorbed gas influences the macroscopic storage term in the gas mass balance. The influence of the sorption time and other parameters will be analysed in the sensitivity study.

Water and gas production rates are plotted in Figure V–18 for one year and half. Water production peaks after one day, at less than $2m^3\ \ day$. Then, desaturation of the reservoir increases the gas permeability and gas production peaks few days after the water, at more than $400m^3\ \ day$ (standard conditions). The bell shape of the production curve is related to the size of the reservoir and the outer boundary conditions. With a small reservoir and an impermeable boundary, a plateau is not observed.

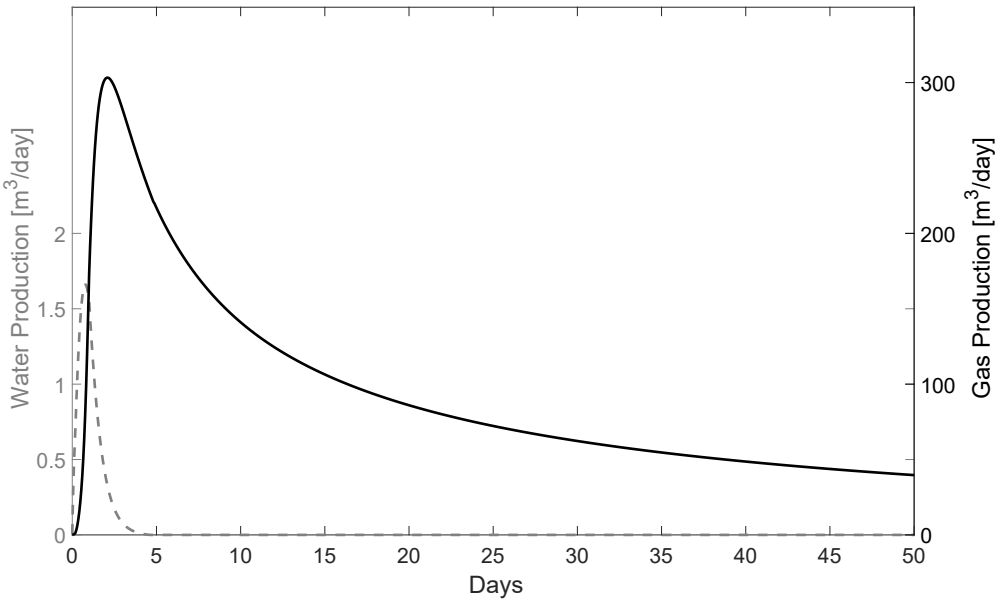

Figure V–18 – Reference case parameters: production curves.

Figure V–19 shows the integration of the gas production with time to give the cumulative gas production curve. The total production tends to $8330m^3$ (dotted line), which is the total volume of gas initially present in the reservoir given the Langmuir's parameters (Table V–1).

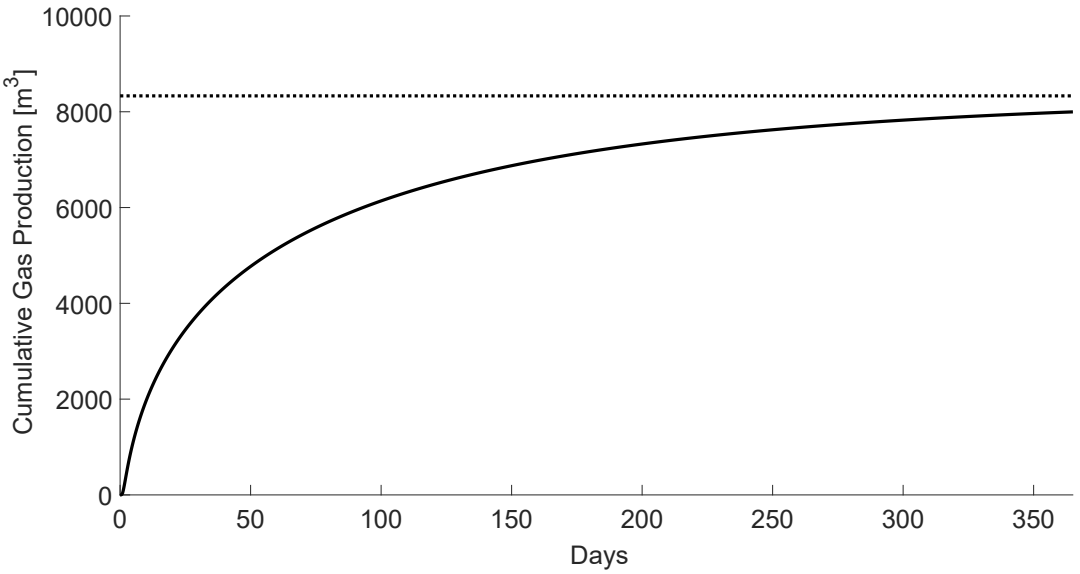

Figure V–19 – Reference case parameters: cumulative gas production

These production curves hides the evolution of the permeability. As no macroscopic permeability is actually used (since there are no macroscopic constitutive laws), a trick is needed to obtain this information. In a conventional model, permeability links the fluxes and the hydraulic gradient. In our multiscale model, we still have a stiffness matrix to link fluxes and pressure gradient. However, this stiffness matrix component contains also the relative permeability evolution [3] following desaturation. The intrinsic

3. Note that the macroscopic relative permeability exists because the same retention curve is used for all the fractures (e.g. entry capillary pressure is independent of the aperture). However, the multiscale approach is not restricted to this case and wanting to calculate unused macroscopic variables is becoming increasingly meaningless.

permeability is then given by:

$$k \quad \frac{\mu_w}{k_{rw} \; _w} \; K^M_{wwx} \tag{V–110}$$

where K^M_{wwx} is the macroscopic stiffness matrix component connecting the water flux towards the well and the corresponding pressure gradient. It is determined at each integration point from the miscrocale finite element computation. Figure V–20 shows the profiles along the seam at different times of the intrinsic permeability evolution. The permeability is almost divided by two after two days with the parameters of this reference case. The effective stress has a larger effect than the shrinkage in this case.

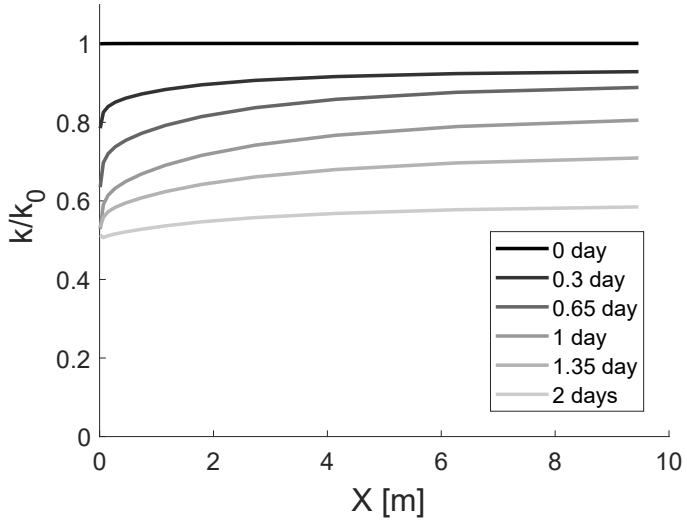

Figure V–20 – Reference case parameters: intrinsic permeability profiles at different times.

In the previous simulation, reservoir boundary conditions were considered with the overburden pressure applied on the top boundary. In Figure V–21, the production is compared against constant volume conditions. The latter conditions increases the production peak as the effect of the matrix shrinkage on the cleats is exacerbated, it is observed in the permeability evolution in Figure V–22. This aspect is discussed later in section 15.2.5 where the effect of the matrix shrinkage is discussed. It is likely these two boundary conditions give a range of the production curve for a real reservoir.

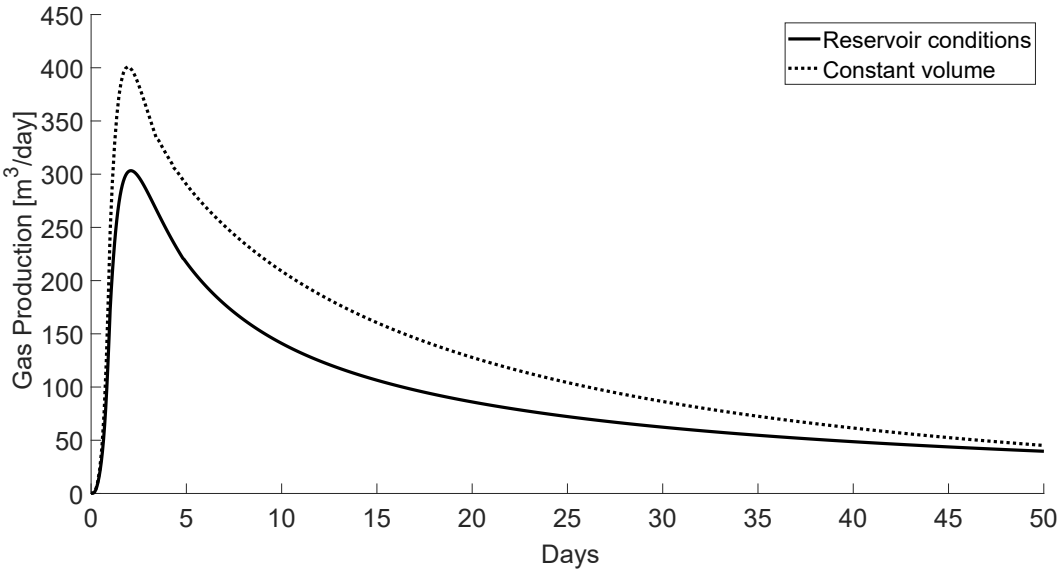

Figure V–21 – Reference case parameters: Influence of the boundary conditions on the gas production.

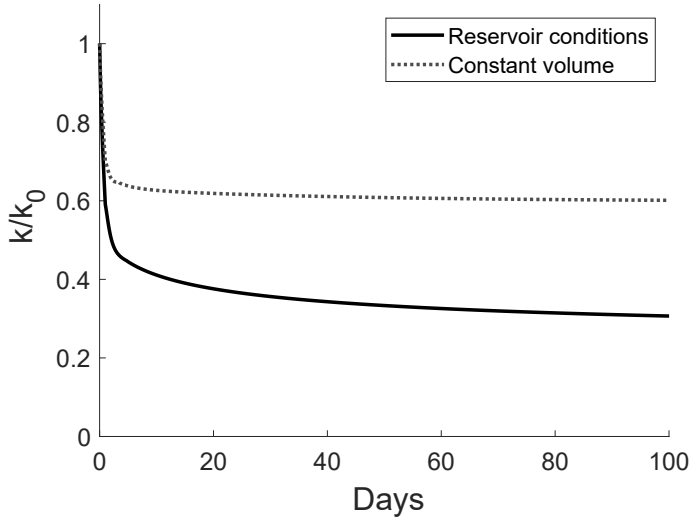

Figure V–22 – Reference case parameters: intrinsic permeability evolution at x 6 6cm.

The microstructure of the reference case (Figure V–14) considers two horizontal continuous fractures while vertically, there is a single fracture which is not straight. It is therefore clear that the permeability of the medium is not isotropic and that the orientation of the microstructure influences the response of the model. Figures V–23 and V–24 give the production curves when rotating the microstructure to 90°. The peak value is approximately divided by two since there is now only one fracture instead of two contributing to the permeability towards the well. However, the meaning of the ratio is not straightforward as the peak is also delayed of few days. Given the peak is lower and later, it naturally takes more time to empty the tank. As the number of fractures is not the same in the two directions, it is difficult to highlight a tortuosity effect just by rotating the REV. This effect is considered in the following (section 15.2.4).

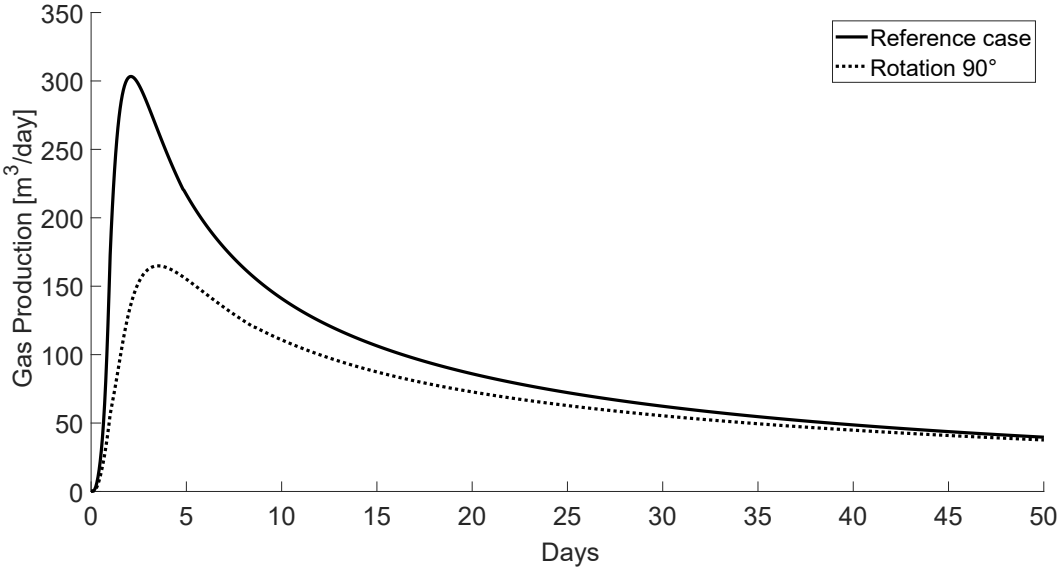

Figure V–23 – Reference case with REV rotation: production curve.

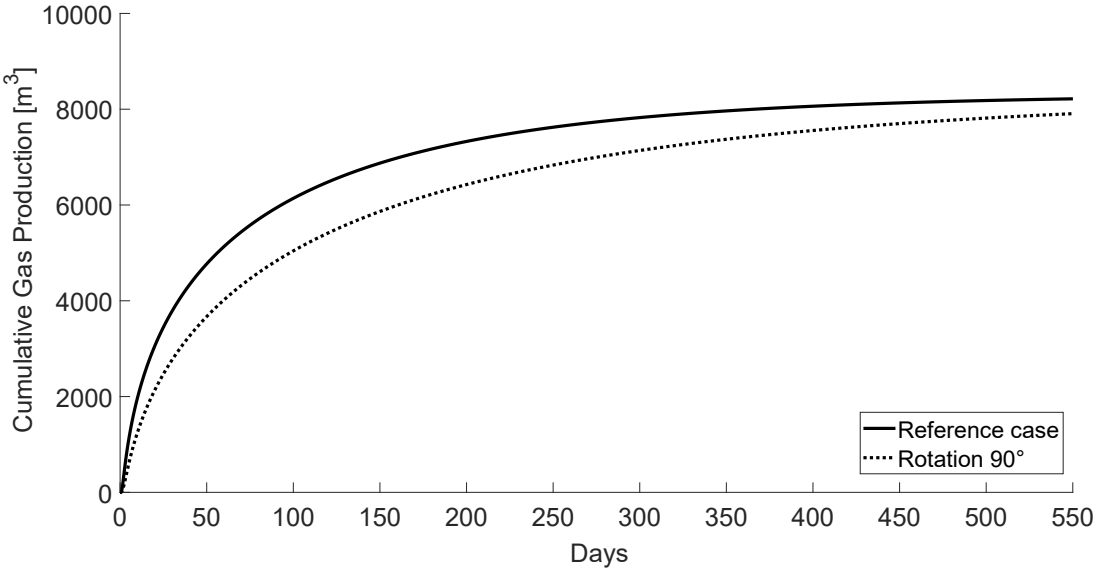

Figure V–24 – Reference case with REV rotation: cumulative gas production

15.2 Sensitivity analysis

A sensitivity analysis is performed to get a better understanding of the model by evaluating the influence of the main parameters on the production curve. This analysis also highlights the hydro-mechanical couplings which are taken into account by the model. The sensitivity study is performed on the aperture, the density and the stiffness of the cleats, the shrinkage coefficient, the Langmuir's parameters, the sorption time and the retention curve.

15.2.1 Cleats aperture

The parameter influencing most directly the response of the model is, with the number of cleats, the aperture of the cleats. The permeability is directly dependent on this aperture (Equation IV–33). Figures

V–25 and V–26 show the influence of the initial aperture of the cleats on the production curves. Higher the aperture, higher the production peak value. The ratios between the peak values are not straightforward since the transient behaviour plays a role in the shrinkage of the matrix. Moreover, the initial stiffnesses are initially not the same at $\sigma' = 2MPa$ (Table V–2). Indeed, the sensitivity study is carried out by modifying one parameter while all others remain equal. But modifying the initial aperture while keeping the same initial normal stiffness for the null stress actually leads to different initial stiffnesses for the given initial stress. The influence of this parameter is shown in the next section.

$\sigma' = 0MPa$	$\sigma' = 2MPa$
$h = 20\mu m$	$h = 10\mu m$
$K_n = 100GPa$	$K_n = 400GPa$
$h = 20\mu m$	$h = 13.33\mu m$
$K_n = 200GPa$	$K_n = 450GPa$
$h = 20\mu m$	$h = 18.18\mu m$
$K_n = 1000GPa$	$K_n = 1210GPa$
$h = 30\mu m$	$h = 18\mu m$
$K_n = 100GPa$	$K_n = 278GPa$
$h = 40\mu m$	$h = 26.67\mu m$
$K_n = 100GPa$	$K_n = 225GPa$

Table V–2 – Initial apertures and normal stiffnesses.

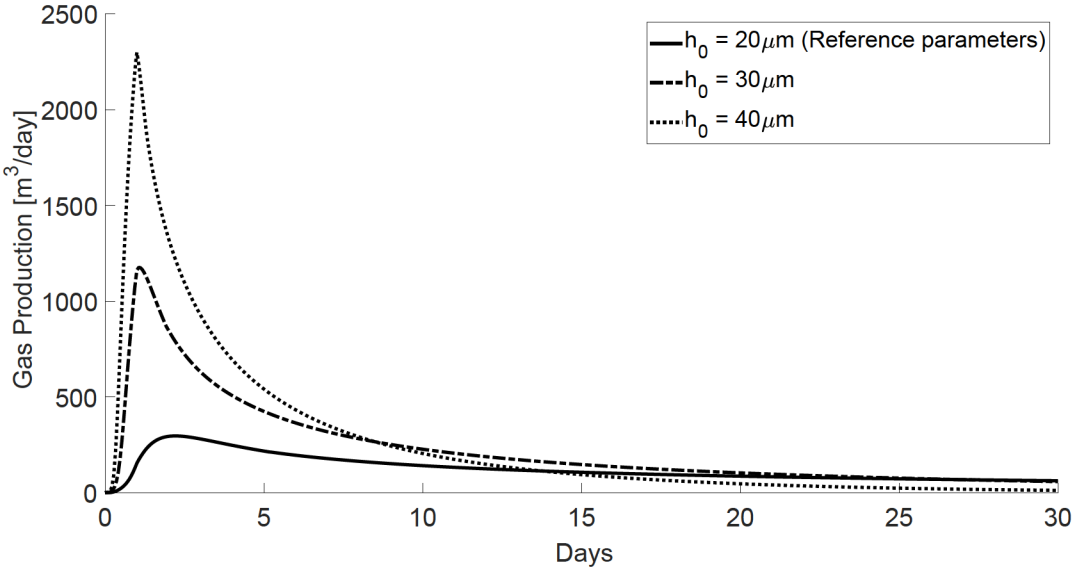

Figure V–25 – Influence of the cleat aperture on the gas production.

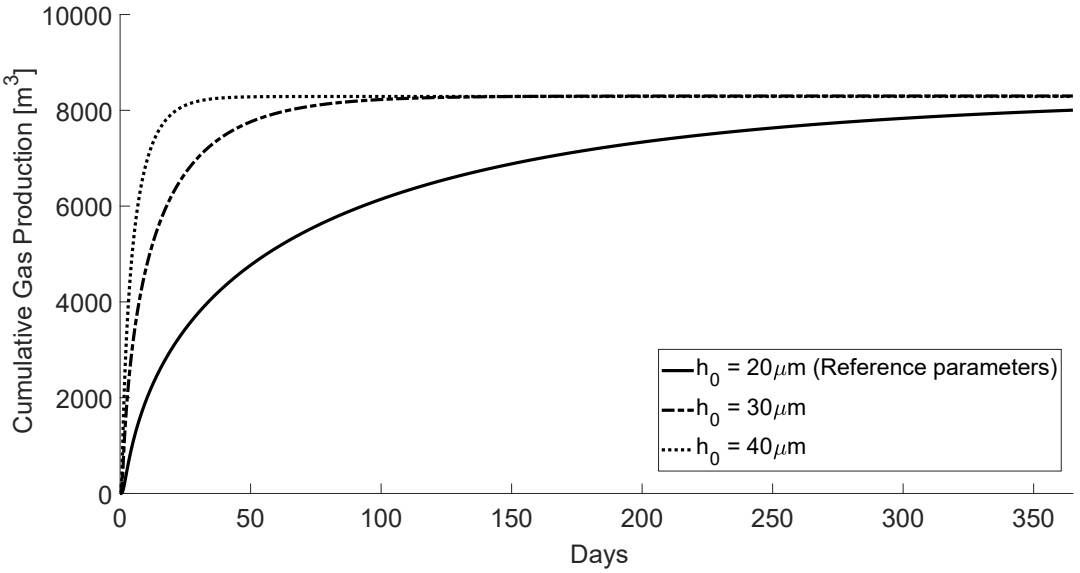

Figure V–26 – Influence of the cleat aperture on the cumulative production.

15.2.2 Cleats stiffness

Figures V–27 and V–28 highlight the influence of the normal stiffness. Three different stiffnesses are compared, varying within an order of magnitude range. Higher the stiffness and higher the production since the aperture is less impacted by the increase of the effective stress following the reservoir depletion.

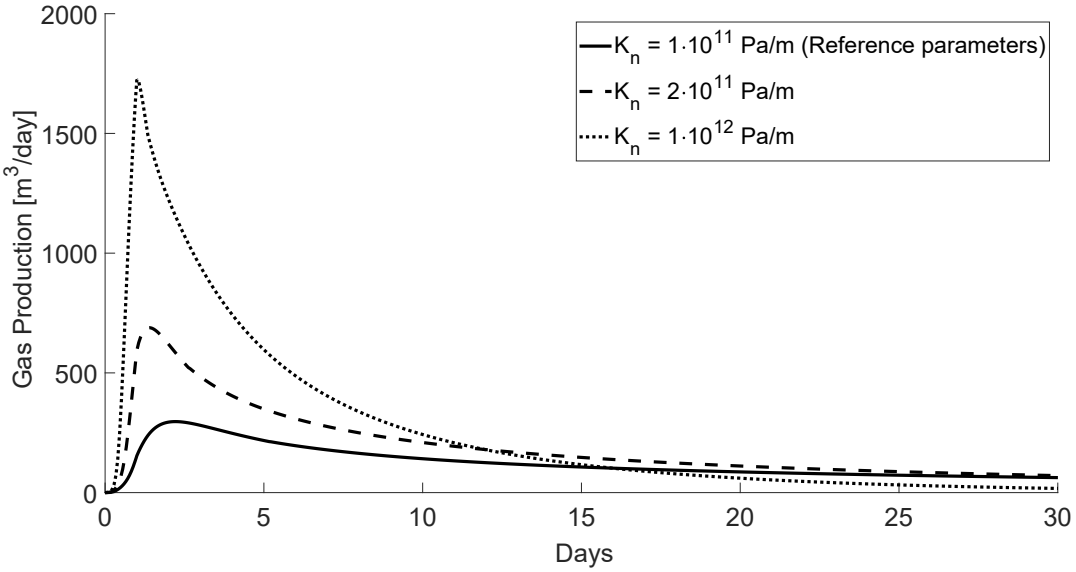

Figure V–27 – Influence of the cleat stiffness on the gas production.

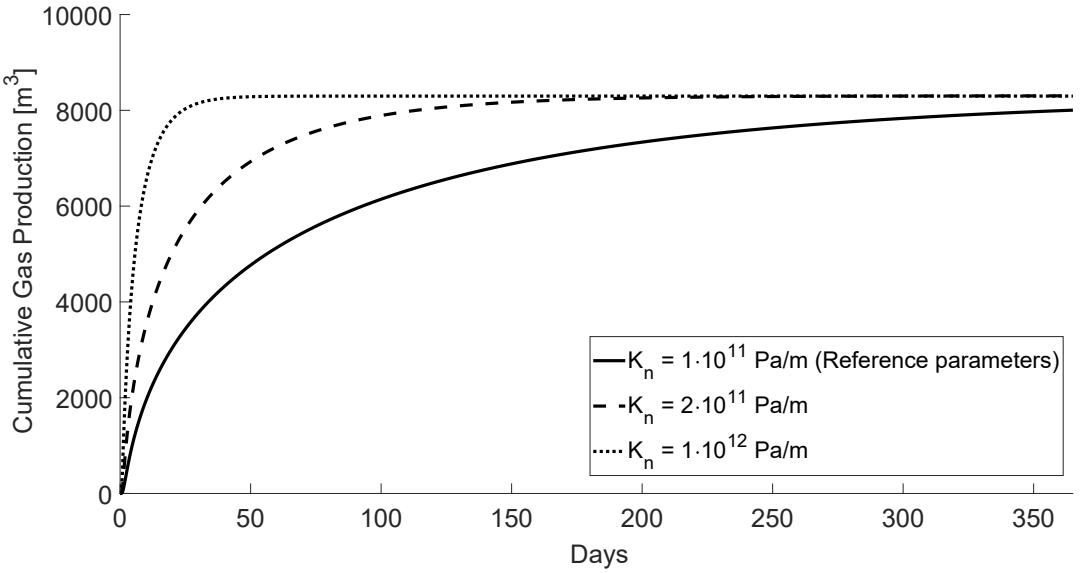

Figure V–28 – Influence of the cleat stiffness on the cumulative production.

15.2.3 Cleats density

The parameter now investigated is the density of the cleats. It may be increased by increasing the number of cleats for the same REV size or decreasing the REV size and keeping the same number of blocks and cleats (Figure V–29). The second option is followed as it has the advantage of not increasing the computation cost.

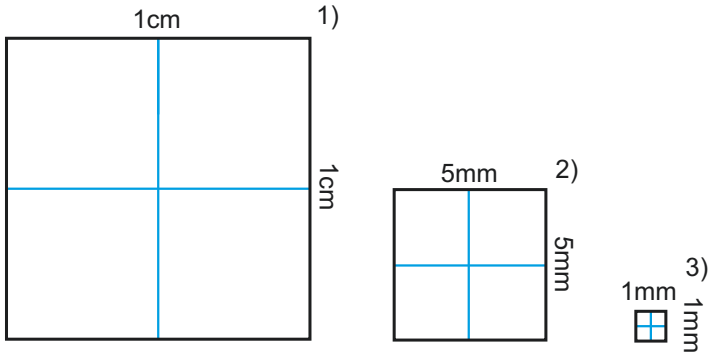

Figure V–29 – Cleat density geometries.

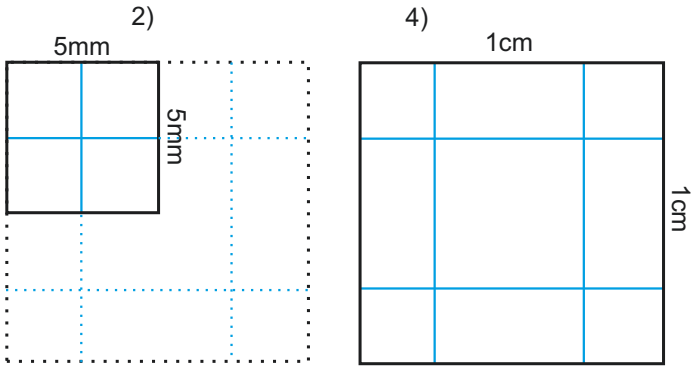

Figure V–30 – REV extension.

Figure V–31 obviously shows that the reservoir is more quickly drained by the 1*mm*-REV (3) than the 5*mm*-REV (2) and the 1*cm*-REV (1) since the most fractured medium presents a greater permeability. The production obtained with the reference REV geometry (0) is presented on the same figure, it matches the curve obtained with the 5*mm*-REV (2). Indeed, these two microstructures present the same density of horizontal fractures. The last geometry (4) corresponds to the extension of the 5*mm*-REV (2) over 1*cm* (Figure V–30), it does not influence the response of the model either. The three curves (0), (2) and (4) are therefore superimposed. If a few simulations give the same result, they do not require the same CPU time. For instance, it took 2*h*30 on a laptop [4] to simulate 600 days using a 5000*s* time step with the REV (2) while it took 9*h* to give the same results with the REV (4). Correctly identifying the unit cell definitely saves time.

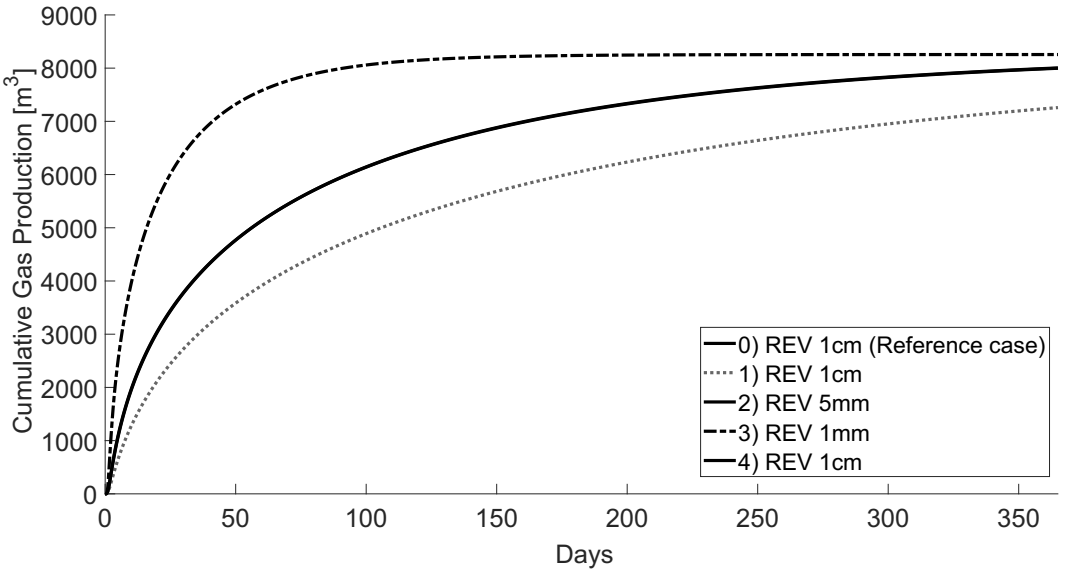

Figure V–31 – Influence of the cleat density on the cumulative production.

15.2.4 Tortuosity effect

Comparing the results obtained with the microstructure 1) from Figure V–31 and the reference microstructure with a 90° rotation, Figure V–32 aims to highlight the tortuosity effect. Indeed, the first REV presents a single straight fracture while the second one presents a tortuous path for the fluid. Tortuosity causes the peak of production to be slightly delayed and decreased.

4. Intel® 6-core processor i7-8750H CPU @ 2 20GHz, RAM 16 0Go.

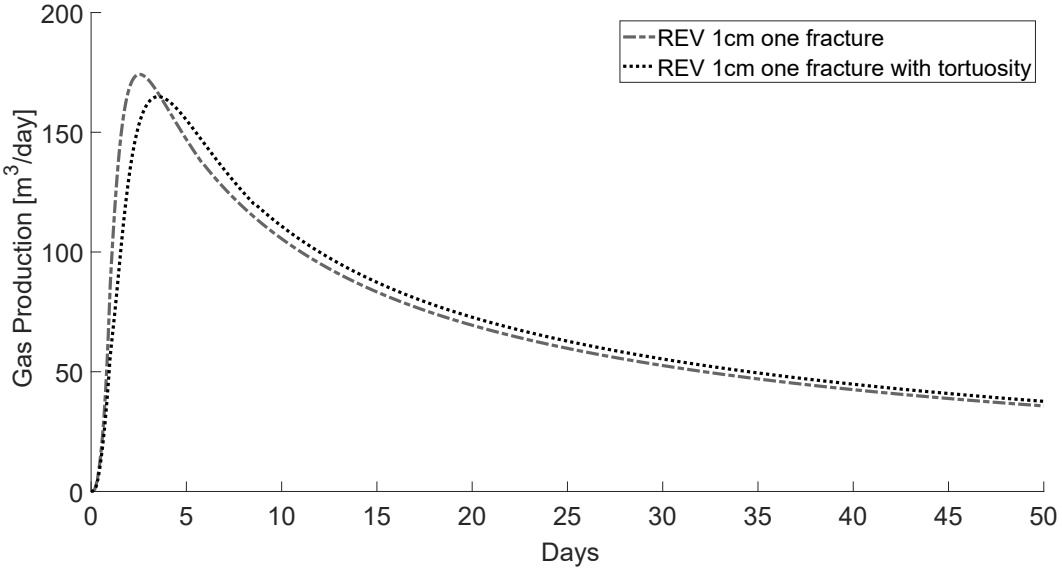

Figure V–32 – Influence of the tortuosity on the gas production.

15.2.5 Hydro-mechanical couplings

The different simulations performed here aims to evaluate both the influence of the matrix shrinkage and the increase of the effective stress on the gas production. On the first hand, the simulations performed with different shrinkage coefficients highlight the positive impact of the shrinkage coefficient on the permeability. On the other hand, comparing the simulation performed with a zero shrinkage coefficient with the one with a constant permeability highlights the negative impact of the increase of the effective stress.

The exercise is first performed with the reservoir boundary conditions (Figure V–33). It appears there is only a little effect of the matrix shrinkage on the permeability. Indeed, the decrease of volume is reflected more in the subsidence than in fracture aperture opening. Figure V–34 shows the subsidence of the seam is linearly proportional to the linear swelling coefficient . The subsidence observed for 0 is due to the increase of effective stress following the depletion.

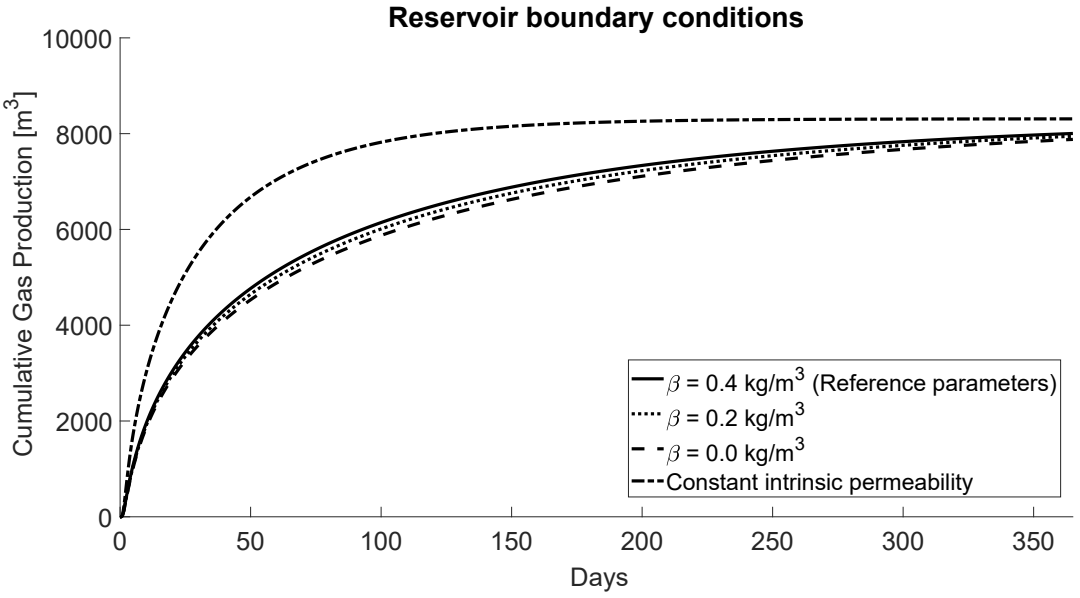

Figure V–33 – Influence of the hydro-mechanical couplings on the cumulative production.

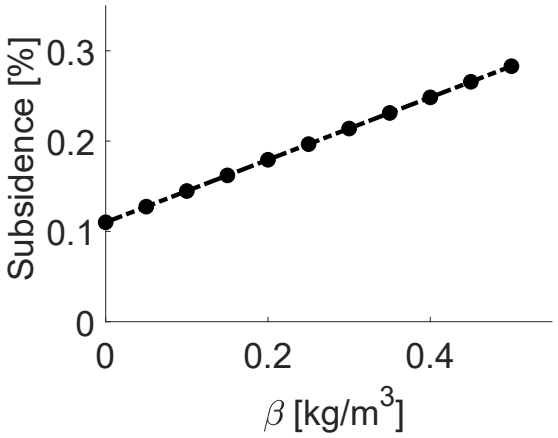

Figure V–34 – Influence of the shrinkage coefficient on the subsidence.

Considering constant volume conditions (Figure V–35), the impact of the shrinkage is clearly more significant. For the chosen set of parameters with 0 4$kg\ m^3$, the negative impact of the effective stress is almost compensated by the positive impact of the shrinkage.

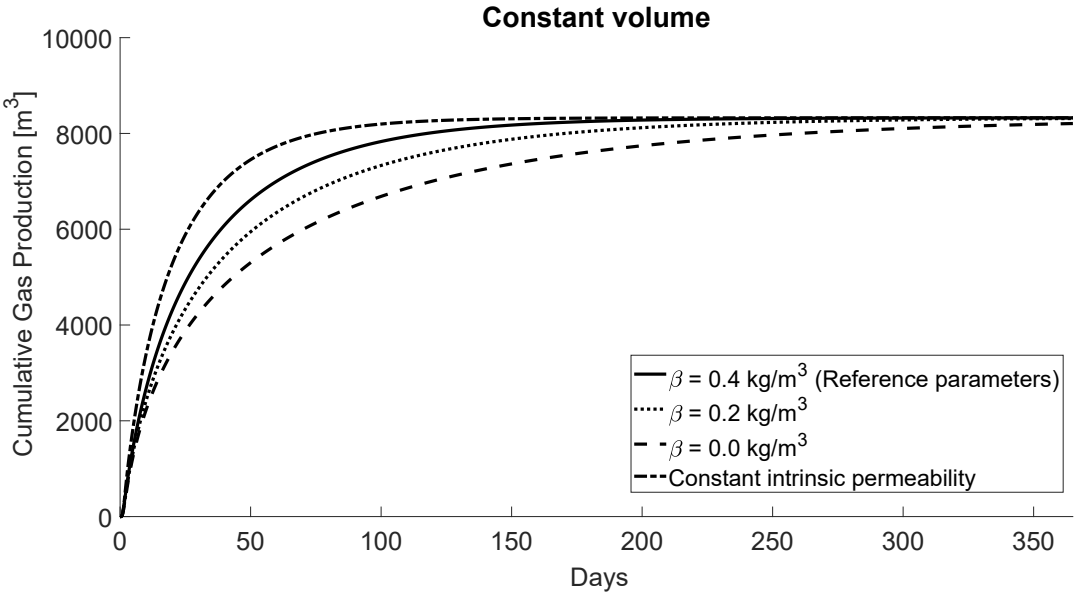

Figure V–35 – Influence of the hydro-mechanical couplings on the cumulative production.

Figure V–36 demonstrates the positive influence of the shrinkage on the permeability evolution.

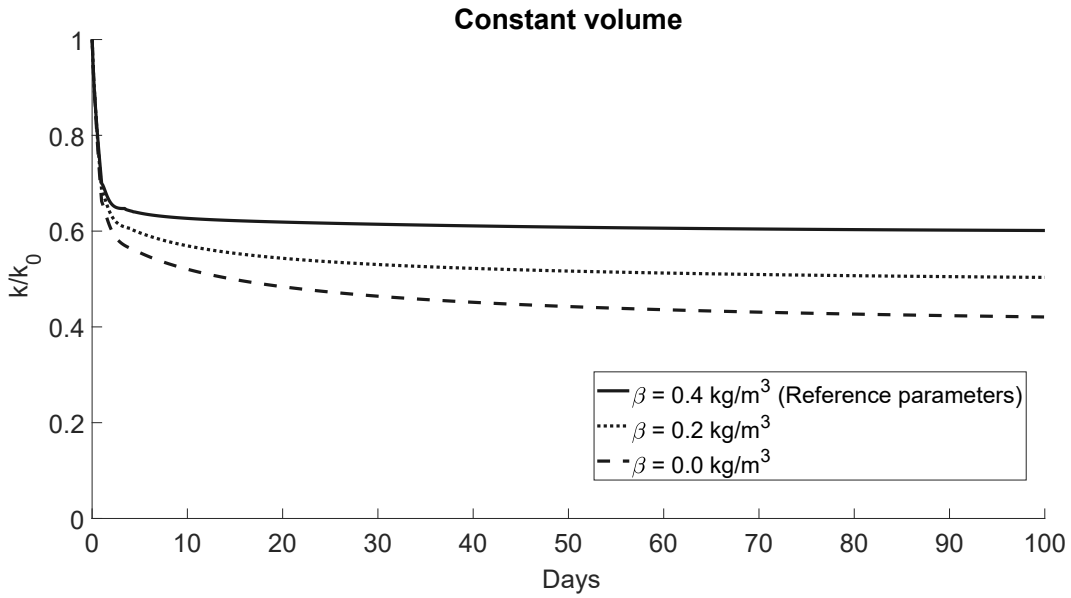

Figure V–36 – Influence of the shrinkage coefficient on the permeability at x 6 6cm.

The question which arises now is which boundary condition should be actually used. Using a 2D REV geometry (in the same plane as the macroscale mesh), there is no other choice than meshing a cleat network separating the matrix blocks (otherwise the permeability is null). Such a structure is little impacted by the shrinkage if subsidence is allowed. However, the actual coal structure is likely to show attachment areas between the blocks while the fluid can bypass these obstacles via the third dimension. It means there are holding points that, locally, almost require volume conservation. Fractures could be therefore much more impacted by internal strains with reservoir boundary conditions than what is modelled with the 2D microsctructure. The two boundary cases applied on the 2D REV from Figures V–14 and V–29 should be therefore considered as two extreme cases for more complex fractures geometries. Depending on the application, gas recovery or gas injection, the most critical boundary conditions case are not the same. In practice, a detailed monitoring of the pressures and relative displacements of the seam would allow a proper quantification of the compaction process [Pineda et al., 2014] and see where it is situated in between the two boundary conditions.

15.2.6 Langmuir's parameters

Langmuir's parameters influence the total volume of gas produced from the reservoir since it is assumed the initial adsorbed gas volume is on the isotherm. For the same initial gas volume, different Langmuir's parameters also impact the desorption kinetics.

Figure V–37 shows for instance that less gas is produced when P_L 0 75MPa instead of 1 5MPa. Indeed, despite the initial gas volume is higher with 0 75MPa, the final volume is also higher and less gas is producible (Table V–3).

Parameters	$V_{ad\,0}$ p 3MPa m^3	$V_{ad\,f}$ p 1MPa m^3	V_{ad} m^3
V_L 0 02m^3 kg; P_L 1 50MPa	20830	12500	8330
V_L 0 01m^3 kg; P_L 1 50MPa	10420	6250	4170
V_L 0 02m^3 kg; P_L 0 75MPa	25000	17850	7150

Table V–3 – Adsorbed gas volumes.

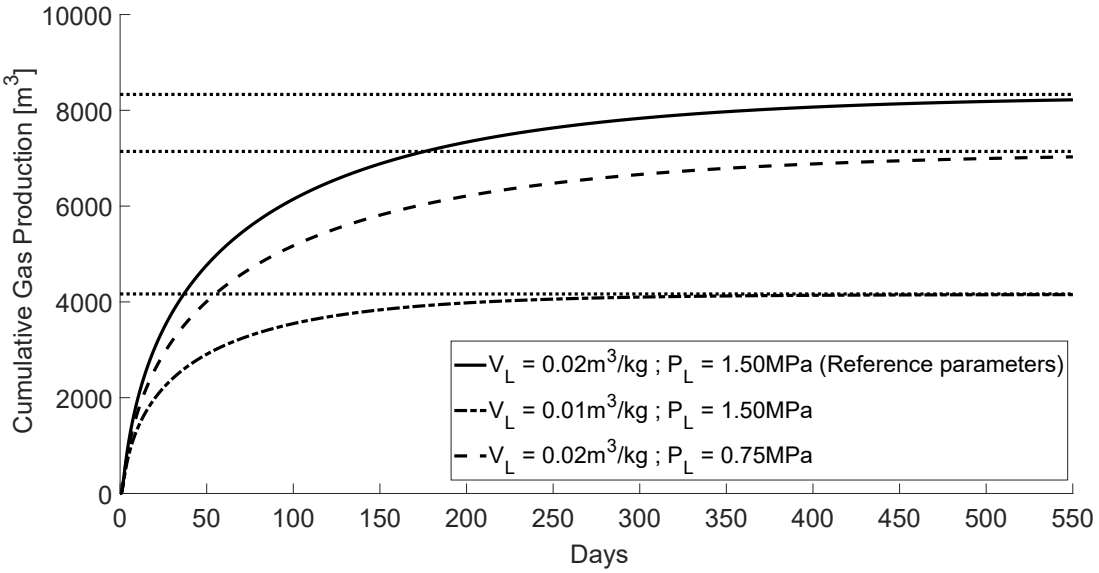

Figure V–37 – Influence of the Langmuir's parameters on the gas production.

15.2.7 Sorption time

Figure V–38 highlights the influence of the sorption time on the production curve. The sorption time coefficient was introduced into the model to take into account the time required to diffuse through the matrix to reach the cleats. The greater the sorption time, the longer it takes to produce the gas.

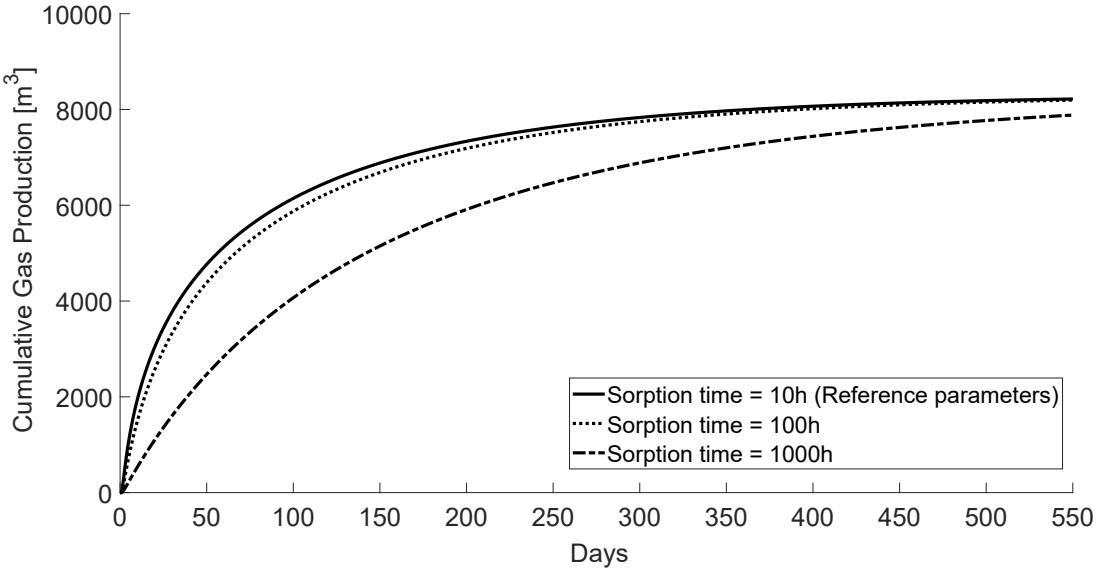

Figure V–38 – Influence of the sorption time on the gas production.

15.2.8 Retention curve

Finally, the last parameters tested are the parameters from the retention curve. Figure V–39 shows that a greater gas entry value p_e delays the production and a greater distribution index speeds up the production. These behaviours are related to the water saturation degree. Figure V–40 shows the saturation degree evolution close to the well for the different retention curves presented in Figure V–41. A lower water saturation degree increases the gas permeability and therefore enhances the gas production.

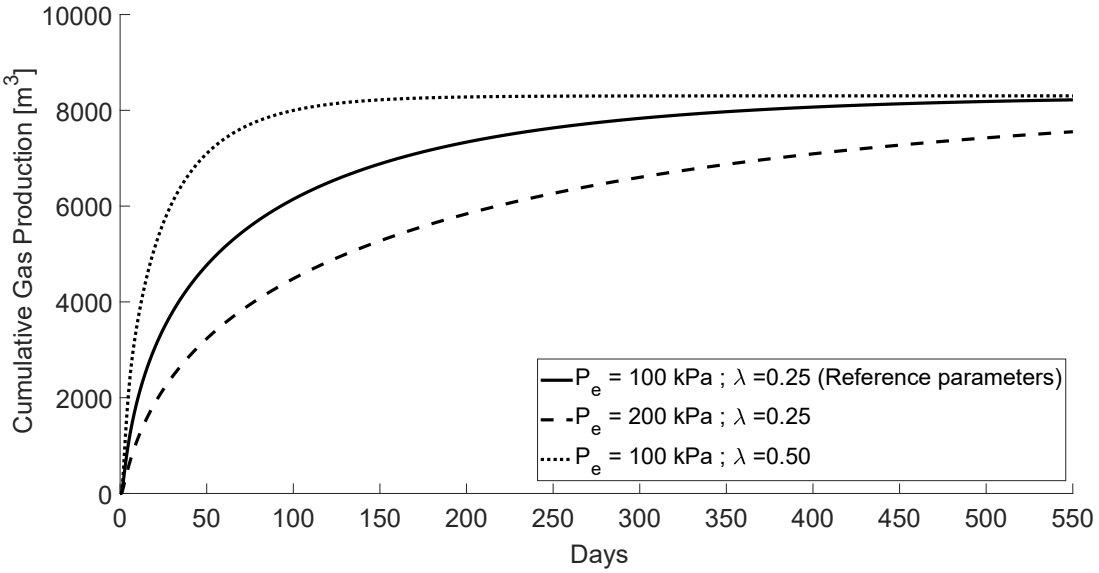

Figure V–39 – Influence of the parameters of the retention curve on the production.

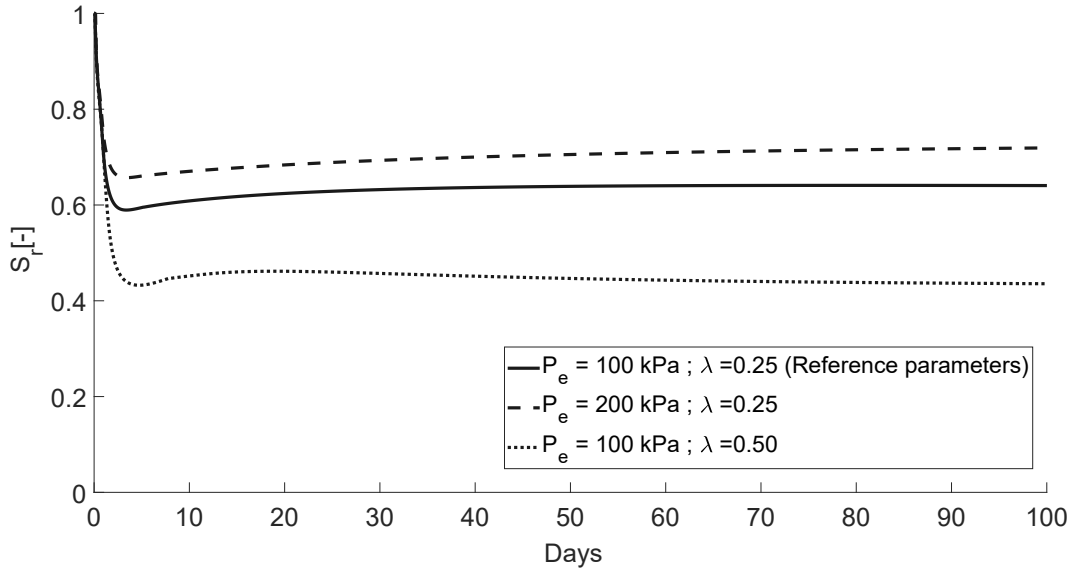

Figure V–40 – Saturation degree with time at x 6 6cm from the well for different retention curves.

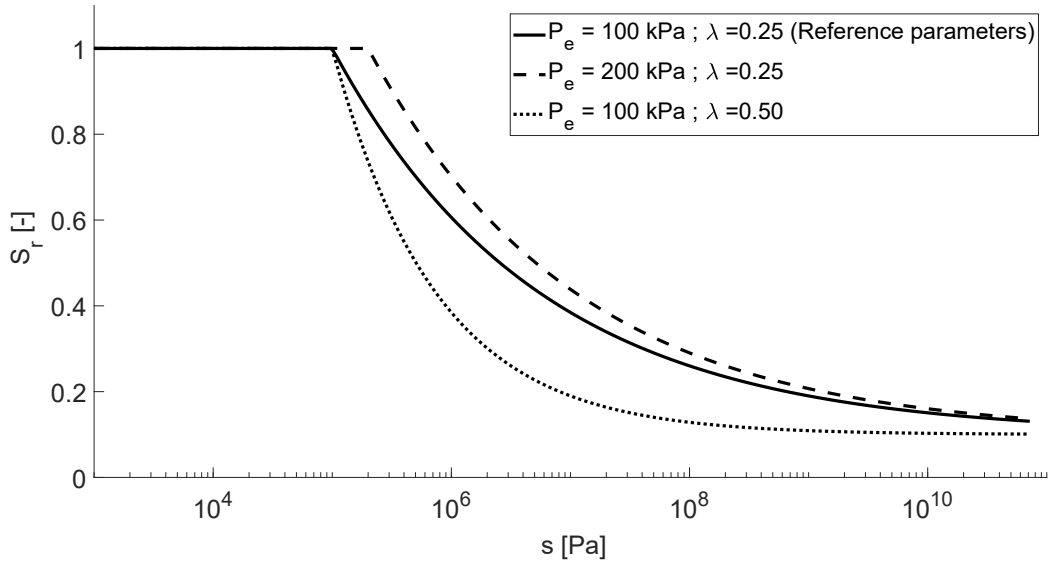

Figure V–41 – Retention curves.

15.3 Horseshoe Canyon case

The pressure and gas rate data presented by [Gerami et al., 2007] are used for a history matching exercise. Reservoir properties are listed in Table V–4, they are the same as presented in Table III–3 in Part III of the thesis. The 300 meters of the reservoir are meshed with 20 macroscopic elements with a first element of $5cm$ like in the reference case.

Parameters	Values
Initial gas pressure (Pa)	1 5E6
Initial water pressure (Pa)	0E6
Temperature (K)	289
Coal density ($kg\ \ m^3$)	1468
Seam thickness (m)	8 99
Langmuir volume V_L ($m^3\ \ kg$)	0 0092
Langmuir pressure P_L (Pa)	4 652E6

Table V–4 – Reservoir parameters [Gerami et al., 2007].

Model parameters used for this history matching exercise are given in Table V–5. The REV geometry considered is that of 2D matrix blocks $1cm$ wide. Note that a 3D REV geometry was considered for the macroscale model in Part III. Some parameters, in particular those related to the cleats, have therefore different values compared to the first history matching exercise. The distinct way to represent the microstructure makes thus difficult the comparison of the two models [5].

5. Besides, the cleat aperture and the cleat normal stiffness are given for the initial stress value in the macroscopic model while it is input for a null stress in the multiscale model. Indeed, the latter model follows the way in which the INTME mechanical interface law has been implemented (with the advantage that the same set of parameters may be defined to simulate triaxial tests with different confinements) while the newly developed macroscale mechanical law ELADUA has maybe more user-friendly input parameters for reservoir modelling.

Parameters	Values
Reservoir radius (m)	282
Overburden pressure (Pa)	5E6
Matrix Young's modulus E_m (Pa)	5E9
Matrix Poisson's ratio $_m$	0 3
Matrix width w (m)	0 01
Cleat aperture* h (m)	107E-6
Cleat normal stiffness* K_n ($Pa\ \ m$)	6 6E9
Cleat shear stiffness K_s ($Pa\ \ m$)	6 6E9
Sorption time $\mathcal{T}$ (hours)	1000
Matrix shrinkage coefficient ($kg\ \ m^3$)	0 5

Table V–5 – Reservoir parameters used to calibrate the FE^2 model for the Horseshoe Canyon case. * Given for a null stress.

The pressure at the well is given as input to the model and the production rate is observed as the response of the model to this loading. Figure V–42 compares the data with the results of the simulation performed with parameters provided in Tables V–4 and V–5. To perform this simulation on a dry reservoir, only one degree of freedom is used at the macroscale, the gas degree of freedom. It means the simulation is performed at constant volume and the hydro-mechanical couplings are maximized at the microscale. It takes only 2 minutes to simulate 800 days with a maximum time step of 10 days.

The fitting looks good overall. The simulation seems to overestimate a bit the production between 200 and 400 days. Actually, it appears that many well pressure points are clearly higher than the main trend during this period. It tends to reduce the production and it may partly explain the difference with the simulation. This simulation concludes the thesis.

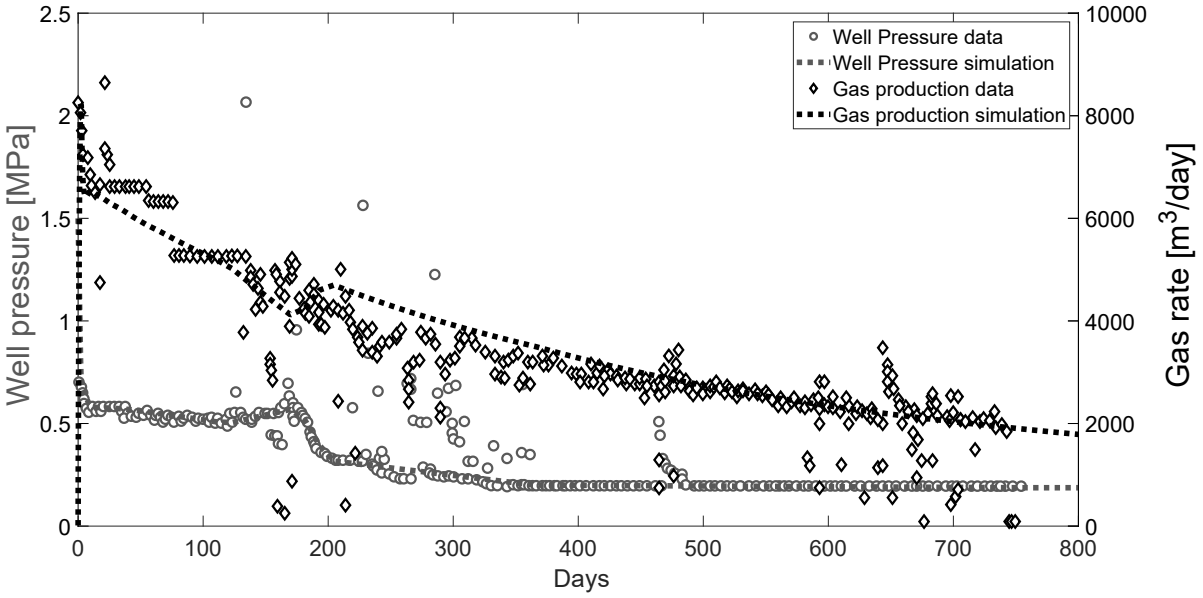

Figure V–42 – Matching exercise with the Horseshoe Canyon data.

Conclusions Part V

In this part, the general principles of the Finite Element Square Method were first presented. Then, the localization and homogenization procedure was applied to the microscale model presented in the previous part in order to develop a multiscale hydro-mechanical model. It follows the work of [Frey, 2010], [Marinelli, 2013] and [Van den Eijnden, 2015] in the Lagamine code. My contributions are of different kinds, we can cite the introduction of a new degree of freedom for gas to deal with multiphase flows, the implementation of adsorption and swelling/shrinkage mechanisms for the modelling of coalbed methane production and CO_2 storage in coal seams, the introduction of some initial stresses and the axisymmetric case for the reservoir modelling. This model was applied to the modelling of one production well. The sensitivity study highlights the role of the main parameters on the response of the model to a pressure drop at the well. Parameters affecting the cleat aperture play of course a significant role in the production curves. But the influence of the boundary conditions on the hydro-mechanical couplings was also highlighted. Finally, the Horseshoe Canyon data were used for a history matching exercise. These same data were also modelled with the macroscopic model. However, the production curve is not compared for the same set of parameters. Indeed, the macroscale simulation considered a 3D microstructure with two sets of cleats towards the well while only a 2D microstructure is implemented for the multiscale model. Besides, the determination of the whole set of independent parameters may be challenging in practice. It is also the reason why it was difficult to find a documented well with all the parameters required to fully test the model against data.

The 2D representative elementary volume means that the set of out-of-plane fractures is not taken into account in the permeability. There is actually nothing to prevent combining 2D at the macroscopic scale with 3D at the microscopic scale, but it would increase the computational cost. This cost could be reduced by implementing static condensation to compute the macroscale stiffness matrix. However, using 3D for the REV and 2D-axisymmetric conditions for the reservoir would overestimate the permeability since it would consider that the third set of fracture is radial with the wellbore. This combination is therefore not recommended for modelling a vertical well. Note that drilling technologies allow now to create horizontal wells (Figure V–43). This case may be modelled with a macroscale mesh in plane strain state which is perpendicular to the well. The microstructure could be either in plane strain or more appropriately in 3D to account all the sets of cleats.

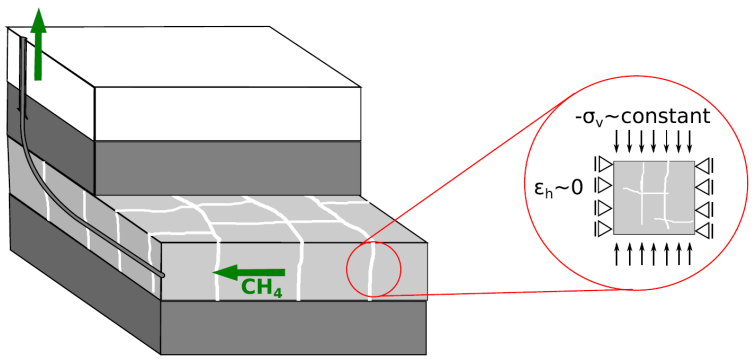

Figure V–43 – Schematic horizontal well intercepting a coal seam. *From* [Espinoza et al., 2015].

Compared to the macroscale model, any fracture network could be used in the REV geometry of the multiscale model. Indeed, the macroscale model is limited to a matchstick geometry while, despite simple unit cells were used in our modelling, this is not a limitation of the multiscale model. Moreover, as physical phenomena are written at the fracture scale, the formulation is sometimes simplified. For instance, there is no Biot's coefficient appearing in the effective stress equation.

Compared to the microscale model, transient effects are not directly considered at the microscale in the multiscale model. The REV boundary value problem is solved under steady state conditions but a sorption time is taken into account for the storage term of the macroscale. The modelling of transient diffusive flows in the matrix would require the implementation of coupled elements with more than 4 nodes to avoid numerical oscillations. In addition, the pressure distribution at the microscopic scale at the end of each time step must be stored in memory to start the next time step.

The multiscale model presented in this part of the thesis is a two-scale model. Actually, more than two scales could be considered to take into account cleats of different lengths and apertures. For example, we could have a continuous reservoir scale, then an intermediate scale with decimetric blocks where each integration point calls the lowest scale where there are millimetric blocks and small fractures. Of course, this would significantly increase the computation cost while the model is already very advanced to take into account hydro-mechanical couplings under unsaturated conditions.

So, thanks to the implementation of this extended FE^2 model in the Lagamine code, new sophisticated tools are now available to model multiphase flow in naturally fractured medium. In this part, the multiscale model was applied to methane recovery but it could also be applied to carbon storage just as gas injection was modelled with the microscale model.

Part VI

Conclusions

16. General conclusions

16.1 Summary

The first part of the thesis presented the context and issues related to gas flows in coal. Coal has a long-standing role in the global power supply and it is now back on the front stage in Europe with its high potential for methane production. Tomorrow, it could also be part of the solution to mitigate the climate change thanks to the carbon capture and storage in coal seams. However, this unconventional reservoir requires some particular models for a proper modelling.

Indeed, contrary to conventional hydrocarbons reservoirs, gas is not compressed into the pore space but it is stored by sorption in the matrix. It is experimentally observed that the variation of the gas content induces a shrinkage or a swelling of the matrix. Moreover, coal is a naturally fractured rock. It can be observed by tomography imaging and deduced from its mechanical behaviour under a compressive path. Then, the sorption-induced strain is likely to affect the cleats aperture. Any change of the network of cleats will likely translate into modifications of the permeability, with consequences for gas production or storage. The second part of the thesis presented an experimental campaign carried out in laboratory which shows an evolution of the permeability with the gas pressure.

This thesis aimed to contribute to the development of some numerical models taking into account properly the hydro-mechanical couplings observed experimentally. A model is used to determine the response of the modelled object to a given load. Depending on the objectives pursued, there are different types of models. Figure VI–1 depicts a direct modelling approach for coal. The geometry of the material is explicitly represented with matrix blocks and cleats and distinct mechanical and hydraulic laws are attributed to both constituents. This scale is the closest to the physics responsible for the evolution of the permeability of the material. Unfortunately, there is a gap between the scale of this model and the scale of the reservoir. This makes this model unusable in practice for the gas production or storage modelling.

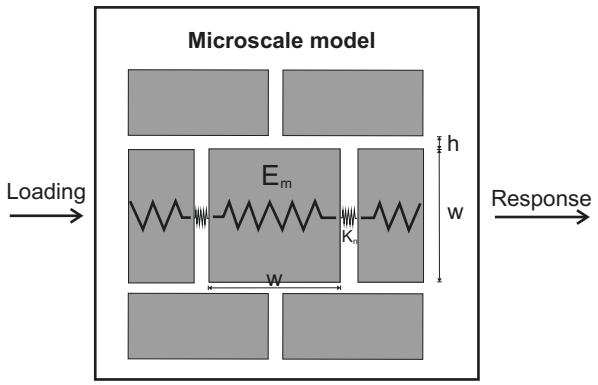

Figure VI–1 – Direct modelling approach.

The question then is how to close the gap. Homogenization is the short answer, but it can be done in different ways. The third part of the thesis presented the approach typically found in the literature, it

consists to homogenize the microscale constitutive laws to develop the macroscale model (Figure VI–2). For instance, the equivalent medium concept considers the global stiffness of the material can be obtained by the harmonic average of the stiffnesses at the lower scale. For the hydraulic part, the equivalent permeability of the medium is the fracture permeability weighted by the space occupied by the fracture. In this third part of the thesis, we developed a coupled macroscale model calculating the evolution of the cleat aperture and the matrix width as a function of the stress state, which depends in particular on the gas content. So, the model takes into account the evolution of the stiffness and permeability of the medium.

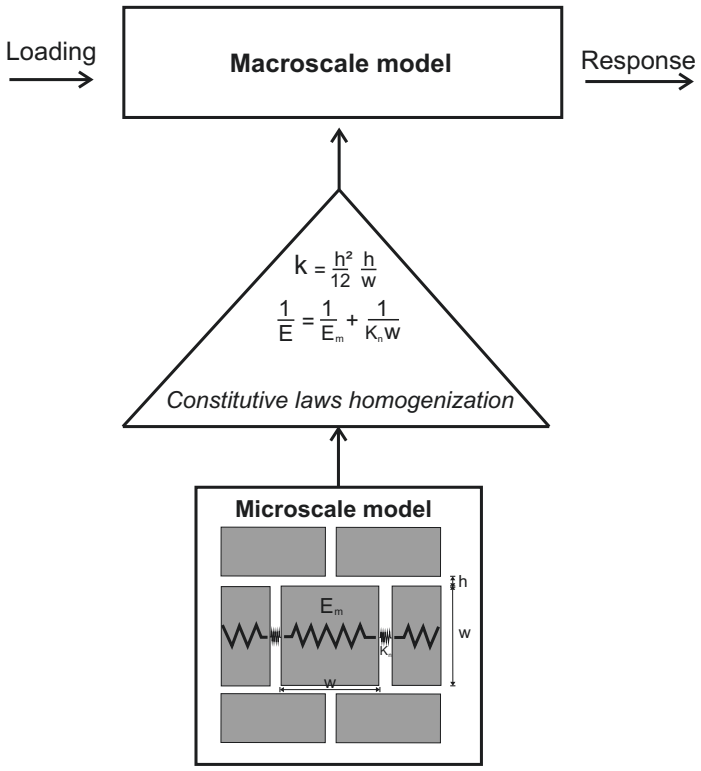

Figure VI–2 – Macroscale modelling approach.

Instead of homogenizing the physics to obtain the reservoir scale model, it is certainly more rational to homogenize the response of the model written at the scale of the physical phenomena taking part in the fluid flow. It is the real multiscale approach (Figure VI–3). The multiscale model is based on a micro-scale model that needed to be developed as a preamble, it was presented in the fourth part of the thesis. In this part, the numerical results of a simple case were compared against the analytical solution developed from the physics agreed in the literature.

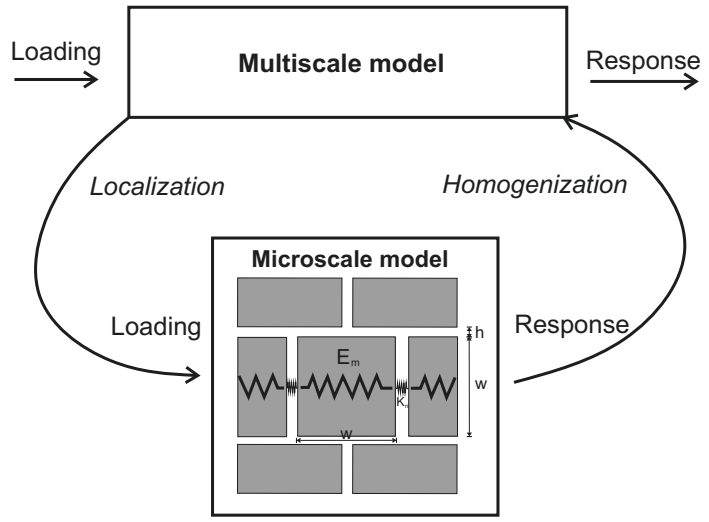

Figure VI–3 – Multiscale modelling approach.

The fifth part of the thesis presented the multiscale model based on the finite element square method. The method requires to localize the loading given at the reservoir scale to the microscale. Then, the boundary value problem is solved on the representative elementary volume with the microscale model. Actually, any model describing the physics involved could be used, it is the model presented independently in the fourth part of the thesis in this case. However, the model is only partly integrated in the multiscale approach since diffusive flows are not explicitly modelled as the REV problem is solved under steady state conditions. Nevertheless, a double-porosity effect is taken into account like for the macroscale model thanks to a sorption time parameter. Once the microscale BVP is solved, the response to the loading is homogenized using appropriate averages and it is sent back to the macroscale. A second BVP problem is then solved at the macroscale knowing the relation between the actions and the reactions thanks to the microscale.

16.2 Original contributions

This work on the modelling of hydro-mechanical couplings in coal is the first thesis carried out on the subject in the geomechanics team of the University of Liège. However, this work builds on previous developments in the Lagamine code. In particular, my PhD work has drawn strength from the unsaturated and coupled models from Collin [Collin, 2003] and the multiscale models from Marinelli [Marinelli, 2013] and Van den Eijnden [Van den Eijnden, 2015].

For the different models, the main original contributions include:

Macroscale model

- The combination of the dual-continuum approach for both mechanical and hydraulic behaviour.
- A permeability evolution directly related to the fracture aperture instead of the porosity evolution.
- A gas mass transfer between the matrix and the fractures evaluated combining a shape factor and a sorption isotherm.

Microscale model

- The expressions for the relative permeability curves for unsaturated flow in a single fracture.
- The justification for using a retention curve for a single fracture.
- The formulation of the Klinkenberg correction factor for two parallel plates.

— The innovative integration of the Langmuir isotherm in the gas transfer between the cleats and the matrix to avoid defining two degrees of freedom for the gas (free and adsorbed state).

— The analytical elastic solution of the swelling problem.

Multiscale model

— A complete reorganization of the input file.

— A new degree of freedom for gas with *ad hoc* laws (see microscale model).

— The consideration of an adsorbed gas with the resulting couplings.

— The implementation of a new mechanical law for the interface (Bandis type).

— The possibility to change the REV size.

— The definition of initial stresses.

— The possibility to use axisymmetric conditions for well production modelling.

16.3 Outlooks

In this thesis, it is assumed the reservoir is naturally fractured, it is generally the case for coal seams. However, hydraulic fracking is sometimes used to create fractures and enhance the production, but the initiation of fractures was out of the scope of the thesis. It is not clear that the model should be developed in this direction, given that European countries are beginning to ban this method of extraction. However, coal failure can happen caused by the drilling of the well and also because of gas depletion.

The drilling phase was not investigated but the damage propagation in the medium surrounding the well could be modelled using a local second gradient model [Chambon et al., 2001, Collin et al., 2006, Pardoen et al., 2015]. The doublescale method can be combined with a local second gradient to model the excavation damaged zone (EDZ) around the well. The application of the FE^2 method to localization problems was developed under water saturated conditions by [Van den Eijnden, 2015] in the context of gallery excavation for deep geological radioactive waste disposal. However, a second-order homogenization technique should be used.

Far from the wellbore, the seam is under zero-lateral strain and constant total vertical stress. Under these conditions, reservoir depletion increases the effective stresses and gas desorption induces a shrinkage of the matrix that is likely to reduce the lateral stresses, it is conducive to a shear failure of the coal [Espinoza et al., 2015]. Then, it could be interesting to introduce a failure criterion in the mechanical model of the matrix. However, the mechanical failure is actually not accompanied by an increase of the permeability but, on the contrary, there may be a plugging of the fractures due to the production of coal fines [Okotie et al., 2011]. This plugging is not easy to take into account with a finite element model.

To continue on the enhanced production, all the models were implemented with a single gas degree of freedom, which means either methane production or carbon storage can be modelled but not the replacement of methane by carbon dioxide. The introduction of a new gas degree of freedom would require to modify the Langmuir's isotherm. Precisely about the temperature, the models were implemented for isothermal conditions and all parameters are introduced for the wanted temperature by the user. Introducing a temperature evolution would require to implement the evolution of all the physical properties with the temperature. In particular for coal, there are a decrease of the sorption capacities and an increase of the diffusion coefficient with the temperature [Salmachi and Haghighi, 2012, Guan et al., 2018]. A new degree of freedom for temperature would allow to simulate thermal stimulation scenarios. The effectiveness of such a stimulation is uncertain given the costs of heating the rock and the negative impact of dilation on permeability just like the swelling.

Something that was not much discussed in the thesis is the inherent randomness accompanying modelling in the earth sciences. Instead of deterministic models where the output is fully determined by a single set of parameters values and the initial conditions, it could be interesting to introduce some ranges

of values (in the form of probability distributions) for each parameter of each constituent of the material. A stochastic approach over the developed model would make it easier to assess production risks associated with the material properties.

In conclusion, this thesis allowed to develop and implement new models taking into account the hydro-mechanical couplings influencing the reservoir permeability during methane production or carbon storage. As just seen above, there is still room for improvement, for instance with stochastic and more degrees of freedom for gas and temperature. However, these new modelling tools now available in the Lagamine code will certainly prove useful for a wide range of applications, also outside coal-related applications. Indeed, the questions that have arisen in this thesis on multiphase flows in a single fracture may also find applications in other media.

As scientists, we step on the shoulders of science, building on the work that has come before us - aiming to inspire a new generation of young scientists to continue once we are gone.

Stephen Hawking

Bibliography

[Al-Jubori et al., 2009] Al-Jubori, A., Johnston, S., Boyer, C., Lambert, S. W., Bustos, O. A., Pashin, J. C., and Wray, A. (2009). Coalbed methane: clean energy for the world. *Oilfield Review*, 21(2):4–13.

[Allardice, 1991] Allardice, D. (1991). The water in brown coal. In *The science of victorian brown coal*, pages 103–150. Elsevier.

[Allardice and Evans, 1971] Allardice, D. and Evans, D. (1971). The brown-coal/water system: Part 1, the effect of temperature on the evolution of water from brown coal. *Fuel*, 50(2):201–210.

[Amadei and Goodman, 1981] Amadei, B. and Goodman, R. (1981). A 3-d constitutive relation for fractured rock masses. *Studies in applied mechanics,f part B*, 5:249–268.

[Aminu et al., 2017] Aminu, M. D., Nabavi, S. A., Rochelle, C. A., and Manovic, V. (2017). A review of developments in carbon dioxide storage. *Applied Energy*, 208:1389–1419.

[Anthoine, 1995] Anthoine, A. (1995). Derivation of the in-plane elastic characteristics of masonry through homogenization theory. *International Journal of Solids and Structures*, 32(2):137–163.

[Argilaga et al., 2016] Argilaga, A., Papachristos, E., Caillerie, D., and Dal Pont, S. (2016). Homogenization of a cracked saturated porous medium: Theoretical aspects and numerical implementation. *International Journal of Solids and Structures*, 94:222–237.

[Arnold, 2013] Arnold, B. (2013). 2 - coal formation. In Osborne, D., editor, *The Coal Handbook: Towards Cleaner Production*, volume 1 of *Woodhead Publishing Series in Energy*. Woodhead Publishing.

[ASTM, 2002] ASTM (2002). Standard practice for proximate analysis of coal and coke (d3172). *Annual Book of ASTM Standards*.

[ASTM, 2007a] ASTM (2007a). Standard practice for proximate analysis of coal and coke (d3172). *Annual Book of ASTM Standards*.

[ASTM, 2007b] ASTM (2007b). Standard test method for volatile matter in the analysis sample of coal and coke (d3175). *Annual Book of ASTM Standards*.

[ASTM, 2011] ASTM (2011). Standard test method for ash in the analysis sample of coal and coke (d3174). *Annual Book of ASTM Standards*.

[ASTM, 2012] ASTM (2012). Classification of coals by rank (d388). *Annual Book of ASTM Standards*, pages 19428–2959.

[Ayoub et al., 1991] Ayoub, J., Colson, L., Hinkel, J., Johnston, D., and Levine, J. (1991). Learning to produce coalbed methane. *Oilfield Review*, 3(1):27–40.

[Bailey and Gray, 1958] Bailey, R. and Gray, V. (1958). Contact angle measurements of water on coal. *Journal of Applied Chemistry*, 8(4):197–202.

[Bandis et al., 1983] Bandis, S., Lumsden, A., and Barton, N. (1983). Fundamentals of rock joint deformation. 20(6):249–268.

[Barenblatt et al., 1960] Barenblatt, G., Zheltov, I. P., and Kochina, I. (1960). Basic concepts in the theory of seepage of homogeneous liquids in fissured rocks [strata]. *Journal of applied mathematics and mechanics*, 24(5):1286–1303.

[Barton et al., 1985] Barton, N., Bandis, S., and Bakhtar, K. (1985). Strength, deformation and conductivity coupling of rock joints. In *International Journal of Rock Mechanics and Mining Sciences & Geomechanics Abstracts*, volume 22, pages 121–140. Elsevier.

[Barton and Choubey, 1977] Barton, N. and Choubey, V. (1977). The shear strength of rock joints in theory and practice. *Rock mechanics*, 10(1-2):1–54.

[Battistutta et al., 2010] Battistutta, E., Van Hemert, P., Lutynski, M., Bruining, H., and Wolf, K.-H. (2010). Swelling and sorption experiments on methane, nitrogen and carbon dioxide on dry selar cornish coal. *International Journal of Coal Geology*, 84(1):39–48.

[Bear, 1972] Bear, J. (1972). *Dynamics of fluids in porous media*.

[Bear et al., 1993] Bear, J., Tsang, C.-F., and De Marsily, G. (1993). *Flow and contaminant transport in fractured rock*. Academic Press.

[Bensoussan et al., 1978] Bensoussan, A., Lions, J.-L., and Papanicolaou, G. (1978). *Asymptotic analysis for periodic structures*, volume 5. North-Holland Publishing Company Amsterdam.

[Berkowitz, 1979] Berkowitz, N. (1979). *An introduction to coal technology*. Elsevier.

[Berkowitz, 1985] Berkowitz, N. (1985). The chemistry of coal.

[Bertrand et al., 2020] Bertrand, F., Buzzi, O., Bésuelle, P., and Collin, F. (2020). Hydro-mechanical modelling of multiphase flow in naturally fractured coalbed using a multi-scale approach. *Journal of Natural Gas Science and Engineering*.

[Bertrand et al., 2019] Bertrand, F., Buzzi, O., and Collin, F. (2019). Cleat-scale modelling of the coal permeability evolution due to sorption-induced strain. *International Journal of Coal Geology*, 216:103320.

[Bertrand et al., 2017] Bertrand, F., Cerfontaine, B., and Collin, F. (2017). A fully coupled hydro-mechanical model for the modeling of coalbed methane recovery. *Journal of Natural Gas Science and Engineering*, 46:307–325.

[Bilbie, 2007] Bilbie, G. (2007). *Modélisation multi-échelle de l'endommagement et de la rupture dans les milieux (quasi-) fragiles*. PhD thesis, Université Joseph-Fourier-Grenoble I.

[Billemont et al., 2013] Billemont, P., Coasne, B., and De Weireld, G. (2013). Adsorption of carbon dioxide, methane, and their mixtures in porous carbons: effect of surface chemistry, water content, and pore disorder. *Langmuir*, 29(10):3328–3338.

[Biot, 1941] Biot, M. A. (1941). General theory of three-dimensional consolidation. *Journal of applied physics*, 12(2):155–164.

[Bishop, 1959] Bishop, A. (1959). The effective stress principle. *Teknisk Ukeblad*, 39:859–863.

[Bowen, 1980] Bowen, R. M. (1980). Incompressible porous media models by use of the theory of mixtures. *International Journal of Engineering Science*, 18(9):1129–1148.

[BP, 2015] BP (2015). Statistical review of world energy.

[Brochard, 2011] Brochard, L. (2011). *Poromécanique et adsorption: Application au gonflement du charbon lors du stockage géologique du carbone*. PhD thesis, Université Paris-Est.

[Brooks and Corey, 1964] Brooks, R. H. and Corey, A. T. (1964). Hydraulic properties of porous media and their relation to drainage design. *Transactions of the ASAE*, 7(1):26–0028.

[Brown et al., 1989] Brown, E., Bray, J., and Santarelli, F. (1989). Influence of stress-dependent elastic moduli on stresses and strains around axisymmetric boreholes. *Rock mechanics and rock engineering*, 22(3):189–203.

[Brunauer et al., 1938] Brunauer, S., Emmett, P. H., and Teller, E. (1938). Adsorption of gases in multimolecular layers. *Journal of the American chemical society*, 60(2):309–319.

[Burdine et al., 1953] Burdine, N. et al. (1953). Relative permeability calculations from pore size distribution data. *Journal of Petroleum Technology*, 5(03):71–78.

[Bustin, 2002] Bustin, M. (2002). Research activities on co2, h2s, and so2 sequestration at ubc. In *Coal-Seq I Forum*, pages 14–15.

[Camacho and Ortiz, 1996] Camacho, G. T. and Ortiz, M. (1996). Computational modelling of impact damage in brittle materials. *International Journal of solids and structures*, 33(20-22):2899–2938.

[Carroll, 2014] Carroll, J. (2014). *Natural gas hydrates: a guide for engineers*. Gulf Professional Publishing.

[Cauchy, 1823] Cauchy, A. L. B. (1823). *Recherches sur l'équilibre et le mouvement intérieur des corps solides ou fluides, élastiques ou non élastiques*. Bulletin de la Société philomatique.

[Ceglarska-Stefaríska, 1994] Ceglarska-Stefaríska, G. (1994). Effect of gas pressure in methane induced swelling on the porous structure of coals. *Studies in Surface Science and Catalysis*, 87:671–677.

[Cerfontaine et al., 2015] Cerfontaine, B., Dieudonné, A.-C., Radu, J.-P., Collin, F., and Charlier, R. (2015). 3d zero-thickness coupled interface finite element: formulation and application. *Computers and Geotechnics*, 69:124–140.

[Chambon et al., 2001] Chambon, R., Caillerie, D., and Matsuchima, T. (2001). Plastic continuum with microstructure, local second gradient theories for geomaterials: localization studies. *International Journal of Solids and Structures*, 38(46-47):8503–8527.

[Chang, 1993] Chang, M.-M. (1993). Deriving the shape factor of a fractured rock matrix. Technical report, National Inst. for Petroleum and Energy Research, Bartlesville, OK (United States).

[Charlier, 1987] Charlier, R. (1987). *Approche unifiée de quelques problèmes non linéaires de mécanique des milieux continus par la méthode des éléments finis (grandes déformations des métaux et des sols, contact unilatéral de solides, conduction thermique et écoulements en milieu poreux)*. PhD thesis, Université de Liège.

[Chen et al., 2004] Chen, C.-Y., Horne, R. N., and Fourar, M. (2004). Experimental study of liquid-gas flow structure effects on relative permeabilities in a fracture. *Water Resources Research*, 40(8).

[Chen et al., 2013] Chen, D., Pan, Z., Liu, J., and Connell, L. D. (2013). An improved relative permeability model for coal reservoirs. *International Journal of Coal Geology*, 109:45–57.

[Chen et al., 2017] Chen, S., Yang, T., Ranjith, P., and Wei, C. (2017). Mechanism of the two-phase flow model for water and gas based on adsorption and desorption in fractured coal and rock. *Rock Mechanics and Rock Engineering*, 50(3):571–586.

[Christensen and Larsen, 2004] Christensen, N. P. and Larsen, M. (2004). Assessing the european potential for geological storage of co2: the gestco project. *Geological Survey of Denmark and Greenland Bulletin*, 4:13–16.

[Clarkson and Bustin, 1997] Clarkson, C. and Bustin, R. (1997). Variation in permeability with lithotype and maceral composition of cretaceous coals of the canadian cordillera. *International Journal of Coal Geology*, 33(2):135–151.

[Clarkson and Bustin, 2000] Clarkson, C. and Bustin, R. (2000). Binary gas adsorption/desorption isotherms: effect of moisture and coal composition upon carbon dioxide selectivity over methane. *International Journal of Coal Geology*, 42(4):241–271.

[Coats et al., 1989] Coats, K. H. et al. (1989). Implicit compositional simulation of single-porosity and dual-porosity reservoirs. In *SPE Symposium on Reservoir Simulation*. Society of Petroleum Engineers.

[Collin, 2003] Collin, F. (2003). *Couplages thermo-hydro-mécaniques dans les sols et les roches tendres partiellement saturés*. PhD thesis, Université de Liège, Belgique.

[Collin et al., 2006] Collin, F., Chambon, R., and Charlier, R. (2006). A finite element method for poro mechanical modelling of geotechnical problems using local second gradient models. *International journal for numerical methods in engineering*, 65(11):1749–1772.

[Connell et al., 2010] Connell, L. D., Lu, M., and Pan, Z. (2010). An analytical coal permeability model for tri-axial strain and stress conditions. *International Journal of Coal Geology*, 84(2):103–114.

[Coppens, 1967] Coppens, P. L. (1967). *Synthèse des propriétés chimiques et physiques des houilles*. Institut National de l'Industrie Charbonnière.

[Corey, 1954] Corey, A. T. (1954). The interrelation between gas and oil relative permeabilities. *Producers monthly*, 19(1):38–41.

[Coussy, 1995] Coussy, O. (1995). *Mechanics of porous continua*. Wiley.

[Crank, 1979] Crank, J. (1979). *The mathematics of diffusion*. Oxford university press.

[Crosdale et al., 1998] Crosdale, P. J., Beamish, B. B., and Valix, M. (1998). Coalbed methane sorption related to coal composition. *International Journal of Coal Geology*, 35(1):147–158.

[Cui and Bustin, 2005] Cui, X. and Bustin, R. M. (2005). Volumetric strain associated with methane desorption and its impact on coalbed gas production from deep coal seams. *Aapg Bulletin*, 89(9):1181–1202.

[Cussler, 2009] Cussler, E. L. (2009). *Diffusion: mass transfer in fluid systems*. Cambridge university press.

[Darcy, 1856] Darcy, H. (1856). *Les fontaines publiques de la ville de Dijon*. Librairie des Corps Impériaux des Ponts et Chaussées et des Mines.

[Davies and Booth, 1961] Davies, L. and Booth, H. (1961). An unsteady flow method for air-permeability measurement of refractory materials. *Ceramic Bulletin*, 40(12):744–47.

[Dawson and Esterle, 2010] Dawson, G. and Esterle, J. (2010). Controls on coal cleat spacing. *International Journal of Coal Geology*, 82(3):213–218.

[Day et al., 2008] Day, S., Fry, R., and Sakurovs, R. (2008). Swelling of australian coals in supercritical co 2. *International Journal of Coal Geology*, 74(1):41–52.

[De Weireld et al., 1999] De Weireld, G., Frere, M., and Jadot, R. (1999). Automated determination of high-temperature and high-pressure gas adsorption isotherms using a magnetic suspension balance. *Measurement Science and Technology*, 10(2):117.

[Deevi and Suuberg, 1987] Deevi, S. and Suuberg, E. (1987). Physical changes accompanying drying of western us lignites. *Fuel*, 66(4):454–460.

[Dieudonné, 2016] Dieudonné, A.-C. (2016). *Hydromechanical behaviour of compacted bentonite: from micro-scale analysis to macro-scale modelling*. PhD thesis, Ph. D. thesis, Université de Liège, Liège, Belgique.

[Dieudonné et al., 2015] Dieudonné, A.-C., Cerfontaine, B., Collin, F., and Charlier, R. (2015). Hydromechanical modelling of shaft sealing for co2 storage. *Engineering geology*, 193:97–105.

[Espinoza et al., 2015] Espinoza, D. N., Pereira, J.-M., Vandamme, M., Dangla, P., and Vidal-Gilbert, S. (2015). Desorption-induced shear failure of coal bed seams during gas depletion. *International Journal of Coal Geology*, 137:142–151.

[Espinoza et al., 2013] Espinoza, D. N., Vandamme, M., Dangla, P., Pereira, J.-M., and Vidal-Gilbert, S. (2013). A transverse isotropic model for microporous solids: Application to coal matrix adsorption and swelling. *Journal of Geophysical Research: Solid Earth*, 118(12):6113–6123.

[Espinoza et al., 2014] Espinoza, D. N., Vandamme, M., Pereira, J.-M., Dangla, P., and Vidal-Gilbert, S. (2014). Measurement and modeling of adsorptive-poromechanical properties of bituminous coal cores exposed to co2: Adsorption, swelling strains, swelling stresses and impact on fracture permeability. *International Journal of Coal Geology*, 134:80–95.

[Euler, 1749] Euler, L. (1749). Scientia navalis seu tractatus de construendis ac dirigendis navibus, 2 vols. *Academiae Scientarum, St. Petersbourg (Russie)*.

[Evans, 1973] Evans, D. G. (1973). Effects of colloidal structure on physical measurements on coals. *Fuel*, 52(2):155–156.

[Evans and Pomeroy, 1966] Evans, I. and Pomeroy, C. D. (1966). *The strength, fracture and workability of coal: a monograph on basic work on coal winning carried out by the Mining Research Establishment, National Coal Board*. Pergamon Press.

[Evershed, 2018] Evershed, N. (2018). An unconventional gas boom: the rise of csg in australia. *The Guardian*.

[Ewen and Thomas, 1989] Ewen, J. and Thomas, H. (1989). Heating unsaturated medium sand. *Geotechnique*, 39(3):455–470.

[Faiz et al., 2007] Faiz, M., Saghafi, A., Barclay, S., Stalker, L., Sherwood, N., Whitford, D., and Scientific, C. (2007). Evaluating geological sequestration of co2 in bituminous coals: The southern sydney basin, australia as a natural analogue. *International journal of greenhouse gas control*, 1(2):223–235.

[Faraj et al., 1996] Faraj, B. S., Fielding, C. R., and Mackinnon, I. D. (1996). Cleat mineralization of upper permian baralaba/rangal coal measures, bowen basin, australia. *Geological Society, London, Special Publications*, 109(1):151–164.

[Feyel and Chaboche, 2000] Feyel, F. and Chaboche, J.-L. (2000). FE^2 multiscale approach for modelling the elastoviscoplastic behaviour of long fibre sic/ti composite materials. *Computer methods in applied mechanics and engineering*, 183(3):309–330.

[Fick, 1855] Fick, A. (1855). Ueber diffusion. *Annalen der Physik*, 170(1):59–86.

[Fish and Wagiman, 1993] Fish, J. and Wagiman, A. (1993). Multiscale finite element method for a locally nonperiodic heterogeneous medium. *Computational Mechanics*, 12(3):164–180.

[Fitzgerald et al., 2005] Fitzgerald, J., Pan, Z., Sudibandriyo, M., Robinson Jr, R., Gasem, K., and Reeves, S. (2005). Adsorption of methane, nitrogen, carbon dioxide and their mixtures on wet tiffany coal. *Fuel*, 84(18):2351–2363.

[Flores, 1998] Flores, R. M. (1998). Coalbed methane: from hazard to resource. *International Journal of Coal Geology*, 35(1):3–26.

[Flores, 2013] Flores, R. M. (2013). *Coal and coalbed gas: fueling the future*. Newnes.

[Fossum, 1985] Fossum, A. (1985). Effective elastic properties for a randomly jointed rock mass. In *International Journal of Rock Mechanics and Mining Sciences & Geomechanics Abstracts*, volume 22, pages 467–470. Pergamon.

[Fourar et al., 1998] Fourar, M., Lenormand, R., et al. (1998). A viscous coupling model for relative permeabilities in fractures. In *SPE Annual Technical Conference and Exhibition*. Society of Petroleum Engineers.

[Frey, 2010] Frey, J. (2010). *Modélisation multi-échelle de l'endommagement hydromécanique des roches argileuses*. PhD thesis, Grenoble, INPG.

[Frey et al., 2013] Frey, J., Chambon, R., and Dascalu, C. (2013). A two-scale poromechanical model for cohesive rocks. *Acta Geotechnica*, 8(2):107–124.

[Gao et al., 2014] Gao, L., Mastalerz, M., and Schimmelmann, A. (2014). Chapter 2 - The Origin of Coalbed Methane. In *Coal Bed Methane*, pages 7 – 29.

[Garrels and Christ, 1965] Garrels, R. M. and Christ, C. L. (1965). Solutions, minerals, and equilibria.

[Gates et al., 1950] Gates, J. I., Lietz, W. T., et al. (1950). Relative permeabilities of california cores by the capillary-pressure method. In *Drilling and Production Practice*. American Petroleum Institute.

[Geers et al., 2010] Geers, M. G., Kouznetsova, V. G., and Brekelmans, W. (2010). Multi-scale computational homogenization: Trends and challenges. *Journal of computational and applied mathematics*, 234(7):2175–2182.

[Gens et al., 1990] Gens, A., Carol, I., and Alonso, E. (1990). A constitutive model for rock joints formulation and numerical implementation. *Computers and Geotechnics*, 9(1-2):3–20.

[Gensterblum et al., 2010] Gensterblum, Y., Van Hemert, P., Billemont, P., Battistutta, E., Busch, A., Krooss, B., De Weireld, G., and Wolf, K.-H. (2010). European inter-laboratory comparison of high pressure co2 sorption isotherms ii: Natural coals. *International Journal of Coal Geology*, 84(2):115–124.

[George and Barakat, 2001] George, J. S. and Barakat, M. (2001). The change in effective stress associated with shrinkage from gas desorption in coal. *International Journal of Coal Geology*, 45(2):105–113.

[Gerami et al., 2007] Gerami, S., Darvish, M. P., Morad, K., Mattar, L., et al. (2007). Type curves for dry cbm reservoirs with equilibrium desorption. In *Canadian International Petroleum Conference*. Petroleum Society of Canada.

[Ghosh et al., 1995] Ghosh, S., Lee, K., and Moorthy, S. (1995). Multiple scale analysis of heterogeneous elastic structures using homogenization theory and voronoi cell finite element method. *International Journal of Solids and Structures*, 32(1):27–62.

[Gilman and Beckie, 2000] Gilman, A. and Beckie, R. (2000). Flow of coal-bed methane to a gallery. *Transport in porous media*, 41(1):1–16.

[Godec et al., 2014] Godec, M., Koperna, G., and Gale, J. (2014). Co2-ecbm: a review of its status and global potential. *Energy Procedia*, 63:5858–5869.

[Golab et al., 2006] Golab, A. N., Carr, P. F., and Palamara, D. R. (2006). Influence of localised igneous activity on cleat dawsonite formation in late permian coal measures, upper hunter valley, australia. *International Journal of Coal Geology*, 66(4):296–304.

[Goodman, 1976] Goodman, R. E. (1976). *Methods of geological engineering in discontinuous rocks*.

[Graham and Houlsby, 1983] Graham, J. and Houlsby, G. (1983). Anisotropic elasticity of a natural clay. *Géotechnique*, 33(2):165–180.

[Gray et al., 1987] Gray, I. et al. (1987). Reservoir engineering in coal seams: Part 1-the physical process of gas storage and movement in coal seams. *SPE Reservoir Engineering*, 2(01):28–34.

[Gu et al., 2005] Gu, F., Chalaturnyk, J., et al. (2005). Analysis of coalbed methane production by reservoir and geomechanical coupling simulation. *Journal of Canadian Petroleum Technology*, 44(10).

[Gu and Chalaturnyk, 2010] Gu, F. and Chalaturnyk, R. (2010). Permeability and porosity models considering anisotropy and discontinuity of coalbeds and application in coupled simulation. *Journal of Petroleum Science and Engineering*, 74(3):113–131.

[Gu et al., 2006] Gu, F., Chalaturnyk, R., et al. (2006). Numerical simulation of stress and strain due to gas sorption/desorption and their effects on in situ permeability of coalbeds. *Journal of Canadian Petroleum Technology*, 45(10).

[Guan et al., 2018] Guan, C., Liu, S., Li, C., Wang, Y., and Zhao, Y. (2018). The temperature effect on the methane and co2 adsorption capacities of illinois coal. *Fuel*, 211:241–250.

[Gunter et al., 1997] Gunter, W., Gentzis, T., Rottenfusser, B., and Richardson, R. (1997). Deep coalbed methane in alberta, canada: a fuel resource with the potential of zero greenhouse gas emissions. *Energy Conversion and Management*, 38:S217–S222.

[Gustafsson and Vasil'ev, 2006] Gustafsson, B. and Vasil'ev, A. (2006). *Conformal and potential analysis in Hele-Shaw cells*. Springer Science & Business Media.

[Gutierrez-Rodriguez et al., 1984] Gutierrez-Rodriguez, J., Purcell Jr, R., and Aplan, F. (1984). Estimating the hydrophobicity of coal. *Colloids and Surfaces*, 12:1–25.

[Habraken, 1989] Habraken, A.-M. (1989). *Contribution à la modélisation du formage des métaux par la méthode des éléments finis*. PhD thesis, Universté de Liège.

[Harpalani and Chen, 1995] Harpalani, S. and Chen, G. (1995). Estimation of changes in fracture porosity of coal with gas emission. *Fuel*, 74(10):1491–1498.

[Harpalani and Chen, 1997] Harpalani, S. and Chen, G. (1997). Influence of gas production induced volumetric strain on permeability of coal. *Geotechnical & Geological Engineering*, 15(4):303–325.

[Harpalani and Schraufnagel, 1990] Harpalani, S. and Schraufnagel, A. (1990). Measurement of parameters impacting methane recovery from coal seams. *International Journal of Mining and Geological Engineering*, 8(4):369–384.

[Havercroft and Consoli, 2018] Havercroft, I. and Consoli, C. (2018). 2018 thought leadership report. the carbon capture and storage readiness index 2018. is the world ready for carbon capture and storage? Technical report, Global CCS Institute.

[Herrin and Deming, 1996] Herrin, J. M. and Deming, D. (1996). Thermal conductivity of us coals. *Journal of Geophysical Research: Solid Earth*, 101(B11):25381–25386.

[Hill, 1965] Hill, R. (1965). A self-consistent mechanics of composite materials. *Journal of the Mechanics and Physics of Solids*, 13(4):213–222.

[Hilt, 1873] Hilt, C. (1873). Die beziehungen zwischen der zusammensetzung und den technischen eigenschaften der steinkohlen. *Ver. Dtsch. Ing. Z.*, 17(2):194–202.

[Intergovernmental Panel on Climate Change - IPCC, 2015] Intergovernmental Panel on Climate Change - IPCC (2015). *Climate change 2014: Mitigation of climate change*, volume 3. Cambridge University Press.

[International Energy Agency - IEA, 2016] International Energy Agency - IEA (2016). Key world energy statistics 2016.

[Ismail et al., 2015] Ismail, A. F., Khulbe, K. C., and Matsuura, T. (2015). *Gas separation membranes*, volume 7. Springer.

[Jaumann, 1911] Jaumann, G. (1911). Geschlossenes system physikalischer und chemischer differentialgesetze. *Sitzungsberichte Akad. Wiss. Wien, IIa*, pages 385–530.

[Jeffrey et al., 1989] Jeffrey, R., Hinkel, J., Nimerick, K., and McLennan, J. (1989). Hydraulic fracturing to enhance production of methane from coal seams. In *The 1989 Coalbed Methane Symposium. Tuscaloosa, Alabama: Paper*, volume 8992, pages 385–394.

[Jing et al., 2016] Jing, Y., Armstrong, R. T., Ramandi, H. L., and Mostaghimi, P. (2016). Coal cleat reconstruction using micro-computed tomography imaging. *Fuel*, 181:286–299.

[Jones et al., 1987] Jones, A., Bell, G., Morales, R., and Schraufnagel, R. (1987). The influence of coal fines/chips on the behavior of hydraulic fracture stimulation treatments. In *The 1987 Coalbed Methane Symposium Proceedings, The University of Alabama, Tuscaloosa, Alabama,(November) pp*, pages 93–102.

[Jones Jr et al., 1975] Jones Jr, F. O. et al. (1975). A laboratory study of the effects of confining pressure on fracture flow and storage capacity in carbonate rocks. *Journal of Petroleum Technology*, 27(01):21–27.

[Joubert et al., 1973] Joubert, J. I., Grein, C. T., and Bienstock, D. (1973). Sorption of methane in moist coal. *Fuel*, 52(3):181–185.

[Jurin, 1718] Jurin, J. (1718). An account of some experiments shown before the royal society; with an enquiry into the cause of the ascent and suspension of water in capillary tubes. *Philosophical Transactions of the Royal Society of London*, 30(355):739–747.

[Karacan, 2003] Karacan, C. Ö. (2003). Heterogeneous sorption and swelling in a confined and stressed coal during co2 injection. *Energy & Fuels*, 17(6):1595–1608.

[Kazemi et al., 1976] Kazemi, H., Merrill Jr, L., Porterfield, K., Zeman, P., et al. (1976). Numerical simulation of water-oil flow in naturally fractured reservoirs. *Society of Petroleum Engineers Journal*, 16(06):317–326.

[Keller Jr, 1987] Keller Jr, D. (1987). The contact angle of water on coal. *Colloids and surfaces*, 22(1):21–35.

[Kewen et al., 2004] Kewen, L. et al. (2004). Theoretical development of the brooks-corey capillary pressure model from fractal modeling of porous media. In *SPE/DOE Symposium on Improved Oil Recovery*. Society of Petroleum Engineers.

[Kissell, 1972] Kissell, F. N. (1972). The methane migration and storage characteristics of the pittsburgh, pocahontas no. 3, and oklahoma hartshorne coalbeds.

[Klinkenberg et al., 1941] Klinkenberg, L. et al. (1941). The permeability of porous media to liquids and gases. In *Drilling and production practice*. American Petroleum Institute.

[Koenig et al., 1989] Koenig, R. A., Bumb, A., McKee, C., Murphy, C., and Ramesh, M. (1989). Application of hydrology to evaluation of coalbed methane reservoirs. topical report, january 1987-december 1988. Technical report, In-Situ, Inc., Laramie, WY (USA).

[Kouznetsova et al., 2001] Kouznetsova, V., Brekelmans, W., and Baaijens, F. (2001). An approach to micro-macro modeling of heterogeneous materials. *Computational Mechanics*, 27(1):37–48.

[Kouznetsova et al., 2002] Kouznetsova, V., Geers, M. G., and Brekelmans, W. M. (2002). Multi-scale constitutive modelling of heterogeneous materials with a gradient-enhanced computational homogenization scheme. *International Journal for Numerical Methods in Engineering*, 54(8):1235–1260.

[Krooss et al., 2002] Krooss, B. v., Van Bergen, F., Gensterblum, Y., Siemons, N., Pagnier, H., and David, P. (2002). High-pressure methane and carbon dioxide adsorption on dry and moisture-equilibrated pennsylvanian coals. *International Journal of Coal Geology*, 51(2):69–92.

[Kundt and Warburg, 1875] Kundt, A. and Warburg, E. (1875). Ueber reibung und wärmeleitung verdünnter gase. *Annalen der Physik*, 232(10):177–211.

[Lake and Srinivasan, 2004] Lake, L. W. and Srinivasan, S. (2004). Statistical scale-up of reservoir properties: concepts and applications. *Journal of Petroleum Science and Engineering*, 44(1-2):27–39.

[Lange, 2010] Lange, I. (2010). Steam versus coking coal and the acid rain program. *Energy Policy*, 38(3):1251–1254.

[Langmuir, 1918] Langmuir, I. (1918). The adsorption of gases on plane surfaces of glass, mica and platinum. *Journal of the American Chemical society*, 40(9):1361–1403.

[Laplace, 1806] Laplace, P.-S. (1806). Sur l'action capillaire. *Supplément au livre X, Traité de Mécanique Céleste*, 349.

[Larsen et al., 1997] Larsen, J. W., Flowers, R. A., Hall, P. J., and Carlson, G. (1997). Structural rearrangement of strained coals. *Energy & Fuels*, 11(5):998–1002.

[Larsson et al., 2010a] Larsson, F., Runesson, K., and Su, F. (2010a). Computational homogenization of uncoupled consolidation in micro-heterogeneous porous media. *International Journal for Numerical and Analytical Methods in Geomechanics*, 34(14):1431–1458.

[Larsson et al., 2010b] Larsson, F., Runesson, K., and Su, F. (2010b). Variationally consistent computational homogenization of transient heat flow. *International Journal for Numerical Methods in Engineering*, 81(13):1659–1686.

[Laubach et al., 1998] Laubach, S., Marrett, R., Olson, J., and Scott, A. (1998). Characteristics and origins of coal cleat: a review. *International Journal of Coal Geology*, 35(1):175–207.

[Lekhnitskii, 1963] Lekhnitskii, S. (1963). *Theory of Elasticity of an Anisotropic Elastic Body*, volume 525. San Francisco: Holden-Day.

[Levine, 1996] Levine, J. R. (1996). Model study of the influence of matrix shrinkage on absolute permeability of coal bed reservoirs. *Geological Society, London, Special Publications*, 109(1):197–212.

[Li et al., 2018] Li, J., Chen, Z., Wu, K., Wang, K., Luo, J., Feng, D., Qu, S., and Li, X. (2018). A multi-site model to determine supercritical methane adsorption in energetically heterogeneous shales. *Chemical Engineering Journal*, 349:438–455.

[Lide, 2004] Lide, D. R. (2004). *CRC handbook of chemistry and physics*, volume 85. CRC press.

[Lim and Aziz, 1995] Lim, K. and Aziz, K. (1995). Matrix-fracture transfer shape factors for dual-porosity simulators. *Journal of Petroleum Science and Engineering*, 13(3):169–178.

[Liu et al., 2009] Liu, H.-H., Rutqvist, J., and Berryman, J. G. (2009). On the relationship between stress and elastic strain for porous and fractured rock. *International Journal of Rock Mechanics and Mining Sciences*, 46(2):289–296.

[Love, 1927] Love, A. (1927). A treatise on the mathematical theory of elasticitycambridge university press. *Cambridge, MA*.

[Lu and Connell, 2007] Lu, M. and Connell, L. D. (2007). A dual-porosity model for gas reservoir flow incorporating adsorption behaviour—part i. theoretical development and asymptotic analyses. *Transport in porous media*, 68(2):153–173.

[Lu et al., 2016] Lu, S., Cheng, Y., and Li, W. (2016). Model development and analysis of the evolution of coal permeability under different boundary conditions. *Journal of Natural Gas Science and Engineering*, 31:129–138.

[Malvern, 1969] Malvern, L. E. (1969). *Introduction to the Mechanics of a Continuous Medium*. Number Monograph.

[Mandel, 1972] Mandel, J. (1972). Plasticité classique et viscoplasticité. CISM Courses and Lectures No. 97.

[Mandelbrot and Pignoni, 1983] Mandelbrot, B. B. and Pignoni, R. (1983). The fractal geometry of nature.

[Marinelli, 2013] Marinelli, F. (2013). *Comportement couplé des géo-matériaux: deux approches de modélisation numérique*. PhD thesis, Université Grenoble Alpes.

[Marinelli et al., 2016] Marinelli, F., Van den Eijnden, A., Sieffert, Y., Chambon, R., and Collin, F. (2016). Modeling of granular solids with computational homogenization: Comparison with biot' s theory. *Finite Elements in Analysis and Design*, 119:45–62.

[Mason and Malinauskas, 1983] Mason, E. A. and Malinauskas, A. (1983). *Gas transport in porous media: the dusty-gas model*, volume 17. Elsevier Science Ltd.

[Massart and Selvadurai, 2014] Massart, T. and Selvadurai, A. (2014). Computational modelling of crack-induced permeability evolution in granite with dilatant cracks. *International journal of rock mechanics and mining sciences*, 70:593–604.

[Massart, 2003] Massart, T. J. (2003). *Multi-scale modeling of damage in masonry structures*. PhD thesis, Technische Universiteit Eindhoven.

[Mazumder et al., 2012] Mazumder, S., Scott, M., and Jiang, J. (2012). Permeability increase in bowen basin coal as a result of matrix shrinkage during primary depletion. *International Journal of Coal Geology*, 96:109–119.

[Mazumder et al., 2011] Mazumder, S., Vermolen, F., Bruining, J., et al. (2011). Analysis of a model for anomalous-diffusion behavior of CO_2 in the macromolecular-network structure of coal. *SPE Journal*, 16(04):856–863.

[Mazzotti et al., 2009] Mazzotti, M., Pini, R., and Storti, G. (2009). Enhanced coalbed methane recovery. *The Journal of Supercritical Fluids*, 47(3):619–627.

[McCants et al., 2001] McCants, C., Spafford, S., and Stevens, S. (2001). Five-spot production pilot on tight spacing: rapid evaluation of a coalbed methane block in the upper silesian coal basin, poland. In *Proc. of the 2001 Int. Coalbed Methane Symposium, University of Alabama, Tuscaloosa*, pages 193–204.

[McNerney et al., 2011] McNerney, J., Farmer, J. D., and Trancik, J. E. (2011). Historical costs of coal-fired electricity and implications for the future. *Energy Policy*, 39(6):3042–3054.

[Medhurst and Brown, 1998] Medhurst, T. and Brown, E. (1998). A study of the mechanical behaviour of coal for pillar design. *International Journal of Rock Mechanics and Mining Sciences*, 35(8):1087–1105.

[Meyers, 2012] Meyers, R. (2012). *Coal structure*. Elsevier.

[Miehe, 1996] Miehe, C. (1996). Numerical computation of algorithmic (consistent) tangent moduli in large-strain computational inelasticity. *Computer methods in applied mechanics and engineering*, 134(3-4):223–240.

[Miehe et al., 1999] Miehe, C., Schröder, J., and Schotte, J. (1999). Computational homogenization analysis in finite plasticity simulation of texture development in polycrystalline materials. *Computer methods in applied mechanics and engineering*, 171(3-4):387–418.

[Mitra et al., 2012] Mitra, A., Harpalani, S., and Liu, S. (2012). Laboratory measurement and modeling of coal permeability with continued methane production: Part 1–laboratory results. *Fuel*, 94:110–116.

[Moore, 2012] Moore, T. A. (2012). Coalbed methane: a review. *International Journal of Coal Geology*, 101:36–81.

[Mora et al., 2009] Mora, C., Wattenbarger, R., et al. (2009). Analysis and verification of dual porosity and cbm shape factors. *Journal of Canadian Petroleum Technology*, 48(02):17–21.

[Moulinec and Suquet, 1998] Moulinec, H. and Suquet, P. (1998). A numerical method for computing the overall response of nonlinear composites with complex microstructure. *Computer methods in applied mechanics and engineering*, 157(1-2):69–94.

[Mualem, 1976] Mualem, Y. (1976). A new model for predicting the hydraulic conductivity of unsaturated porous media. *Water resources research*, 12(3):513–522.

[Murata et al., 2000] Murata, S., Hosokawa, M., Kidena, K., and Nomura, M. (2000). Analysis of oxygen-functional groups in brown coals. *Fuel processing technology*, 67(3):231–243.

[Myers, 2002] Myers, A. (2002). Thermodynamics of adsorption in porous materials. *AIChE Journal*, 48(1):145–160.

[Navier, 1820] Navier, C. (1820). *Mémoire sur la flexion des plans élastiques*.

[Neuman, 1977] Neuman, S. P. (1977). Theoretical derivation of darcy's law. *Acta Mechanica*, 25(3-4):153–170.

[Newman, 1955] Newman, P. (1955). Plastic flow in coal. *British Journal of Applied Physics*, 6(10):348.

[Newton, 1687] Newton, I. (1687). *Philosophiae naturalis principia mathematica*.

[Nguyen et al., 2014] Nguyen, T. K., Combe, G., Caillerie, D., and Desrues, J. (2014). Fem dem modelling of cohesive granular materials: numerical homogenisation and multi-scale simulations. *Acta Geophysica*, 62(5):1109–1126.

[Nikolai et al., 2019] Nikolai, P., Rabiyat, B., Aslan, A., and Ilmutdin, A. (2019). Supercritical co2: Properties and technological applications-a review. *Journal of Thermal Science*, 28(3):394–430.

[Nikoosokhan et al., 2012] Nikoosokhan, S., Vandamme, M., and Dangla, P. (2012). A poromechanical model for coal seams injected with carbon dioxide: from an isotherm of adsorption to a swelling of the reservoir. *Oil & Gas Science and Technology–Revue d'IFP Energies nouvelles*, 67(5):777–786.

[Nitka et al., 2011] Nitka, M., Combe, G., Dascalu, C., and Desrues, J. (2011). Two-scale modeling of granular materials: a dem-fem approach. *Granular Matter*, 13(3):277–281.

[Nuth and Laloui, 2008] Nuth, M. and Laloui, L. (2008). Effective stress concept in unsaturated soils: clarification and validation of a unified framework. *International journal for numerical and analytical methods in Geomechanics*, 32(7):771–801.

[O'Keefe et al., 2013] O'Keefe, J. M., Bechtel, A., Christanis, K., Dai, S., DiMichele, W. A., Eble, C. F., Esterle, J. S., Mastalerz, M., Raymond, A. L., Valentim, B. V., et al. (2013). On the fundamental difference between coal rank and coal type. *International Journal of Coal Geology*, 118:58–87.

[Okotie et al., 2011] Okotie, V. U., Moore, R. L., et al. (2011). Well-production challenges and solutions in a mature, very-low-pressure coalbed-methane reservoir. *SPE Production & Operations*, 26(02):149–161.

[Olivella et al., 1994] Olivella, S., Carrera, J., Gens, A., and Alonso, E. (1994). Nonisothermal multiphase flow of brine and gas through saline media. *Transport in porous media*, 15(3):271–293.

[Olsson and Barton, 2001] Olsson, R. and Barton, N. (2001). An improved model for hydromechanical coupling during shearing of rock joints. *International Journal of Rock Mechanics and Mining Sciences*, 38(3):317–329.

[Ottiger et al., 2008] Ottiger, S., Pini, R., Storti, G., and Mazzotti, M. (2008). Competitive adsorption equilibria of CO_2 and CH_4 on a dry coal. *Adsorption*, 14(4-5):539–556.

[Özdemir et al., 2008] Özdemir, I., Brekelmans, W., and Geers, M. (2008). Computational homogenization for heat conduction in heterogeneous solids. *International journal for numerical methods in engineering*, 73(2):185–204.

[Özdemir, 2009] Özdemir, I. I. (2009). *Multi-scale modelling of thermal shock damage in refractory materials*. PhD thesis, Technische Universiteit Eindhoven.

[Palmer, 2010] Palmer, I. (2010). Coalbed methane completions: a world view. *International Journal of Coal Geology*, 82(3):184–195.

[Palmer et al., 1996] Palmer, I., Mansoori, J., et al. (1996). How permeability depends on stress and pore pressure in coalbeds: a new model. In *SPE Annual Technical Conference and Exhibition*. Society of Petroleum Engineers.

[Pan and Connell, 2007] Pan, Z. and Connell, L. D. (2007). A theoretical model for gas adsorption-induced coal swelling. *International Journal of Coal Geology*, 69(4):243–252.

[Pan and Connell, 2012] Pan, Z. and Connell, L. D. (2012). Modelling permeability for coal reservoirs: a review of analytical models and testing data. *International Journal of Coal Geology*, 92:1–44.

[Panday and Corapcioglu, 1989] Panday, S. and Corapcioglu, M. Y. (1989). Reservoir transport equations by compositional approach. *Transport in Porous Media*, 4(4):369–393.

[Pardoen et al., 2015] Pardoen, B., Levasseur, S., and Collin, F. (2015). Using local second gradient model and shear strain localisation to model the excavation damaged zone in unsaturated claystone. *Rock Mechanics and Rock Engineering*, 48(2):691–714.

[Patching, 1965] Patching, T. (1965). Variations in permeability of coal. In *Proc. 3d Rock Mech. Symp., Univ. of Toronto*.

[Paterson, 1986] Paterson, L. (1986). A model for outbursts in coal. In *International Journal of Rock Mechanics and Mining Sciences & Geomechanics Abstracts*, volume 23, pages 327–332. Elsevier.

[Paterson et al., 1992] Paterson, L., Meaney, K., and Smyth, M. (1992). Measurements of relative permeability, absolute permeability and fracture geometry in coal. In *Coalbed Methane Symposium*, pages 19–21.

[Peaceman et al., 1978] Peaceman, D. W. et al. (1978). Interpretation of well-block pressures in numerical reservoir simulation (includes associated paper 6988). *Society of Petroleum Engineers Journal*, 18(03):183–194.

[Peng et al., 2017] Peng, Y., Liu, J., Pan, Z., Connell, L. D., Chen, Z., and Qu, H. (2017). Impact of coal matrix strains on the evolution of permeability. *Fuel*, 189:270–283.

[Pereira et al., 2010] Pereira, J.-M., Coussy, O., Alonso, E. E., Vaunat, J., and Olivella, S. (2010). Is the degree of saturation a good candidate for bishop's x parameter? *arXiv preprint arXiv:1010.2608*.

[Pham et al., 2013] Pham, K., Kouznetsova, V. G., and Geers, M. G. (2013). Transient computational homogenization for heterogeneous materials under dynamic excitation. *Journal of the Mechanics and Physics of Solids*, 61(11):2125–2146.

[Piessens and Dusar, 2004] Piessens, K. and Dusar, M. (2004). Feasibility of CO_2 sequestration in abandoned coal mines in belgium. *Geologica Belgica*.

[Pineda et al., 2014] Pineda, J., Sheng, D., et al. (2014). Coal seam gas extraction and their potential effects on surface subsidence: an overview. In *7th International Congress on Environmental Geotechnics: iceg2014*, page 370. Engineers Australia.

[Purcell et al., 1949] Purcell, W. et al. (1949). Capillary pressures-their measurement using mercury and the calculation of permeability therefrom. *Journal of Petroleum Technology*, 1(02):39–48.

[Puri et al., 1990] Puri, R., Yee, D., et al. (1990). Enhanced coalbed methane recovery. In *SPE Annual Technical Conference and Exhibition*. Society of Petroleum Engineers.

[Queensland Government, 2007] Queensland Government (2007). Climatesmart 2050 - queensland climate change strategy 2007: a low-carbon future. Technical report, Queensland Government.

[Quintard and Whitaker, 1996] Quintard, M. and Whitaker, S. (1996). Transport in chemically and mechanically heterogeneous porous media. ii: Comparison with numerical experiments for slightly compressible single-phase flow. *Advances in water resources*, 19(1):49–60.

[Rathnaweera et al., 2016] Rathnaweera, T., Ranjith, P., and Perera, M. (2016). Experimental investigation of geochemical and mineralogical effects of co2 sequestration on flow characteristics of reservoir rock in deep saline aquifers. *Scientific reports*, 6:19362.

[Reeves et al., 2003] Reeves, S., Taillefert, A., and Pekot, L. (2003). Allison unit co2-ecbm pilot: A reservoir modeling study.

[Reeves, 2003] Reeves, S. R. (2003). Assessment of co2 sequestration and ecbm potential of us coalbeds. Technical report, Advanced Resources International, Incorporated.

[Reiss, 1980] Reiss, L. H. (1980). *The reservoir engineering aspects of fractured formations*, volume 3. Editions Technip.

[Reynolds et al., 1903] Reynolds, O., Brightmore, A. W., and Moorby, W. H. (1903). *Papers on Mechanical and Physical Subjects: The sub-mechanics of the universe*, volume 3. The University Press.

[Robertson et al., 2007] Robertson, E. P., Christiansen, R. L., et al. (2007). Modeling laboratory permeability in coal using sorption-induced strain data. *SPE Reservoir Evaluation & Engineering*, 10(03):260–269.

[Romero et al., 2005] Romero, E., Garcıa, I., and Knobelsdorf, J. (2005). Gas permeability evolution of a sand/bentonite during controlled-suction paths. In *Proceedings of the international symposium on advanced experimental unsaturated soil mechanics*, pages 385–390.

[Romm, 1966] Romm, E. S. (1966). *Fluid flow in fractured rocks (in Russian)*. Nedra Publishing House.

[Ruthven, 1984] Ruthven, D. M. (1984). *Principles of adsorption and adsorption processes*. John Wiley & Sons.

[Salmachi and Haghighi, 2012] Salmachi, A. and Haghighi, M. (2012). Feasibility study of thermally enhanced gas recovery of coal seam gas reservoirs using geothermal resources. *Energy & Fuels*, 26(8):5048–5059.

[Salmachi and Yarmohammadtooski, 2015] Salmachi, A. and Yarmohammadtooski, Z. (2015). Production data analysis of coalbed methane wells to estimate the time required to reach to peak of gas production. *International Journal of Coal Geology*, 141:33–41.

[Sanchez-Palencia and Zaoui, 1985] Sanchez-Palencia, E. and Zaoui, A. (1985). 1985. *Homogenization techniques for composite media*.

[Sander, 2015] Sander, R. (2015). Compilation of henry's law constants (version 4.0) for water as solvent. *Atmospheric Chemistry & Physics*, 15(8).

[Sawyer et al., 1990] Sawyer, W., Paul, G., Schraufnagel, R., et al. (1990). Development and application of a 3-d coalbed simulator. In *Annual technical meeting*. Petroleum Society of Canada.

[Schopf, 1956] Schopf, J. M. (1956). A definition of coal. *Economic geology*, 51(6):521–527.

[Schrefler, 1984] Schrefler, B. (1984). *The finite element method in soil consolidation*. PhD thesis, University College of Swansea.

[Schröder, 2014] Schröder, J. (2014). A numerical two-scale homogenization scheme: the fe2-method. In *Plasticity and Beyond*, pages 1–64. Springer.

[Schwerer et al., 1984] Schwerer, F., Pavone, A., et al. (1984). Effect of pressure-dependent permeability on well-test analyses and long-term production of methane from coal seams. In *SPE Unconventional Gas Recovery Symposium*. Society of Petroleum Engineers.

[Seidle, 2011] Seidle, J. (2011). *Fundamentals of coalbed methane reservoir engineering*. PennWell Books.

[Seidle et al., 1992] Seidle, J., Jeansonne, M., Erickson, D., et al. (1992). Application of matchstick geometry to stress dependent permeability in coals. In *SPE rocky mountain regional meeting*. Society of Petroleum Engineers.

[Seidle et al., 1995] Seidle, J. R., Huitt, L., et al. (1995). Experimental measurement of coal matrix shrinkage due to gas desorption and implications for cleat permeability increases. In *International meeting on petroleum Engineering*. Society of Petroleum Engineers.

[Seiphoori et al., 2014] Seiphoori, A., Ferrari, A., and Laloui, L. (2014). Water retention behaviour and microstructural evolution of mx-80 bentonite during wetting and drying cycles. *Géotechnique*, 64(9):721–734.

[Selley and Sonnenberg, 2014] Selley, R. C. and Sonnenberg, S. A. (2014). *Elements of petroleum geology*. Academic Press.

[Sevenster, 1959] Sevenster, P. (1959). Diffusion of gases through coal. *Fuel*, 38(4):403–418.

[Shahtalebi et al., 2016] Shahtalebi, A., Khan, C., Dmyterko, A., Shukla, P., and Rudolph, V. (2016). Investigation of thermal stimulation of coal seam gas fields for accelerated gas recovery. *Fuel*, 180:301–313.

[Shi and Durucan, 2003] Shi, J. and Durucan, S. (2003). A bidisperse pore diffusion model for methane displacement desorption in coal by CO_2 injection. *Fuel*, 82(10):1219–1229.

[Shi and Durucan, 2004] Shi, J. and Durucan, S. (2004). Drawdown induced changes in permeability of coalbeds: a new interpretation of the reservoir response to primary recovery. *Transport in porous media*, 56(1):1–16.

[Shi et al., 2006] Shi, J. Q., Durucan, S., and Syahrial, E. (2006). Reservoir depletion induced changes in coalbed permeability and implications for enhanced cbm recovery using co2 injection. *Geologica Belgica*.

[Shi et al., 2014] Shi, J.-Q., Pan, Z., and Durucan, S. (2014). Analytical models for coal permeability changes during coalbed methane recovery: Model comparison and performance evaluation. *International Journal of Coal Geology*, 136:17–24.

[Siemons et al., 2006] Siemons, N., Bruining, H., Castelijns, H., and Wolf, K.-H. (2006). Pressure dependence of the contact angle in a co2–h2o–coal system. *Journal of colloid and interface science*, 297(2):755–761.

[Siriwardane et al., 2009] Siriwardane, H., Haljasmaa, I., McLendon, R., Irdi, G., Soong, Y., and Bromhal, G. (2009). Influence of carbon dioxide on coal permeability determined by pressure transient methods. *International Journal of Coal Geology*, 77(1-2):109–118.

[Smit et al., 1998] Smit, R., Brekelmans, W., and Meijer, H. (1998). Prediction of the mechanical behavior of nonlinear heterogeneous systems by multi-level finite element modeling. *Computer Methods in Applied Mechanics and Engineering*, 155(1):181–192.

[Smyth and Buckley, 1993] Smyth, M. and Buckley, M. J. (1993). Statistical analysis of the microlithotype sequences in the bulli seam, australia, and relevance to permeability for coal gas. *International journal of coal geology*, 22(3-4):167–187.

[Somerton et al., 1975] Somerton, W. H., Soylemezoglu, I., and Dudley, R. (1975). Effect of stress on permeability of coal. 12(5):129–145.

[Span and Wagner, 1996] Span, R. and Wagner, W. (1996). A new equation of state for carbon dioxide covering the fluid region from the triple-point temperature to 1100 k at pressures up to 800 mpa. *Journal of physical and chemical reference data*, 25(6):1509–1596.

[Stopes, 1919] Stopes, M. C. (1919). On the four visible ingredients in banded bituminous coal: studies in the composition of coal, no. 1. *Proceedings of the Royal Society of London. Series B, Containing Papers of a Biological Character*, 90(633):470–487.

[Su et al., 2011] Su, F., Larsson, F., and Runesson, K. (2011). Computational homogenization of coupled consolidation problems in micro-heterogeneous porous media. *International Journal for Numerical Methods in Engineering*, 88(11):1198–1218.

[Suquet, 1987] Suquet, P. (1987). Elements of homogenization for inelastic solid mechanics. *Homogenization techniques for composite media*, 272:193–278.

[Szwilski, 1984] Szwilski, A. (1984). Determination of the anisotropic elastic moduli of coal. In *International Journal of Rock Mechanics and Mining Sciences & Geomechanics Abstracts*, volume 21, pages 3–12. Elsevier.

[Tang et al., 2011] Tang, A. M., Cui, Y.-J., Richard, G., and Défossez, P. (2011). A study on the air permeability as affected by compression of three french soils. *Geoderma*, 162(1-2):171–181.

[Terada et al., 2000] Terada, K., Hori, M., Kyoya, T., and Kikuchi, N. (2000). Simulation of the multi-scale convergence in computational homogenization approaches. *International Journal of Solids and Structures*, 37(16):2285–2311.

[Terada and Kikuchi, 1995] Terada, K. and Kikuchi, N. (1995). Nonlinear homogenization method for practical applications. *ASME applied mechanics division-publications-AMD*, 212:1–16.

[Terzaghi et al., 1996] Terzaghi, K., Peck, R. B., and Mesri, G. (1996). *Soil mechanics in engineering practice*. John Wiley & Sons.

[Terzaghi, 1936] Terzaghi, K. v. (1936). The shearing resistance of saturated soils and the angle between the planes of shear. In *Proceedings of the 1st international conference on soil mechanics and foundation engineering*, volume 1, pages 54–56. Harvard University Press Cambridge, MA.

[Thakur et al., 2014] Thakur, P., Schatzel, S., and Aminian, K. (2014). *Coal bed methane: From prospect to pipeline*. Elsevier.

[Thimons and Kissell, 1973] Thimons, E. D. and Kissell, F. N. (1973). Diffusion of methane through coal. *Fuel*, 52(4):274–280.

[Thomas, 2002] Thomas, L. (2002). *Coal geology*. John Wiley & Sons.

[Tremain et al., 1991] Tremain, C. M., Laubach, S. E., and Whitehead III, N. H. (1991). Coal fracture (cleat) patterns in upper cretaceous fruitland formation, san juan basin, colorado and new mexico-implications for coalbed methane exploration and development.

[Tuncay and Corapcioglu, 1995] Tuncay, K. and Corapcioglu, M. Y. (1995). Effective stress principle for saturated fractured porous media. *Water Resources Research*, 31(12):3103–3106.

[Ueda et al., 1989] Ueda, Y., Murata, S., Watanabe, Y., Funatsu, K., et al. (1989). Investigation of the shape factor used in the dual-porosity reservoir simulator. In *SPE Asia-Pacific Conference*. Society of Petroleum Engineers.

[Uren, 1985] Uren, R. (1985). *Stratigraphy and Depositional Environments of the Wittingham Coal Measures, Kayuga Area, Hunter Valley, New South Wales*. PhD thesis, University of Newcastle.

[U.S. Environmental Protection Agency, 2009] U.S. Environmental Protection Agency (2009). Coal mine methane recovery: A primer.

[Van den Eijnden, 2015] Van den Eijnden, B. (2015). *Multi-scale modelling of the hydro-mechanical behaviour of argillaceuous rocks*. PhD thesis, Université Grenoble Alpes.

[Van der Sluis et al., 2000] Van der Sluis, O., Schreurs, P., Brekelmans, W., and Meijer, H. (2000). Overall behaviour of heterogeneous elastoviscoplastic materials: effect of microstructural modelling. *Mechanics of Materials*, 32(8):449–462.

[Van Genuchten, 1980] Van Genuchten, M. T. (1980). A closed-form equation for predicting the hydraulic conductivity of unsaturated soils. *Soil science society of America journal*, 44(5):892–898.

[van Golf-Racht, 1982] van Golf-Racht, T. D. (1982). *Fundamentals of fractured reservoir engineering*, volume 12. Elsevier.

[Villar et al., 2005] Villar, M., Romero, E., and Lloret, A. (2005). Thermo-mechanical and geochemical effects on the permeability of high-density clays. In *Proceedings of the international symposium on large scale field tests in granite. Advances in understanding engineered clay barriers. In: Alonso EE, Ledesma A (eds) AA Balkema Publishers, Leiden*, pages 177–191.

[Wang et al., 2017] Wang, K., Du, F., and Wang, G. (2017). Investigation of gas pressure and temperature effects on the permeability and steady-state time of chinese anthracite coal: an experimental study. *Journal of Natural Gas Science and Engineering*, 40:179–188.

[Wang et al., 2011] Wang, S., Elsworth, D., and Liu, J. (2011). Permeability evolution in fractured coal: the roles of fracture geometry and water-content. *International Journal of Coal Geology*, 87(1):13–25.

[Warren et al., 1963] Warren, J., Root, P. J., et al. (1963). The behavior of naturally fractured reservoirs. *Society of Petroleum Engineers Journal*, 3(03):245–255.

[Wei et al., 2007] Wei, X. R., Wang, G. X., Massarotto, P., Golding, S. D., Rudolph, V., et al. (2007). A review on recent advances in the numerical simulation for coalbed-methane-recovery process. *SPE Reservoir Evaluation & Engineering*, 10(06):657–666.

[White et al., 2005] White, C. M., Smith, D. H., Jones, K. L., Goodman, A. L., Jikich, S. A., LaCount, R. B., DuBose, S. B., Ozdemir, E., Morsi, B. I., and Schroeder, K. T. (2005). Sequestration of carbon dioxide in coal with enhanced coalbed methane recovery a review. *Energy & Fuels*, 19(3):659–724.

[Witherspoon et al., 1980] Witherspoon, P. A., Wang, J., Iwai, K., and Gale, J. (1980). Validity of cubic law for fluid flow in a deformable rock fracture. *Water resources research*, 16(6):1016–1024.

[Wu et al., 2015] Wu, K., Li, X., Wang, C., Yu, W., and Chen, Z. (2015). Model for surface diffusion of adsorbed gas in nanopores of shale gas reservoirs. *Industrial & Engineering Chemistry Research*, 54(12):3225–3236.

[Xia et al., 2008] Xia, X., d'Alnoncourt, R. N., and Muhler, M. (2008). Entropy of adsorption of carbon monoxide on energetically heterogeneous surfaces. *Journal of Thermal Analysis and Calorimetry*, 91(1):167–172.

[Xia et al., 2006] Xia, X., Litvinov, S., and Muhler, M. (2006). Consistent approach to adsorption thermodynamics on heterogeneous surfaces using different empirical energy distribution models. *Langmuir*, 22(19):8063–8070.

[Yoshimi and Osterberg, 1963] Yoshimi, Y. and Osterberg, J. (1963). Compression of partially saturated cohesive soils. *Journal of the Soil Mechanics and Foundations Division*, 89(4):1–24.

[Young, 1805] Young, T. (1805). An essay on the cohesion of fluids. *Philosophical transactions of the royal society of London*, (95):65–87.

[Yu et al., 2008] Yu, H., Zhou, L., Guo, W., Cheng, J., and Hu, Q. (2008). Predictions of the adsorption equilibrium of methane/carbon dioxide binary gas on coals using langmuir and ideal adsorbed solution theory under feed gas conditions. *International Journal of Coal Geology*, 73(2):115–129.

[Yu et al., 2013] Yu, J., Tahmasebi, A., Han, Y., Yin, F., and Li, X. (2013). A review on water in low rank coals: The existence, interaction with coal structure and effects on coal utilization. *Fuel Processing Technology*, 106:9–20.

[Yuster et al., 1951] Yuster, S. et al. (1951). Theoretical considerations of multiphase flow in idealized capillary systems. In *Proceedings of the 3rd World Petroleum Congress, Section II, The Hague*, volume 2, pages 437–445.

[Zienkiewicz and Taylor, 2000] Zienkiewicz, O. C. and Taylor, R. L. (2000). *The finite element method: solid mechanics*, volume 2. Butterworth-heinemann.

[Zimmerman et al., 1993] Zimmerman, R. W., Chen, G., Hadgu, T., and Bodvarsson, G. S. (1993). A numerical dual-porosity model with semianalytical treatment of fracture/matrix flow. *Water resources research*, 29(7):2127–2137.

[Zimmerman et al., 1986] Zimmerman, R. W., Somerton, W. H., and King, M. S. (1986). Compressibility of porous rocks. *Journal of Geophysical Research: Solid Earth*, 91(B12):12765–12777.

Appendices

A. Stiffness matrix by Static condensation

Following the static condensation procedure to determine the required macroscale stiffness matrix $[A^M]$, the following empty frame for the systems of equations is build:

$$\begin{bmatrix} []_{(10x10)} & []_{(10x\ n_m)} & []_{(10x\ n_w)} & []_{(10x\ n_g)} \\ []_{(n_m x10)} & []_{(n_m x\ n_m)} & []_{(n_m x\ n_w)} & []_{(n_m x\ n_g)} \\ []_{(n_w x10)} & []_{(n_w x\ n_m)} & []_{(n_w x\ n_w)} & []_{(n_w x\ n_g)} \\ []_{(n_g x10)} & []_{(n_g x\ n_m)} & []_{(n_g x\ n_w)} & []_{(n_g x\ n_g)} \end{bmatrix} \begin{Bmatrix} \{\delta U^M\}_{(10)} \\ \{\delta u^m\}_{(n_m)} \\ \{\delta p_w^m\}_{(n_w)} \\ \{\delta p_g^m\}_{(n_g)} \end{Bmatrix} = \begin{Bmatrix} \{\}_{(10)} \\ \{\delta f^m\}_{(n_m)} \\ \{\delta q_w^m\}_{(n_w)} \\ \{\delta q_g^m\}_{(n_g)} \end{Bmatrix} \tag{VI–1}$$

In accordance with the decomposition of the microkinematics, the variables δp_w^m and δp_g^m are split in two parts, one is related to the variation of the macro pressures and the other one to the macro pressure gradients and the micro fluctuations:

$$\delta p_w^m = \delta p_w^M + \delta \hat{p}_w \tag{VI–2}$$

and

$$\delta p_g^m = \delta p_g^M + \delta \hat{p}_g \tag{VI–3}$$

Actually, δp_w^M and δp_g^M are already respectively the 7$^{\text{th}}$ and 10$^{\text{th}}$ components of $\{\delta U^M\}$. In order to obtain some fluid pressure terms accounting for the macroscale fluid pressure gradients and being independent from p_w^M and p_g^M, a system with the infinitesimal variations $\delta \hat{p}_w$ and $\delta \hat{p}_g$ is preferred to δp_w^m and δp_g^m.

For now, this system of equations is ill-posed as it does not contain the information of the boundary conditions yet. The system will be reduced by eliminating the dependent degrees of freedom located on the follow boundary and using the averaging summations defining the macroscale stress and fluxes. First, in order to fill the frame (VI–1), the partial derivatives equations describing the variation of the response need to be derived for the nodal force balance, the fluid mass balance and the macroscale specific fluid mass.

Variation of nodal forces

The variations of stresses depend on the variations of the macroscale pressure and the nodal displacements. The relation of the variation of nodal residual forces is written as follow:

$$\{\delta f^m\} = [K_{mm}]\{\delta u^m\} \ + \ [K_{mW}]\ \delta p_w^M \ + \ [K_{mG}]\ \delta p_g^M \tag{VI–4}$$

The matrix $[K_{mm}]$ is the one used to solve the mechanical problem for constant fluid pressures, it does not require further developments. The matrices $[K_{mW}]$ and $[K_{mG}]$ take into account the variations of fluid pressures acting normally on the matrix boundaries.

The variations of these hydraulic pressures, $\{\delta f^{p_w}\}$ and $\{\delta f^{p_g}\}$, are dependent on the variations of the macroscale fluid pressures δp_w^M and δp_g^M:

$$\{\delta f^{p_w}\} = \begin{bmatrix} 0 \\ -\delta\left(S_r p_w^M\right) \end{bmatrix} \tag{VI–5}$$

$$\{\delta f^{p_g}\} = \begin{bmatrix} 0 \\ -\delta\left((1-S_r)p_g^M\right) \end{bmatrix} \tag{VI–6}$$

The numerical integrations of the variations of the nodal contributions of the fluid pressures on the the residual forces of the interface elements lead to the following element matrices $[K_{mW}]^{eI}$ and $[K_{mG}]^{eI}$:

$$[K_{mW}]^{eI} = \sum_{IP}[B^I][A^I] \begin{bmatrix} \frac{\partial f_t^{p_w}}{\partial p_w^M} \\ \frac{\partial f_n^{p_w}}{\partial p_w^M} \end{bmatrix} \det\left(J_{ij}^I\right) W_G \tag{VI–7}$$

and

$$[K_{mG}]^{eI} = \sum_{IP}[B^I][A^I] \begin{bmatrix} \frac{\partial f_t^{p_g}}{\partial p_g^M} \\ \frac{\partial f_n^{p_g}}{\partial p_g^M} \end{bmatrix} \det\left(J_{ij}^I\right) W_G \tag{VI–8}$$

where the partial derivatives are

$$\frac{\partial f_t^{p_w}}{\partial p_w^M} = 0 \tag{VI–9}$$

$$\frac{\partial f_n^{p_w}}{\partial p_w^M} = -p_w^M \frac{\partial S_r}{\partial p_w^M} - S_r \tag{VI–10}$$

$$\frac{\partial f_t^{p_g}}{\partial p_g^M} = 0 \tag{VI–11}$$

$$\frac{\partial f_n^{p_g}}{\partial p_g^M} = p_g^M \frac{\partial S_r}{\partial p_g^M} - (1-S_r) \tag{VI–12}$$

These interface element matrices hold the following relations:

$$\{\delta f^{p_w}\}^{eI} = [K_{mW}]^{eI}\ \delta p_w^M \tag{VI–13}$$

and

$$\{\delta f^{p_g}\}^{eI} = [K_{mG}]^{eI}\ \delta p_g^M \tag{VI–14}$$

Finally, the assembly of the element matrices provides the global matrices $[K_{mW}]$ and $[K_{mG}]$.

Variation of fluid fluxes

The variation of the macroscale fluid fluxes $\{\delta q_w^M\}$ and $\{\delta q_g^M\}$ may be decomposed into some volumetric parts $\{\delta q_w^{M,V}\}$ and $\{\delta q_g^{M,V}\}$, and rheological parts $\{\delta q_w^{M,R}\}$ and $\{\delta q_g^{M,R}\}$. The volumetric fluxes are dependent on the configuration of the REV and the pressure gradients whereas the rheological parts depend on the variations of the fluid densities and the relative permeabilities which are only influenced by the macroscale fluid pressures.

For the volumetric parts, the variations $\{\delta q_w^{M,V}\}$ and $\{\delta q_g^{M,V}\}$ are dependent on the microscale kinematics $\{\delta u^m\}$, $\{\delta \hat{p}_w\}$ and $\{\delta \hat{p}_g\}$. On the microscale, the volumetric part of the variation of the nodal water mass balance writes

$$\{\delta q_w^{m,V}\} = [K_{wm}]\{\delta u^m\} + [K_{ww}]\{\delta \hat{p}_w\} + [K_{wg}]\{\delta \hat{p}_g\} \tag{VI–15}$$

and for gas, it reads

$$\{\delta q_g^{m,V}\} = [K_{gm}]\{\delta u^m\} + [K_{gw}]\{\delta \hat{p}_w\} + [K_{gg}]\{\delta \hat{p}_g\} \tag{VI–16}$$

The matrices $[K_{wm}]$ and $[K_{gm}]$ contain the partial derivatives of the interface mass fluxes ω_w^l and ω_g^l with respect to the nodal displacements $U_{(i)}^{Node}$.

For water, the derivatives of Equation (V–64) are:

$$\frac{\partial \omega_w^l}{\partial U_{(i)}^{Node}} = [p_w^m(n_2) - p_w^m(n_1)] \; \frac{\rho_w \, k_{rw}}{\mu_w} \frac{\partial \Phi^l}{\partial U_{(i)}^{Node}} \tag{VI–17}$$

The transmissivity can be rewritten as the integral over the parent element, it reads

$$\Phi^l = \left(\int_{-1}^{+1} \frac{1}{\kappa(s)} \, J \, d\xi \right)^{-1} \tag{VI–18}$$

Then, the partial derivatives can be developed:

$$\frac{\partial \Phi^l}{\partial U_{(i)}^{Node}} = -(\Phi^l)^2 \frac{\partial}{\partial U_{(i)}^{Node}} \left(\int_{-1}^{+1} \frac{1}{\kappa(\xi)} \, J \, d\xi \right) = -12(\Phi^l)^2 \, \frac{\partial}{\partial U_{(i)}^{Node}} \left(\int_{-1}^{+1} h_b(\xi)^{-3} \, \det(J_{ij}^I) \, d\xi \right) \tag{VI–19}$$

Replacing the integral by the weighed sum over the integration points, we have:

$$\begin{aligned} \frac{\partial \Phi^l}{\partial U_{(i)}^{Node}} &= -12(\Phi^l)^2 \, \frac{\partial}{\partial U_{(i)}^{Node}} \left(\sum_{IP} h_b(\xi)^{-3} \, J \, W_G \right) \\ &= \sum_{IP} \left(36(\Phi_w^l)^2 \, h_b(\xi)^{-4} \right) J \, W_G \, \frac{\partial h_b(\xi)}{\partial U_{(i)}^{Node}} \end{aligned} \tag{VI–20}$$

The relation between the residual mass balance at the interface hydraulic nodes $\{q\}^{eI}$ and the interface mass flux w^l is

$$\{q\}^{eI} = \begin{bmatrix} -1 \\ 1 \end{bmatrix} \omega^l \tag{VI–21}$$

Then, the element coupling matrix $[K_{wm}]^e$ holding the following relation:

$$\{\delta q\}^{eI} = [K_{wm}]^{eI} \left\{ \delta U^{Node} \right\} \tag{VI–22}$$

is given by:

$$[K_{wm}]^{eI} = \frac{\rho_w \, k_{rw}}{\mu_w} [p_w(n_2) - p_w(n_1)] \begin{bmatrix} -1 \\ 1 \end{bmatrix} \left[\frac{\partial \Phi_w^l}{\partial U_{(1x8)}^{Node}} \right] \tag{VI–23}$$

The matrix $[K_{wm}]$ is finally found assembling the element matrices $[K_{wm}]^{eI}$.

For gas, the partial derivatives of the flux defined by Equation (V–67) with respect to the displacements of the nodal coordinates $U_{(i)}^{Node}$ are:

$$\frac{\partial \omega_g^l}{\partial U_{(i)}^{Node}} = \left([p_g^m(n_2) - p_g^m(n_1)] \; \frac{\rho_{g,f} \, k_{rg}}{\mu_g} + [p_w^m(n_2) - p_w^m(n_1)] \, H_g \, \rho_{g,f} \, \frac{k_{rw}}{\mu_w} \right) \frac{\partial \Phi^l}{\partial U_{(i)}^{Node}} \tag{VI–24}$$

The element matrices $[K_{gm}]^{eI}$ are then derived from Equation (VI–24) and these matrices are assembled to find the matrix $[K_{gm}]$.

Then, the matrix $[K_{ww}]$ is

$$[K_{ww}] = \frac{\rho_w \, k_{rw}}{\mu_w} \begin{bmatrix} \phi^A & 0 & -\phi^A & 0 & 0 \\ 0 & \phi^B & -\phi^B & 0 & 0 \\ -\phi^A & -\phi^B & \phi^A + \phi^B + \phi^C + \phi^D & -\phi^C & -\phi^D \\ 0 & 0 & -\phi^C & \phi^C & 0 \\ 0 & 0 & -\phi^D & 0 & \phi^D \end{bmatrix} \tag{VI–25}$$

The matrix $[K_{wg}]$ is null if water vapour is not considered.

$$[K_{wg}] = [0] \tag{VI–26}$$

For gas, as gas dissolved in the water may be considered, the matrix $[K_{gw}]$ is not null. Moreover, the matrix $[K_{gg}]$ has to account for the gas fluxes in the interfaces but also for the diffusive fluxes in the matrix.

Finally, the variations of the rheological macroscale fluid fluxes can be computed entirely on the macroscale level. In a matrix form, it reads

$$\{\delta q_w^{M,R}\} = [M_{ww}^1]\{\delta p_w^M\} + [M_{wg}^1]\{\delta p_g^M\} \tag{VI–27}$$

and

$$\{\delta q_g^{M,R}\} = [M_{gg}^1]\{\delta p_g^M\} + [M_{gw}^1]\{\delta p_w^M\} \tag{VI–28}$$

where the matrices $[M_{ww}^1]$, $[M_{wg}^1]$, $[M_{gg}^1]$ and $[M_{gw}^1]$ are computed as follow:

$$[M_{ww}^1] = \left(\frac{\rho_{w0}}{\rho_w}\frac{1}{\chi_w} + \frac{1}{k_{rw}}\frac{\partial k_{rw}}{\partial p_w^M}\right)\begin{bmatrix} q_{w_1}^M \\ q_{w_2}^M \end{bmatrix} \tag{VI–29}$$

$$[M_{wg}^1] = \frac{1}{k_{rw}}\frac{\partial k_{rw}}{\partial p_g^M}\begin{bmatrix} q_{w_1}^M \\ q_{w_2}^M \end{bmatrix} \tag{VI–30}$$

$$[M_{gg}^1] = \left(\frac{\rho_{g0}}{\rho_g}\frac{1}{p_{g0}^M} + \frac{1}{k_{rg}}\frac{\partial k_{rg}}{\partial p_g^M}\right)\begin{bmatrix} q_{g_1}^M \\ q_{g_2}^M \end{bmatrix} + H_g\,\frac{\rho_{g0}}{\rho_g}\frac{1}{p_{g0}^M}\begin{bmatrix} q_{w_1}^M \\ q_{w_2}^M \end{bmatrix} \tag{VI–31}$$

$$[M_{gw}^1] = \frac{1}{k_{rg}}\frac{\partial k_{rg}}{\partial p_w^M}\begin{bmatrix} q_{g_1}^M \\ q_{g_2}^M \end{bmatrix} \tag{VI–32}$$

In these definitions, the derivatives of the relative permeabilities with respect to the fluid pressures are, in the case of coal, the derivatives of the expressions given in Equations (IV–60) and (IV–61) using the retention curve given by Equation (IV–72).

Variation of specific fluid mass

In the same way as the fluid fluxes, the variation of the fluid masses M_w^M and M_g^M can be divided in volumetric and rheological parts:

$$\{\delta M_w^{M,V}\} = [V_w^1]\{\delta u^m\} \tag{VI–33}$$

$$\{\delta M_w^{M,R}\} = [M_{ww}^2]\{\delta p_w^M\} + [M_{wg}^2]\{\delta p_g^M\} \tag{VI–34}$$

$$\{\delta M_g^{M,V}\} = [V_g^1]\{\delta u^m\} \tag{VI–35}$$

$$\{\delta M_g^{M,R}\} = [M_{gg}^2]\{\delta p_g^M\} + [M_{gw}^2]\{\delta p_w^M\} \tag{VI–36}$$

The volumetric parts require the relation between the variations of the hydraulic apertures h_b and the nodal displacements. From Equation (V–76), we have

$$\delta h_b = \begin{bmatrix} 0 & \frac{\partial h_b}{\partial h} \end{bmatrix}[A^I][B^I]\left\{\delta U^{Node}\right\} \tag{VI–37}$$

From the relation between the hydraulic and mechanical apertures detailed in section 9.2.3, the partial derivative $\frac{\partial h_b}{\partial h}$ is

$$\begin{aligned} \frac{\partial h_b}{\partial h} &= 1 \quad \text{if } h \geqslant 0 \\ &= 0 \quad \text{if } h < 0 \end{aligned} \tag{VI–38}$$

The numerical integration of the variation of the hydraulic aperture over the interface elements defines then the element matrices $[V_w^1]^e$ and $[V_g^1]^e$ as:

$$[V_w^1]^e = \frac{1}{\Omega} \sum_{IP} \rho_w \, S_r \, \left[0 \quad \frac{\partial h_b}{\partial h} \right] [A^I][B^I] \, \det(J_{ij}) \, W_G \tag{VI–39}$$

and

$$[V_g^1]^e = \frac{1}{\Omega} \sum_{IP} \left(\rho_{g,f} \, (1 - S_r) + \rho_{g,f}^d \, S_r \right) \, \left[0 \quad \frac{\partial h_b}{\partial h} \right] [A^I][B^I] \, \det(J_{ij}) \, W_G \tag{VI–40}$$

which hold the relations:

$$\delta M_w^{M,V\,e} = [V_w^1]^e \left\{ \delta U^{Node} \right\} \tag{VI–41}$$

and

$$\delta M_g^{M,V\,e} = [V_g^1]^e \left\{ \delta U^{Node} \right\} \tag{VI–42}$$

where $M_w^{M,V\,e}$ and $M_w^{M,V\,e}$ are the contributions of the volumetric part to the variations of the water and gas masses in the interface element. The global matrices $[V_w^1]$ and $[V_g^1]$ are obtained by assembly of the element matrices.

The rheological parts are more straightforward. For water, the matrices $[M_{ww}^2]$ and $[M_{wg}^2]$ are given by:

$$[M_{ww}^2] = \left(\frac{\rho_{w0}}{\rho_w} \frac{1}{\chi_w} + \frac{1}{S_r} \frac{\partial S_r}{\partial p_w^M} \right) \, M_w^M \tag{VI–43}$$

$$[M_{wg}^2] = \frac{1}{S_r} \frac{\partial S_r}{\partial p_{g,f}^M} \, M_w^M \tag{VI–44}$$

For gas, the matrices $[M_{gg}^2]$ and $[M_{gw}^2]$ are:

$$[M_{gg}^2] = \left(\frac{\rho_{g0}}{\rho_{g,f}} \frac{1}{p_{g0}^M} + \frac{-1}{1 - S_r} \frac{\partial S_r}{\partial p_g^M} \right) M_g^g + H_g \, \frac{\rho_{g0}}{\rho_{g,f}} \frac{1}{p_{g0}^M} \, M_g^d \tag{VI–45}$$

$$[M_{gw}^2] = \frac{-1}{1 - S_r} \frac{\partial S_r}{\partial p_w^M} \, M_g^g \tag{VI–46}$$

Assembly

The matrices containing the equations for the variations of forces, fluid fluxes and fluid mass are now assembled to lead to the following system of equations:

$$
\begin{bmatrix}
0_{4x4} & 0_{4x2} & 0_{4x1} & 0_{4x2} & 0_{4x1} \\
0_{2x4} & 0_{2x2} & M^1_{ww}{}_{2x1} & 0_{2x2} & M^1_{wg}{}_{2x1} \\
0_{1x4} & 0_{1x2} & M^2_{ww}{}_{1x1} & 0_{1x2} & M^2_{wg}{}_{1x1} \\
0_{2x4} & 0_{2x2} & M^1_{gw}{}_{2x1} & 0_{2x2} & M^1_{gg}{}_{2x1} \\
0_{1x4} & 0_{1x2} & M^2_{gw}{}_{1x1} & 0_{1x2} & M^2_{gg}{}_{1x1}
\end{bmatrix}
\begin{bmatrix}
0_{4\,x\,n_m} & 0_{4\,x\,n_w} & 0_{4\,x\,n_g} \\
0_{2\,x\,n_m} & 0_{2\,x\,n_w} & 0_{2\,x\,n_g} \\
V^1_w{}_{1\,x\,n_m} & 0_{1\,x\,n_w} & 0_{1\,x\,n_g} \\
0_{2\,x\,n_m} & 0_{2\,x\,n_w} & 0_{2\,x\,n_g} \\
V^1_g{}_{1\,x\,n_m} & 0_{1\,x\,n_w} & 0_{1\,x\,n_g}
\end{bmatrix}
\begin{matrix} M \\ p^M_w \\ p^M_w \\ p^M_g \\ p^M_g \end{matrix}_{10}
$$

$$
\begin{bmatrix}
0_{n_m x\,4} & 0_{n_m x\,2} & K_{mW}{}_{n_m x\,1} & 0_{n_m x\,2} & K_{mG}{}_{n_m x\,1} \\
0_{n_w x\,4} & 0_{n_w x\,2} & 0_{n_w x\,1} & 0_{n_w x\,2} & 0_{n_w x\,1} \\
0_{n_g x\,4} & 0_{n_g x\,2} & 0_{n_g x\,1} & 0_{n_g x\,2} & 0_{n_g x\,1}
\end{bmatrix}
\begin{bmatrix}
K_{mm}{}_{n_m x\,n_m} & 0_{n_m x\,n_w} & 0_{n_m x\,n_g} \\
K_{wm}{}_{n_w x\,n_m} & K_{ww}{}_{n_w x\,n_w} & K_{wg}{}_{n_w x\,n_g} \\
K_{gm}{}_{n_g x\,n_m} & K_{gw}{}_{n_g x\,n_w} & K_{gg}{}_{n_g x\,n_g}
\end{bmatrix}
\begin{matrix} u^m{}_{n_m} \\ p^m_w{}_{n_w} \\ p^m_g{}_{n_g} \end{matrix}
$$

$$
\begin{matrix} 0 \\ q^{M\,R}_w \\ M^M_w \\ q^{M\,R}_g \\ M^M_g \end{matrix}_{10}
$$

$$
\begin{matrix} f^m{}_{n_m} \\ q^{m\,V}_w{}_{n_w} \\ q^{m\,V}_g{}_{n_g} \end{matrix}
$$

(VI–47)

Reduction

This system of equations can be reduced by eliminating the dependent degrees of freedom using the boundary conditions given by Equations (V–33) to (V–38). In addition, the averaging summations given by Equations (V–97, (V–101) and (V–101) are also used to result in the following reduced system:

$$
\begin{bmatrix}
T^1_{\ 4x4} & 0_{\ 4x2} & T^2_{\ 4x1} & 0_{\ 4x2} & T^3_{\ 4x1} \\
T^4_{\ 2x4} & T^5_{\ 2x2} & M^1_{w\ 2x1} & 0_{\ 2x2} & 0_{\ 2x1} \\
T^6_{\ 1x4} & 0_{\ 1x2} & M^2_{w\ 1x1} & 0_{\ 1x2} & 0_{\ 1x1} \\
T^7_{\ 2x4} & 0_{\ 2x2} & 0_{\ 2x1} & T^8_{\ 2x2} & M^1_{g\ 2x1} \\
T^9_{\ 1x4} & 0_{\ 1x2} & 0_{\ 1x1} & 0_{\ 1x2} & M^2_{g\ 1x1}
\end{bmatrix}
\begin{bmatrix}
T^{10}_{\ 4\ x\ n_m} & 0_{\ 4\ x\ n_w} & 0_{\ 4\ x\ n_g} \\
T^{11}_{\ 2\ x\ n_m} & T^{12}_{\ 2\ x\ n_w} & T^{13}_{\ 2\ x\ n_g} \\
V^1_{w\ 1\ x\ n_m} & 0_{\ 1\ x\ n_w} & 0_{\ 1\ x\ n_g} \\
T^{14}_{\ 2\ x\ n_m} & T^{15}_{\ 2\ x\ n_w} & T^{16}_{\ 2\ x\ n_g} \\
V^1_{g\ 1\ x\ n_m} & 0_{\ 1\ x\ n_w} & 0_{\ 1\ x\ n_g}
\end{bmatrix}
\begin{bmatrix}
M \\ p_w^M \\ p_w^M \\ p_g^M \\ p_g^M
\end{bmatrix}_{10}
$$

$$
\begin{bmatrix}
T^{17}_{\ n_m x\ 4} & 0_{\ n_m x\ 2} & K_{mW\ n_m x\ 1} & 0_{\ n_m x\ 2} & K_{mG\ n_m x\ 1} \\
T^{18}_{\ n_w x\ 4} & T^{19}_{\ n_w x\ 2} & 0_{\ n_w x\ 1} & T^{20}_{\ n_w x\ 2} & 0_{\ n_w x\ 1} \\
T^{21}_{\ n_g x\ 4} & T^{22}_{\ n_g x\ 2} & 0_{\ n_g x\ 1} & T^{23}_{\ n_g x\ 2} & 0_{\ n_g x\ 1}
\end{bmatrix}
\begin{bmatrix}
C_{mm\ n_m x\ n_m} & 0_{\ n_m x\ n_w} & 0_{\ n_m x\ n_g} \\
K_{wm\ n_w x\ n_m} & K_{ww\ n_w x\ n_w} & K_{wg\ n_w x\ n_g} \\
K_{gm\ n_g x\ n_m} & K_{gw\ n_g x\ n_w} & K_{gg\ n_g x\ n_g}
\end{bmatrix}
\begin{bmatrix}
u^{\ m}_{\ n_m} \\ p_w^{\ m}_{\ n_w} \\ p_g^{\ m}_{\ n_g}
\end{bmatrix}
$$

$$
\begin{bmatrix}
M \\ q_w^M \\ M_w^M \\ q_g^M \\ M_g^M
\end{bmatrix}_{10}
\quad
\begin{bmatrix}
0_{\ n_m} \\ 0_{\ n_w} \\ 0_{\ n_g}
\end{bmatrix}
\tag{VI–48}
$$

with $T^{1\ \ 23}$ some temporary matrices. The superscript $\ $ indicates the reduced form of the original matrices with n_m, n_w and n_g the numbers of independent mechanical, water and gas degrees of freedom.

Condensation

The system of Equations (VI–48) is shortly written as

$$
\begin{bmatrix}
T_A & T_B \\
T_C & T_D
\end{bmatrix}
\begin{bmatrix}
U^M_{\ 10} \\ U^{\ m}
\end{bmatrix}
=
\begin{bmatrix}
^M_{\ 10} \\ 0
\end{bmatrix}
\tag{VI–49}
$$

where the matrices $T_{A\ \ D}$ are some reduced matrices and $U^{\ m}$ contains the independent microscale degrees of freedom.

This system of equations is then reduced on the ten macroscopic variables ^{M} to obtain the stiffness matrix A^M required to solve Equation (V–108). It is finally given by:

$$
A^M_{\ 10x10} \quad T_A \quad T_B \ T_D \ ^1 \ T_C \tag{VI–50}
$$